

MODELLING TECHNIQUES FOR
1-3 COMPOSITE TRANSDUCERS

Presented by

JOHN A HOSSACK

In the fulfilment of the requirement
for the degree of
Doctor of Philosophy
of the
University of Strathclyde

Department of Electronic and Electrical Engineering

MARCH 1990

GLASGOW

The copyright of this thesis belongs to the author under the terms of the United Kingdom Copyrights Act as qualified by University of Strathclyde Regulation 3.49. Due acknowledgement must always be made of the use of any material contained in, or derived from, this thesis.

LIST OF CONTENTS

	PAGE
ABSTRACT	(vi)
LIST OF SYMBOLS	(vii)
DEFINITION OF AXES	(x)
CHAPTER I	
INTRODUCTION	
1.1 Ultrasonic transducers	1
1.2 Composite transducers	4
1.3 Aims and contributions of the thesis	7
CHAPTER II	
REVIEW OF THE MODELLING AND DESIGN OF COMPOSITE PIEZOELECTRIC TRANSDUCERS	
2.1 Introduction	11
2.2 Hydrophone applications	12
i) 1-3 Connectivity	
ii) 0-3 Connectivity	
2.3 Biomedical Applications	19
2.4 Array applications	24
2.5 Modelling composite transducer parameters	26
2.6 Modelling the performance of composite transducers	32
2.7 Inter rod resonant activity	36
2.8 Finite element analysis	38
2.9 Concluding remarks	41
CHAPTER III	
FINITE ELEMENT ANALYSIS OF COMPOSITE TRANSDUCER STRUCTURES	
3.1 Introduction	44
3.2 Review of the Finite Element Method	45
3.3 Verification of the ANSYS Finite Element Code for piezoelectric structures	57

3.4	Finite Element Analysis of composite structures	59
3.5	Finite Element Analysis of array structures	63
3.6	Concluding Remarks	64

CHAPTER 4

INVESTIGATION OF MATERIALS AND CONFIGURATIONS

4.1	Introduction	65
4.2	Selection of constituent materials	66
	i) Selection of ceramic	
	ii) Selection of polymer	
	iii) Influence of modified polymers on composite transducer characteristics	
4.3	Selection of geometry	79
	i) Introduction	
	ii) Dependence of wave velocity on ceramic volume fraction	
	iii) Dependence of velocity on ceramic pillar width to height ratio	
	iv) Dependence of coupling coefficient on ceramic volume fraction	
	v) Dependence of coupling coefficient on ceramic pillar width to height ratio	
	vi) Conclusions on volume fraction and pillar width to height ratio	
4.4	Comparison of the characteristics obtained when alternative pillar geometries are employed	90
	i) Circular pillars	
	ii) Triangular pillars	
	iii) Rectangular pillars	
	iv) Tapered pillars	
4.5	Methods for enhancing device bandwidth	99
	i) Diverse thickness	
	ii) Diverse pillar configurations	
4.6	Concluding remarks	102

CHAPTER V

MODELLING THE CHARACTERISTICS OF COMPOSITE PIEZOELECTRIC TRANSDUCERS

5.1	Introduction	104
5.2	Review and extension of Smith's thickness mode parameter model for composite transducers	105

5.3	Development of a suitable thickness mode transducer model	109
5.4	Inclusion of loss in the thickness mode transducer model	115
5.5	Modelling the operational impedance of a composite piezoelectric transducer	121
	i) General characteristics of the impedance model	
	ii) Influence of internal loss on transducer impedance	
	iii) Influence of a matching layer on transducer impedance	
	iv) Influence of acoustic backing on transducer impedance	
5.6	Modelling the transmission characteristics of a composite piezoelectric transducer	132
	i) General transmission model	
	ii) Transmission characteristics of composite transducers under CW excitation	
	iii) Transmission characteristics of composite transducers under transient excitation	
5.7	Modelling the reception characteristics of a composite piezoelectric transducer	138
	i) General reception model	
	ii) Reception characteristics of composite transducers under CW excitation	
5.8	Modelling the pulse-echo characteristics of a composite piezoelectric transducer	141
	i) General pulse-echo model	
	ii) Pulse-echo characteristics of composite transducers under CW excitation	
	iii) Pulse-echo characteristics of composite transducers under transient excitation	
5.9	Concluding Remarks	147

CHAPTER VI

ELECTROMECHANICAL AND SPATIAL FIELD CHARACTERISTICS OF COMPOSITE ARRAYS

6.1	Introduction	148
6.2	Review of important imaging strategies and requisite array characteristics	150
6.3	Theoretical spatial field characteristics of array elements	156

6.4	Field characteristics of practical elements	173
	i) Introduction	
	ii) Field characteristics of isolated elements	
	iii) Field characteristics of practical composite elements operating under CW excitation	
	iv) Field characteristics of practical composite elements operating under transient excitation	
	v) Comparison of the spatial characteristics of composite and conventional array elements	
6.5	Electromechanical characteristics of composite arrays	185
	i) Permittivity	
	ii) Velocity	
	iii) Electromechanical coupling coefficient	
6.6	Performance of focused arrays	193
	i) Introduction	
	ii) Theoretical response of focused beams	
	iii) Practical implementation of a focused array	
	iv) Theoretical and measured field response of focused arrays	
	vi) Synthetic focusing in reception	
6.7	Characteristics of two-dimensional arrays	202
	i) Introduction	
	ii) Electromechanical and spatial field characteristics of 2-D array elements	
	iv) Imaging performance of the prototype 2-D composite array	
6.8	Concluding remarks	208

CHAPTER VII

MODELLING THE CHARACTERISTICS OF STACKED COMPOSITE TRANSDUCERS

7.1	Introduction	210
7.2	Development of a stacked transducer model	214
	i) Independent electrical excitation/ loading of the active layers	
	ii) Parallel electrical excitation/ loading of the active layers	
7.3	Performance of stacked composite structures	218
	i) Impedance as a function of the number of layers	
	ii) Transmission performance of stacked composite transducers	
	iii) Reception performance of stacked composite transducers	
	iv) Pulse-echo performance of stacked composite transducers	

7.4 Asymmetric stacked composite structures	236	
i) Diverse layer thickness		
ii) Diverse layer electrical loading		
iii) Diverse layer material characteristics		
7.5 Concluding remarks	242	
CHAPTER VIII		
CONCLUSIONS, APPLICATIONS AND RECOMMENDATIONS FOR FURTHER WORK		
8.1 Concluding Summary	244	
8.2 Applications of composite transducers	247	
i) Advanced arrays		
ii) Low frequency/ high bandwidth transducers		
8.3 Recommendations for further work	249	
i) Manufacture		
ii) Wave attenuation		
iii) Uniformity of vibration within composite structures		
iv) Performance of composite materials in arrays		
v) Stacked composite structures		
ACKNOWLEDGEMENTS	252	
REFERENCES AND BIBLIOBIOGRAPHY	253	
APPENDICES		
Appendix A	Material Parameters	259
Appendix B	Composite manufacture	263
Appendix C	Probe and array manufacture	267
Appendix D	Depolarisation in a 1-3 composite	273
Appendix E	Experimental techniques	277
Appendix F	List of publications arising from the thesis	283

ABSTRACT

A selection of novel modelling techniques are presented for predicting the behaviour of a thickness mode composite piezoelectric transducer comprising an array of ceramic pillars embedded in a polymer matrix. Finite element analysis is employed to establish the vibrational and electromechanical characteristics of an arbitrary composite structure. Thereafter, the equivalent thickness mode transducer parameters are employed in a modified transducer model to establish the impedance, transmission and reception characteristics. A novel algorithm for calculating the acoustic pressure profile, resulting from an arbitrarily excited, rectangular aperture is employed to determine the field structure of the composite transducer. This algorithm is incorporated into an array model capable of predicting the field characteristics of steered and focused arrays. Theoretical and practical results, for composite, sliced and monolithic ceramic arrays are compared. Finally, low frequency, stacked composite structures are considered. A range of novel characteristics are obtained by using, to full advantage, the versatility of composite materials. It is believed that these modelling techniques, which have been verified experimentally, offer considerable insight into composite transducer behaviour and are conducive to effective, computer based, design.

LIST OF SYMBOLS

The following is a list of the more important symbols found in the thesis. Less significant symbols are defined within the text as required. These symbols comply with the relevant IEEE standard [1].

The subscript 'x' defines the relevant translational direction. These may take the values 1, 2 or 3 and relate to the axis notation illustrated in Figure 1.0. Where a symbol has subscript 'xy', then 'x' and 'y' may take values between 1 and 6. Directions 4, 5, 6 relate to rotational components, as defined in Figure 1.0.

SYMBOL	MEANING	UNIT
a	Attenuation coefficient	
a_{dB}	Attenuation coefficient (dB)	dBm^{-1}
a_n	Attenuation coefficient (nepers)	nm^{-1}
C (superscript)	Denotes ceramic phase	
c	Speed	ms^{-1}
c_{xy}	Elastic stiffness constant	Pa or Nm^{-2}
C	Capacitance	F
D (superscript)	Constant electric displacement	
d	Device thickness	m
d_{xy}	Piezoelectric strain coefficient	mV^{-1}
D_x	Electric displacement	FVm^{-2}
E (superscript)	Constant electric field	
e_{xy}	Piezoelectric stress constant	Cm^{-1}

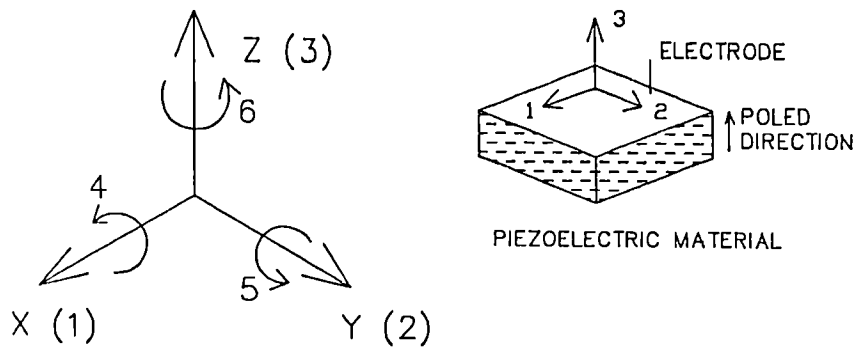
SYMBOL	MEANING	UNIT
E_x	Electric field	Vm^{-1}
f	Frequency	Hz
f_m	Frequency of minimum impedance	Hz
f_n	Frequency of maximum impedance	Hz
F	Force	N
g_{xy}	Piezoelectric voltage constant	VmN^{-1}
h_{xy}	Piezoelectric stiffness constant	Vm^{-1}
$h(x,t)$	Velocity potential impulse response at point 'x'	$Nmskg^{-1}$
I	Current	A
j	Complex operator - $\sqrt{(-1)}$	
k_{xy}	Piezoelectric coupling coefficient	
L	Inductance	H
l	Length	m
P (superscript)	Denotes polymer phase	
P	Pressure	Pa or Nm^{-2}
Q	Charge	C
Q_m	Mechanical Q factor	
R	Resistance	
S (superscript)	Constant strain conditions	
s	Laplace operator	
s_{xy}	Elastic compliance constant	m^2N^{-1}
S_x	Strain component	
T (superscript)	Constant stress conditions	
t	Time	s
T	Thickness transit time	s
T_x	Stress	Pa or Nm^{-2}
$[]^T$	Matrix transpose	

SYMBOL	MEANING	UNIT
u	Displacement	m
U	Electrical load factor	
v	Ceramic volume fraction	
v_x	Velocity	ms^{-1}
V	Potential difference	V
w	Angular frequency	$\text{Radians}\cdot\text{s}^{-1}$
Y	Admittance	S
Z	Impedance	Ω
Z_m	Mechanical impedance	Rayl
α	'Is proportional to'	
δ	Virtual operator	
ϵ	Permittivity	Fm^{-1}
ρ	Density	kgm^{-3}
λ	Wavelength	m
σ	Poisson ratio	
φ	Potential	V
x	Arbitrary observation point in an acoustic field	
$\Phi(x,t)$	Velocity potential at point 'x'	$\text{Nm}\cdot\text{s}\cdot\text{kg}^{-1}$

The Laplace operator is 's', and Laplace quantities are denoted by a bar symbol ($\bar{}$)

AXIS CONVENTION

The following axis convention has been used throughout the thesis.



3 is the 'thickness' direction
1 and 2 are 'lateral' directions
4, 5 and 6 are rotational directions

Figure 1.0 Axis convention

CHAPTER I

INTRODUCTION

1.1 ULTRASONIC TRANSDUCERS

The ability to propagate and receive acoustic signals through opaque materials forms the basis of several important technologies. These include active sonar, medical imaging and non-destructive examination (NDE). Each of these relies upon the ability to convert efficiently, electrical signals to acoustic signals, and vice versa. This conversion is normally achieved using synthetic piezoelectric materials. In particular, various formulations of Lead Zirconate Titanate (PZT) have dominated the piezoelectric transducer field. Previously favoured natural piezoelectric materials, such as quartz and Rochelle salt, rapidly became obsolescent with the advent of these newer, superior materials. The use of these materials in thickness mode transducers for NDE, biomedical imaging and sonar is commonplace.

Increasingly, arrays of discrete piezoelectric elements are employed so that multiple acoustic scans can be made. This data is then processed digitally in a computer and an image of the target reconstructed. Generally, the technology associated with the electronics and processing hardware of acoustic systems has progressed more rapidly than that of transducers. Thus, the future development of these systems is often limited by available transducer technology. Piezoelectric ceramics possess a number of inherent deficiencies. These deficiencies are most evident when the operating medium is a fluid.

Firstly, ceramics are invariably poorly matched acoustically to fluid media. This results in a high degree of reflection at the ceramic/ fluid interface, and this in turn, results in low bandwidth. High bandwidth is desirable for the majority of acoustic systems. Where transient excitation is employed, high bandwidth is required so that the resulting acoustic pulse is short. A short pulse is normally required if a high imaging resolution is to be achieved.

Piezoelectric ceramics frequently possess relatively low electromechanical coupling coefficients. Although the thickness mode coupling coefficient may attain the value of 0.7 for certain configurations, it is limited, in practice, to approximately 0.5 in thin plates. This reduced value is a consequence of elastic stiffening in the thickness direction, as a result of Poisson ratio coupling from the larger lateral dimension.

Piezoelectric transducers must also be designed carefully so as to avoid spurious parasitic resonant activity in the vicinity of the thickness operating frequency. This restriction is particularly critical in array design, where the geometry of the elements is influenced by the desired spatial sampling characteristics of the array.

In recent years, two new ceramics, namely modified Lead Titanate (PT) and Lead Metaniobate (PN), have become available. These materials exhibit far less coupling between the thickness and lateral directions. However,

their disappointingly low piezoelectric efficiency and electrical permittivity has inhibited their widespread acceptance as a suitable transducer material. Furthermore, their acoustic match to water is, only slightly, if at all, improved over that of PZT.

Polyvinylidene Fluoride (PVDF), which is a piezoelectric polymer, became available in the 1970s. It is therefore well matched to fluid media and exhibits few extraneous parasitic modes of vibration. However, in the context of active transducer design, it has several fundamental flaws. It is normally only available in very thin sheets, and hence is generally only applicable for operation at frequencies above approximately 2MHz. It is frequently necessary to stack several layers of the material together in order to achieve the desired centre frequency. Additionally, PVDF possesses a low electromechanical coupling coefficient - typically 0.3. It also has a very low electrical permittivity, and hence is a poor transmitter of ultrasound since very high voltages are required to achieve adequate charge transfer. The relative permittivity is typically 10, and compares extremely unfavourably with that available in PZT ceramics (800).

It is evident that both ceramic and polymer transducer materials possess both desirable and undesirable properties. There is therefore a motivation to develop a material with intermediate properties. This would be designed to achieve the best balance of the properties of both ceramic and polymer materials.

1.2 COMPOSITE TRANSDUCERS

Over the past few years a diverse variety of composite transducer designs have been proposed. Generally, these combine an active piezoelectric ceramic phase and a passive polymer phase. The aim has been to achieve high electromechanical efficiency and low acoustic impedance simultaneously. The more important designs are reviewed in Chapter II. This thesis is primarily concerned with the design and modelling of 1-3 composite transducers. Figure 1.1 illustrates the general configuration of one of these transducers, which comprises piezoelectric ceramic pillars embedded in a polymer matrix. The rods are connected continuously in one direction, while the polymer is connected continuously in three directions. Hence, this configuration is described as possessing 1-3 connectivity.

The choice of 1-3 connectivity is discussed in detail in Chapter II. The principal advantages of this design are the simplicity of manufacture and the ease with which it may be analysed theoretically. 1-3 composites are normally manufactured by slicing a series of perpendicular slots in a piece of piezoelectric ceramic [2]. The spaces between the resulting array of ceramic pillars are subsequently filled with a suitable polymer. A low cost saw is suitable for manufacture and the characteristics of the resulting structure may be altered, in an easily controllable manner, by simply varying the saw cut width or pitch. A wide range of device characteristics are achievable using this technique. Some of the other connectivities, for

example 0-3 and 3-3, are difficult and expensive to manufacture in a controllable fashion. The regular, well defined geometry which the 1-3 connectivity possesses, makes it amenable to theoretical analysis. By making simplifying approximations regarding the stress, strain and electric field in the structure, a set of simple formulae may be derived for an 'equivalent' homogeneous material [3]. These formulae are perfectly adequate for the majority of practical applications. The ratio of ceramic volume to total volume is probably the most important parameter in the design of a composite transducer, and is termed the 'ceramic volume fraction'. Generally, lower ceramic volume fraction composite transducers have been favoured, since they simultaneously possess low acoustic impedance and a relatively high electromechanical efficiency. Unfortunately, there has been a tendency for designers to pursue optimal device material parameters, rather than considering the complete transducer system characteristics. Thus, the consequence of using a low ceramic volume fraction, with a low permittivity, has been largely ignored. In some practical configurations, a less efficient ceramic transducer will produce a higher signal level than a similar composite transducer, simply because it has a higher capacitance, and consequently a lower operating impedance. This means that the transducer requires a lower excitation voltage in transmission and is less susceptible to electrical loading effects in reception. The requirement for a comprehensive modelling strategy, encompassing equivalent thickness mode

material parameter estimation, and practical device simulation is readily apparent.

Without doubt, composite transducer materials have a role in array applications. The anisotropic nature of 1-3 materials makes them attractive for use in arrays wherein the elements are defined by the electrodes alone. It has been proposed that there is sufficient mechanical and electrical isolation between elements, that subdicing is unnecessary [4]. However, the electromechanical and spatial field characteristics of practical composite array elements have, in some respects, been disappointing.

Although composite transducers have few advantages over conventional ceramic transducers for the NDE of metallic media, they have considerable potential for the examination of lossy and porous media. In particular, wood and concrete are difficult materials to examine. The successful examination of these materials requires a transducer operating at a relatively low frequency so that frequency dependent attenuation and scattering is minimised. However, the design and application of suitable composite structures, specifically designed for the NDE of lossy media, has received no attention in the literature.

1.3 AIMS AND CONTRIBUTIONS OF THE THESIS

A comprehensive modelling strategy for composite transducers is presented. In developing this strategy, the aim has been to establish a greater understanding of the behaviour of a complete range of composite transducers, and arrays, under practical operating conditions. This knowledge relates to the internal behaviour of the composite material, the performance of composite transducers operating within a practical acoustic system, and the acoustic field characteristics of typical composite structures.

The contribution made by this thesis encompasses several aspects of the modelling of composite transducers.

1. Finite Element Analysis

A comprehensive range of materials and geometries are analysed. The aim is to identify those configurations which produce the best thickness mode transducers. This quality is measured in terms of uniformity of vibration and electromechanical coupling efficiency. The dependence of these factors on composite structure geometry is thoroughly investigated. The results obtained are compared with those obtained using Smith's unidimensional model [3] for predicting equivalent composite transducer parameters.

2. Thickness mode transducer modelling

Once it has been established that a specified design is practical, and will provide uniform thickness mode vibration, the equivalent thickness mode parameters may be

substituted into a suitable transducer model. Although the equivalent circuit analogies developed by Mason [5], and Krimoltz, Leedom and Matthei (KLM) [6] may be used, a more versatile model, based on that developed by Hayward [7] has been used here. This model incorporates the effects of matching layers, backing media, source/receiver electrical circuitry and distance, and frequency, related attenuation.

A wide range of practical composite transducer systems is analysed using this model. Designs, which produce an optimal performance with respect to a specific requirement, are identified using these techniques.

3. Composite array modelling

Thickness mode modelling is extended to include the modelling of array elements. In particular, the electromechanical and spatial field characteristics of array elements are investigated. Finite element analysis is used to determine the electromechanical efficiency and aperture displacement function for a variety of designs. It is concluded that these functions are rather more complex than was previously assumed.

A novel technique for evaluating the acoustic pressure profile resulting from an arbitrarily excited rectangular aperture is presented. This is extended to account for non-uniform vibration and is used in conjunction with the thickness mode model. Hence, a complete model for predicting the pressure response at an arbitrary point,

due to any particular design of composite transducer operating under an arbitrary excitation, is obtained.

This model is used as the basis of a transducer array model, which can predict the acoustic field profile of steered or focused ultrasonic arrays. A high specification array controller has been developed to permit experimental verification of the theoretical results obtained.

4. Array imaging

Prototype one dimensional composite arrays have been fabricated. The practical imaging performance of these arrays compare favourably with that of conventional sliced and monolithic ceramic arrays. These arrays are used in a synthetic focusing mode and hence the image quality is superior to that which would be obtained using B-scan methods.

A novel two dimensional composite array has been designed and tested. The electromechanical, spatial field and imaging characteristics of this array are investigated. Satisfactory three dimensional images are obtained using this array.

5. Modelling of stacked composite structures

The impedance, transmission and reception characteristics of a range of stacked, low frequency, composite transducers are investigated. In addition to the theoretical modelling of stacked transducers, several practical stacked, composite structures have been fabricated. The modelling technique has formed the basis

of an investigation of some novel, multi-resonant, stacked transducer designs.

Throughout the thesis, theoretical results have been verified with experimental results. Generally, good correlation is exhibited and any significant deviations are discussed and explained. During this process, reliable manufacturing processes for the fabrication of composite transducers and arrays have been developed.

Chapters III and IV describe the finite element analysis of a range of composite configurations. In Chapter V, a comprehensive thickness mode model for composite transducers is discussed and verified for a wide variety of practical designs. Chapter VI considers the electromechanical and acoustic properties of composite materials where they are used in arrays. The chapter also contains a comparison of the practical imaging performance of a selection of one and two dimensional arrays. Finally, the modelling and performance of practical, stacked composite structures are considered in Chapter VII.

CHAPTER II

REVIEW OF THE MODELLING AND DESIGN OF COMPOSITE PIEZOELECTRIC TRANSDUCERS

2.1 INTRODUCTION

This chapter presents a review of the important theories and results relating to composite transducers described in the literature. The aim of the chapter is to identify those aspects of composite transducer technology which require further investigation.

The earliest application of composite transducers was in low frequency hydrophones. This work is briefly reviewed and findings relevant to active transducer operation are highlighted. Thereafter, previous work concerning array and biomedical applications is presented. Finally, theoretical models for determining the equivalent material parameters, device performance and complex resonant activity of composite transducers, are reviewed and their validity assessed. A brief review of finite element modelling of composite transducer behaviour is also presented.

2.2 HYDROPHONE APPLICATIONS

Originally, composite piezoelectric materials were developed, for use in low frequency hydrophones in the late 1970s. Unfortunately, although conventional Lead Zirconate Titanate materials possess a high piezoelectric efficiency, they are very inefficient when used in a hydrostatic mode. This is because, in hydrostatic operation, the charge induced due to laterally applied pressure almost cancels the charge generated via the thickness direction. The aim in manufacturing a composite hydrophone is to decouple laterally applied energy from the ceramic by embedding the ceramic material in a soft polymer matrix. A review of this work is described by Newnham et al [8]. Excellent results have been obtained and these have been compared using the $g_h d_h$ hydrostatic figure of merit. The unit, g_h , is the hydrostatic charge coefficient with units mV-m/N. For example the $d_h g_h$ figure for PZT 5A may be increased from $100 \times 10^{-15} \text{m}^2/\text{N}$ to $100,000 \times 10^{-15} \text{m}^2/\text{N}$ in a composite transducer comprising PZT pillars embedded in a foamed epoxy resin [8]. In comparison, the $d_h g_h$ figure for the other principal hydrophone material, PVDF, is $1100 \times 10^{-15} \text{m}^2/\text{N}$.

A variety of geometries have been considered for use in composite transducer manufacture. Newnham et al have introduced a convention for describing the connectivity of composite transducers [9,10]. There are ten basic connectivities for a two phase system. In this convention two numbers are normally used. The first describes the

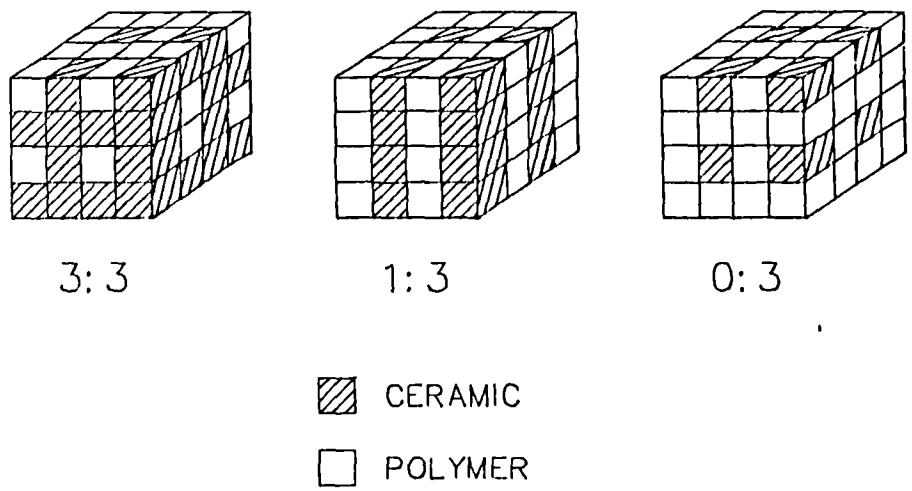


Figure 2.1 The three principal practical configurations of composite transducer.

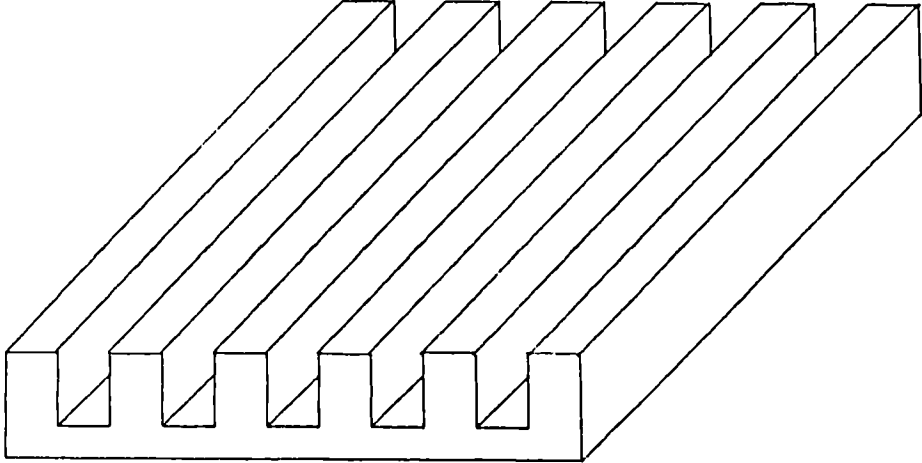
number of mutually perpendicular directions in which the ceramic phase is continuous. The second number, and third if required, describes the number of directions in which the polymer, or other materials, are continuous. The three most important connectivities are 3-3, 1-3 and 0-3. These are illustrated in Figure 2.1. 3-3 transducers were the first type to be manufactured. This process involved the use of a cumbersome coral replamine technique [10], which is now virtually obsolete.

2.2 i) 1-3 Connectivity

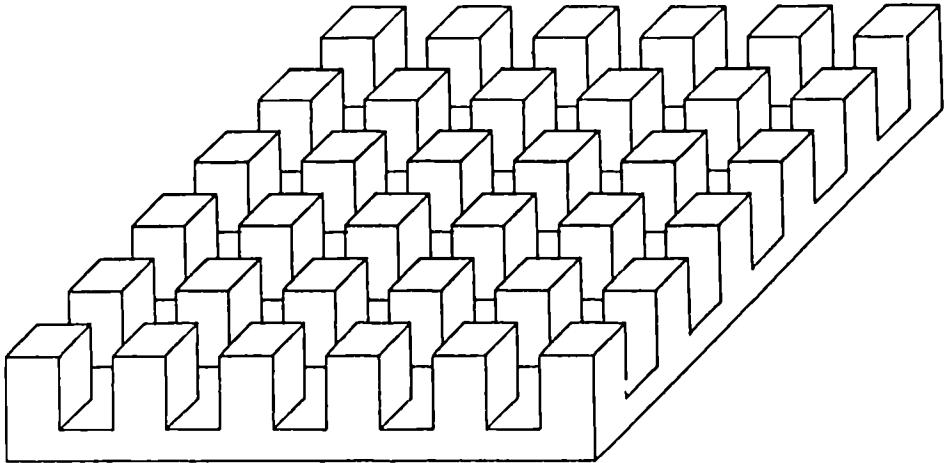
1-3 transducers have been comprehensively investigated. These have the greatest potential for application in active transducers. The 1-3 connectivity comprises of piezoelectric pillars orientated in the thickness direction. These are embedded in a polymer matrix. The original method of manufacture involved the separate extrusion of fine piezoceramic pillars which were fired prior to positioning in an intricate mould. The complete assembly was potted with a suitable polymer and a section of the required thickness sliced from the resulting block of composite material. The transducer was then electroded and poled.

An alternative, and very much simpler, process was developed by Savakus [2]. A prepolarised ceramic disc, as supplied conventionally by the manufacturer, is mounted on a diamond saw. A series of parallel cuts are made in the disc. The disc is then rotated through 90° and a second series of cuts made, as illustrated in Figure 2.2. This

Figure 2.2 Simplified manufacture of a 1-3 composite using two perpendicular sets of parallel sawn slots.



After first set of cuts



After second set of cuts

process leaves an array of square pillars. The spaces between these pillars are filled using a suitable polymer. The transducer is then lapped to the required thickness and electroded. As the ceramic is prepolarised, further poling is not necessary, although this may be desirable in the unlikely event that substantial depoling has occurred during manufacture.

The latter of these two manufacturing techniques is vastly more attractive for the construction of composite transducers possessing ceramic volume fractions greater than approximately 15%. Not only is there a significant saving in manufacturing time and complexity, but the capital cost of the equipment is small compared to that required for extruding ceramic pillars. The sawing technique also affords great versatility in that a complete range of ceramic volume fractions is achievable by simply varying the saw cut thickness and/or pitch.

1-3 composites have received a considerable amount of interest for use in hydrophones. Almost without exception, researchers have selected a high permittivity Lead Zirconate Titanate (PZT) ceramic and a cold curing polymer. The majority of commercial polymers are unsuitable because they require temperatures and pressures during manufacture which are incompatible with fragile ceramic pillars. Hence epoxy or polyurethane resins have been used almost universally. Polyurethane possesses a lower Young's modulus ($1 \times 10^9 \text{ Nm}^{-2}$ versus $3 \times 10^9 \text{ Nm}^{-2}$) and a higher Poisson ratio (0.48 versus 0.35).

In hydrophone operation the softer polymer is favoured because more of the laterally applied stress is decoupled from the ceramic. However, because polyurethane possesses a high Poisson ratio, any arbitrary thickness displacement will result in a significant lateral displacement.

The problems caused by an incompressible polymer phase is common to all applications of composites - including high frequency applications. Klicker has proposed a means of overcoming this problem by introducing porosity into the polymer phase [11], and thus making it compressible. By adding a small quantity of water to a polyurethane polymer, carbon dioxide bubbles are formed in the final cured polymer. Porosities of between 5% and 50% have been obtained by varying the proportion of water and the cure temperature. Excellent hydrostatic piezoelectric coefficients were obtained. On an average of seventeen results, an improvement in d_h of twice that for a non foamed epoxy composite, and three times that for pure PZT-5A were obtained. The $d_h g_h$ figure of merit was a factor of ten greater for the porous composite than for the non voided composite.

An alternative method for reducing the Poisson ratio of the polymer is to stiffen it by including glass fibres. This process has been investigated by Haun et al [12]. Although glass fibres possess a high elastic modulus, their Poisson ratio is only 0.28 and hence the net Poisson ratio of a glass fibre reinforced polymer is less than

that of a pure polymer. The inclusion of glass fibres reduces the effective d_{31} without reducing the coupling of thickness stresses. It also enhances the strength and depth capability of the material. At low volume fractions of glass, the Poisson ratio of the polymer is reduced, but at higher volume fractions of glass, the overall stiffness is increased and net sensitivity is reduced. At the optimum glass fibre composition, the $d_h g_h$ figure of merit for epoxy composites is twice that for a similar device without glass fibre inclusions. For similar devices fabricated with polyurethane, an order of magnitude improvement in $d_h g_h$ is achievable by the inclusion of glass fibres. These responses can be improved further by the use of a fibre reinforced porous polyurethane polymer. In this case the $d_h g_h$ figure of merit is approximately a hundred times greater than that for a transducer containing non-porous, non-reinforced polymer.

The above work suggests that for hydrophone operation, the performance of a composite may be improved dramatically by taking steps to reduce the Poisson ratio of the polymer. However, the inclusion of voids in the polymer may reduce the thickness mode operating efficiency of the transducer and the inclusion of glass fibres in an active transducer may present practical manufacturing problems.

Runt et al [13] have considered the influence of ceramic/polymer adhesion on the efficiency of composite transducers. 1-3 composites were manufactured with, and without, the use of ceramic surface treatment prior to

potting. It was found that the use of an organosilane coupling coefficient agent resulted in a 15% increase in d_{33} . In contrast, if a mould release agent was applied to the ceramic pillars prior to potting, d_{33} was reduced by 9%. This work serves to emphasise the importance of maximising the effectiveness of the ceramic/ epoxy bond by the use of a suitable manufacturing process.

Montero de Espinosa et al have recently proposed an alternative method for the manufacture of 1-3 transducers [14]. This technique involves rolling a heavy metal cylinder over a ceramic disc and inducing fractures across the disc. By scribing or partially dicing the ceramic disc, the density of the fracturing may be partially controlled. It is claimed that devices manufactured by this method suffer little lateral inter-element vibrational activity because of the random geometries of the resulting pillars. However, the method is suitable only for high volume fraction composites and is difficult to control in the laboratory environment. Furthermore, the thickness mode coupling coefficient is not measurably improved when compared with that of a ceramic disc.

2.2 ii) 0-3 Connectivity

Composite transducers, comprising piezoceramic powder dispersed in a fully connected polymer matrix, have also been investigated. This connectivity (0-3) offers excellent potential for low cost, large scale manufacture, as it dispenses with the need to fabricate ceramic pillars. However, manufacture would require considerable

large scale equipment and the quality of the product, in terms of particle size, spacing etc., is difficult to control. The major problem with the 0-3 connectivity is that the poling of the resultant composite is problematic because individual particles are separated by thin films of polymer possessing low dielectric permittivity. This configuration requires the use of very high poling voltages, with the danger of breakdown if any inconsistencies in the mixture exist. It has been shown by Sa-Gong et al [15] that this problem may be circumvented by the inclusion of a small quantity of semiconducting material (either carbon or germanium) in the polymer. However, the net piezoelectric efficiency is still less than that of an ordinary 1-3 composite transducer. Hence, 0-3 transducers appear to show promise only for applications where large scale manufacture is envisaged and cost is more important than performance. 0-3 transducers appear to exhibit little potential as a viable active transducer material and no significant work on their application to this field of work has been carried out.

2.3 BIOMEDICAL APPLICATIONS

During the development of composite transducers for hydrophone applications, it was recognised that similar, high efficiency, devices could be used for wideband active operation in biomedical transducers. These transducers normally have a centre frequency between one and three megahertz and are commonly used in electronically steered arrays to produce images of human internal organs. The excellent matching to low impedance media and low Q of composite transducers offered the prospect of excellent imaging performance. Gururaja et al [6] investigated the high frequency applications of composite materials on a purely experimental basis using Erikson's standard tone burst pulse-echo method [17]. This method involves exciting the transducer with a sinusoidal voltage, of approximately twenty cycles duration, and measuring the echo response from a large, thick planar reflector. 1-3, 3-3, 3-1 and 2-2 devices were compared. 3-1 devices comprise of ceramic plates with holes drilled out and then filled with the polymer. 2-2 devices are formed by laminating alternate plates of PZT and polymer side by side. The conclusion of this work was that only 1-3 composite transducers were worth serious consideration as an active transducer material. However, 0-3 transducers were not included in the comparison because the technology for their successful manufacture had not been developed at that time.

Gururaja et al subsequently performed more extensive investigation of 1-3 composite transducers for active operation [18,19]. A range of devices, including reference commercial PZT devices, were analysed experimentally using Erikson's tone burst method. The peak pulse sensitivity-bandwidth product was selected as the figure of merit in the comparison. The significance of device thickness, ceramic volume fraction and pillar shape were each investigated.

In pulse echo operation at 2.28MHz, it was found that the signal gain bandwidth product (GBP) of the 30% unbacked device was comparable to that of the reference backed commercial transducer (Rohe 5601). It was observed that electrical isolation from the 50 Ω source impedance of the generator, using back-to-back zener diodes, was required to obtain meaningful results. Inclusion of diode isolation permitted the reference transducer to operate far more efficiently and in this case, the pulse-echo signal GBP of the reference device was twice that of any of the composite transducers. Gururaja also observed that pillars with aspect ratios of 0.5 exhibited better performance than those with ratios of 0.3.

No thorough explanation for these results is given. Also, only devices in the ceramic volume fraction range 10% to 30% were analysed, although there is no reason to suppose that the devices at higher volume fractions perform any worse. The omission of these higher volume devices, and the lack of detailed explanation reveals a considerable

gap in the understanding of active composite transducer behaviour. However, the results demonstrate very clearly that active composites should possess a fine lateral scale, so that it can be assumed that the ceramic and polymer phases are effectively tied and uniform vibration results. Otherwise, the pillars will tend to vibrate independently of the polymer phase and none of the advantages of using a composite will be realised.

A range of devices were tested for reception sensitivity. In this case, it was found that if the lateral shear wavelength in the polymer was similar to the inter-element spacing, then parasitic modes are set up and net performance degraded. This implies that for optimal reception performance a fine lateral pillar structure is required. It was also found that, for the best example tested, the figure of merit (peak sensitivity GBP) was three times greater than for PZT.

The transmission performance of the same transducers was also measured. It was observed, that for identical excitation, transmission efficiency was proportional to the ceramic volume fraction. However, no direct comparison between a reference ceramic transducer and the composite transducers was made.

The transmission, reception and pulse-echo results have not been explained comprehensively. Furthermore, only a limited range of devices were used and no reference ceramic transducer was used in some of the experiments.

The acoustic impedance of the transducers were determined experimentally and theoretically using three different techniques. In the transmission technique, a wave is transmitted to the specimen, and the time spacing between the front surface echo and the rear surface echo in the resultant reflected pulse-echo train used to calculate velocity. Hence, if the density is known, the impedance can be calculated. The reflection technique involves measuring the amplitude of a reflected pulse and hence determining the acoustic impedance from the reflection coefficient. Finally, the resonance technique involves calculating the thickness velocity from the mechanical resonant frequency and hence calculating impedance. The results of these methods were compared and it was found that only in the case of composites possessing a fine lateral scale at moderate frequencies, that is, less than 1MHz, could consistent results, in agreement with theory, be obtained. In the case that composites were operating at higher frequencies, and possessed a relatively coarse lateral scale, the ceramic pillars vibrated independently and exhibited a higher velocity. This resulted in a higher than expected acoustic impedance.

The effect of increased temperature on the electromechanical properties of the transducers was also considered. In a thick composite transducer, with a fine lateral scale, as the temperature increased above the glass transition temperature two observations could be made. Firstly, the coupling coefficient rose rapidly from

0.55 to approximately 0.7. This implies that at low temperatures the pillars are mechanically tied together and are partially clamped in the lateral direction. At higher temperatures, the polymer softens and the pillars vibrate freely and therefore exhibit a coupling coefficient close to that associated with a free pillar ($k_{33} = 0.7$). Secondly, the mechanical Q factor reduced as the device became lossier. The polymer was becoming more attenuative and absorbing more energy. However, when the experiment was repeated for a thin composite, with a relatively coarse lateral scale, and short stubby pillars, no significant deviation in coupling coefficient was measured for increasing temperature. The fact that it remained at the relatively high level of 0.7 suggests very clearly that the pillars were weakly coupled mechanically to the epoxy, even at low temperatures.

Gururaja also considered the effect of using a quarter wavelength matching layer. For a 500kHz transducer, possessing a fine lateral scale, excellent results were obtained. A very wideband response was obtained, with a Q of 1.8, and this is in agreement with the results that would be expected from standard matching theory [20].

2.4 ARRAY APPLICATIONS

The advent of rapidly improving and cheaper computer power has made the processing of ultrasonic array data far more feasible. A carefully designed array may be electronically steered and focused to generate images without the need for either moving any transducer or having to use clumsy, mechanical focusing. The interest in wideband, high resolution imaging arrays for medical diagnostics is well established, and it is for this application that composite transducer arrays have been investigated.

Shaulov and Smith [4] have demonstrated the use of a 4.5MHz composite transducer array. Using a Mylar quarter wavelength matching layer, and a light backing, a -20dB pulse length of three to four cycles was obtained. Thus it is possible to make electrical connections to the back surface, because the provision of a heavy, lossy backing is unnecessary. In the array described, the elements were 1mm (three wavelengths) wide and hence the resultant element directivities were narrow. Nevertheless, high quality images were obtained using electronic steering. The electrical and mechanical inter-element coupling was measured as -40dB and -50dB respectively to the second next adjacent element. Thus, a high degree of inter-element isolation has been achieved without the need to slice the array, as is normally the case in ceramic arrays.

More recently, Shaulov et al demonstrated curved annular composite arrays for operation at 3MHz [21]. Normally, it is difficult to manufacture suitable biomedical annular arrays because the curved ceramic elements need to be sliced to provide sufficient isolation. However, the composite material circumvented the need for slicing and excellent results were obtained by defining the elements by the electrode alone. Excellent inter-element isolation, acoustic field performance and bandwidth were obtained. Furthermore, the array was successfully electronically focused.

The limited amount of work on composite arrays suggests that they have considerable potential. Not only has excellent element performance been achieved, but the fabrication technique permits the location of the electrical connections immediately behind the active element, and hence two dimensional, and complex geometry, arrays are possible.

Shaulov et al have also demonstrated the viability of a bi-plane composite phased arrays [22]. It is composed of two linear arrays arranged on perpendicular axes, defined on each side of a square composite plate. Each linear array may be used sequentially to obtain orthogonal scans. Significantly, this paper also discussed the presence of Lamb type modes propagating within the composite structure. These resulted in element directivity characteristics which were slightly degraded from the ideal theoretical response.

2.5 MODELLING COMPOSITE TRANSDUCER PARAMETERS

A well designed active composite transducer will vibrate uniformly in a pure thickness fashion. It should therefore be possible to predict equivalent thickness mode transducer parameters for uniformly vibrating composite transducers.

The most comprehensive article on the prediction of equivalent thickness mode parameters was published by Smith et al in 1985 [3]. Smith produced equivalent thickness mode parameters by simultaneously solving the piezoelectric-elastic equations for both phases.

The general form of the equations for the ceramic and polymer phases are as described in Equations 2.1 and 2.2.

$$\begin{aligned}
 \text{CERAMIC } T_1^C &= c_{11}^C E_{S_1}^C + c_{12}^C E_{S_2}^C + c_{13}^C E_{S_3}^C - e_{13}^C E_3^C \\
 T_2^C &= c_{21}^C E_{S_1}^C + c_{22}^C E_{S_2}^C + c_{23}^C E_{S_3}^C - e_{23}^C E_3^C \\
 T_3^C &= c_{31}^C E_{S_1}^C + c_{32}^C E_{S_2}^C + c_{33}^C E_{S_3}^C - e_{33}^C E_3^C \\
 D_3^C &= e_{31}^C E_{S_1}^C + e_{32}^C E_{S_2}^C + e_{33}^C E_{S_3}^C - \epsilon_{33}^C E_3^C
 \end{aligned} \tag{2.1}$$

$$\begin{aligned}
 \text{POLYMER } T_1^P &= c_{11}^P S_1^P + c_{12}^P S_2^P + c_{13}^P S_3^P \\
 T_2^P &= c_{21}^P S_1^P + c_{22}^P S_2^P + c_{23}^P S_3^P \\
 T_3^P &= c_{31}^P S_1^P + c_{32}^P S_2^P + c_{33}^P S_3^P \\
 D_3^P &= \epsilon_{33}^P E_3^C
 \end{aligned} \tag{2.2}$$

In the case of the elastic parameters, superscript E denotes the parameter for the ceramic phase under a constant electric field.

Superscript C denotes the strain in the ceramic parameters while P denotes strain in the polymer parameters.

The lateral directions are denoted by subscript 1 and 2 while the thickness direction is denoted by subscript 3.

This conventional notation is described in Figure 1.0. and all other notation conforms with the relevant IEEE standard [1].

It has been assumed that the top and bottom surfaces are electroded. Therefore a finite electric field exists only in the thickness direction and that this value is common to both polymer and ceramic phases.

It may also be assumed that symmetry exists in the X-Y plane. Therefore, the following simplifications may be made:

$$\begin{aligned}T_1 &= T_2 && \text{Stresses equal} \\S_1 &= S_2 && \text{Strains equal} \\c_{13} &= c_{23}\end{aligned}$$

The equations relating to the polymer are greatly simplified if it is assumed that the material is isotropic. Hence:

$$\begin{aligned}c_{11} &= c_{22} = c_{33} \\c_{12} &= c_{13} = c_{23}\end{aligned}$$

Therefore Equations 2.1 and 2.2 may be simplified to Equations 2.3 and 2.4.

$$\begin{aligned}
\text{CERAMIC } T_1^C &= (c_{11}^E + c_{12}^E)S_1^C + c_{13}^E S_3^C - e_{13}^E E_3^C \\
T_3^C &= 2c_{31}^E S_1^C + c_{33}^E S_3^C - e_{33}^E E_3^C \\
D_3^C &= 2e_{31}^E S_1^C + e_{33}^E S_3^C - \epsilon_{33}^E E_3^C
\end{aligned}
\tag{2.3}$$

$$\begin{aligned}
\text{POLYMER } T_1^P &= (c_{11} + c_{12})S_1^P + c_{13}S_3^P \\
T_3^P &= 2c_{12}S_1^P + c_{11}S_3^P \\
D_3^P &= \epsilon_{33}E_3^C
\end{aligned}
\tag{2.4}$$

A number of assumptions are made which permit simplification and the simultaneous solution of these equations. Firstly, it is assumed that the lateral scale is very fine, and hence any inter-rod resonant modes are at high frequencies well separated from the thickness mode.

At this point it is necessary to introduce the concept of the ceramic volume fraction, v . It defines the proportion of the composite material which is ceramic. In a regular 1-3 structure it is derived from the cross sectional geometry in the X-Y plane.

Three key thickness mode assumptions are made:

- a) The thickness strains in both phases are equal

$$S_3^C = S_3^P$$

- b) The net lateral strain is zero. This implies that in the lateral direction, the strains in the two phases are complementary.

$$vS_1^C + (1-v)S_1^P = 0$$

c) The lateral stresses are equal in both phases

$$T_1^C = T_1^P$$

It may be argued that assumption c) is incompatible with assumption b). This is because both strain and stress are being simultaneously constrained without taking account of their elastic moduli. This point may be clarified by considering assumption b). If the sum total of the two strains is zero, then one of these must be negative. Therefore, by Hooke's Law the stress in one of the phases must also be opposite in polarity from the other. This is in contradiction to assumption c).

It is believed that any error resulting from these assumptions would have a small effect on the overall calculated value. In fact, errors arising from the uncertainty of the actual material parameters, which have a tolerance of at least 5%, are far more significant. Furthermore, these assumptions are essential if a useful set of equations is to be derived. The necessary algebraic manipulation required to obtain the equivalent thickness mode parameters, using Equations 2.3 and 2.4 and the assumptions discussed above, is described in the literature [3]. The following thickness mode equations are obtained.

$$\begin{aligned} T_3 &= c_{33}^E S_3 - e_{33} E_3 \\ D_3 &= e_{33} S_3 - \epsilon_{33} E_3 \end{aligned} \tag{2.5}$$

Where BOLD characters denote the equivalent thickness mode parameters of the composite, as defined below.

$$c_{33}^E = v[c_{33}^E - 2(c_{13}^E - c_{12}^P)^2/c(v)] + (1-v)c_{11}^P \quad 2.6$$

$$e_{33} = v[e_{33} - 2e_{31}(c_{13}^E - c_{12}^P)/c(v)] \quad 2.7$$

$$\epsilon_{33}^S = v[\epsilon_{33}^S + 2e_{31}^2/c(v)] + (1-v)\epsilon_{11}^P \quad 2.8$$

Where $c(v)$ is defined:

$$c(v) = c_{11}^E + c_{12}^E + (v/(1-v))(c_{11}^P + c_{12}^P) \quad 2.9$$

$$\rho = v\rho^C + (1-v)\rho^P \quad 2.10$$

Additionally, the parameters c_{13}^E and e_{31} may be calculated [23].

$$c_{13}^E = \frac{c_{12}(c_{11}^E + c_{12}^E) + vc_{13}^E(c_{11}^E - c_{12}^E)}{(1-v)c(v)} \quad 2.11$$

$$e_{31} = \left[\frac{1 - (c_{11}^E + c_{12}^E)}{c(v)} \right] e_{31} \quad 2.12$$

The parameters s_{13}^E , s_{33}^E , d_{31} and d_{33} , can also be calculated [23]. However, these parameters are not relevant to thickness mode operating transducers.

Using the above expressions, the thickness mode coupling coefficient, k_t , thickness direction stiffness c_{33}^D , piezoelectric coefficient, h_{33} , acoustic impedance, and longitudinal wave velocity may be evaluated as indicated in Equations 2.13 to 2.17 [24].

$$k_t = e_{33}^2 / \sqrt{(c_{33}^D \epsilon_{33}^S)} \quad 2.13$$

$$c_{33}^D = c_{33}^E + e_{33}^2 / \epsilon_{33}^S \quad 2.14$$

$$h_{33} = e_{33} / \epsilon_{33}^S \quad 2.15$$

$$Z_C = \sqrt{(c_{33}^D \rho)} \quad 2.16$$

$$c = \sqrt{(c_{33}^D / \rho)} \quad 2.17$$

The results obtained using these equations are generally sufficiently accurate for practical purposes, and the significance of results that may be obtained for different materials and varying volume fractions are discussed in Chapter IV.

Hashimoto and Yamaguchi have obtained very similar theoretical results to those of Smith et al using a different approach [25]. This involves expressing the elastic equations in matrix form, which are then split into unknown and known quantities. Making similar assumptions to those used by Smith, and using matrix manipulation methods, the equivalent piezoelectric and elastic parameters for the composite material are expressed. The method is more versatile than that used by Smith and provides equations for the equivalent rotational parameters, c_{44} , c_{55} and c_{66} , as well the linear parameters c_{13} , c_{33} , e_{31} etc. However, the method was originally derived for one dimensional composites and the extension to two dimensional composite analysis results in extremely clumsy equations requiring iterative methods for complete solution. Despite the versatility of this technique, Smith's method is superior for practical application because it exhibits a similar degree of accuracy and can be implemented far more efficiently.

2.6 MODELLING THE PERFORMANCE OF COMPOSITE TRANSDUCERS

Clearly there is a wide variety of possible designs of composite transducers. Amongst the parameters that may be controlled in a practical design are area, thickness, ceramic/ polymer material, ceramic volume fraction, backing, matching and electrical loading. Therefore, there is a requirement for a means of systematic design to take account of the above variables so that an optimal design can be achieved without the need for a wasteful, time consuming 'trial-and-error' method. Ideally, a comprehensive computer model should be available. Unfortunately, relatively little work has been performed in this field.

The most straightforward means of generating a computer model for composite transducers is to combine a model for transducer parameters with a conventional thickness mode transducer model. Amongst the suitable thickness mode models are the circuit analogies by Mason [5] and Leedom et al (KLM) [6] and the linear systems modelling approach by Hayward [7]. Although the models have differing implementations, they are based on the same fundamental mechanical and piezoelectric equations and hence the choice between models is determined principally by the versatility of the implementation being used. For example, the KLM model is more versatile than the Mason model and hence is the preferred model between the two. Smith et al [26] have used a simple transducer model in combination with the KLM model. A limited selection of results were

presented for a 500kHz, 25% ceramic volume fraction, 19mm diameter air-backed composite transducer disc. Measurements and simulations of impedance (air loaded and water loaded), transmission and reception efficiency were made. Excellent results were obtained in each case. Smith subsequently considered the farfield CW directivity of the same disc. Again excellent agreement between theory and experiment was obtained. This work clearly indicates the validity of a simple combined transducer model. However, only a single configuration was modelled and hence the validity of the model for the general case has not been proven. Furthermore, no attempt was made to model the effects of backing, matching, and electrical loading. Internal mechanical loss within the transducer was not considered. The mechanical losses within composite transducers are greater than for ceramic devices and may exert a significant effect on the measured characteristics.

The work of Smith has been extended by Ih and Lee [27] to take account of internal losses. An effective attenuation coefficient is determined from the maximum electrical resistance at resonance. The coefficient is used to generate a phase delay by replacing the normally real wave constant, k , in the KLM transmission line, by a complex quantity given by : $k = w/c - j\alpha$. The angular frequency is w , the wave velocity is c , and α is the attenuation coefficient [28]. The attenuation coefficient was determined experimentally for a 40%, 3MHz composite and a

reference PZT disc. As expected, the attenuation coefficient of the composite was significantly higher than that for the reference PZT disc. Ih and Lee have shown that, when the transducer is modelled including mechanical loss, a significantly more accurate simulation results. Clearly the impact of mechanical loss on the overall result is dependent on the transducer load parameters. For example, if the transducer is heavily loaded, the influence of transducer internal loss is relatively small. Ih and Lee have also included the effect of a matching layer in their simulations and have concluded that the round trip insertion loss (pulse-echo) is increased by two to three decibels at the midband frequency when loss is considered for the particular configuration under examination. The new lossy model developed by Ih and Lee is more precise than that used by Smith, but its accuracy for the general case has not been verified. This is because only a single transducer configuration has been considered and it is not clear if electrical loading effects were included in the model. Also, the attenuation coefficient was obtained experimentally, and no attempt has been made to predict its numerical value for an arbitrary composite configuration.

The two models described for predicting composite transducer behaviour possess considerable potential as useful comprehensive design/ simulation tools. However, there are omissions in the published work which require clarification. In particular, there is a need to extend

the modelling to take account of backing, acoustic matching and electrical matching. This work would then need to be comprehensively verified for a wide range of possible configurations and its validity verified. A comprehensive model, which meets these requirements, is presented in Chapter V.

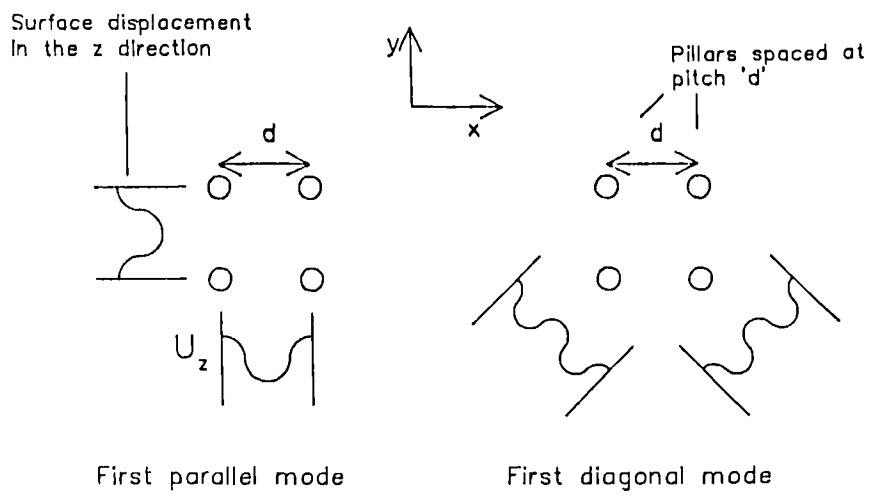


Figure 2.3 Configuration of the first two inter-pillar resonant modes.

2.7 INTER ROD RESONANT ACTIVITY

There has been theoretical interest in the inter pillar resonant activity found within composite structures. These are caused by the regular geometry normally associated with 1-3 composite structures and the presence of strongly reflective surfaces, at regular intervals, in the lateral direction. These reflective surfaces are inherently present due to the large acoustic mismatch between piezoelectric ceramics and most polymers. In practical designs, the influence of inter pillar activity can be eliminated by designing them so that the lateral resonant modes occur at frequencies far separated from the fundamental thickness mode. This is achieved by using a fine scale structure consisting of tall, thin pillars which are closely spaced.

Auld et al have presented the most comprehensive work on inter pillar resonant activity [29,30]. A relatively complex, and precise, theory based on Bragg scattering has been developed for predicting lateral resonant modes. This theory is strictly only applicable to low volume fraction devices, in which the pillar diameter is small compared to the inter pillar spacing. Typically, ceramic volume fractions of 10% are considered. The two principal modes are described in Figure 2.3. The first corresponds to transverse modes propagating in the X and Y directions with the pillar centres occupying nodal positions. A complete wavelength exists between adjacent elements. A stopband exists for the case that the pillar pitch is half

a wavelength, but in this case there is no resonant scattering from the X to the Y propagating wave. That is, the X and Y propagating waves cannot exist simultaneously. The next mode which can exist for the given boundary conditions is for a diagonally propagating mode. In this case, the lowest order mode which satisfies the conditions has two wavelengths between diagonally adjacent pillars.

Auld has also considered the attenuation of laterally propagating waves in one dimensional composite structures [31]. This involves considering the stopband structures and developing Floquet solutions. The net result is that if the inter pillar spacing corresponds to one wavelength of a laterally propagating wave, then a wide stopband exists. This results in considerable attenuation of the wave. The proposed application of such a theory is for linear composite arrays, where it is desirable to limit energy propagating between elements. Unfortunately, the spacing of the pillars in such an array is frequently limited by other factors.

2.8 FINITE ELEMENT ANALYSIS

It has recently been recognised that finite element analysis has a valuable role in the investigation of the vibrational characteristics of composite transducers. The complex geometry of the pillar and polymer structure, at the microscopic level, precludes the use of simple linear equations, except for the approximate calculation of material properties for a limited range of geometries. Finite element analysis may be used to investigate resonant modes within the pillars and between them. The influence of geometry and material property parameters may also be examined.

Yamaguchi et al presented an analysis of the dispersion characteristics of 1-3 composite transducers in 1987 [32]. This work considered the influence of the periodicity of the structure on the thickness and first two lateral inter-pillar modes, as described by Auld [29] and discussed in section 2.7. It was observed that the interaction between these lateral modes, and the thickness mode, was significant if relatively wide inter-pillar spacings were used. In this case, the coupling coefficient associated with the thickness mode was considerably reduced from that encountered in a similar structure with the same volume fraction but possessing a finer lateral scale. It was also observed that the nature of the lateral resonant activity in a structure possessing rectangular section pillars was different from that encountered when square section pillars were employed. These phenomena,

which also depend on component material properties and volume fraction, require further investigation. Yamaguchi concluded that the simple quasi-static models of Smith [3] and Hashimoto [25] are perfectly adequate for structures with a fine lateral scale. If the periodicity was greater than one sixth of a wavelength, then the values of wave velocity and coupling coefficient were found to be strongly dispersive.

Jeng et al [33] extended the work of Yamaguchi by including the effects of internal losses and fluid loading. Loss is included by adding a frequency and stiffness dependent term to the overall system equation and fluid loading is represented as part of the excitation function. This theory was used to obtain expressions for transmission efficiency and impedance for both a pure ceramic disc and a 1-3 composite disc. Although no experimental verification is shown, the results are in agreement with the known characteristics of both materials. The composite exhibits a pure undistorted resonant activity, whereas the response of the pure ceramic disc is distorted in the plots of both transmission efficiency and impedance.

The recent work on finite element analysis of composite structures serves to verify the importance of this method to the understanding of composite transducer behaviour. In particular, it is well suited to the analysis of the influence of pillar geometry and material property parameters on the vibrational characteristics. Chapter III

presents the theory for the analysis of composite structures and this is used in Chapter IV to investigate new configurations. In Chapter VI, finite element analysis is applied to the investigation of the vibrational, and electromechanical performance of composite transducer arrays.

2.9 CONCLUDING REMARKS

A considerable amount of practical work has established that the 1-3 type connectivity exhibits the greatest potential as an improved active transducer material. In addition to its higher efficiency than other configurations, it is by far the simplest configuration in terms of ease of design, manufacturing and analysis from a theoretical viewpoint.

The results of work on the use of 1-3 materials in hydrophones emphasise the importance of the choice of materials and the influence of polymer characteristics on overall performance. A simple and effective manufacturing technique based on a slice and fill technique has been established as providing the best means of manufacture.

The practical results of Gururaja et al, concerning the application of these materials to medical ultrasonics demonstrate a number of deviations between expected and measured performance. Only a limited range of devices were considered and no satisfactory explanation given for the performance. It is clear that a comprehensive model for predicting device performance, which includes the effects of internal loss, backing, matching and electrical loading, is required. This model should be verified for a very much wider range of devices than those previously considered. This approach would make use of the models available for predicting composite transducer parameters developed by Smith et al [18], or obtained by finite element analysis, and extend the work performed by Smith

et al [25] and Ih and Lee [26].

The work performed using composite materials as a component in electronically scanned ultrasonic arrays has been limited. The advantages of composite materials, in terms of matching, and low inter-element coupling, suggests that they possess considerable potential for use in arrays. An analysis of their performance would involve the use of finite element analysis for determining inter-element coupling activity and the aperture displacement profiles. This may be combined with more conventional transducer modelling, taking account of backing, matching and electrical loading. Eventually, the field profile could be predicted using a modified diffraction theory.

The recent work on finite element analysis indicates the potential of this method for the accurate characterisation of various configurations of composite transducers. There is clearly a need for an extension of this work to cover array and stacked structures.

There are a number of other gaps in the literature relating to composite transducers. These include the absence of any devices being reported for operation below 500kHz, no active multilayered, stacked structures and no examination of their potential for use in the NDE of low impedance, lossy media. These configurations and applications are addressed in later chapters.

LIST OF SYMBOLS SPECIFIC TO FINITE ELEMENT FORMULATIONS

Finite element analysis has developed a unique set of notation. It is preferable to adopt this symbolisation during the discussion of a finite element formulation. Further details may be found in a standard text [36].

SYMBOL	MEANING
[B]	'Shape' matrix
[c]	Elastic stiffness matrix
[C]	Mechanical damping matrix
[D]	Electric displacement matrix
[e]	Piezoelectric matrix
f_x	Interpolation function, converting nodal values to continuous values
{F}	Force vector
[K_{xy}]	'Stiffness' matrix
[m]	Mass matrix
{Q}	Charge vector
{T}	Stress vector
[] ^T	Matrix transpose
u	Displacement
{u}	Displacement vector
U	Work
U_E	Elastic energy
U_D	Dielectric energy
U_M	Electromechanical energy
α	Loss matrix multiplier
{ φ }	Potential vector
λ	Eigenvalue
{ φ }	Eigenvector

CHAPTER III

FINITE ELEMENT ANALYSIS OF COMPOSITE TRANSDUCER STRUCTURES

3.1 INTRODUCTION

The piezoelectric equations describing the behaviour of resonators are sufficiently complex that closed form solutions are only obtainable for the simplest geometries. Thus, unless the resonator exhibits unidimensional thickness mode vibration, or similar simple modes of operation, then numerical methods are required for the solution of the equations. Traditional variational methods based on the Rayleigh-Ritz method [34], have been superseded by extremely versatile Finite Element Analysis (FEA). Allik and Hughes extended the established structural Finite Element Method (FEM) to include piezoelectric effects in 1970 [35], and since then this has provided the basis for most of the subsequent work on the FEA of piezoelectric media. The principal application of piezoelectric FEA is for the modal analysis of complex mass-spring transducer assemblies, and hence the method has become well developed and proven.

The type of transducer being considered here is expected to exhibit thickness mode type operation. However, on a microscopic scale, where an individual pillar and the adjacent polymer are being considered, the interaction and vibrational modes may be highly complex. Hence, the versatility of FEA, in terms of its ability to model arbitrary geometries, has considerable potential in any thorough analysis of the behaviour of composite piezoelectric structures.

3.2 REVIEW OF THE FINITE ELEMENT METHOD

The FEM embraces a vast variety of mathematical techniques and has been applied to a wide range of engineering problems. These include static, harmonically vibrating, and transiently excited structural analyses, magnetic, electrostatic and acoustic field analyses, and thermal analysis. Therefore, only aspects of the method relevant to this work will be discussed. The reader is directed to one of the standard references on the FEM for further information on the numerous applications and implementations [36].

In the analysis of piezoelectric transducers, the types of analysis which are of interest include:

1. Static Excitation
2. Harmonic Excitation
3. Modal (resonance)
4. Electric Fields
5. Acoustic Fields

The general concept of the FEM is that the structure being analysed is considered as an assemblage of discrete pieces (elements) that are connected together at a finite number of points (nodes). In the real structure, the number of nodes is infinite, but due to the finite limitations of the numerical process, only a limited number of elements and nodes are used.

Although the physical description of the structure is approximate, the mathematical system used for the analysis

is exact. Using the principle of minimum energy, an approximate displacement function is chosen to derive a correlation of nodal forces to nodal displacements. This displacement function is known as the stiffness matrix - conventionally denoted by $[K]$. A set of linear algebraic equations can be formed since equilibrium is imposed at every node. These equations are solved to evaluate the nodal displacements, and hence the stresses and strains within each element can be evaluated.

The finite element formulation used here is based on the variational principle of virtual work. The starting point of this approach may be described by considering an existing system in equilibrium. If a virtual displacement is applied, the principle of virtual work states that the sum of work done by the applied force, and the stored potential energy resulting from this force, is zero. The variational method is a finite element technique for solving this system and is an improved and more versatile method than the Rayleigh-Ritz method used by Holland and Eer Nisse for electroelastic problems [34]. The Rayleigh-Ritz method requires the selection of trial functions, which is impractical for complex geometries.

Before stating the variational problem, it is necessary to define the constitutive equations relating stress, displacement and voltage. In the simple, well established non-piezoelectric case, the constitutive relationship is Hooke's Law.

Hooke's Law in matrix form:

$$[T] = [c][S] \quad 3.1$$

[T] : Stress matrix with three linear components and three rotational components

[c] : Six by six stiffness matrix

[S] : Strain matrix

In a piezoelectric material, Hooke's Law is modified by the product of applied electric field and the piezoelectric constant. Similarly, Maxwell's equation for a dielectric is modified by a quantity proportional to the applied stress.

$$[T] = [c][S] - [e][E]$$

$$[D] = [e]^T [S] + [\epsilon][E]$$

3.2

Inclusion of the relationship governing the electric field, permits the resulting finite element formulation to analyse simple electrical field problems as well as elastic effects. Hence, electric fields governed by Poisson's equation may be conveniently analysed by a versatile finite element model. Naturally, if electric field analysis is of prime concern, then simpler, more efficient, but less versatile formulations may be derived.

In the general case, the above matrices may have three mutually perpendicular linear components. In the analysis of the complex geometrical structures being studied here, it is preferable to retain all these components. However, the problem may be simplified considerably if the

matrices are reduced to two dimensions. This results in a considerable saving in computational effort and is perfectly valid for a wide range of structures.

In addition to the constitutive relationships, the equilibrium of forces and compatibility of deformations must also be satisfied between adjacent elements.

The variational principle for piezoelectric media may be stated as:

$$\int_V \delta U_{In} dv = \int_V \delta U_{Ex} dv$$

INTERNAL WORK EXTERNAL WORK

$\delta = \text{Virtual Operator}$
3.3

The analysis of a real system requires a versatile means of converting the actual nodal displacements and voltages, to their corresponding mathematically equivalent parameters as used in the finite element matrices. This is achieved via interpolation, or 'shape', functions, which are primarily determined by the physical geometry of the system. These functions are defined as f_u and f_φ which relate 'i' nodal values of mechanical displacement and electrical potential to their continuous equivalents.

$$\{u\} = [f_u]\{u_i\}$$

$$\varphi = [f_\varphi]\{\varphi_i\}$$

3.4

The expression for displacement in Equation 3.4 may be converted to a relationship in terms of strain by differentiating displacement with respect to distance. Likewise, an equation for the electric field may be derived from the expression for potential.

Thus:

$$\begin{aligned} \{S\} &= [B_u]\{u_i\} \\ \{E\} &= -[B_\varphi]\{\varphi_i\} \end{aligned} \quad 3.5$$

Where:

$[B_u]$ and $[B_\varphi]$ are the modified shape functions. Substitution of these equations into equation 3.2 results in the following two general equilibrium equations.

$$\begin{aligned} [m]\{\ddot{u}_i\} + [K_{uu}]\{u_i\} + [K_{u\varphi}]\{\varphi_i\} &= \{F\} \\ [K_{\varphi u}]\{u_i\} + [K_{\varphi\varphi}]\{\varphi_i\} &= \{Q\} \end{aligned} \quad 3.6$$

Where:

$$\begin{aligned} [K_{uu}] &= \int_v [B_u]^T [c] [B_u] dv && \text{Stiffness matrix} \\ [K_{u\varphi}] &= \int_v [B_u]^T [e] [B_\varphi] dv && \text{Piezoelectric} \\ &&& \text{'stiffness' matrix} \\ [K_{\varphi u}] &= \int_v [B_\varphi]^T [e]^T [B_u] dv && \text{Piezoelectric} \\ &&& \text{'stiffness' matrix} \\ [K_{\varphi\varphi}] &= - \int_v [B_\varphi]^T [\epsilon] [B_\varphi] dv && \text{Dielectric} \\ &&& \text{'stiffness' matrix} \\ [m] &= \rho \int_v [f_u]^T [f_u] dv && \text{Mass matrix} \\ \{F\} &= \int_v [f_u]^T [F_i] dv && \text{Force vector} \\ \{Q\} &= - \int_v [f_\varphi] (\varphi_i) dv && \text{Charge vector} \end{aligned}$$

Equation 3.6 may be solved for static, harmonic, or free resonant forms of excitation. Once the nodal displacements and voltages are determined, the stress and electric field may be evaluated by substitution into the following equation.

$$\{T\} = [c][B_u]\{u_i\} + [e][B_\varphi]\{\varphi_i\}$$

$$\{D\} = [e]^T[B_u]\{u_i\} - [\epsilon][B_\varphi]\{\varphi_i\} \quad 3.8$$

The elastic, dielectric and electromechanical energies of the system may also be calculated. From these energies, the electromechanical coupling coefficient of the material may be determined [24].

$$k_e = U_M / \sqrt{(U_E U_D)} \quad 3.8$$

Where:

Elastic energy is defined:

$$U_E = \frac{1}{2} \{u_i\}^T [K_{uu}]\{u_i\}$$

Dielectric energy is defined:

$$U_D = \frac{1}{2} \{\varphi_i\}^T [K_{\varphi\varphi}]\{\varphi_i\}$$

Electromechanical energy is defined:

$$U_M = \frac{1}{4} (\{u_i\}^T [K_{u\varphi}]\{\varphi_i\} + \{\varphi_i\}^T [K_{\varphi u}]\{u_i\})$$

Static Analysis

In this case \dot{u} is zero and hence equation 3.6 is reduced to the following matrix form.

$$\begin{bmatrix} K_{uu} & K_{u\varphi} \\ K_{u\varphi} & K_{\varphi\varphi} \end{bmatrix} \begin{bmatrix} u \\ \varphi \end{bmatrix} = \begin{bmatrix} F \\ Q \end{bmatrix} \quad 3.9$$

The matrix equation is formulated with the excitation quantities (force or voltage) included. It is necessary to impose displacement or voltage constraints on parts of the structure so that the matrix problem is non-singular. Equation 3.9 is solved using standard matrix manipulation techniques. Typically, Gaussian elimination is used, although the choice of technique may depend on the symmetry within the matrix.

Harmonic analysis

In a harmonic analysis, the excitation function is of the form described below.

$$F(t) = \{F_0\} e^{j\omega t + \varphi}$$

$$V(t) = \{V_0\} e^{j\omega t + \varphi}$$

$\omega = \text{angular frequency}$
 $\varphi = \text{phase shift}$

3.10

Therefore $\{u\}$ may be replaced by $\{u_0\} e^{j\omega t + \varphi}$ in Equation 3.6. Additionally, in harmonic analysis, mechanical loss may be included by the addition of a frequency dependent damping component. This damping term, $[C]$, is the product of the real stiffness matrix $[K]$ and a matrix multiplier, α , which defines the amount of loss. In piezoelectric analyses, α is a function of the mechanical Q_m factor. This Q_m factor is also a function of the attenuation coefficient of the material, defined in terms of loss, in units of nepers or dB, per unit length at a specific frequency. Losses in composite structures may be significant and ideally a separate loss quantity should be used for the ceramic and polymer phases.

Dielectric losses may be incorporated. This is achieved by making the permittivity matrix complex and adding imaginary components to the $[K_{\varphi\varphi}]$ matrix. The resulting matrix is formulated using the $\tan\delta$ dielectric loss factor. This factor is the ratio of resistance to reactance in a dielectric. Hence, the following expression defining the imaginary component of permittivity is obtained.

$$[\epsilon]^i = -\tan\delta [\epsilon]^r$$

Hence, for harmonic analysis, equation 3.6 takes the form shown below.

$$\begin{bmatrix} K_{uu} + j\omega C_{uu} - \omega^2 m_{uu} & K_{u\varphi} \\ K_{u\varphi}^T & K_{\varphi\varphi}^r + jK_{\varphi\varphi}^i \end{bmatrix} \begin{bmatrix} u_o e^{j\omega t + \varphi} \\ \varphi_o e^{j\omega t + \varphi} \end{bmatrix} = \begin{bmatrix} F_o e^{j\omega t + \varphi} \\ (1/j\omega) I e^{j\omega t + \varphi} \end{bmatrix} \quad 3.11$$

A static condensation of the voltage degrees of freedom permits the equation to be simplified to [35]:

$$([K^*] + j\omega[C_{uu}](\omega) - \omega^2[m_{uu}])(u) = (F^*) \quad 3.12$$

Where K^* is the condensed electroelastic stiffness matrix.

$$[K^*] = [K_{uu}] - [K_{u\varphi}] ([K_{\varphi\varphi}^r + j[K_{\varphi\varphi}^i])^{-1} [K_{\varphi u}]$$

$$(F^*) = (F) - [K_{u\varphi}] [K_{\varphi\varphi}]^{-1} (Q) \quad 3.13$$

Hence the stiffness matrix $[K]$, loss matrix $[C]$, and mass matrix $[M]$ may be assembled with the sinusoidal forcing function (F) applied at a particular frequency. Gaussian elimination is used to obtain the unknown quantities, which are the displacements in this case. The corresponding potential may then be recovered.

$$\{\varphi_i\} = ([K_{\varphi\varphi}]^r + j[K_{\varphi\varphi}]^i)^{-1} (\{Q\} - [K_{u\varphi}]\{u\}) \quad 3.14$$

Hence, for a given sinusoidal applied voltage, or force, the resulting displacement may be obtained. If fluid elements are included, pressure at points in the acoustic field may also be determined. In practice using finite element analysis to determine field profiles is extremely expensive in a computational sense and is not considered further for that reason. These aspects have been discussed in detail by Lerch [37].

Since, for a specific applied voltage, the resulting charge appearing on the top surface of the transducer is determined, it is then possible to calculate the device impedance. The applied signal is sinusoidal, and therefore current may be determined from the time derivative of the charge.

$$I = \frac{d}{dt}(Q_o) e^{j\omega t} \quad 3.15$$

The impedance is generally complex and therefore it is necessary to determine the current at 0° and 90° to evaluate the real and imaginary components. Using a knowledge of these components, and the magnitude of the applied voltage, the spectral impedance characteristics may be determined by repeating the process over a range of frequencies.

Modal analysis

The determination of the natural resonant mode shapes and frequencies is the principal application of finite element analysis to piezoelectric transducer design. For this analysis, the forcing functions $\{F\}$ and $\{Q\}$ in equation 3.6 are zero. Hence the equation reduces to:

$$\begin{aligned} [m]\{u_i\} + [K_{uu}]\{u_i\} + [K_{u\varphi}]\{\varphi_i\} &= \{0\} \\ [K_{\varphi u}]\{u_i\} + [K_{\varphi\varphi}]\{\varphi_i\} &= \{0\} \end{aligned} \quad 3.16$$

Where:

$$\begin{aligned} \{u\} &= \{\varphi_i\} \cos w_i t \\ \{\varphi_i\} &= \text{eigenvector of the } i^{\text{th}} \text{ natural frequency} \end{aligned}$$

Therefore:

$$\begin{aligned} \ddot{\{u\}} &= -w_i^2 \{\varphi_i\} \cos w_i t \\ \ddot{\{u\}} &= -w_i^2 \{u\} \end{aligned}$$

Furthermore, a static condensation, identical to that described in Equations 3.12 and 3.13, may be used to simplify Equation 3.16 to the form of Equation 3.17.

$$([K^*] - w_i^2 [m])\{\varphi_i\} = \{0\} \quad 3.17$$

This may be represented in a general eigenvalue problem form.

$$[K^*]\varphi_i = \lambda_i [m]\varphi_i \quad 3.18$$

Where λ_i is the i^{th} eigenvalue. This may be reduced to the following form using the technique outlined below [36]:

$$[B]\{\Phi_i\} = \lambda_i \{\Phi_i\} \quad 3.19$$

Where:

$$\{\Phi_i\} = [L]^T \{\varphi_i\} \quad \text{and} \quad [B] = [T]^T [A] [T]$$

This process involves first changing the mass matrix, $[m]$, into the form $[L][L]^T$ using Cholesky decomposition. $[L]$ is a lower triangular matrix which is simpler to manipulate than a full matrix. Then, Householder's method is used to evaluate $[B]$ which is a tridiagonal form of a matrix $[A]$, where $[A]$ is defined as follows. $[T]$ is the matrix constructed so that $[B]$ is tridiagonal.

$$[A] = [L]^{-1} [K] [L]^T^{-1} \quad 3.20$$

Hence $[B]$ contains the eigenvalues and from these, the eigenvectors (modal displacement vectors) are determined

$$\{\varphi_i\} = [L]^T^{-1} [T]\{u_i\} \quad 3.21$$

Guyan reduction

Clearly, in a three dimensional problem, where every node may have degrees of freedom in each of three mutually perpendicular directions, and a voltage degree of freedom, then the size of the finite element matrices may become extremely large. Therefore, the matrix processes used in eigenvalue extraction can become unwieldy.

Guyan reduction allows a reduction in matrix size with minimal loss of accuracy. The user selects those degrees of freedom which are considered to be most important for the case in question. Typically, in a thickness vibrating structure, displacements in the thickness direction are

selected to be the 'master' degrees of freedom. At the other nodes, their corresponding positions in the mass and stiffness matrices are eliminated via a condensation process. This process, described by Guyan [38], permits accurate determination of the reduced stiffness matrix, but a slightly less accurate determination of the mass matrix. Thus, the potential energy of the system is unchanged but the kinetic energy is modified and slightly less accurate results are obtained at high frequencies. In a typical case, a 0.6% error in predicted thickness resonant frequency was observed for a 75% reduction in the number of 'master' degrees of freedom retained in a system.

Writing an FEM package to perform these procedures, including the necessary input, output and graphics, requires several man-years of work. Fortunately the commercially available ANSYS code [39], implements piezoelectric analysis using the theory presented in this section. The package is sufficiently versatile so as to permit the analysis of arbitrarily shaped piezoelectric, and composite piezoelectric, structures. The accuracy of the package is firstly verified, and then the analysis of new composite structures is discussed.

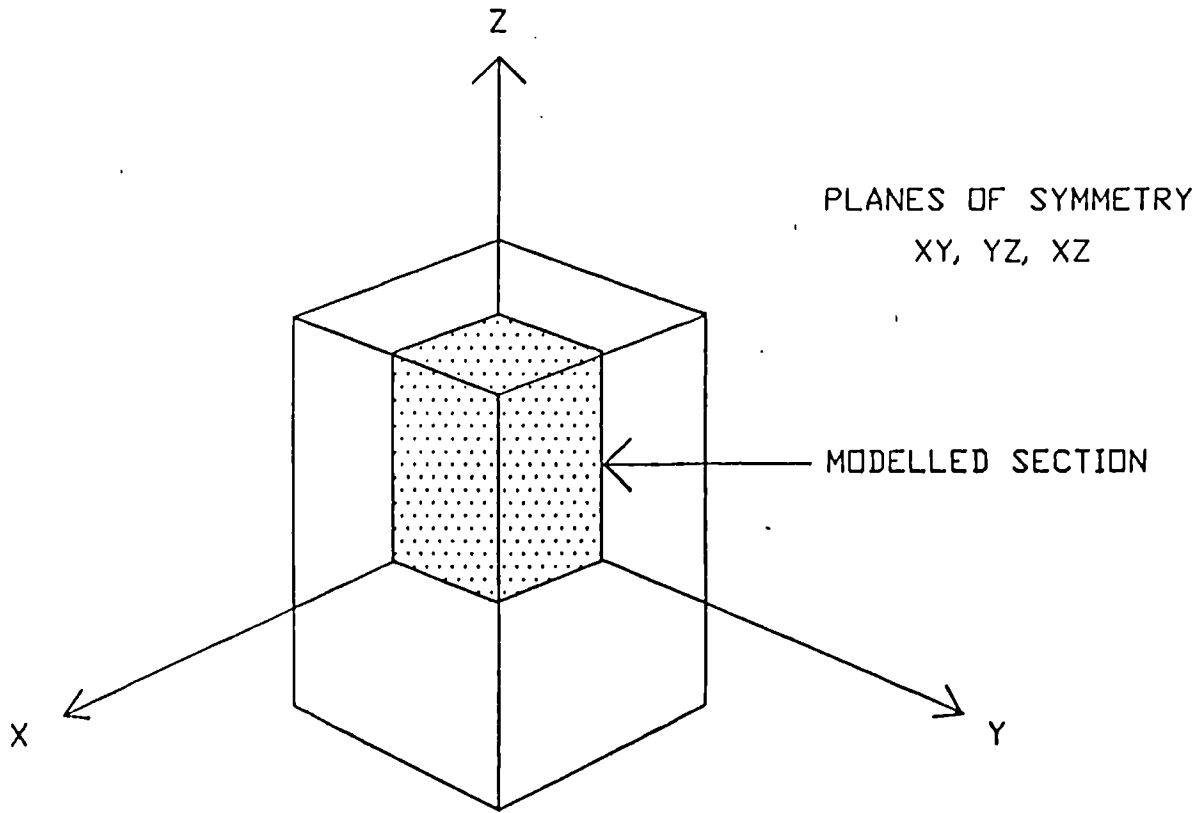


Figure 3.1 One eighth section of pillar structure used for finite element analysis purposes.

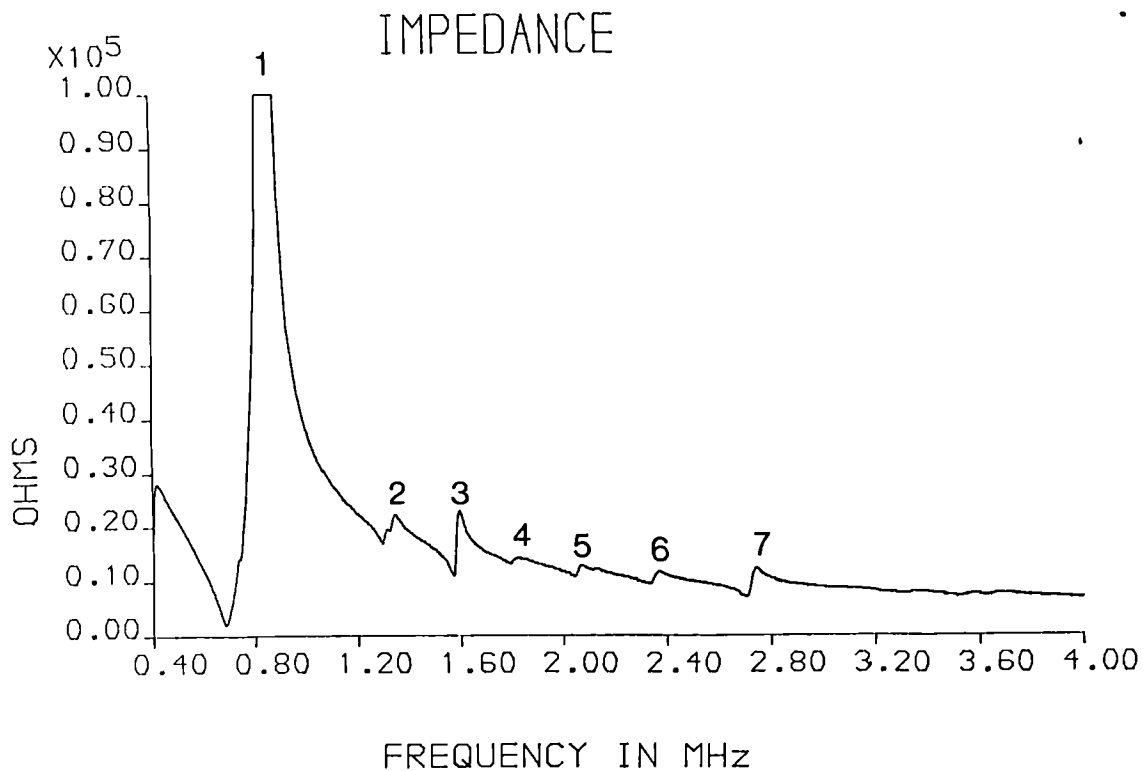


Figure 3.2 Impedance magnitude characteristics of a 1.2 x 1.2 x 2mm ceramic pillar.

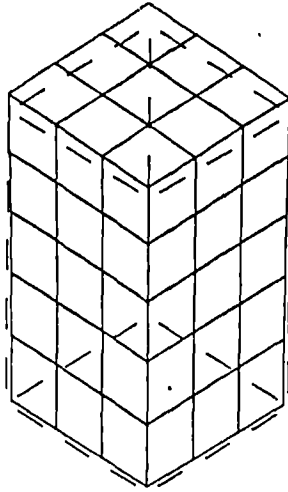
3.3 VERIFICATION OF THE ANSYS FEM CODE FOR PIEZOELECTRIC STRUCTURES

Although ANSYS has been verified for predicting the vibrational characteristics of PZT 4 cubes by Ostergaard [40], it was decided that further verification, for elements similar to those found in composite structures, would be valuable. This provided the essential confidence for further progress to more sophisticated, composite structures.

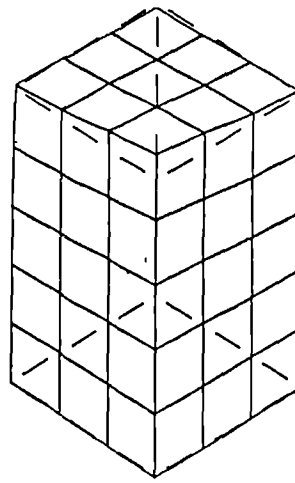
A small, square section, ceramic pillar, typical of the type that may be encountered in a composite transducer has been analysed. The pillar analysed possessed dimensions 1.2 x 1.2 x 2.0mm and is illustrated in Figure 3.1. Again the geometry possesses three planes of symmetry and hence a one eighth section is sufficient to model the entire pillar accurately. The impedance plot is depicted in Figure 3.2, in which several main resonances are apparent. Mechanical resonances were simulated using the ANSYS package and the results in Table 3.1 obtained. The mode number refers to the corresponding mode indicated on the impedance magnitude response (Figure 3.2). The mode shapes are illustrated in Figure 3.3. The fundamental thickness mode is clearly shown by the uniform thickness displacement in first mode plot (Figure 3.3.1). The other modes are very much weaker and more complex in form. Although it is impossible, from a practical viewpoint, to categorically associate the resonant modes predicted using finite element analysis with particular resonances evident

Figure 3.3 Resonant modes of the ceramic pillar.

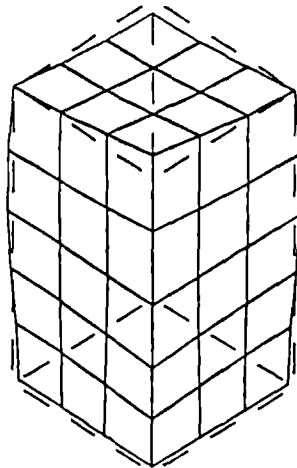
Mode 1



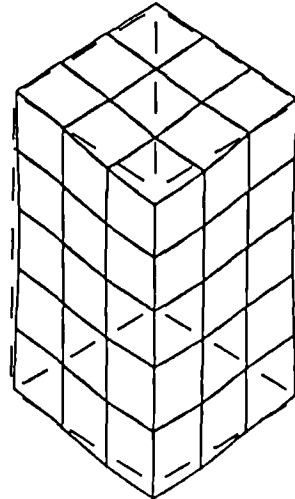
Mode 2



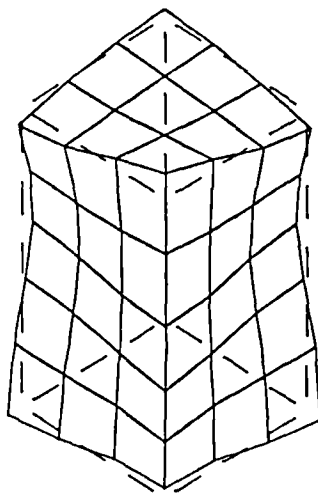
Mode 3



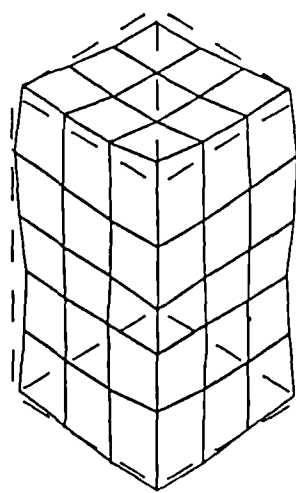
Mode 4



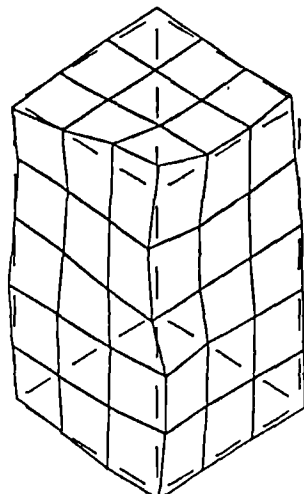
Mode 5



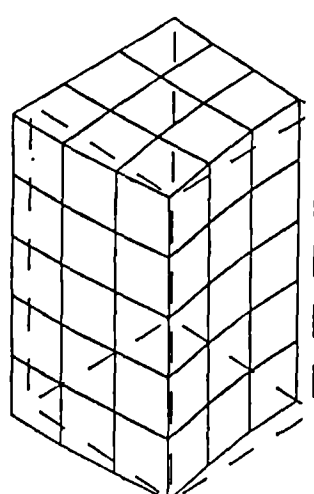
Mode 6



Mode 7



Mode 8



in the experimental impedance plot, the close correlation between the theoretical and experimental resonant frequencies suggest that the predicted modes do, in fact, correlate with the measured resonances.

TABLE 3.1.

Measured and theoretical natural resonant frequencies of a 1.2 x 1.2 x 2mm thick PZT 5A ceramic element. Frequencies in MHz. Mode numbers corresponds to modes illustrated in Figure 3.3

MODE	EXPERIMENT	ANSYS
1	0.860	0.891
2	1.385	1.369
3	1.646	1.649
4	1.872	1.882
5	2.145	2.185
6	2.435	2.491
7	2.825	2.874

Finite element analysis predicted a distinctive lateral mode at 1.029MHz and this is illustrated in Figure 3.3.8. Surprisingly, this mode is totally absent from the impedance profile. However, the mode is antisymmetric about the diagonal on the lateral plane and therefore contraction at one position is exactly matched by an expansion of equal magnitude at another position. No net thickness motion results.

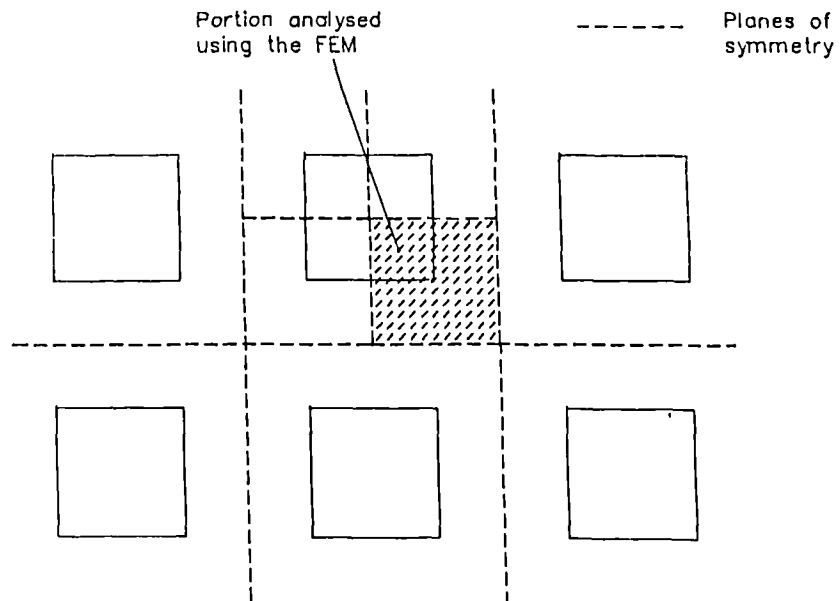


Figure 3.4 Description of the symmetry occurring in a regular composite structure.
 Axis of symmetry :-----

3.4 FINITE ELEMENT ANALYSIS OF COMPOSITE STRUCTURES

Having verified the accuracy of ANSYS for analysing piezoelectric structures, the extension to the analysis of composite materials may be made. The polymer is analysed using similar elements to those used for the ceramic, except that the material parameters are different and the piezoelectric coefficients are zero.

It will be assumed generally that the composite consists of square section piezoelectric pillars spaced periodically in the polymer matrix. Therefore, the symmetry of the problem permits the analysis of a single unit cell to be used as a valid representation of the behaviour of the entire structure. This assumes that planes of symmetry exist on the lateral faces of the cell which implies that no nodal displacement perpendicular to the plane of symmetry may occur. This concept for modelling the unit cell is illustrated in Figure 3.4.

It is also evident that quarter symmetry exists in the X-Y plane of cells containing rectangular or circular cross-section ceramic pillars. Additionally, the cell is symmetrical in the thickness direction. Hence the analysis of a one eighth section of the unit cell will provide a valid simulation, provided that the modes of vibration are also symmetrical. Certain modes of vibration are restricted by the imposition of incorrect planes of symmetry. For example, if half symmetry is assumed in the thickness direction, the fundamental thickness mode is unrestricted by the plane. However, the second harmonic,

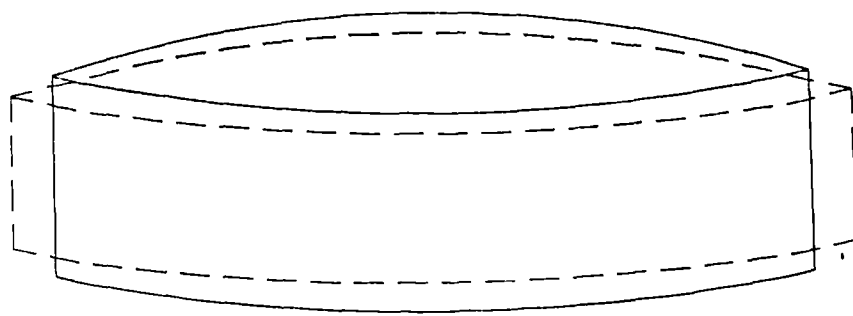
which consists of compression in either the top or bottom half, and expansion in the opposite half, is antisymmetric. Fortunately, the second harmonic in the thickness mode is of very limited practical significance. Nevertheless, the importance of foreseeing the consequences of imposing planes of symmetry in a structure should always be borne in mind. Furthermore, there are two distinct forms that the boundary conditions on the lateral faces of the unit cell may take.

1. Zero net displacement

By definition, a pure thickness mode resonator exhibits zero net lateral displacement. The transducer is said to be 'laterally clamped', since the geometry of the device is such that straight forward Poisson ratio coupling cannot occur. Although, this assumption is perfectly valid for homogeneous materials, the situation in a composite material is far more complex, since the device is relatively free in the lateral direction due to the inclusion of the polymer.

2. Continuity of stress

In this configuration the lateral boundaries are free to displace, but continuity of displacement at the boundaries is conserved because all the cells behave similarly. There is no nodal displacement perpendicular to the boundary plane, but the entire plane may displace together in response to coupling from the thickness direction. Thus there is continuity of stress between the ceramic and polymer phases.



————— STATIC
- - - - - PLANAR VIBRATION

Figure 3.5 Fundamental planar mode of a transducer disc

However, these two conditions are mutually exclusive. If there is zero net displacement, then if one phase experiences a compressing strain, the other must experience an extending strain. Since both materials possess finite, positive values of elastic constants, Hooke's Law implies that one must have a stress opposite in polarity to the other. It is probable that the actual condition lies somewhere between the two extremes. That is, neither zero net lateral displacement nor continuity of stress actually exists. The consequences of these two types of condition are discussed in Chapter IV.

Clearly, by analysing a portion of a unit cell, with boundary conditions, it is not possible to predict the fundamental planar mode of vibration of entire composite discs. This mode is illustrated in Figure 3.5. However, these modes are generally relatively insignificant in composite transducers, although they may be strong in homogeneous ceramic discs. The advantage gained by analysing only a small portion of the entire structure, is that very fine, high quality meshes are viable from a computational point of view. The importance of minimising computational effort in FEA is usually paramount, since even relatively simple analyses require a large computational effort. Typically, the mesh used for a composite structure comprises of a six by six mesh in the X-Y plane, and four elements in the thickness, Z, direction. An example of a typical finite element mesh for a composite material is illustrated in Figure 3.6. The

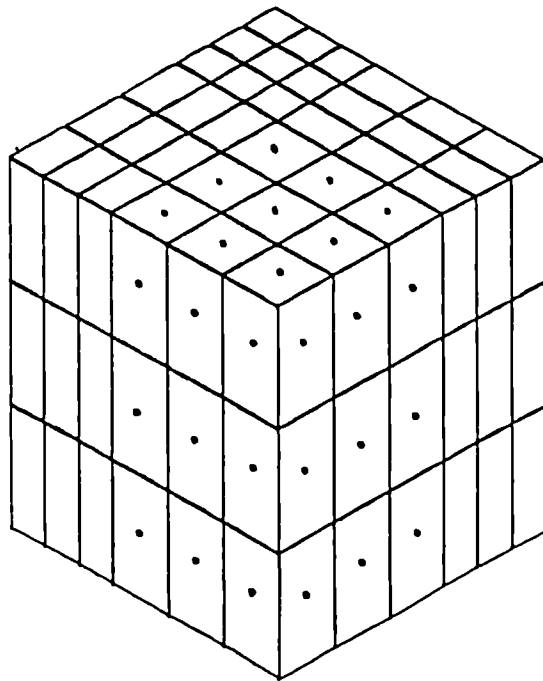


Figure 3.6 Typical finite element mesh of a composite structure. It is assumed that planes of symmetry exist on the four lateral faces and on the base.

Ceramic



Polymer



convention of denoting the ceramic phase with a dot in the relevant element is used throughout the thesis. A tight mesh results in a more accurate answer, particularly for higher frequency, and more geometrically complex, modes of vibration. Also, the validity of the answers can be confirmed to a certain extent, by checking that increasingly more complex meshes result in solutions which converge to a single, more accurate answer [36]. It would also be preferable to use a finer mesh in the vicinity of the ceramic/ polymer interface, where the most complex distortions may be expected. However, for the majority of analyses, involving simple thickness mode operation, relatively coarse meshes are perfectly adequate.

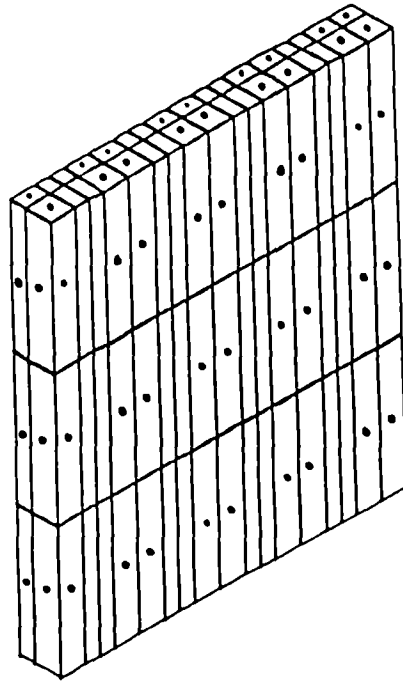


Figure 3.7 Typical finite element mesh of a composite array structure. It is assumed that planes of symmetry exist on the four lateral faces and on the base.

Ceramic



Polymer



3.5 FINITE ELEMENT ANALYSIS OF ARRAY STRUCTURES

Finite element analysis has already been established as a powerful tool in the vibrational analysis of conventional sliced piezoceramic arrays. It can be used to determine the displacement profile of the vibration aperture and hence the associated field profile [37]. It can also be used to determine magnitude and phase information regarding both mechanical and electrical coupling.

The geometric complexity of composite arrays necessitates the use of a two dimensional cross sectional slice for finite element purposes. In practice, the array is simulated as a single row of pillars and associated polymer, and boundary conditions are employed to impose the symmetry that is found in the actual array. This is perfectly valid for the analysis of conventional one dimensional arrays. A typical composite array, finite element mesh, is illustrated in Figure 3.7. In view of the limited capacity of the available ANSYS package, and the computer host, only a limited number of composite pillars may be simulated successfully. However, this is not a serious restriction, as the normal requirement for approximately half wavelength spacing between elements, limits the number of pillars in practical arrays. It is evident that the influence of the matching layer and backing may also be simulated by including these in the finite element mesh.

3.6 CONCLUDING REMARKS

The theoretical basis for finite element analysis of composite piezoelectric materials, both single transducer, and array configurations, has been presented. The use of the commercially available ANSYS finite element package has been discussed and its accuracy for piezoelectric analysis verified. This package is sufficiently well developed and proven that it may be applied as a valid design/ analysis tool for a very wide variety of configurations. Examples of finite element analysis of a wide range of composite configurations will be presented, and where appropriate, verified with experimental and alternative theoretical approaches, in subsequent chapters.

CHAPTER IV

INVESTIGATION OF MATERIALS AND CONFIGURATIONS

4.1 INTRODUCTION

A composite transducer comprises at least two materials possessing complementary properties. Clearly, there is a wide variety of choice in terms of the materials and geometry. This offers the transducer designer a diverse, and previously unknown, choice of configurations and associated material properties. It is therefore essential that a systematic approach is taken during the design process. This chapter considers firstly the choice of constituent materials, and thereafter, some practical geometries. The aim is to achieve an optimal design in terms of some basic desirable properties.

In any transducer design process, at least some of the desired properties are mutually exclusive and therefore an early judgement must be made regarding relative priorities. This is particularly true of the compromise between peak sensitivity and bandwidth. However, in general terms, the following properties are desirable.

1. High electromechanical coupling efficiency
2. Optimised acoustic match to the load media
3. High electrical permittivity
4. Pure, undistorted thickness mode vibration
5. Low electrical resistance losses

4.2 SELECTION OF MATERIALS

The material properties of the constituent phases provides an approximate indication of how the composite device will behave. This is particularly true for the ceramic phase.

4.2 i) Selection of ceramic

The three main types of piezoelectric ceramic are Lead Zirconate Titanate (PZT), modified Lead Titanate (PT) and Lead Metaniobate (PN). The characteristics of the most widely used formulations are detailed in Table A1 in Appendix A. Each of these materials possesses broadly similar mechanical properties. PT, and to lesser extent PN, exhibit less thickness to lateral mechanical and piezoelectric cross coupling. This is determined by their relatively low c_{13}^D and h_{13} coefficients. This feature makes them suitable for use in arrays where lateral activity within, and between, elements is highly undesirable. Furthermore, in a composite structure, if the ceramic exhibits significant mechanical cross coupling then thickness strains in the ceramic may result in undesirable antiphase thickness strains being induced in the polymer.

The major deficiency with PT and PN is their low electrical permittivity. Permittivity determines device impedance and is particularly crucial to transmission efficiency. PZT is available in a variety of formulations; some of which possess extremely high permittivities. PZT also possesses the highest electromechanical coupling coefficient. The peak signal level, and bandwidth, of the

response of a transducer in both transmission and reception is determined, to an extent, by this coefficient. When the ceramics are operating in a bar type mode, similar to that encountered in a composite, the coupling coefficient of the PZT materials are at least 40% higher than in either PT or PN..

Although a discussion of the material parameters favours the use of PZT ceramics in composite transducers, it is worthwhile investigating the expected performance of practical transducer designs under typical operating conditions. The actual performance is a complex function of device geometry, and electrical and mechanical loading, and therefore a comprehensive analysis is essential. Additionally, a comparison of the performance of the ceramic materials with PVDF and a typical composite design will provide information regarding the likely extent of the advantages obtainable by employing composite materials.

The relative transmission, reception and pulse-echo performance of these piezoelectric materials have been compared for one particular set of typical operating conditions. The performance of a 40% PZT 5A composite, and PVDF, are included in the comparison. It will be assumed, in this case, that each transducer is operating into water via a quarter wavelength matching layer possessing the optimum acoustic impedance for that particular material [20]. Furthermore, each piezoelectric element is backed by a medium possessing an acoustic impedance half that of the

TABLE 4.1

Theoretical comparison of the transmission, reception and pulse-echo characteristics of selected transducer materials. All transducers are 30 x 30 mm across and possess a 500kHz centre frequency. They possess a backing with impedance half that of their own impedance, and a quarter wavelength matching layer possessing the optimal acoustic impedance. Maximum values are in bold and minimum values are underlined

	PZT 4	PZT 5A	PZT 5H	PT	PN	COMP.	PVDF
Z_A	34.5	33.7	34.3	34.3	26.2	13.6	4.2
Z_{OPT}	7.19	7.11	7.17	7.17	6.27	4.52	2.50
F_{MAX}	0.65	0.72	1.00	0.31	0.26	0.53	<u>0.02</u>
F_{GBP}	0.65	0.71	1.00	0.31	0.29	0.69	<u>0.03</u>
$R_{MAX} \infty$	0.53	0.42	0.35	1.00	<u>0.33</u>	0.74	0.81
$R_{MAX} 658$	0.41	0.36	0.31	0.39	0.25	0.48	<u>0.05</u>
$R_{GBP} \infty$	0.49	0.39	<u>0.32</u>	0.91	0.37	0.80	1.00
$R_{GBP} 658$	0.40	0.34	0.30	0.41	0.28	0.62	<u>0.07</u>
PE_{MAX}	0.82	0.73	0.83	0.75	0.22	1.00	<u>0.05</u>
PE_{GBP}	0.67	0.59	0.68	0.61	0.19	1.00	<u>0.05</u>

Z_A Acoustic impedance of material (unit MRayl)

Z_{OPT} Optimum acoustic impedance for a matching to water

F_{MAX} Normalised peak CW pressure output (source impedance = 0Ω)

F_{GBP} normalised pressure GBP output (source impedance = 0Ω)

$R_{MAX} \infty$ Normalised peak CW reception sensitivity for infinite receiver impedance

$R_{MAX} 658$ Normalised peak CW reception sensitivity for receiver impedance of 658Ω .

$R_{GBP} \infty$ Normalised reception GBP for infinite receiver impedance

$R_{GBP} 658$ Normalised reception GBP for receiver impedance of 658Ω

PE_{MAX} Normalised peak CW pulse-echo sensitivity for a source impedance = 0Ω and receiver impedance = ∞

PE_{GBP} Normalised pulse-echo GBP for a source impedance = 0Ω and receiver impedance = ∞

piezoelectric material. Therefore, this analysis ought to provide a genuine and fair comparison to be made for transducers operating under nearly optimal conditions. Notice that if wide bandwidth is required, a perfectly matched backing is desirable. However, the highest feasible acoustic impedance obtainable in a backing is approximately 15 MRayl and hence perfect backing of ceramic transducers is virtually impossible. Therefore it may be argued that the comparison presented here discriminates slightly against the low impedance piezoelectric materials. It should also be noted that PVDF is not generally available in single sheet form for frequencies below approximately 2MHz. The results presented in Table 4.1 are for transducers possessing a mechanical resonant frequency of 500kHz and lateral dimensions 30 x 30mm. The acoustic impedance of the material, and the optimum impedance for a matching layer design for operation into water are indicated. In addition to comparing peak sensitivity, the Gain Bandwidth Product (GBP) is also shown. The calculation of the GBP employs the -3dB bandwidth for transmission and reception. The -6dB bandwidth is used for the pulse-echo result because it is a two way mode of operation. GBP is a useful figure of merit as, for the majority of pulse-echo applications, both peak sensitivity and bandwidth are required. The combination of both of these features results in a large amplitude, short duration pulse response. In acoustic imaging these characteristics produce a sharply focused image with a high overall signal to noise ratio.

The transmission results indicate the peak level obtained from a CW source possessing a 0Ω internal impedance. PZT exhibits the highest response level as a consequence of its high permittivity and piezoelectric coupling efficiency. In comparison, the transmission performance of PVDF is extremely poor. The transmission GBP results largely reflect the peak CW results since the bandwidths of the transducers are very similar. However, the GBP of composite and PVDF devices are increased relative to the others because of their superior matching.

In contrast, the results for reception sensitivity operating into an infinite receiver load impedance, indicate that Lead Titanate and PVDF possess the highest sensitivities. As a consequence of their low permittivities, these material produce a higher voltage for given quantity of charge across their electrodes. The GBP of the PVDF is higher than that of PT as a result of its improved match the water load and consequent wider bandwidth.

The reception results have been repeated under conditions of moderate electrical loading. In this case, it is assumed that the receiver possesses an impedance of 658Ω . This figure corresponds to a load impedance/ clamped capacitance product of 10^{-6} for the PZT 5A transducer. The actual load resistance required to achieve the desired loading effect depends on the capacitance, and hence geometry, of the transducer under investigation. Clearly the effect of this electrical load will be most pronounced

in the transducers possessing the lowest permittivities. This is borne out in the results and, in this case, the composite device provides the highest sensitivity. PVDF exhibits the highest reception GBP when the receiver load impedance is infinite. However, in the case where the receiver load impedance is 658Ω , the composite provides a GBP significantly higher than that obtained by any other material. It should also be noticed that although the high permittivity associated with PZT 5H is advantageous in transmission, it is a handicap in reception. This is true only where the receiver load impedance is not giving rise to significant loading effects.

The composite transducer exhibits the best overall pulse-echo performance. The three PZT materials possess broadly similar overall sensitivities although, in this case, PZT 5A is slightly lower. The results for PN and PVDF are disappointing in comparison to the others.

This brief investigation has highlighted the contrasting features of the various materials available. Taking account of the need to retain high permittivity in a composite material, the results suggest that a high permittivity PZT material be used. Thus, either PZT 5A or PZT 5H should be employed. The precise selection of material, and configuration, will depend on the relative importance of transmission, reception and bandwidth performance. PT and PN are clearly inappropriate for use in a composite transducer. Furthermore, PVDF does not exhibit a performance competitive with that obtainable

TABLE 4.2

Comparison of selected materials

	EPOXY ^a	POLYURETHANE ^b	POLYESTER ^b	PZT 5A ^c
DENSITY	1140	1300	1200	7750
Youngs Mod.	6.0	1.5	6.0	106.0
σ	0.35	0.48	0.35	0.35
ϵ_r	4	4	4	830
$\tan\delta$	0.008	0.006	0.0005	0.02
See Note 3	13	>10	>10	2
See Note 4	70	150	80	1.5
See Note 5	0.1	0.8	0.3	0
See Note 6	0.0005	0.02	0.001	-

NOTES

- a) CIBA GEIGY CY1301:HY1300 Bisphenol epoxy
b) Typical values derived from 'Modern Plastics Encyclopedia' Plastics Catalogue Corp. New York, 1986
c) Vernitron Applications Bulletin 66011/F

1. Density in units kgm^{-3}
2. Young's modulus in units GPa
3. Dielectric strength (MVm^{-1})
4. Coefficient of linear thermal expansion ($\times 10^{-6}/^{\circ}\text{C}$)
5. Water absorption (ASTM Test D570)
6. Linear cure shrinkage

from the other materials - except in the case that it is used as a receiver operating into a high impedance load.

4.2 i) Selection of polymer

The polymer selected for use in a composite transducer should possess the following properties.

1. Strong adhesion to the ceramic
2. Low water permeability
3. High dielectric strength
4. Low viscosity in the liquid state
5. Low Poisson ratio
6. Low coefficient of thermal expansion

Although there is a vast range of modern polymers available, very few meet all of these requirements. Polyethylene, and similar thermoplastics, require high temperature and pressure during the moulding process. In fact, only epoxy, polyurethane and polyester satisfy the essential requirements. The properties of these materials are compared with those of a typical PZT ceramic in Table 4.2. Polyurethane and epoxy have been utilised extensively in composite transducer manufacture. Epoxy resin is generally favoured in preference to Polyurethane because it possesses a higher stiffness and lower Poisson ratio. The Poisson ratio of pure polyurethane is close to the maximum theoretical value of 0.5, and hence it is virtually incompressible. This is undesirable in a composite transducer because, as the active ceramic element contracts in the thickness direction, and

consequently expands in the lateral direction, it squeezes the polymer, inducing expansion in the thickness direction. In effect, the polymer and ceramic operate antiphase and hence the net surface displacement is reduced.

It is clear that the dielectric strength and electrical loss factor of all the polymers are vastly superior to those of the available ceramics. It is desirable that, during manufacture, material shrinkage is low in order to minimise static lateral prestressing of the ceramic pillars. Furthermore, thermally induced interfacial stresses should be minimised by using a polymer with a coefficient of expansion which is close to that of the ceramic. Additionally, water permeability should be minimal for under water applications. On the basis of these requirements, it is evident that an epoxy resin is vastly superior to polyurethane. Although the properties of polyesters are only slightly inferior to those of epoxies, they have received little attention by designers of composite transducers.

The epoxy resin systems described in Appendix A are used throughout this thesis. In particular, CIBA-GEIGY CY1301/HY1300 is used unless stated otherwise. However, it is worthwhile briefly considering the effects of polymer stiffness and Poisson ratio on composite material characteristics, since it is possible to modify the properties of a polymer by the inclusion of a filler.

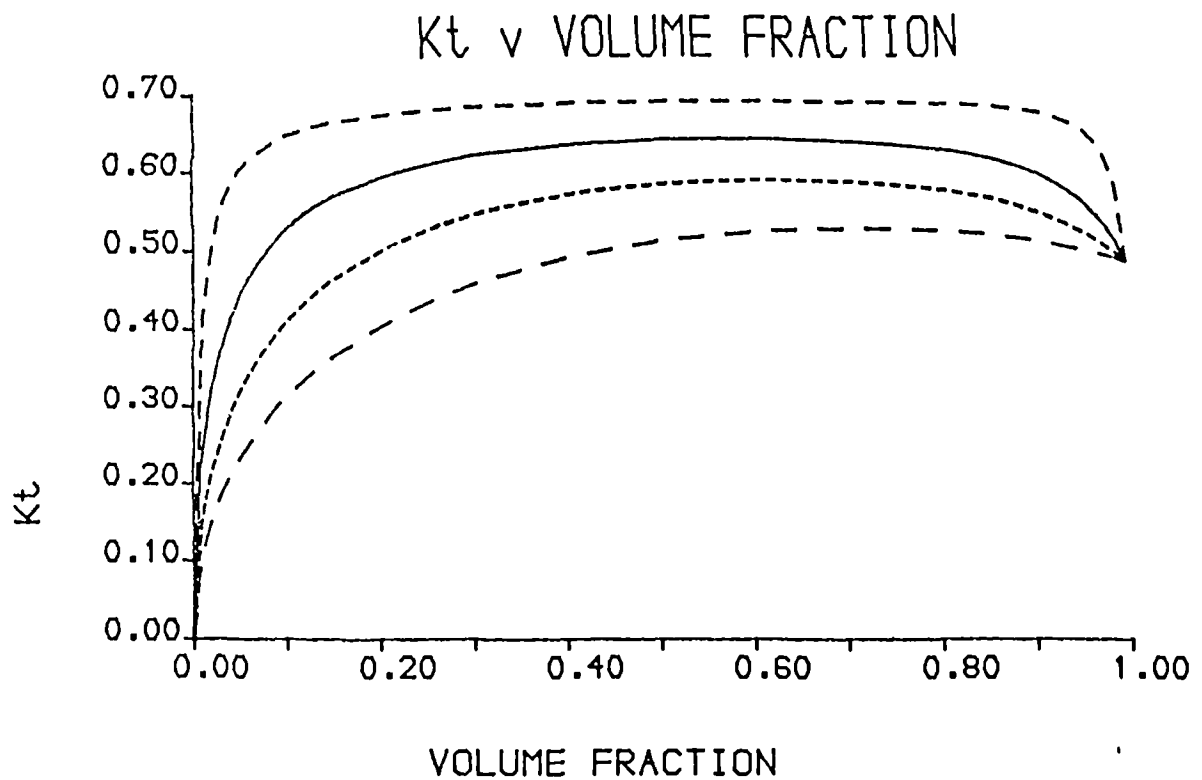


Figure 4.1 Dependence of thickness coupling coefficient on ceramic volume fraction for four different polymers.

- Polymer A CY1301/HY1300
- Polymer B Glass bead loaded CY1301
- Polymer C Glass microballoon loaded CY1301
- . - . - Polymer D Tungsten loaded CY1301

4.2 i) Influence of modified polymers on composite transducer characteristics

Smith's model [3] for predicting the material properties of a composite has been used to predict the thickness mode coupling coefficient as a function of ceramic volume fraction for a selection of polymer configurations. Since the stiffness, density and permittivity of the polymer are small in comparison to that of the ceramic, the acoustic impedance and permittivity of a composite transducer is largely independent of the properties of the polymer, except at very low ceramic volumes. However, the coupling coefficient is a complex function determined partially by the polymer stiffness and Poisson ratio. Figure 4.1 compares the dependence of coupling coefficient on volume fraction for four different polymer configurations - namely, pure epoxy (Polymer A), glass bead loaded epoxy (Polymer B), glass microballoon loaded epoxy (Polymer C) and tungsten powder loaded epoxy (Polymer D). Typical compositions and material properties for these materials are illustrated in Table 4.3. Figure 4.1 indicates that the highest coupling efficiency is obtained when Polymer C is used. In this case, the coupling coefficient approximates to that found in free ceramic pillars ($k_{33} = 0.7$). Increasing stiffness and density results in a lower coupling efficiency. In the extreme case, the coupling coefficient of the composite may be lower than that obtained in a pure ceramic disc.

TABLE 4.3

Propertiers of selected modified polymers

POLYMER	A	B	C	D
DENSITY	1140	1950	500	10000
$c_{33}^D \times 10^9$	8.0	20.0	2.0	40.0
σ	0.35	0.30	0.10	0.30

KEY

Compositions (% weight of constituents)

- A) 100% CIBA GEIGY CY1301/HY1300 epoxy
- B) 75% Glass particles (50 - 100 μ m across)
25% CIBA GEIGY CY1301/HY1300 epoxy
- C) 60% Glass microballoons (70 μ m across)
40% CIBA GEIGY CY1301/HY1300 epoxy
- D) 50% Tungsten particles (5 μ m across)
50% CIBA GEIGY CY1301/HY1300 epoxy

NB The material parameters of these polymers are highly variable. The values presented here are typical.

TABLE 4.4

Comparison of transmission and pulse-echo performace of microballoon loaded and pure epoxy composite transducers.

	MICROBALLOON	PURE EPOXY
k_t	0.632	0.612
TRANSMISSION		
Peak pressure	1.00	0.95
Centre frequency (kHz)	406	435
Gain Bandwidth Product	0.95	1.00
PULSE ECHO		
Peak voltage	0.83	1.00
Centre frequency (kHz)	417	445
Gain Bandwidth Product	0.72	1.00

Although these results may appear to favour a light, lossy polymer, a high coupling efficiency will not necessarily result in a high pulse-echo sensitivity. Prototype 40% ceramic volume fraction, airbacked transducers were constructed with both pure epoxy and microballoon loaded epoxy phases. As expected, the microballoon transducer possesses a higher coupling efficiency - 0.632 versus 0.612 for the pure epoxy case. The experimental transmission and pulse-echo results are illustrated in Table 4.4. In transmission, the microballoon transducer possesses a marginally higher peak efficiency but a slightly reduced gain bandwidth product. This suggests that a greater loss of energy is occurring in the microballoon transducer than in the pure epoxy transducer. However, in pulse-echo operation, the difference between the two responses is more marked. The pure epoxy transducer exhibits a slightly higher peak sensitivity and a markedly higher gain bandwidth product. This is despite the fact that the microballoon loaded transducer possesses a higher electromechanical coupling coefficient.

The bandwidth of a composite transducer may be extended by employing a heavy, loaded polymer. Increasing the internal mechanical loss of a transducer results in a lower mechanical Q_m factor and hence increased bandwidth. This process works in a similar manner to a backing medium, but operates from within the transducer rather than externally. The mechanical loss of a composite transducer may be increased by using a lossy, loaded polymer.

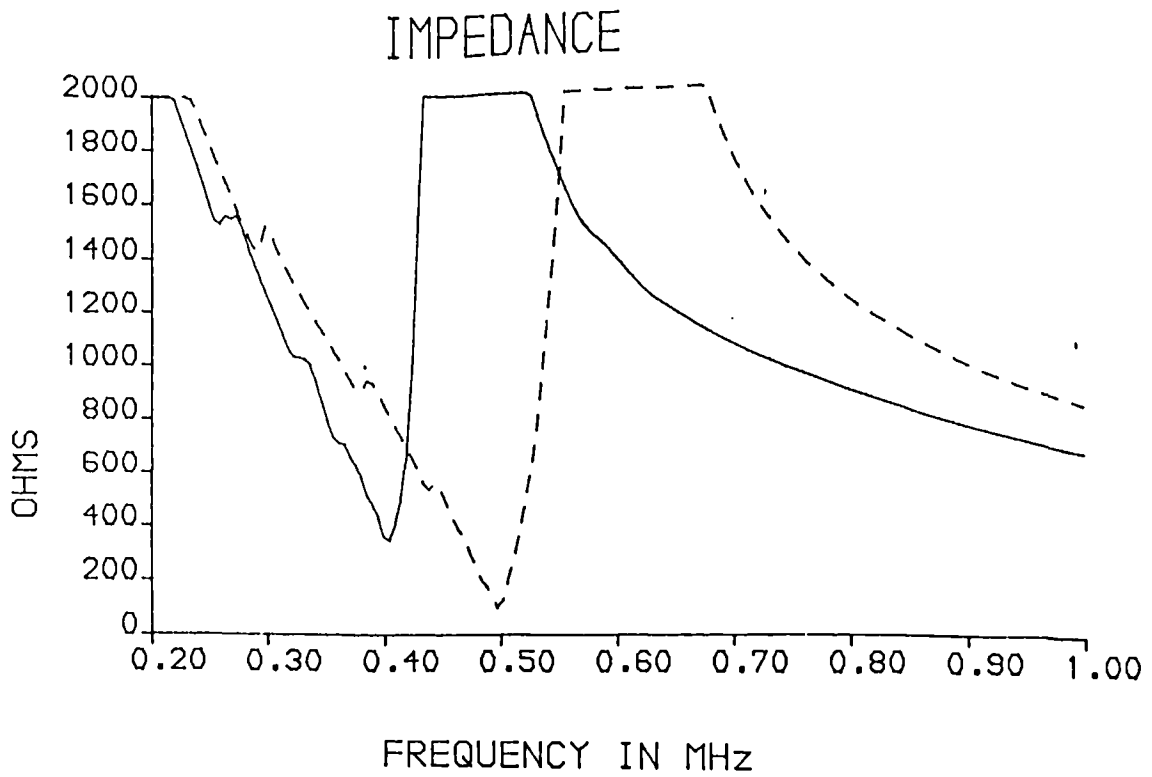


Figure 4.2 Impedance magnitude characteristics of 40% composite transducers containing tungsten loaded and pure epoxy resin.
 Tungsten loaded epoxy _____
 Pure epoxy -----

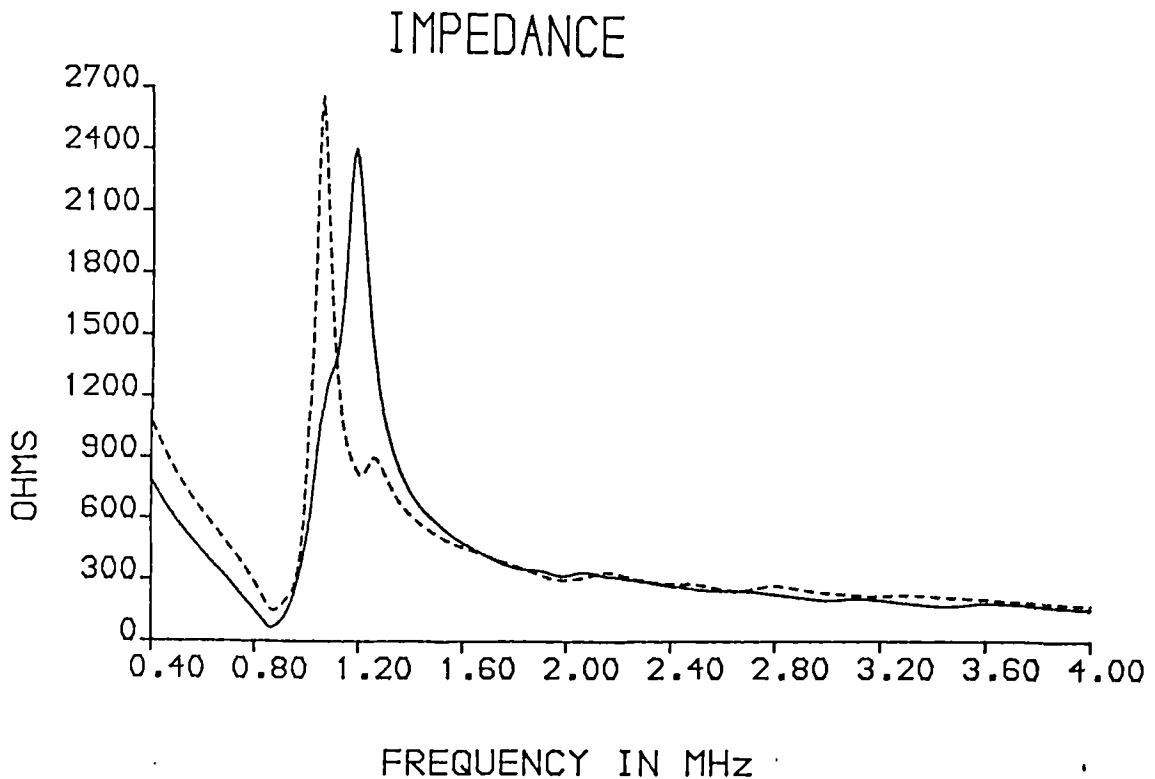


Figure 4.3 Impedance magnitude characteristics of 40% composite transducers containing soft and hard epoxy resins.
 CY208/HY956 (soft) _____
 CY1301/HY1300 (hard) -----

Choosing a polymer/ particle system suitable for a composite transducer involves compromise. A heavy particle is required and this suggests the use of a dense metal. Typically, tungsten particles are favoured for backings, but in this case, care must be taken to ensure that there is no risk of electrical breakdown between the opposite electrodes of the transducer. Therefore, a high concentration of metal is inappropriate. Also, the use of a large number of smaller particles will reduce the risk of breakdown by increasing the number of insulating polymer bonds between particles. Alternatively, metal oxides, which possess lower densities, may be employed.

To evaluate this, a 500kHz 40% transducer was made using a polymer containing 80% by weight, 5 μ m tungsten powder. The impedance profile of this device is compared to a reference transducer containing pure epoxy polymer in Figure 4.2. These devices possess the same dimensions and ceramic volume fraction and hence the capacitances of the two devices are identical. In accordance with expectation, the loaded polymer transducer has a higher impedance minimum, and hence lower Q, and consequently, greater bandwidth. The resonant frequency has been shifted downwards to a significant extent as a result of the lower overall acoustic velocity in the tungsten loaded epoxy.

Alternatively, or in addition to using a loading medium, lossier polymers may be employed. However, care must be taken to ensure that uniform vibration is still obtained. The consequences of using a more compliant polymer on vibrational characteristics are considered in section 4.3 v). Also, it is important that efficient energy transfer between ceramic and polymer is occurring, and that the pillars are not vibrating independently as an array of separate sources. Figure 4.3 compares the impedance magnitude response of two 40% 1MHz composite transducers. Both possess ceramic pillar width to height ratios of approximately 0.6, but one contains a soft epoxy (CY208/HY956) while the other contains a hard epoxy (CY1301/HY1300). Details of the material properties of these two polymers are contained in Appendix A. The response of the soft epoxy device demonstrates little of the lateral resonant activity evident in the response of the hard epoxy device. These results suggest that improved characteristics have been obtained by using a soft polymer. However, the extent of energy transfer between ceramic and polymer has not been evaluated in a definitive fashion.

An alternative method of investigating the influence of a soft, lossier epoxy is to measure the characteristics of a composite transducer over a range of temperatures up to, and beyond, the glass transition temperature of the polymer. Coupling coefficient, longitudinal velocity and mechanical Q were measured for a 500kHz 40% composite

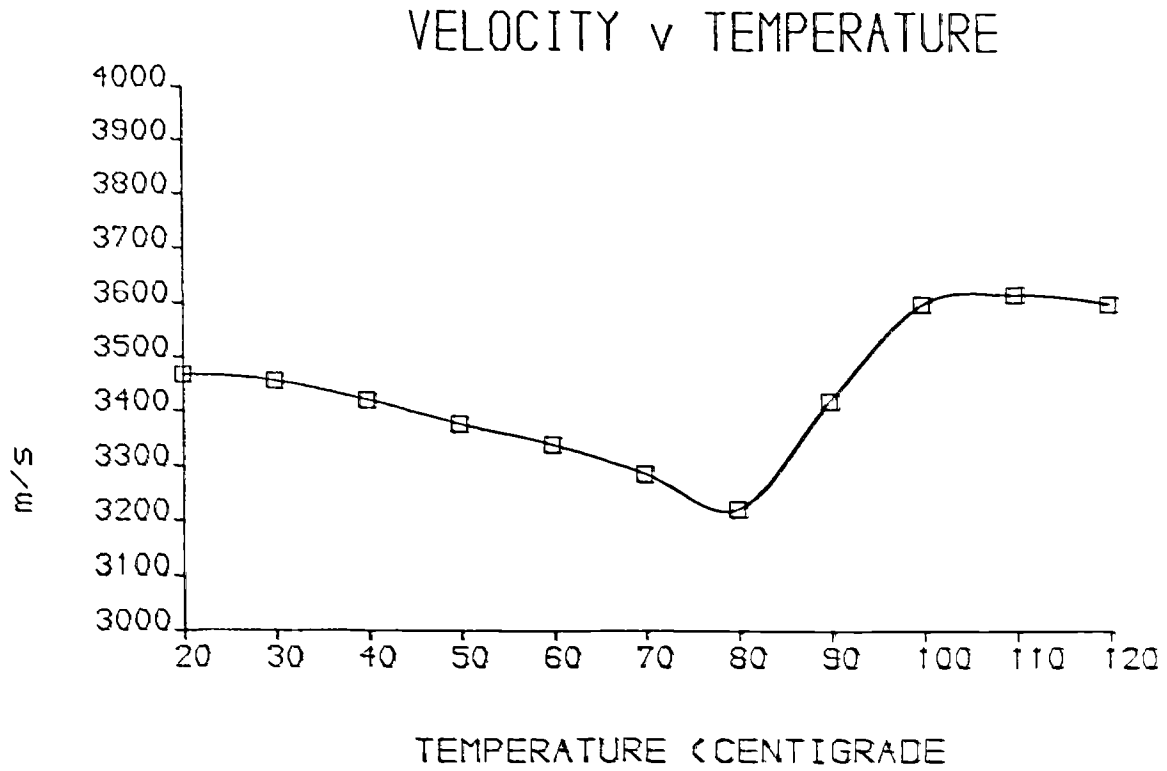


Figure 4.4 Dependence of longitudinal wave velocity on temperature in a 40% 500kHz transducer.

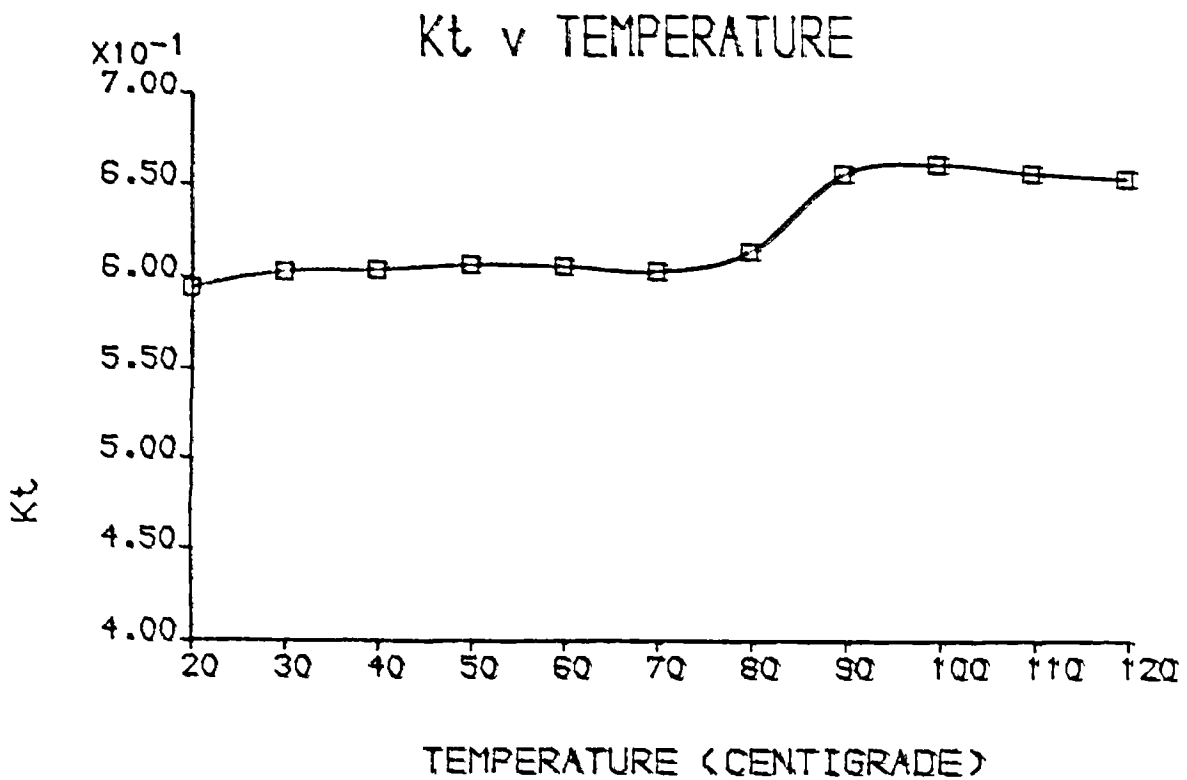


Figure 4.5 Dependence of thickness coupling coefficient on temperature in a 40% 500kHz transducer.

transducer over the range 20°C to 120°C. The polymer used was MY753:CY208 (50:50)-HY956 as described in Appendix A. This material possesses a glass transition temperature of approximately 90°C. Figure 4.4 illustrates the dependence of velocity on temperature. As the temperature increases, the velocity reduces because of the reducing stiffness of the polymer phase. However, above the glass transition temperature, the velocity rises dramatically. At these temperatures the ceramic pillars vibrate as if they are almost completely isolated. Therefore, the wave velocity tends towards that encountered in pure ceramic pillars rather than that found in a composite device. The velocity observed from Figure 4.8, for temperatures higher than 90°C, approaches the nominal longitudinal wave velocity of 3700ms^{-1} for pure PZT 5A ceramic pillars. This result has important practical applications. If the observed wave velocity in a composite is higher than expected, and approaches that obtained in isolated ceramic elements, then it can be surmised that the transducer is not behaving as a true, uniform composite resonator.

Figure 4.5 illustrates the dependence of the thickness coupling coefficient over the same temperature range. The coupling coefficient is essentially constant over the temperature range up to the glass transition temperature of the polymer. At higher temperatures, the pillars vibrate more freely and their effective thickness coupling coefficient tends towards that found in isolated ceramic pillars ($k_{33} = 0.70$). The transition is

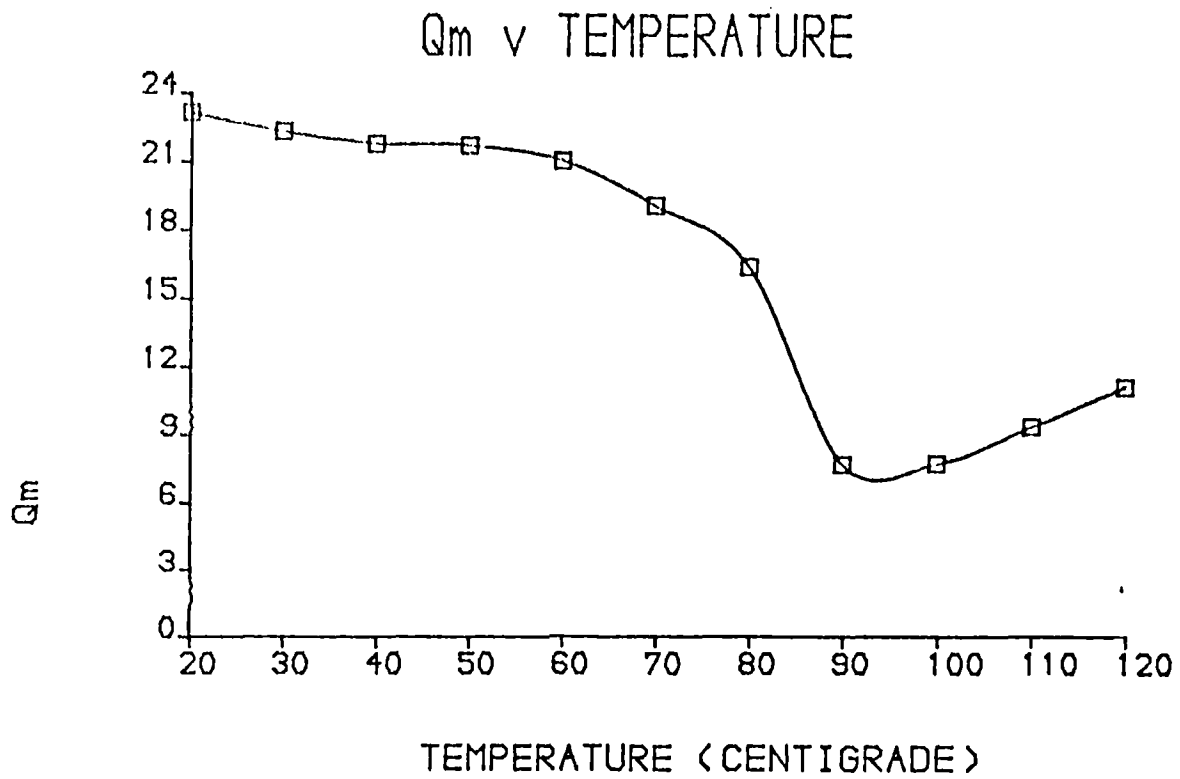


Figure 4.6 Dependence of mechanical Q factor on temperature in a 40% 500kHz transducer.

remarkably well defined. The reason for the coupling coefficient not attaining the nominal k_{33} value is probably slight residual lateral clamping by the polymer and depoling induced during the slicing process. This is discussed further in Chapter V and Appendix D.

Figure 4.6 illustrates the dependence of the mechanical Q_m factor for the same range of temperatures. As the temperature increases, the polymer becomes more attenuative, and hence the Q_m factor reduces. This trend is most marked between 80°C and 90°C. The Q_m reaches a minimum value of 7.7 at 90°C and increases slightly at higher temperatures. This is because the polymer is becoming softer and hence the Q_m of the material approaches the Q_m factor associated with isolated ceramic pillars.

These temperature effects are reversible and no measurable hysteresis effect was observed. However, repeated excessive thermal cycling must lead ultimately to reduced performance, as a result of weakening inter-facial bonds between the ceramic and polymer phases.

In conclusion, if a loaded, or lossy, polymer is used, care must be taken to ensure that acoustic losses within the polymer are not excessive. In practice, it would appear that homogeneous polymeric materials are generally preferable to those containing fillers. Also, from a manufacturing viewpoint, filled polymers are more viscous and may suffer uneven particle settling during curing.

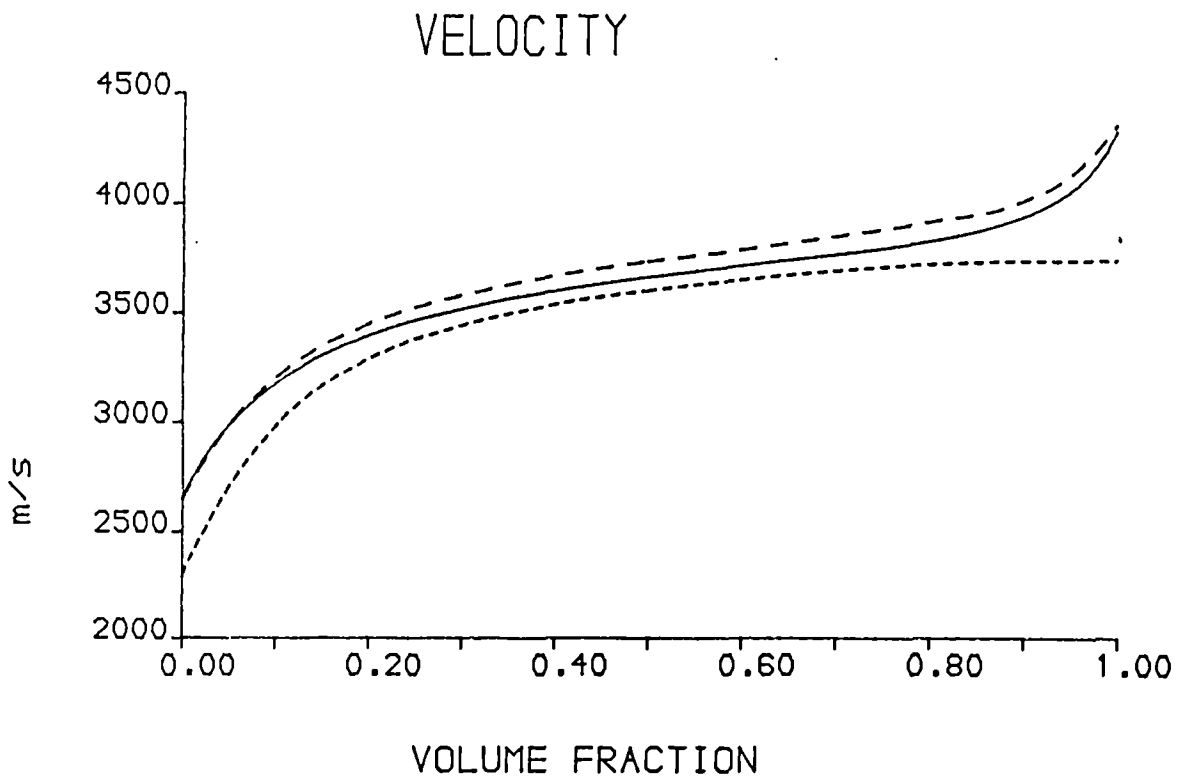


Figure 4.7 Theoretical longitudinal wave velocity in a composite transducer, as a function of ceramic volume fraction.
 Smith's model [3] _____
 FEM 'laterally clamped' - - - - -
 FEM 'laterally free' - . - . - .

4.3 SELECTION OF GEOMETRY

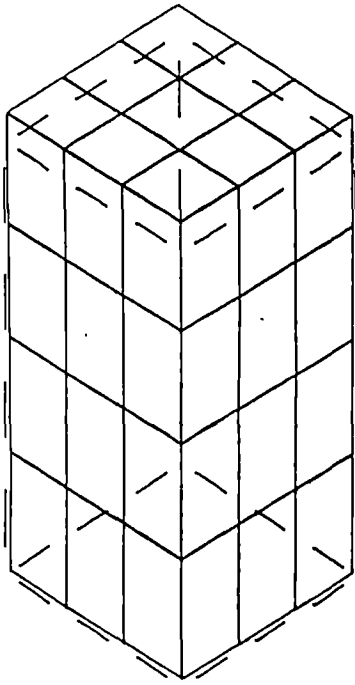
4.3 i) Introduction

Various configurations of transducer and manufacturing method have already been analysed in Chapter II. It was concluded that the simplest and most effective manufacturing method is the 'slice and fill' technique described by Savakus [2]. This naturally suggests that the transducer will consist of a regular matrix of square section pillars. However, transducer behaviour, in terms of longitudinal wave velocity and coupling coefficient is a complex function of both ceramic volume fraction and pillar width to height ratio. Finite element analysis provides the only practical means of investigating these effects. It is also useful to compare results obtained by finite element analysis with those obtained using Smith's one dimensional approximate model [3]. These results are initially considered only for square section pillars. Subsequently, the differences obtained by using alternative pillar geometries are discussed.

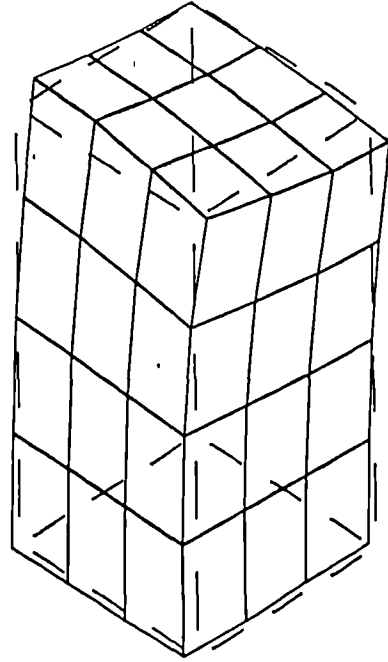
4.3 ii) Dependence of wave velocity on ceramic volume fraction

Figure 4.7 illustrates the predicted longitudinal wave velocity in a composite structure for a complete range of ceramic volume fractions. The finite element analysis was performed assuming that the ceramic pillars possess a width to height (aspect) ratio of 0.1. This aspect ratio is sufficiently small that Smith's one dimensional model

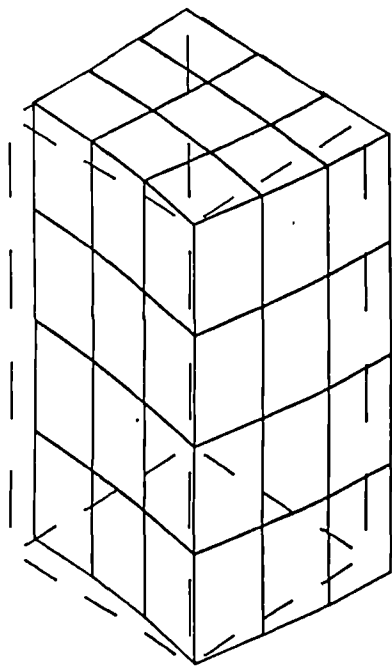
is applicable to this geometry. As discussed in Chapter III, there are two distinct types of boundary conditions that may be applied during finite element analysis. 'Laterally clamped' conditions imply that all motion perpendicular to the lateral boundary planes is suppressed. However, 'laterally free' conditions permit motion of the lateral boundary plane, but all nodal displacements must be compatible with the motion of the entire plane. As would be expected, the 'laterally clamped' condition has resulted in a slightly higher velocity in comparison to the 'laterally free' conditions. This is because lateral stiffening is mechanically coupled into increased thickness stiffening. The results obtained using Smith's model lie intermediate between the two finite element results and demonstrate perfectly adequate accuracy for this configuration. The 'laterally free' boundary condition is clearly inappropriate for both the pure ceramic case and for the pure polymer case. However, in the midrange, it is evident that Smith's model does not correspond exactly with the 'laterally clamped' finite element results. This is because the model assumes that ceramic and polymer lateral stresses are equal and this configuration equates more closely with the 'laterally free' conditions.





Thickness mode



First lateral mode



Second lateral mode

Figure 4.8 Resonant modes of a ceramic pillar possessing an aspect ratio of 0.5. One eighth section.
 Static 
 Modal displacement 

4.3 iii) Dependence of longitudinal velocity on ceramic pillar width to height ratio.

Finite element analysis has been used to investigate the dependence of longitudinal wave velocity on pillar width to height ratio for several ceramic volume fractions. However, before considering the case for a composite transducer, it is worthwhile analysing the dependence of the resonant vibrational modes on aspect ratio, in an isolated, square section ceramic pillar. Therefore, any features apparent in the composite response may be attributed specifically to vibrational phenomena occurring within the ceramic pillars, or alternatively, within the polymer phase. The first three significant modes of vibration in 3mm high PZT 5A ceramic pillars have been investigated. These modes are illustrated in Figure 4.8, for the case of a pillar possessing an aspect ratio of 0.5. The analysis was then extended for aspect ratios ranging from 0.1 to 0.9. An upper limit of 0.9 is used because determining the nature of the modes of vibration at higher aspect ratios becomes significantly more difficult. The dependence of velocity on aspect ratio, illustrated in Figure 4.9, has been calculated from the fundamental mechanical resonant frequency by assuming half wavelength resonance and using the relationship $v = f \lambda$. The frequencies of these modes are indicated in Table 4.5. The short circuit thickness resonant frequency has also been recorded, since the electromechanical coupling coefficient associated with a mode may be determined from these frequencies. This is discussed in section 4.3 iv).

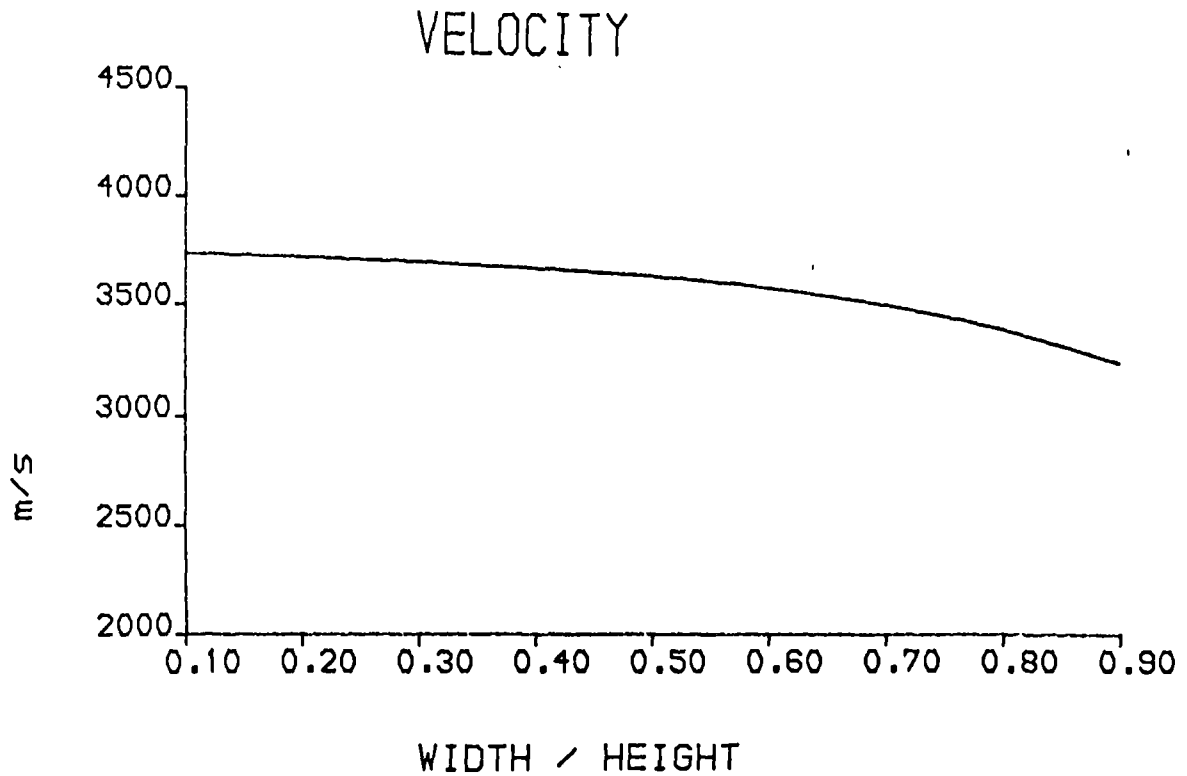


Figure 4.9 Dependence of longitudinal wave velocity on aspect ratio in a square section ceramic pillar.

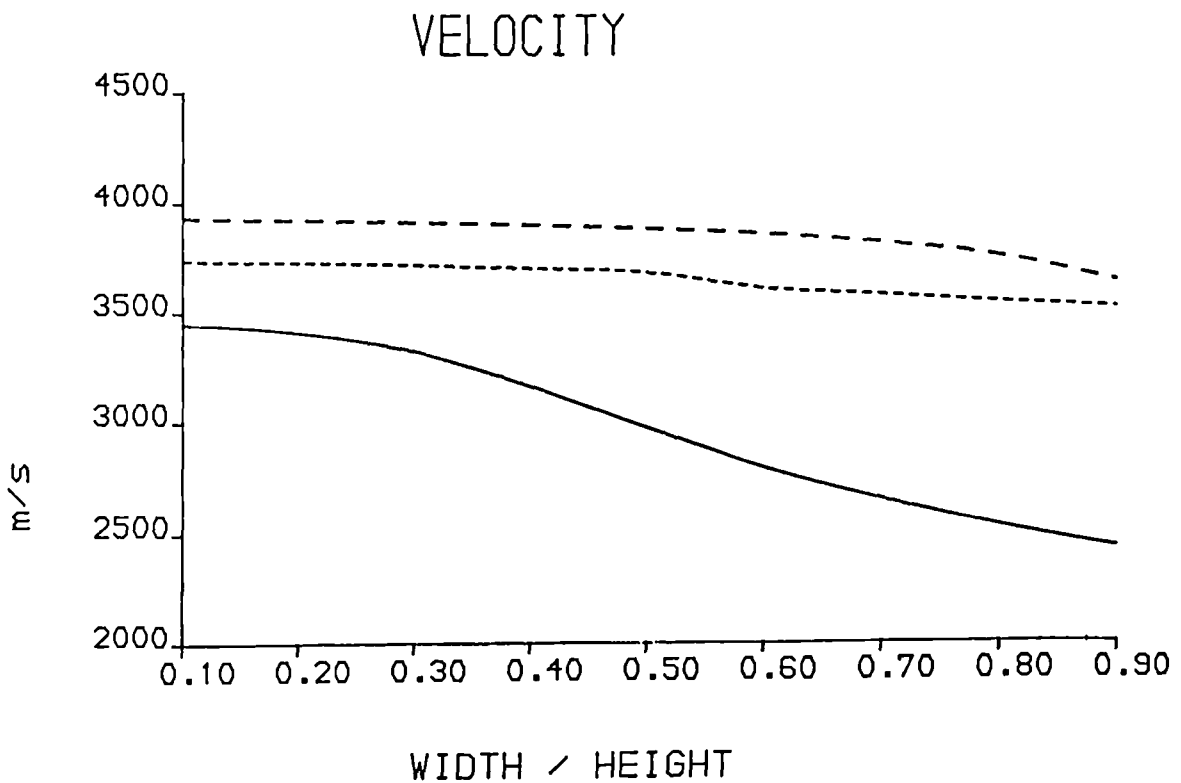


Figure 4.10 Dependence of longitudinal wave velocity on aspect ratio in a square section pillar composite for three ceramic volume fractions.
 Ceramic volume fraction = 20% —————
 Ceramic volume fraction = 50% - - - - -
 Ceramic volume fraction = 80% - . - . - .

Table 4.5 indicates that the thickness resonant frequencies fall steadily as the aspect ratio increases. Furthermore, the frequencies of the two lateral modes fall far more rapidly, and for the cases that the aspect ratios are greater than 0.8, the lateral modes are occurring at frequencies intermediate between the short circuit and open circuit thickness mode frequencies. It may be expected that the presence of the lateral modes close to the thickness mode resonant frequencies could lead to strong parasitic interference with the thickness mode. However, the steady, uninterrupted shape of the thickness velocity curve suggests that this is not happening. The significance of the lateral modes is considered in further detail in section 4.3 v).

Finite element analysis of composite transducer sections has been performed for volume fractions of 20%, 50% and 80%. These analyses have assumed 'laterally clamped' boundary conditions. Figure 4.10 illustrates the dependence of wave velocity on pillar aspect ratio at three volume fractions of interest. All exhibit reducing velocity at greater aspect ratios. However, the trend is significantly more marked for the case of the 20% transducer. The analysis previously presented for the isolated ceramic pillars, indicates that the significant reduction in longitudinal wave velocity is due to strong coupling to resonant activity in the polymer phase. The explanation for this becomes evident when the electromechanical coupling coefficients of the resonant

TABLE 4.5

Frequencies of resonant modes in 3mm thick ceramic pillars. (Frequencies in kHz)

W/H	THICKNESS		LATERAL	
	f_m	f_n	f_{1n}	f_{2n}
0.1	462	622	2050	3719
0.2	460	621	1971	2818
0.3	457	618	1311	1370
0.4	452	614	966	1020
0.5	448	608	760	823
0.6	440	599	628	686
0.7	431	586	541	588
0.8	420	568	480	514
0.9	408	543	438	457

modes are considered in section 4.3 v).

4.3 iv) Dependence of coupling coefficient on ceramic volume fraction.

The dependence of coupling coefficient on ceramic volume fraction has been determined using finite element analysis. As in the case of longitudinal wave velocity, it is profitable to compare the results obtained with those derived using Smith's simple one dimensional model. Although the coupling coefficient may be determined from the ratios of elastic, dielectric and electromechanical energies, as discussed in Chapter III, it is generally preferable to derive the coefficient from the frequencies of short circuit and open circuit resonance. This allows an effective measured coupling coefficient to be associated with a specific vibrational mode and provides an indication of the relative significance of the various modes present in the structure. However, it is inevitable that when the frequencies of several modes are in close proximity, this coefficient is susceptible to numerical error. Since the modal analysis assumes no loss, the short circuit resonant frequency equates to the electrical resonant frequency (f_m). This corresponds to the impedance minimum. Likewise, the open circuit resonant frequency equates to the mechanical resonant frequency (f_n). Hence, the following expression for determining the electromechanical coupling coefficient is applicable [1].

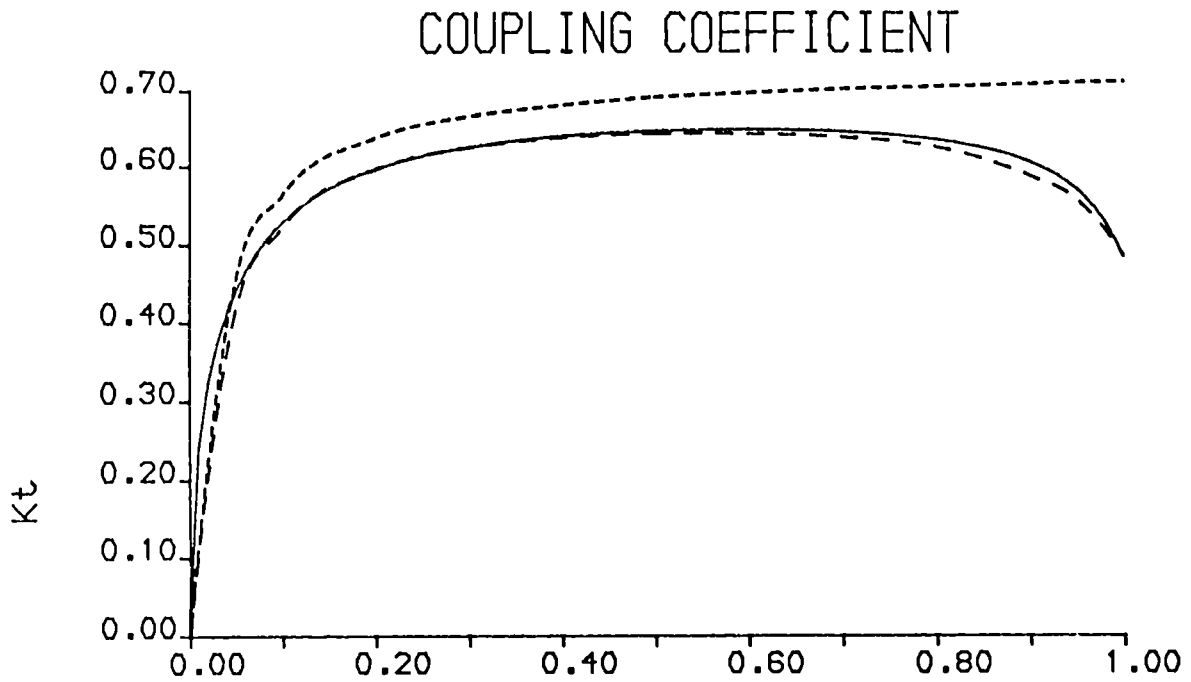


Figure 4.11 Thickness mode coupling coefficient in a composite transducer, as a function of ceramic volume fraction, using three models.

Smith's model [3] —————
 FEA 'laterally clamped' - - - - -
 FEA 'laterally free' -

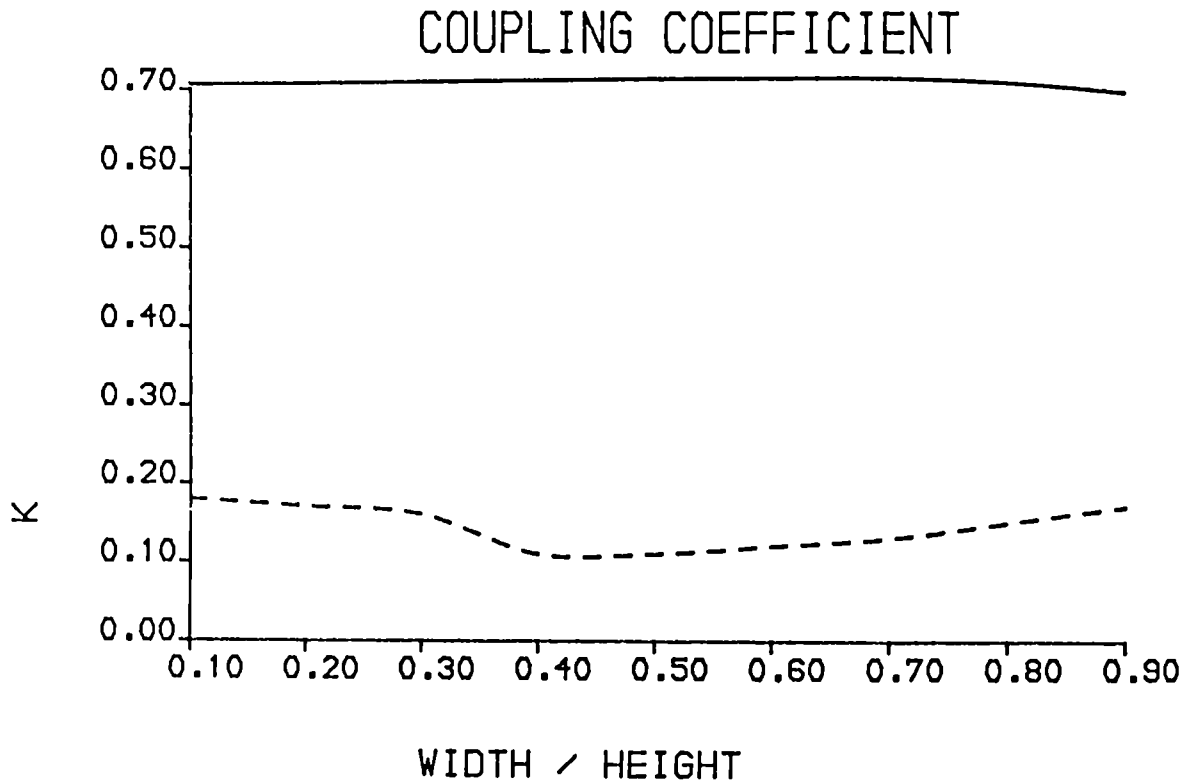


Figure 4.12 Dependence of effective thickness mode coupling coefficient on aspect ratio in isolated ceramic pillars.

Thickness ————— Lateral - - - - -

$$k^2 = \frac{\frac{\pi f_m}{2 f_n}}{\tan \left[\frac{\pi f_m}{2 f_n} \right]}$$

Figure 4.11 illustrates the predicted thickness mode coupling coefficient over the complete range of ceramic volume fractions. Again, finite element analysis was performed assuming that the pillars possess aspect ratios of 0.1 so that valid comparison could be made with results obtained from Smith's model. The finite element analysis results were obtained for both 'laterally free' and 'laterally clamped' conditions. These results are analogous to those obtained under section 4.3 ii), in that the results obtained from Smith's model lie intermediate between those obtained using finite element analysis with 'laterally clamped' and 'laterally free' conditions. Again, the 'laterally clamped' conditions are more appropriate to the 100% ceramic case, where the coupling coefficient is expected to conform to the coupling coefficient observed in a thin thickness mode disc. The 'laterally free' coupling coefficient of a pure ceramic pillar corresponds to k_{33} (0.70) while the 'laterally clamped' coupling coefficient of a pure ceramic transducer corresponds to k_t (0.486). The significant enhancement in coupling coefficient that may be obtained by eliminating lateral clamping is evident. Overall, it is believed that the laterally clamped boundary condition is generally more realistic and is therefore used in all subsequent

finite element analysis. Clearly, the numerical simplicity of Smith's model makes it ideal for practical use. The correlation between results obtained from Smith's model and practical experimental values are discussed in Chapter V.

4.3 v) Dependence of coupling coefficient on ceramic pillar width to height ratio.

Before considering the influence of pillar aspect ratio on coupling coefficient in a composite transducer, it is worthwhile investigating the dependence in isolated ceramic pillars. This will assist in identifying whether the source of any phenomena observed in composite structures is within the ceramic phase or within the polymer phase.

The dependence of coupling coefficient on pillar aspect ratio for the thickness and first lateral modes, as discussed and illustrated in section 4.3 ii), is outlined in Figure 4.12. The coupling coefficient associated with the second lateral mode is extremely low (< 0.02). The coupling coefficient of the principal thickness mode remains at a high level over the entire range that has been considered. Although not clear in the figure, there is a distinct correlation between maximum thickness coupling efficiency and a minimum in lateral resonant activity. Thus, the peak coupling coefficient is observed in the pillars possessing aspect ratios in the range 0.4

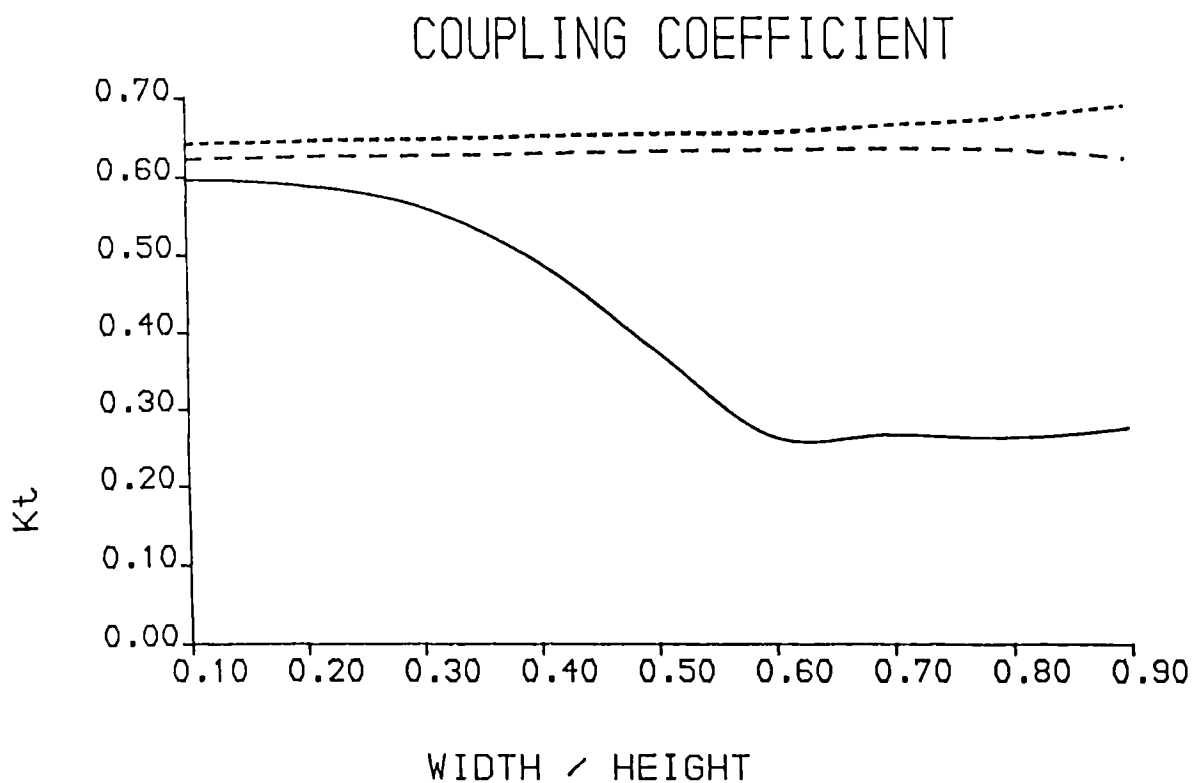
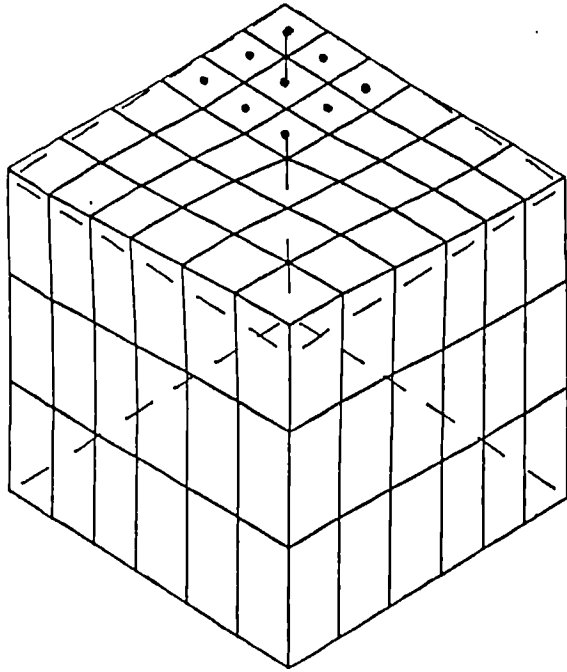


Figure 4.13 Dependence of effective thickness mode coupling coefficient in a composite transducer, as a function of pillar aspect ratio, for three volume fractions.
 Ceramic volume fraction = 20% —————
 Ceramic volume fraction = 50% - - - - -
 Ceramic volume fraction = 80% - . - . - .

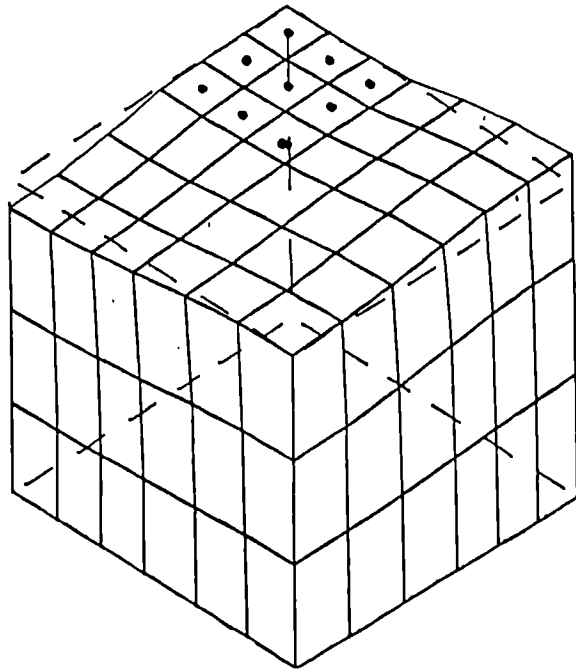
to 0.7.

The hypothesis that strong lateral resonant activity has the effect of reducing thickness coupling efficiency is sensible from an intuitive viewpoint. A similar observation and hypothesis has been made for a related effect observed in long, tall, thin, plank-type array elements [42]. Although the second lateral resonant mode appears significant, in that relatively uniform expansion/contraction is observed, the mode is in fact only very weakly coupled to the thickness mode. This is because the mode is antisymmetric about the diagonals of the pillar. A contraction in one direction is matched by an equal and opposite expansion in the perpendicular direction, and hence no net thickness effect is observed.

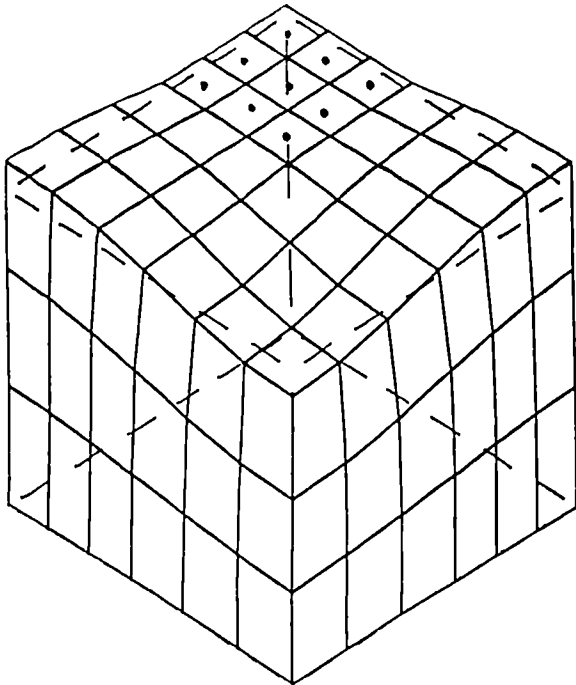
Analysis of the dependence of thickness coupling coefficient on ceramic pillar aspect ratio was performed for composite transducers possessing volume fractions of 20%, 50% and 80%. The results of this analysis are illustrated in Figure 4.13. In the case of the 50% and 80% devices, a high, level coupling efficiency is observed over the entire range considered. However, the coupling coefficient of the 20% device exhibits a significant, progressive degradation for aspect ratios greater than 0.3. The previous analysis for the isolated ceramic pillars implies that the cause of this degradation must be due to activity in the polymer phase, since no significant variation in thickness coupling coefficient, as a function of pillar aspect ratio was observed. The 20% device has



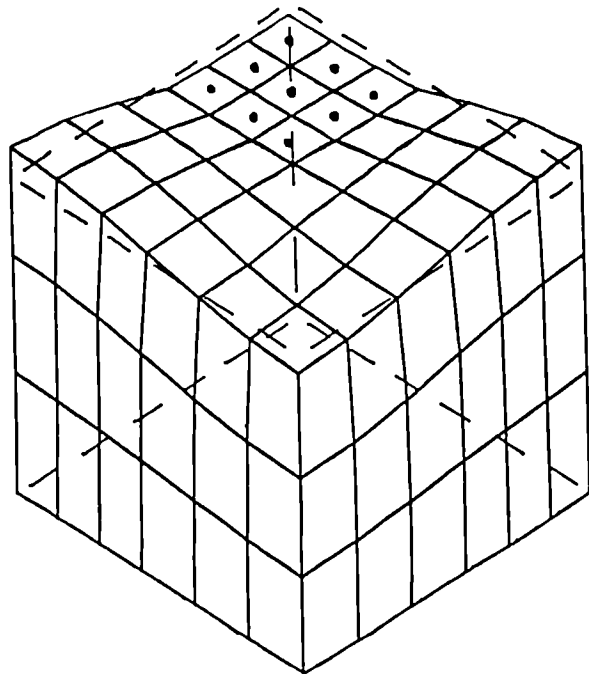
Thickness mode



First lateral mode



Second lateral mode



Third lateral mode

Figure 4.14 Resonant modes of a 20% composite, possessing square section pillars with aspect ratio of 0.5. One eighth section.

Static
 Modal displacement

the greatest inter-rod spacing. Therefore the frequencies of the inter-rod lateral resonant modes are closer to the thickness mode resonant frequency, than is the case for the 50% and 80% devices. Inter-pillar resonances are those which occur within the polymer between the ceramic pillars. These should not be confused with internal pillar resonances which occur within the ceramic pillars, between the lateral faces of the pillars. There are three observable lateral modes in the vicinity of the thickness mode. Figure 4.14 illustrates these modes for a 20% composite possessing a pillar aspect ratio of 0.5. The first of these lateral modes is antisymmetric about the diagonals in the X-Y plane. Therefore, no net thickness effect is observed. The coupling coefficient associated with this mode is therefore very small and never exceeds 0.07 over the range of interest. Figure 4.15 illustrates the dependence of the coupling coefficient of the two significant lateral modes, and the thickness modes, as a function of pillar aspect ratio. The second lateral mode becomes progressively stronger for increasing aspect ratios, but reduces again when the aspect ratio exceeds 0.5. The third lateral resonant mode becomes significant at aspect ratios greater than approximately 0.5. The lateral modes become rather complex for aspect ratios greater than 0.8 and no meaningful results could be obtained. As in the case of the isolated ceramic pillar, there is a clear correlation between high thickness resonant activity and low lateral resonant activity. Referring to Table 4.6, which indicates the frequencies of

COUPLING COEFFICIENT

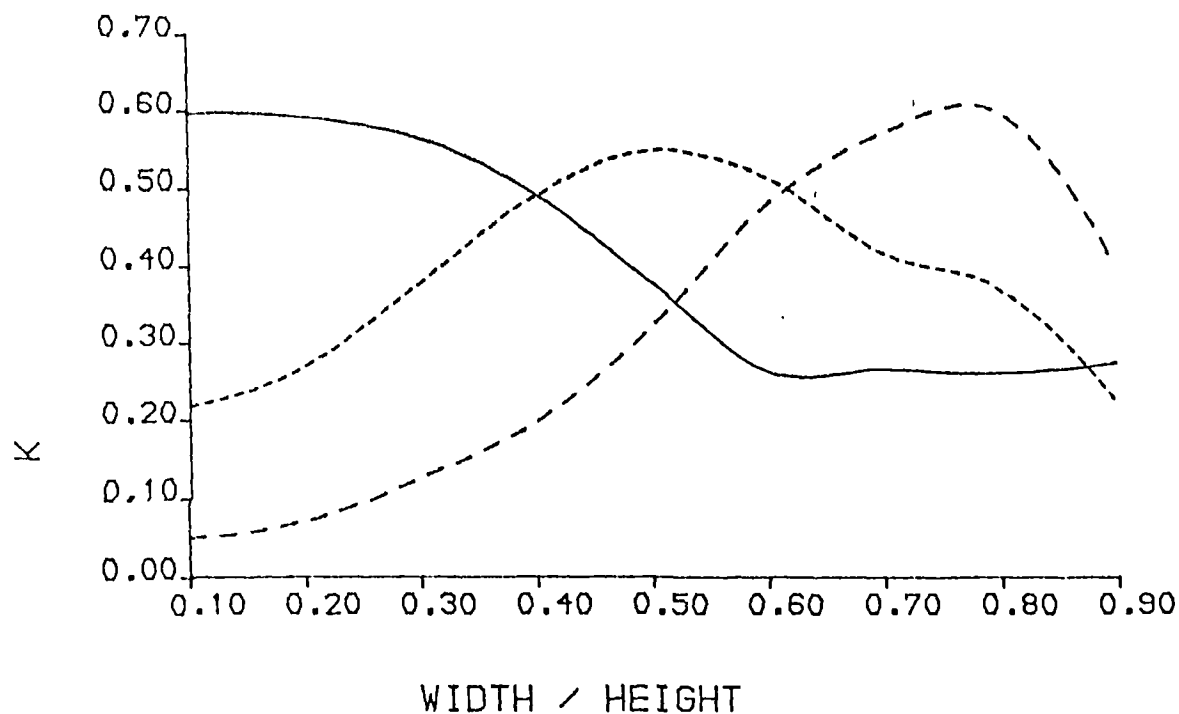


Figure 4.15 Dependence of effective coupling coefficient associated with the thickness and second and third lateral modes in a 20% square section composite possessing a pillar aspect ratio of 0.5.

Thickness mode _____
 Second lateral mode - - - - -
 Third lateral mode - . - . - .

TABLE 4.6

Frequencies of resonant modes in 3mm thick 20% composite transducers. (Frequencies in kHz)

W/H	THICKNESS		LATERAL		
	f_m	f_n	f_{1n}	f_{2n}	f_{3n}
0.1	477	575	1802	1780	1297
0.2	475	568	1195	964	1195
0.3	473	554	808	721	995
0.4	470	527	628	626	767
0.5	466	496	532	581	657
0.6	452	466	472	533	610
0.7	429	443	435	589	499
0.8	410	423	411	572	474
0.9	395	406	394	460	463

the three lateral modes and the thickness mode, it is also evident that the frequencies of the lateral modes are close to the thickness mode frequencies for the case that reduced thickness coupling efficiency is observed. Therefore, these resonant modes are closely coupled. However, in the 50% and 80% devices, the lateral modes occur at far higher frequencies because the pillars are more closely packed. In fact, the coupling coefficient of the second lateral mode in the 50% transducer attained a level of 0.29 for an aspect ratio of 0.8. This is still far less than the value of 0.56 attained in the case of the 20% device. The lateral activity in the 80% device is even weaker.

It may be noted also that the coupling of strong lateral activity into the thickness direction observed in the 20% device, also corresponds to a reduction in the apparent wave velocity, as observed in Figure 4.10. Again, no significant effect on velocity was observed for the 50% and 80% devices which possess far less resonant activity.

Since the influence of lateral resonant activity is determined by the proximity of the relevant frequencies of the modes to the thickness resonant frequencies, it is evident that the extent of lateral resonant activity is also a function of the elastic properties of the polymer. Clearly, a reduced elastic stiffness will result in the lateral resonance occurring at lower frequencies in the polymer. The above analysis was repeated assuming that the polymer was more compliant. In this case, the polymer

COUPLING COEFFICIENT

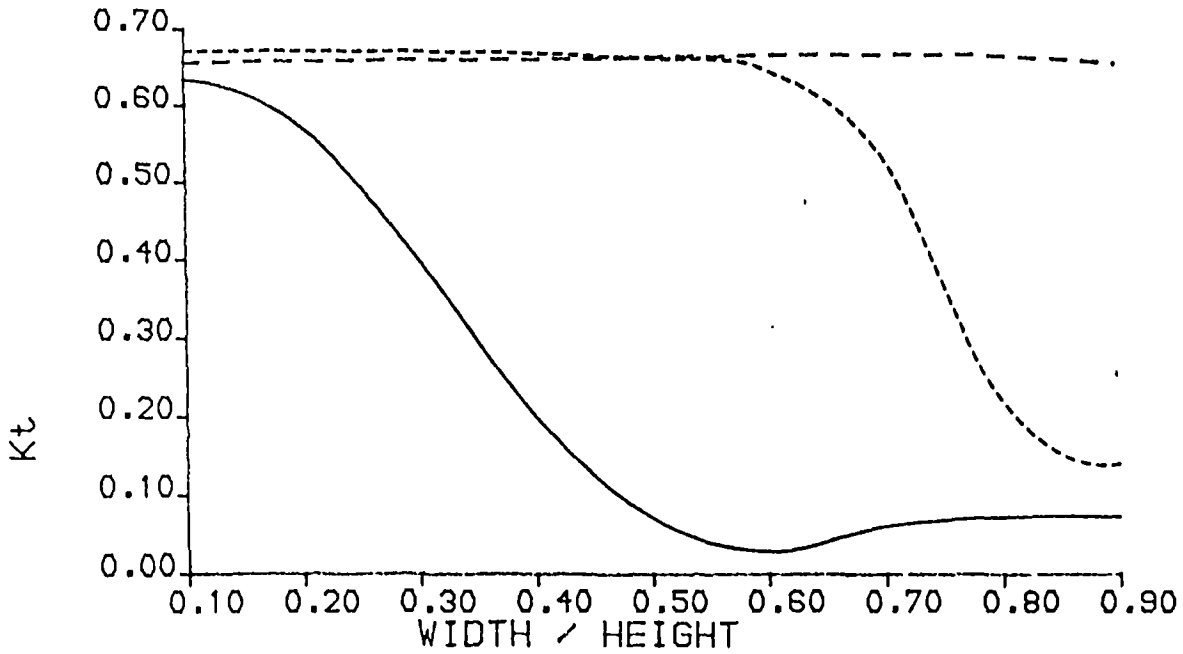


Figure 4.16 Dependence of effective thickness coupling coefficient in a 20% square section composite possessing a pillar aspect ratio of 0.5 and a polymer elastic modulus of 3GPa
 20% ————— 50% - - - - - 80% - . - . - .

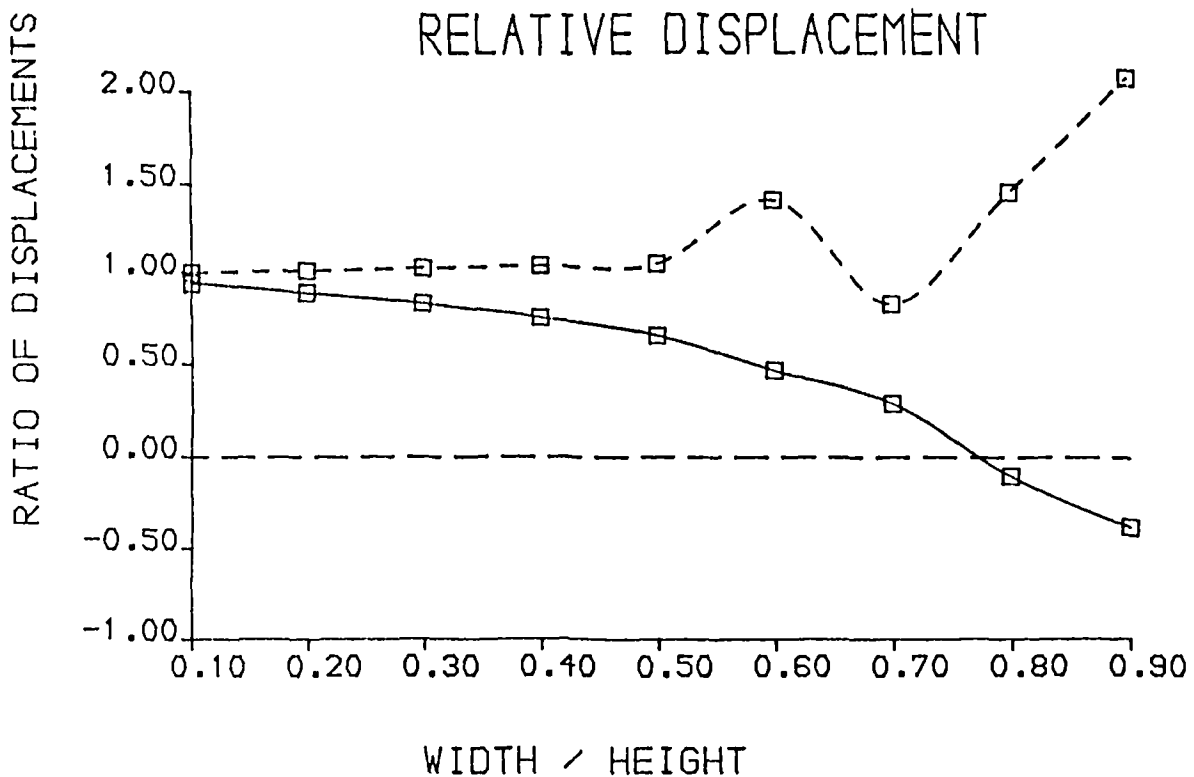


Figure 4.17 Dependence of the ratio of polymer displacement to ceramic thickness displacement on pillar aspect ratio in a 50% composite.
 $U_{POLYMER} / U_{CERAMIC}$ measured at f_n —————
 $U_{POLYMER} / U_{CERAMIC}$ measured at f_m - - - - -

possessed a Young's modulus of $3 \times 10^9 \text{Nm}^{-2}$, instead of $6 \times 10^9 \text{Nm}^{-2}$, as used previously. Figure 4.16 illustrates the new dependence of coupling coefficient on the pillar aspect ratio. Clearly, significant lateral activity is occurring for far lower aspect ratios than was previously the case for the 20% device. The activity is also seriously affecting the thickness coupling at high aspect ratios in the 50% device. The 80% device still exhibits no significant lateral resonant activity.

4.3 vi) Conclusions on volume fraction and width to height ratio

The results presented above for the longitudinal velocity and coupling coefficient demonstrate the need to avoid parasitic lateral resonant activity. This may be achieved by either, employing high ceramic volume fractions, or by using small pillar aspect ratios. The stiffness of the polymer should also be borne in mind when trying to avoid lateral resonant activity. However, the most uniform thickness vibration will generally be obtained when low pillar aspect ratios are employed. Figure 4.17 illustrates the ratio of ceramic pillar centre thickness displacement to polymer centre thickness displacement for a 50% transducer for a range of pillar width to height ratios. The degradation in uniformity is evident as the pillar aspect ratio increases. At electrical resonance, the ceramic pillars tend to displace further than the polymer. It is only at very high aspect ratios, that significant antiphase polymer motion is encountered.

COUPLING COEFFICIENT

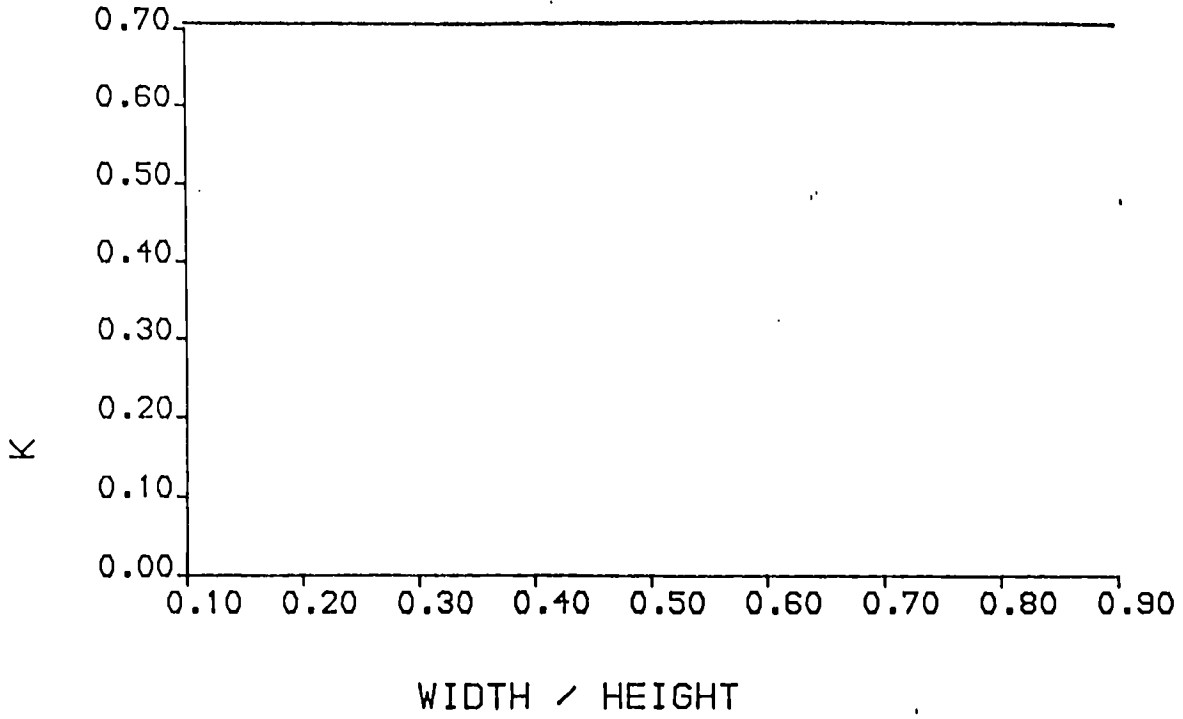


Figure 4.18 Dependence of effective thickness coupling coefficient on aspect ratio in a circular ceramic pillar.

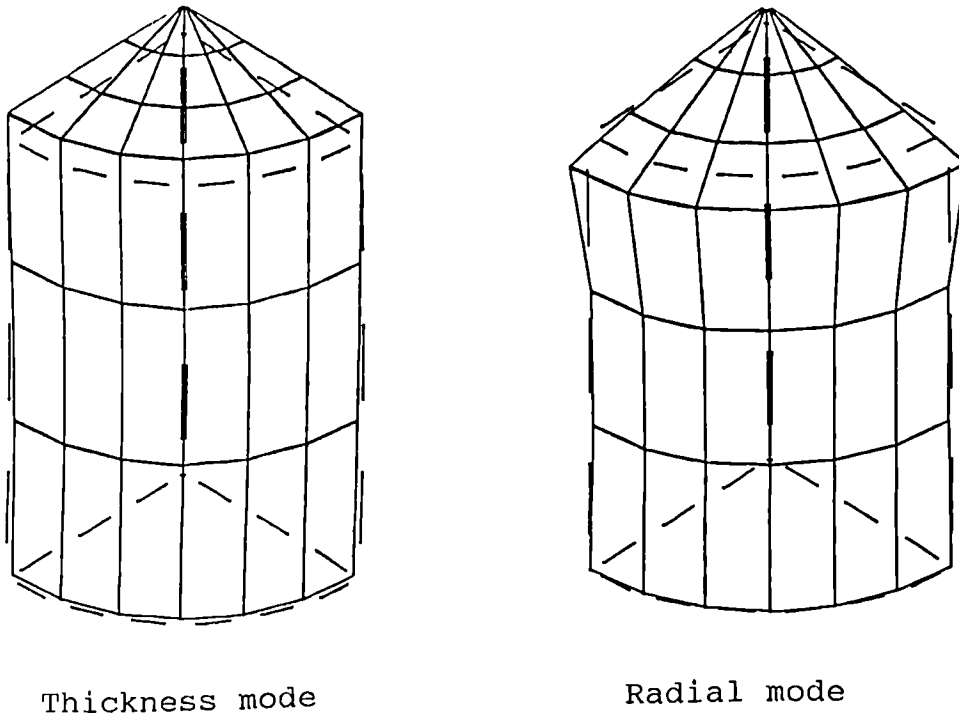


Figure 4.19 Resonant modes in a circular section ceramic rod possessing an aspect ratio of 0.5. One eighth section.

Static

Modal displacement

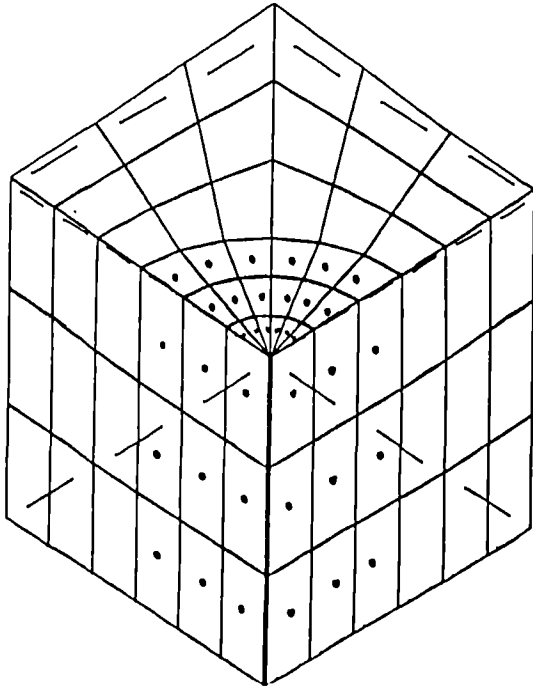
4.4 COMPARISON OF THE CHARACTERISTICS OBTAINED WHEN ALTERNATIVE PILLAR GEOMETRIES ARE EMPLOYED

Since the thickness coupling coefficient has been determined to be a function of lateral resonant activity, there is clearly scope for influencing device efficiency by judicious choice of ceramic pillar shape. However, the square section pillar geometry previously discussed is generally the easiest to fabricate.

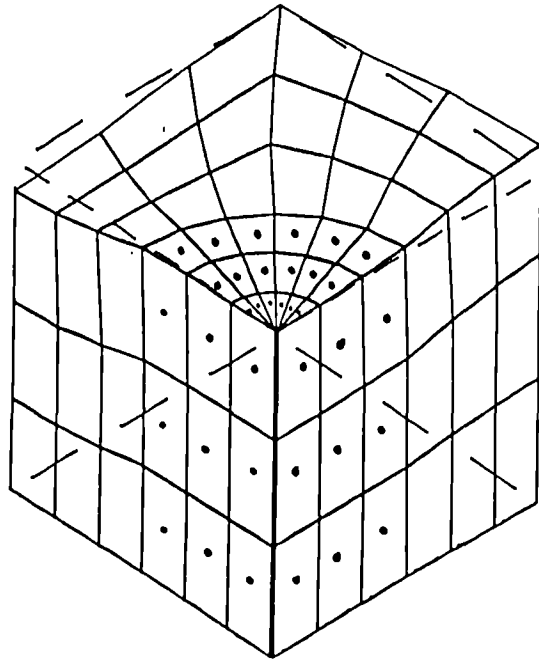
4.4 i) Circular pillars

The circular pillar geometry has been used widely for practical composites despite the associated manufacturing complexity [18,19]. Circular ceramic pillars exhibit radial modes of vibration in contrast to the lateral modes found in square section pillars. A radial mode possesses axisymmetry and therefore net lateral expansion/contraction is observed. It would be expected that this would translate into an effect on thickness mode activity.

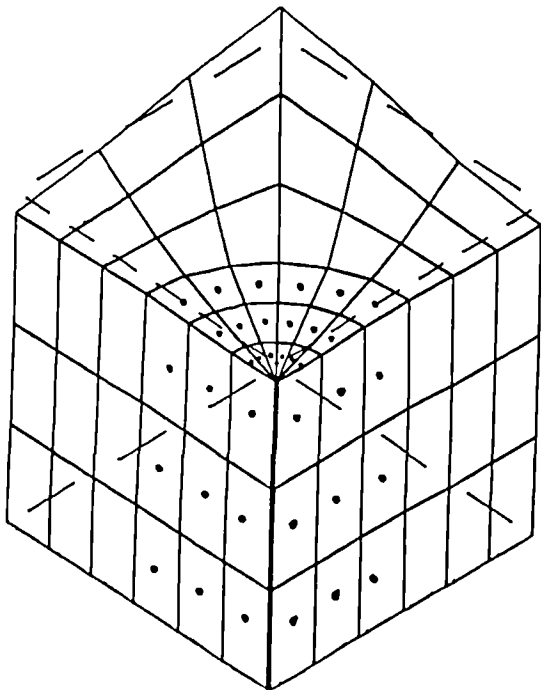
Figure 4.18 illustrates the dependence of thickness coupling coefficient on ceramic pillar diameter to height ratio. The curve is almost identical to that observed for the square pillar. This suggests a lack of strongly coupled radial resonant activity. The thickness mode and lateral mode, for an aspect ratio of 0.5, are illustrated in Figure 4.19. The coupling coefficient associated with the radial mode for this configuration is 0.213 and is therefore at a level comparable to that obtained for the lateral modes in a square section pillar.



Thickness mode



Second lateral mode



First lateral mode

Figure 4.20 Resonant modes in a 20% circular section composite possessing a pillar aspect ratio of 0.5. One eighth section.
 Static
 Modal displacement

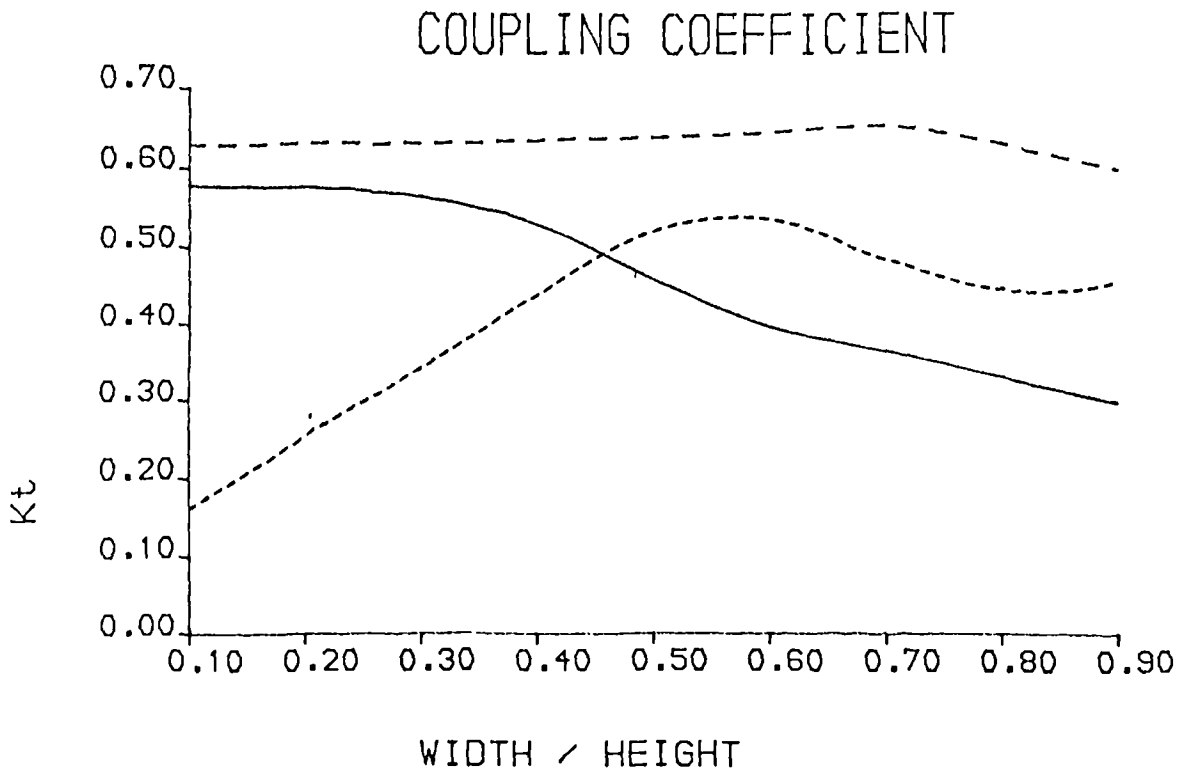


Figure 4.21 Dependence of effective coupling coefficient of thickness and first lateral mode in a 20% circular section composite possessing a pillar aspect ratio of 0.5. The thickness coupling coefficient of a 50% composite is included for comparison.

Thickness mode 20% —————
 Thickness mode 50% - - - - -
 First lateral mode 20% - · - · -

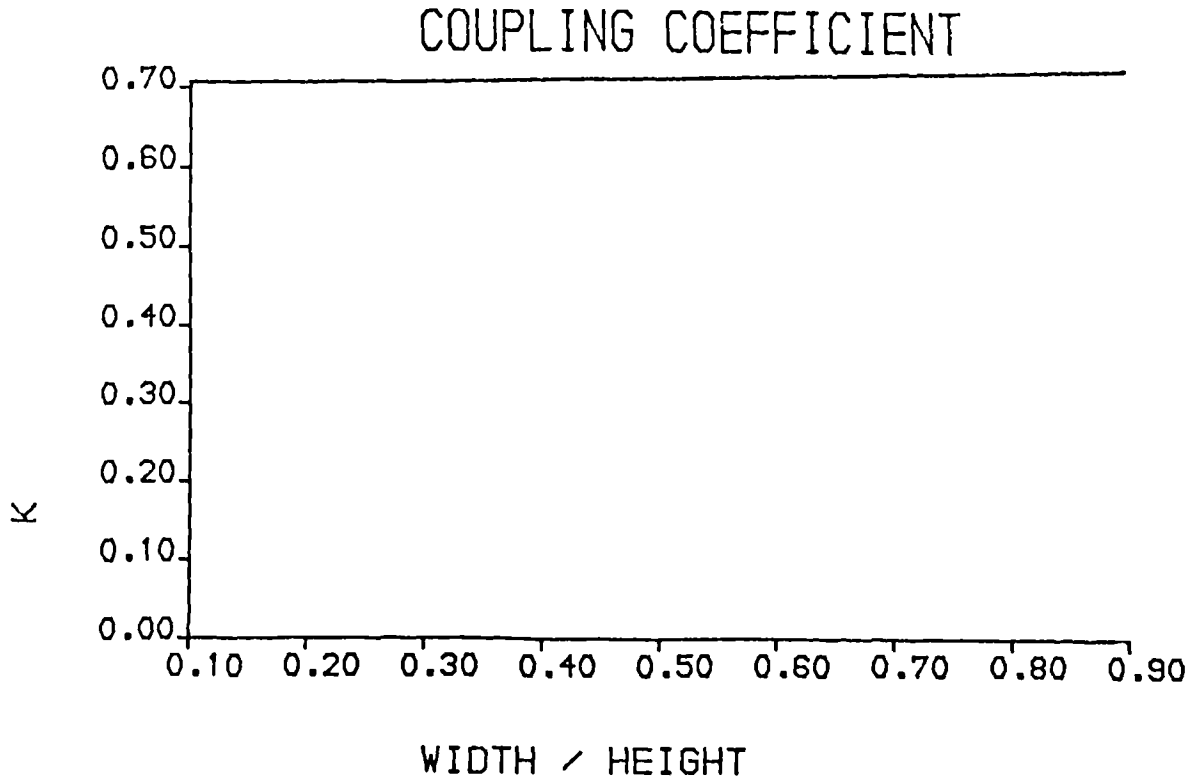


Figure 4.22 Dependence of the effective thickness coupling coefficient on aspect ratio in a triangular section ceramic pillar

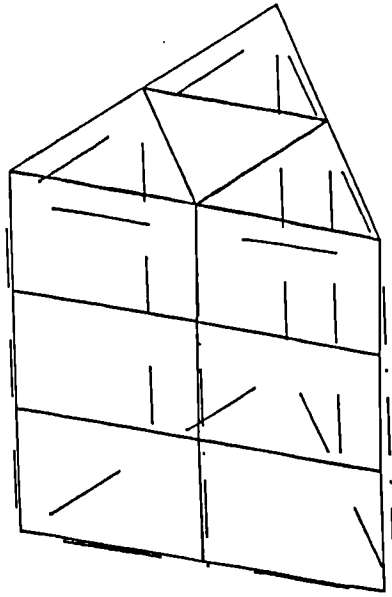


Figure 4.23 Thickness resonant mode in a triangular section ceramic pillar possessing an aspect ratio of 0.5. Half section.

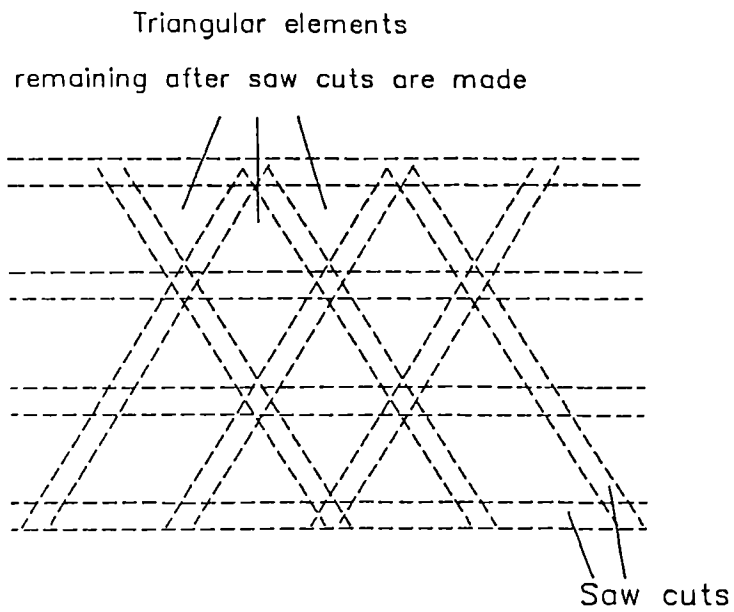
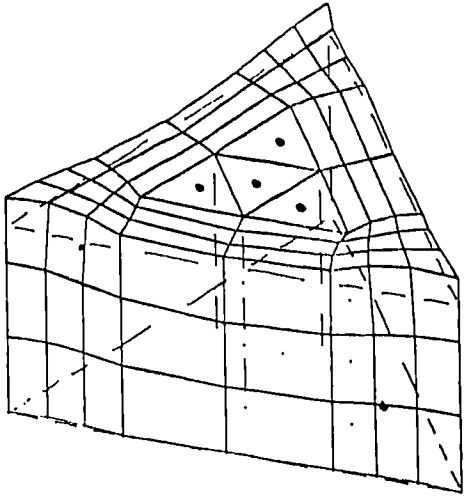
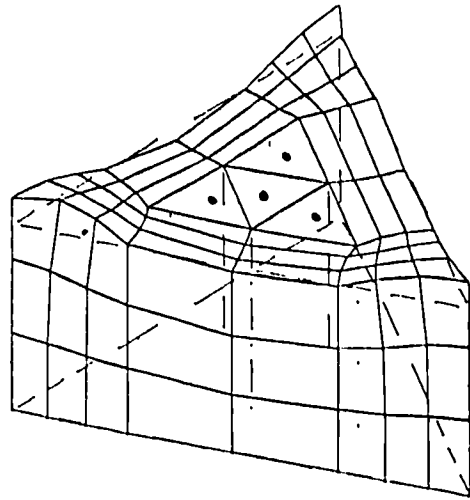


Figure 4.24 Orientation of triangular pillars achieved using 'slice and fill' approach.

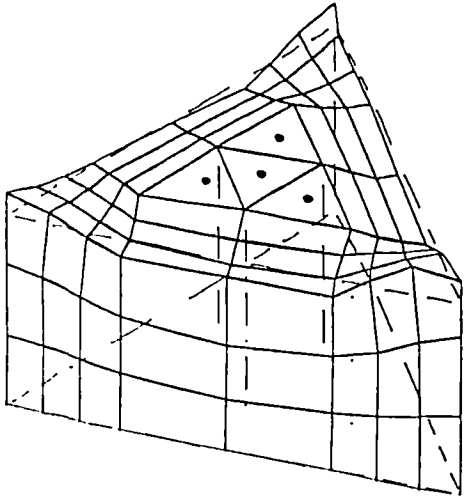
The dependence of coupling coefficient on pillar aspect ratio has also been investigated for a circular pillar geometry composite. In this case, there are two significant lateral modes in addition to the thickness mode. The modal displacement profiles for these modes are illustrated in Figure 4.20. Figure 4.21 illustrates a comparison between the thickness and lateral mode coupling coefficients on pillar aspect ratio. The ceramic volume fraction is 20% and therefore comparison with Figure 4.13, which illustrates the dependence for a square section geometry, is possible. In this case, there is a significant reduction in thickness coupling coefficient at increasing aspect ratios. This is matched by a steady increase in the electromechanical coupling coefficient associated with the first lateral mode. The dependence of lateral electromechanical coupling coefficient on aspect ratio in the circular pillar geometry composite is different from that found in the square section geometry but the net effect on thickness mode coupling is similar. Figure 4.21 also illustrates the dependence of thickness mode coupling on pillar aspect ratio in a 50% circular pillar geometry composite. This curve is similar to that obtained for the square section pillar in that the lateral activity in the 50% device is far less than in the 20% device and hence the thickness coupling coefficient remains at a high level over the range of aspect ratios considered. Again, the elastic properties of the polymer have a profound influence on the extent and frequency of lateral resonant activity.



Thickness mode





First lateral mode



Second lateral mode

Figure 4.25 Resonant modes in a 20% triangular element composite possessing a pillar aspect ratio of 0.5. Half section.

Static 
 Modal displacement 

4.4 ii) Triangular pillars

A triangular pillar possesses a geometry which would be expected to exhibit neither simple lateral modes nor planar type modes of vibration. Therefore, this geometry might be expected to exhibit minimal lateral activity when incorporated into a composite transducer.

Figure 4.22 illustrates the dependence of thickness mode coupling coefficient on aspect ratio in isolated triangular ceramic elements. The aspect ratio is defined by the ratio of the length of the side to the pillar height. Figure 4.23 illustrates the thickness mode in a triangular pillar possessing an aspect ratio of 0.5. No particularly significant lateral type modes were observed. The lack of strong lateral activity is reflected in the high level of thickness coupling efficiency observed over the range of aspect ratios considered.

Triangular pillars may be orientated within a composite in a number of different configurations. The simplest orientation is illustrated in Figure 4.24. This permits a 'slice and fill' approach to be adopted during manufacture. However, the presence of parallel faces gives rise to the possibility of lateral resonant activity. This orientation is analysed initially.

Two lateral resonant modes, in addition to the thickness mode, were observed in this type of composite. These are illustrated in Figure 4.25 for a 20% composite possessing a pillar aspect ratio of 0.5. The dependence of the

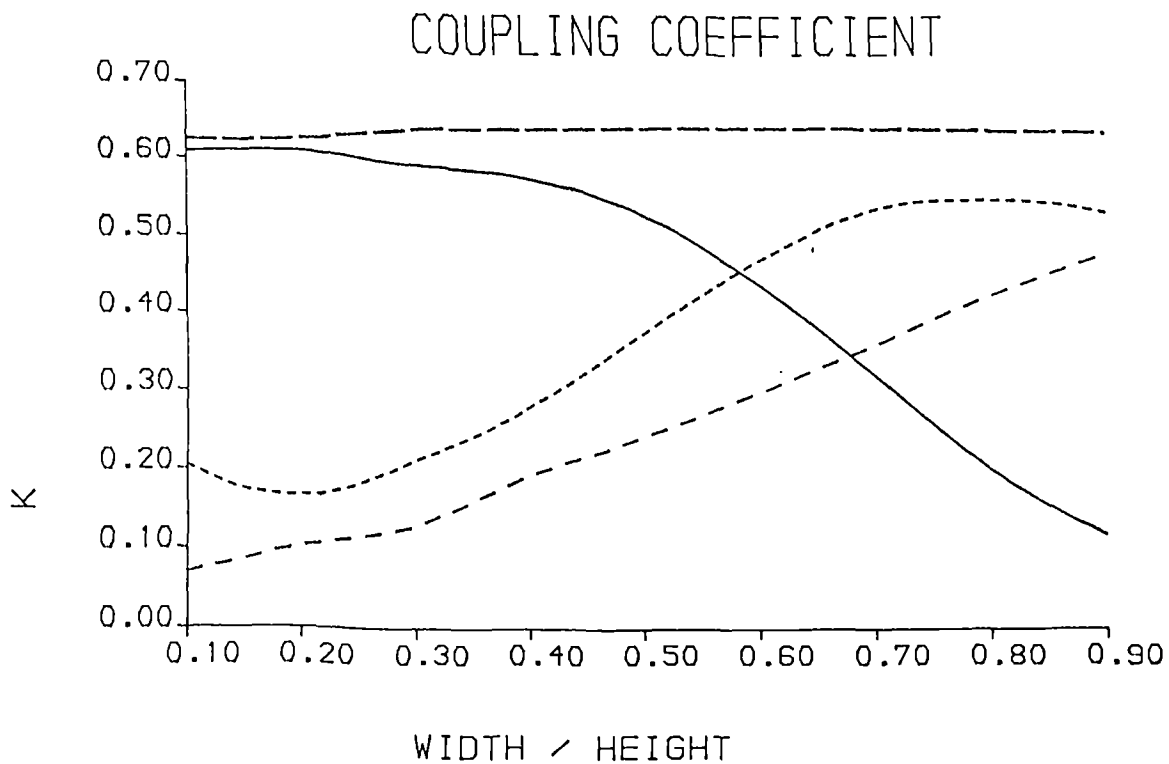


Figure 4.26 Dependence of effective coupling coefficient associated with the thickness and lateral modes on pillar aspect ratio in a 20% triangular element composite.

Thickness mode
 First lateral mode
 Second lateral mode
 Thickness mode 50%

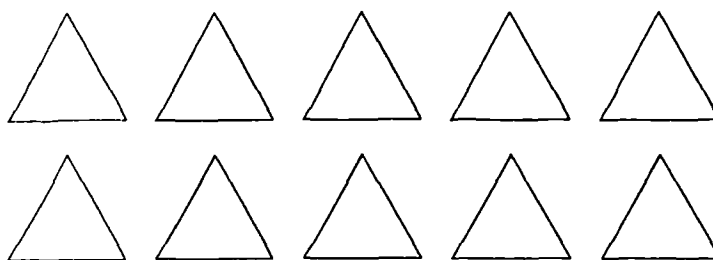


Figure 4.27 Alternative configuration of a triangular element composite which possesses no facing, parallel surfaces.

coupling coefficients associated with these modes are compared in Figure 4.26. In a trend similar to that previously observed for the square and circular cross-section elements, the thickness coupling coefficient reduces as the aspect ratio increases. This is matched by a general increase in lateral resonant activity. The dependence of the thickness coupling coefficient in a 50% composite is also illustrated for comparison. Again, only weak lateral activity was observed at frequencies well separated from the thickness mode. Therefore, the thickness coupling coefficient remains high over the range of aspect ratios considered.

The configuration of composite illustrated in Figure 4.27. was also analysed. In this configuration, there are no parallel faces between elements. However, this type of composite requires each pillar element to be individually positioned, and is therefore costly. Figure 4.28 illustrates the dependence of thickness mode coupling coefficient on aspect ratio for a 20% composite transducer possessing the geometry illustrated in Figure 4.27. In this case, coupling coefficient is largely independent of pillar aspect ratio. As expected, no significant lateral activity was observed. Two practical prototype 1MHz triangular element devices were fabricated possessing the two different pillar configurations. The magnitude profiles of these are illustrated in Figure 4.29. The device possessing parallel adjacent ceramic faces clearly exhibits two lateral modes. In comparison, the other

COUPLING COEFFICIENT

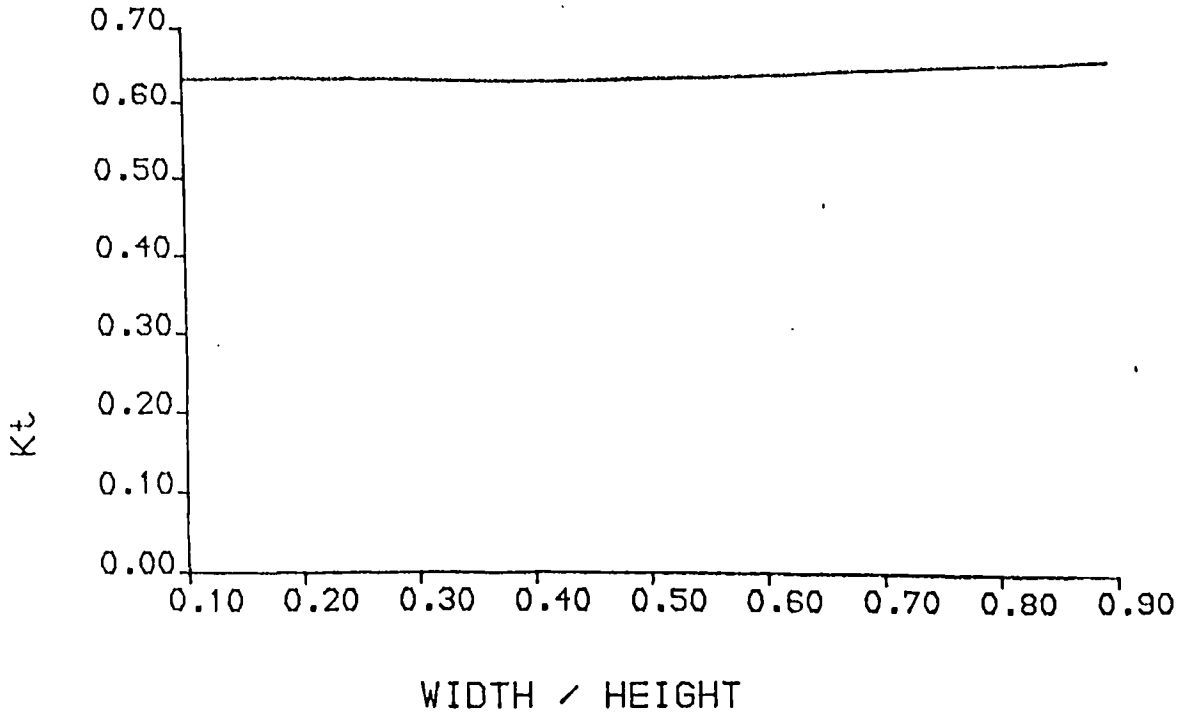


Figure 4.28 Dependence of effective thickness coupling coefficient on pillar aspect ratio in a 20% triangular element composite. (Alternative pillar configuration.)

IMPEDANCE

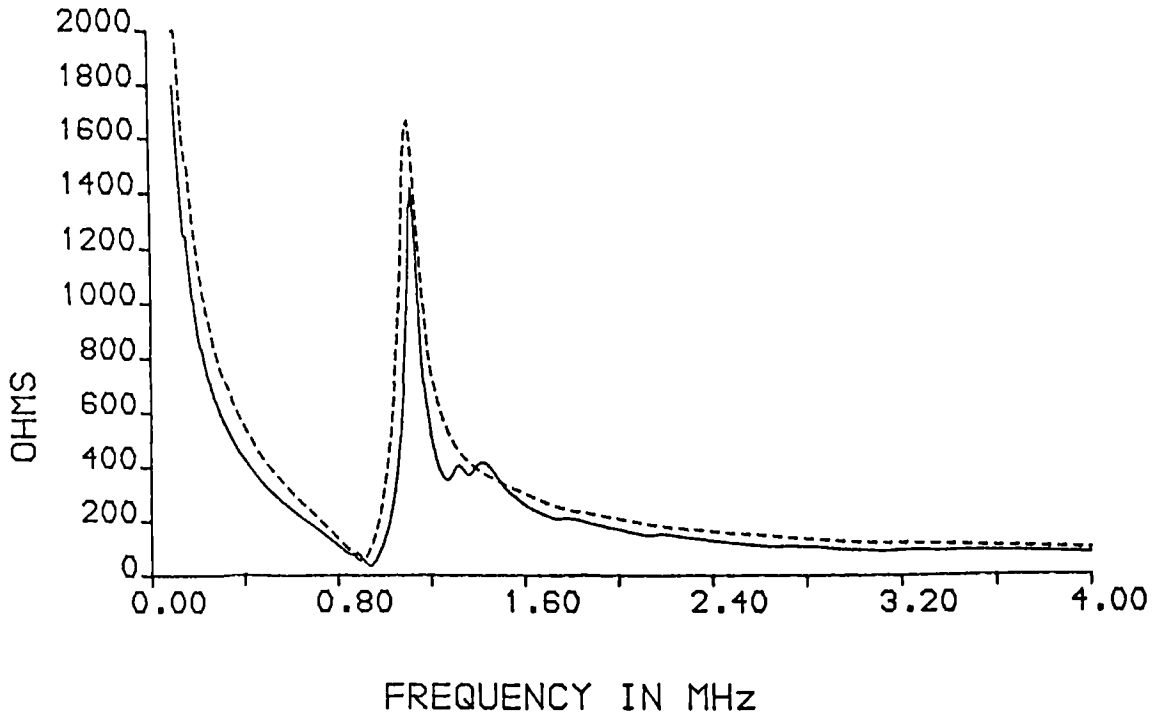


Figure 4.29 Impedance magnitude characteristics of two 30% 1MHz triangular element composites possessing pillar aspect ratios of 0.6.

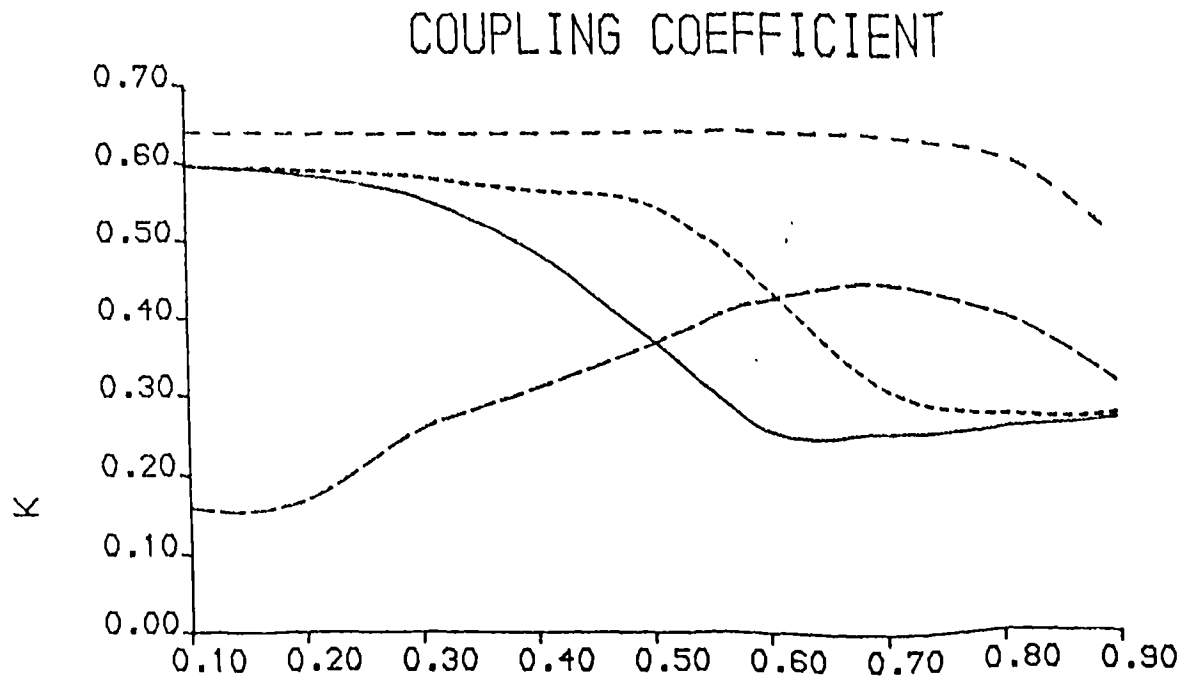
Regular pillar configuration (As per Figure 4.24) ———
 Alternative pillar configuration (As per Figure 4.27) - - - - -

composite transducer demonstrates a single, undistorted thickness mode resonance.

4.4 iii) Rectangular pillars

A rectangular pillar geometry has also been briefly investigated. Clearly, the resonant modes in a rectangular pillar depend on the relative widths of the sides. If one dimension is considerably larger than the other, then the resonant activity in that direction is effectively isolated from the activity in the other direction. This allows the activity to be analysed using a two dimensional model rather than requiring a three dimensional approach. It is believed that a composite possessing an array of long strip ceramic elements is not practical. This design offers no advantages over conventional composite designs and the material properties along axes parallel and perpendicular to the planes of the strip elements would be different. This may lead to degraded vibrational and acoustic characteristics.

A brief study of composites possessing pillars with length to width ratios of two is made here. The analysis may be extended to other configurations if required. Figure 4.30 illustrates the dependence of thickness coupling coefficient on aspect ratios for 20% and 50% composite transducers. The longer side is used when defining the width to height ratio. Therefore, the actual aspect ratio



WIDTH / HEIGHT

Figure 4.30 Dependence of effective coupling coefficient associated with thickness and lateral modes on pillar aspect ratio in 20% and 50% rectangular element composites.

Thickness mode rectangular pillar (20%) -----
 Thickness mode rectangular pillar (50%) - - - - -
 Thickness mode square pillar (20%) _____
 Lateral mode rectangular pillar (20%) - - - - -

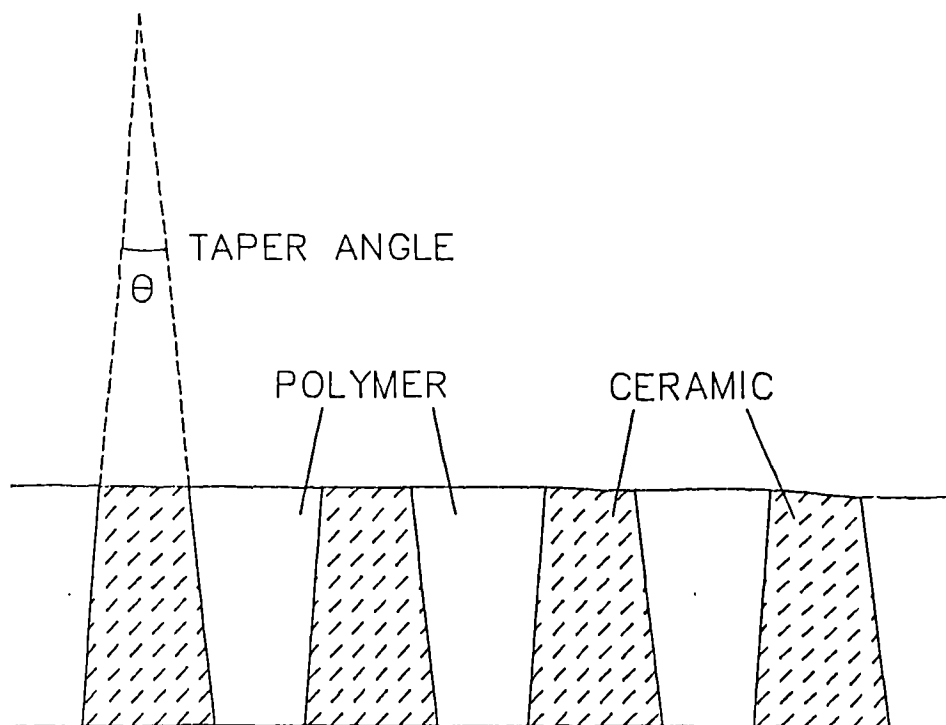
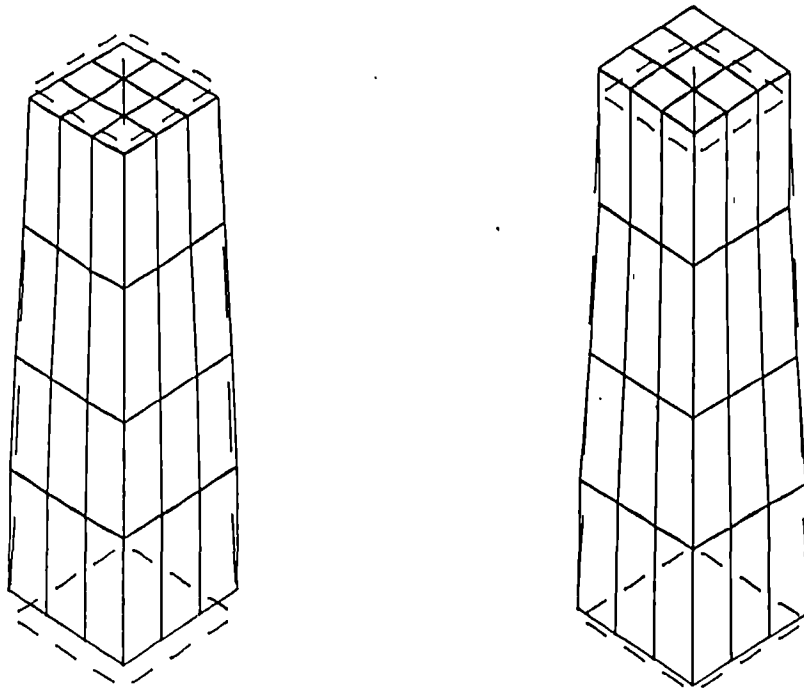


Figure 4.31 Typical cross-section of a tapered pillar composite.

of the narrower side is half of that shown in the figure. Hence, direct comparison with previous results is not possible. However, the same trends are apparent in the curves. Laterally resonant activity, at increasing aspect ratios, gives rise to degradation in the thickness coupling coefficient. No significant lateral activity occurs in the 50% device over the range of aspect ratios considered, and hence the thickness coupling coefficient remains at a high level. The vibrational characteristics of the elements becomes highly complex when one side, and not the other is greater than the thickness dimension.

4.4 iv) Tapered pillars

It is proposed that lateral resonant activity in a composite comprising square section pillars may be reduced by employing pillars possessing a taper in the thickness direction. Thus, the pillars possess smaller lateral dimensions at the top than at the bottom of the transducer. Manufacture of this type of geometry may be accomplished by the use of saw blade with a tapered cross-section. A typical cross-section of a tapered element device is illustrated in Figure 4.31. The dependence of coupling coefficient on aspect ratio in ceramic pillars has been investigated for two different taper angles. The taper angle is the angle between the opposite lateral faces and is described in Figure 4.31. Clearly, only relatively small angles are feasible. A significant secondary mode was observed in tapered pillars, but not in parallel pillars. This mode is



Thickness mode

Secondary mode

Figure 4.32 Resonant modes in ceramic pillar possessing a mean aspect ratio of 0.5 and a 10° taper angle.

Static

Modal displacement

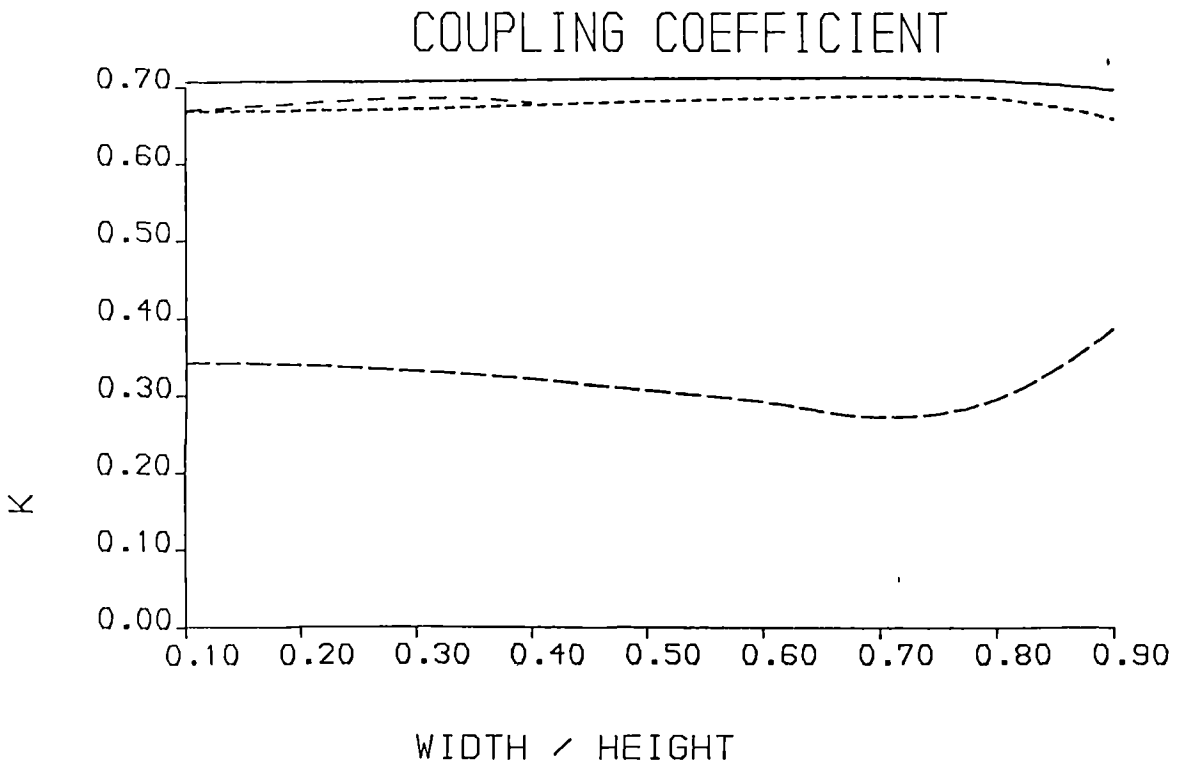


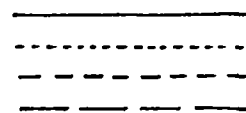
Figure 4.33 Dependence of effective coupling coefficient on pillar aspect ratio for various tapers

Thickness mode for 0° taper

Thickness mode for 10° taper

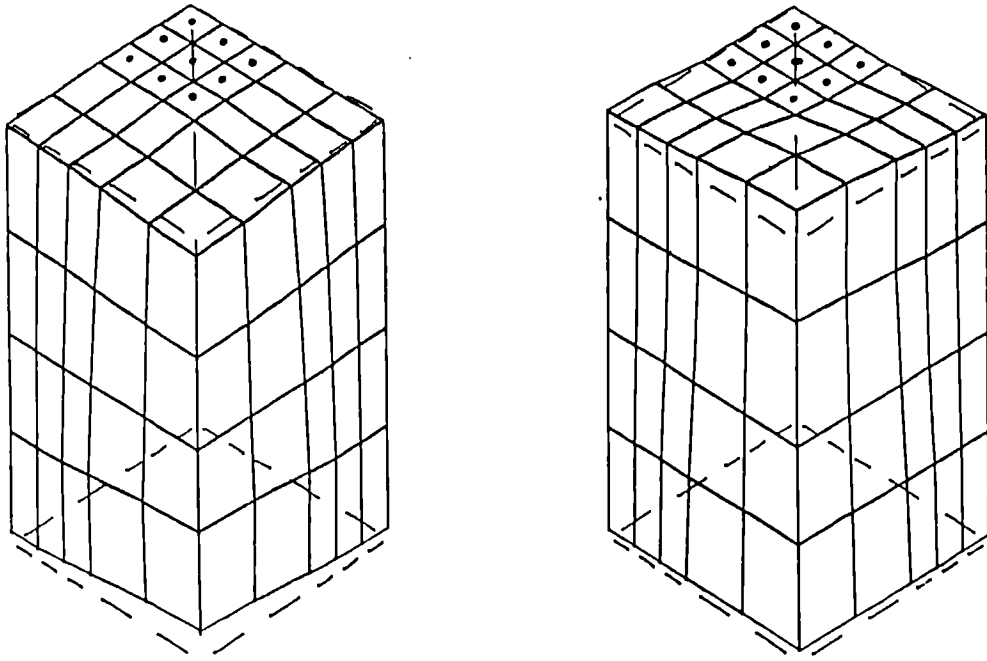
Thickness mode for 20° taper

Secondary mode for 10° taper



illustrated in Figure 4.32 for a 10° taper pillar possessing a mean aspect ratio of 0.5. This mode, which is relatively strong in comparison with the secondary modes found in regular parallel pillar structure, is believed to be associated with the second harmonic of the thickness resonance. At the second harmonic frequency, in a parallel pillar structure, thickness contraction in one half is exactly matched by thickness extension in the other half. Consequently, there is no net resonant activity. However, in a tapered structure, the variation in cross-sectional area along the thickness direction of the pillar, results in an inability to achieve complete cancellation in modes associated with the second harmonic of the thickness fundamental mode.

The dependence of thickness mode coupling coefficient on mean aspect ratio, for pillars possessing taper angles of 0° , 10° and 20° are illustrated in Figure 4.33. The coupling coefficient associated with the secondary mode in the 10° structure is also illustrated for comparison. The thickness mode coupling coefficients in the tapered pillars are marginally lower than those encountered in the parallel structure. Also, the secondary mode possesses a significant coupling coefficient, which increases as a function of pillar aspect ratio. No results were recorded for aspect ratios greater than 0.4, for the 20° tapered pillar because the frequencies of thickness and secondary modes become virtually coincident and no meaningful results could be obtained.



Thickness mode

Lateral mode

Figure 4.34 Resonant modes in a 20%, 10° tapered pillar composite structure possessing a mean pillar aspect ratio of 0.5.
 Static — — — — —
 Modal displacement —————

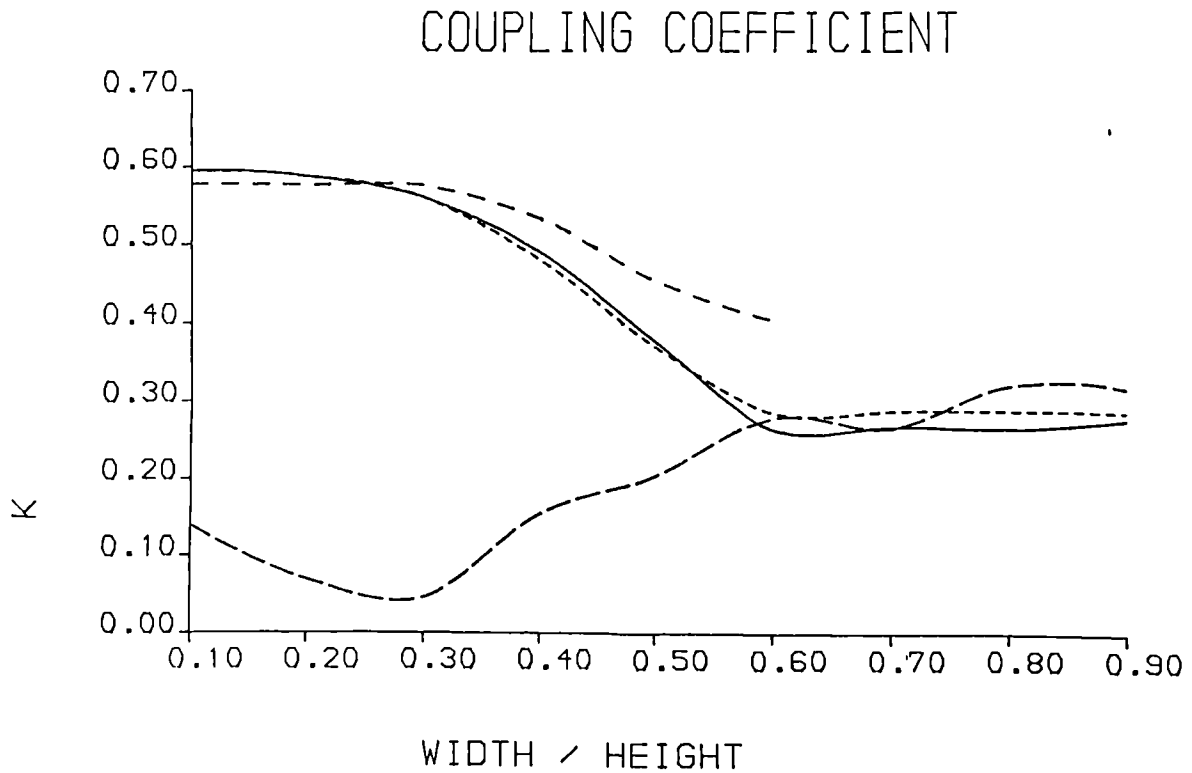


Figure 4.35 Dependence of effective coupling coefficient associated with the thickness and lateral modes in a 20%, tapered pillar, composite transducer.
 Thickness mode for 0° taper —————
 Thickness mode for 10° taper - - - - -
 Thickness mode for 20° taper - - - - -
 Secondary mode for 10° taper — — — — —

The use of tapered pillars in composite transducers has been briefly investigated. In addition to the thickness resonance, one significant lateral-type mode was observed. These are illustrated in Figure 4.34 for a 20% composite, possessing pillars with a mean aspect ratio of 0.5, and a taper angle of 10° . Other, weaker, lateral modes are evident at high pillar aspect ratios. Figure 4.35 illustrates the dependence of the thickness coupling coefficient on pillar aspect ratio for pillar taper angles of 0° , 10° and 20° . The ceramic volume fraction is 20%. The lateral mode coupling coefficient for the 10° design is illustrated for comparison. The results for the thickness coupling coefficients for the 0° and 10° designs are similar. However, the tapered designs generally possess slightly reduced coupling coefficients. The lateral coupling coefficient increases as a function of pillar aspect ratio. However, it does not attain the level of resonant activity observed in a similar parallel pillar structure - illustrated in Figure 4.15. Nevertheless, thickness coupling reduces as lateral activity increases, and hence, the trend is in agreement with previous discussion. The 20° design exhibits a deteriorating thickness coupling coefficient as a function of pillar aspect ratio. At aspect ratios greater than 0.6, complex vibrational activity in the vicinity of the thickness mode resonance was observed and no meaningful results could be obtained.

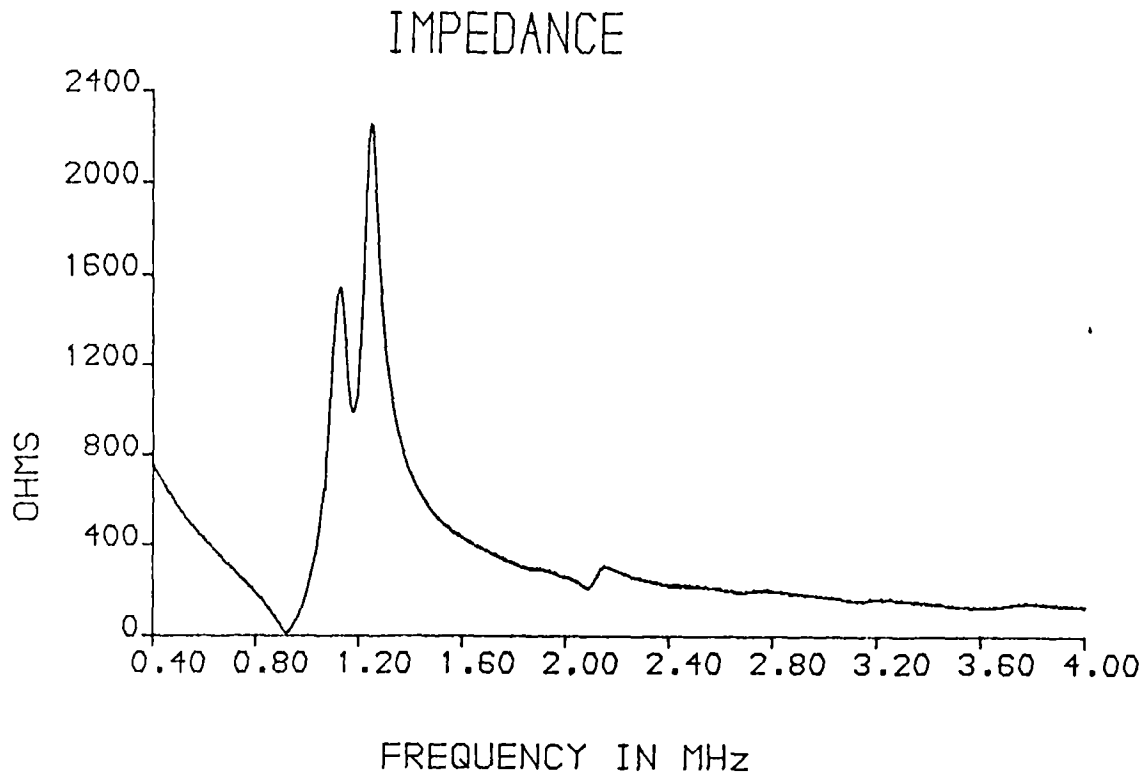


Figure 4.36 Impedance magnitude characteristic of a prototype 40% 1MHz composite a 8° pillar taper.

A prototype 8° taper, 40% ceramic 1MHz composite transducer has been fabricated. The mean aspect ratio of the ceramic pillars is 0.7. The impedance profile of this device, illustrated in Figure 4.36, indicates the presence of a strong lateral-type mode in the vicinity of the thickness mode resonance. Clearly, care must be taken in the design of tapered pillar composite structures if strong parasitic resonant activity is to be avoided. Although there is scope for further work regarding the use of tapered pillar geometries, it would appear that there are far simpler methods available for suppressing strong lateral resonant activity. This may be achieved primarily by the use of low aspect ratio ceramic pillars.

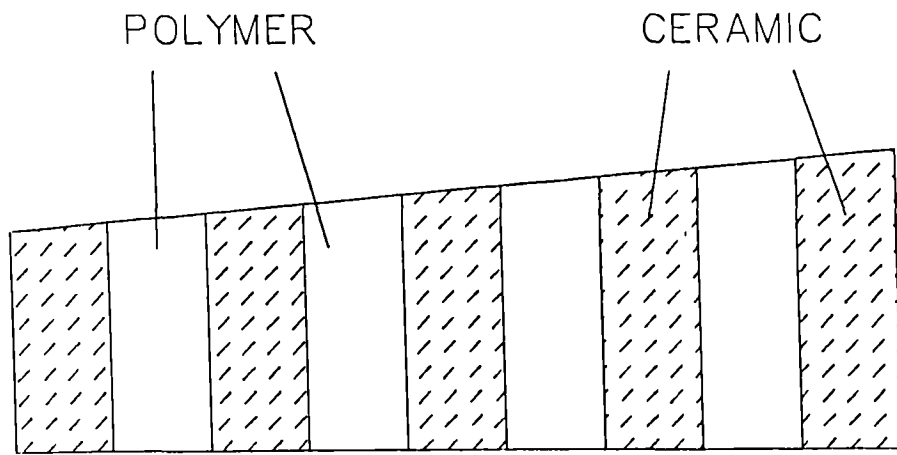


Figure 4.37 Typical cross-section of nonuniform thickness composite plate.

4.5 METHODS FOR ENHANCING DEVICE BANDWIDTH

The versatility of composite transducers allows the designer to take steps to maximise bandwidth. This may be achieved by a number of novel methods.

4.5 i) Diverse thickness

A conventional thickness mode transducer has a strong narrow resonant frequency range determined by the device thickness and wave velocity. However, if the ceramic plate possesses non-uniform thickness, then strong resonant activity cannot exist at any point on the plate because lateral mechanical coupling effectively clamps the entire plate. This explains why this method of bandwidth extension has only occasionally been used.

However, in a composite transducer, if one portion is resonant and another portion is not, then the non-resonant region will not significantly clamp the other region because of the effect of the relatively soft polymer filler. This may be verified using finite element analysis. Figure 4.37 illustrates the cross-section of a sloping thickness composite plate. The thickness varies from 3.0mm to 3.5mm and hence the electrical resonant frequency varies approximately from 500kHz to 400kHz. Figure 4.38 illustrates the structure under excitation at 400kHz. In this case the thicker end is resonating more strongly, as evidenced by the greater displacements. Figure 4.39 illustrates the structure when subjected to a 500kHz excitation. In this case the opposite end resonates more strongly.

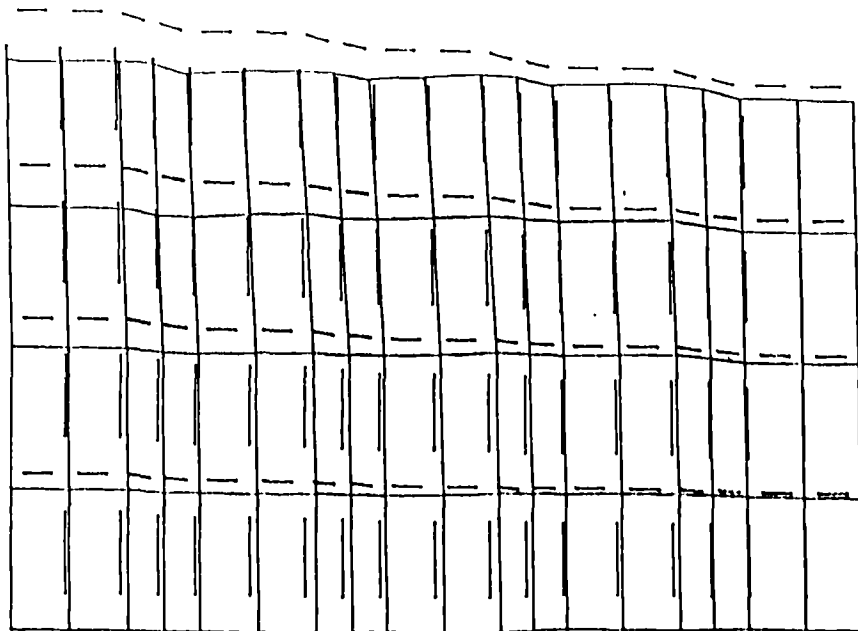


Figure 4.38 Displacement in the nonuniform structure for excitation at 400kHz.

Displaced ——— Undisplaced - - - -

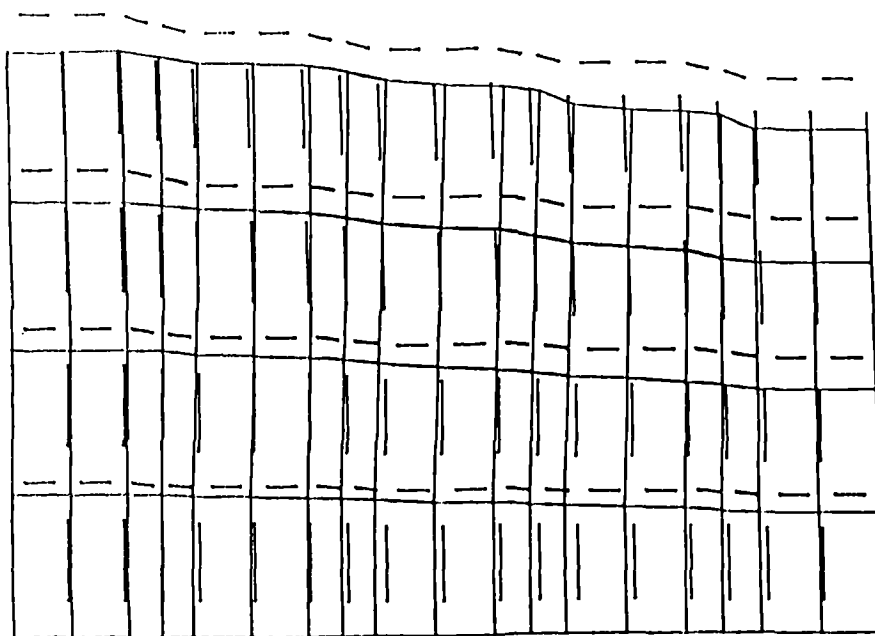


Figure 4.39 Displacement in the nonuniform structure for excitation at 500kHz.

Displaced ——— Undisplaced - . - - -

These results have been verified practically. Figure 4.40 illustrates the impedance curve of both a uniformly thick composite transducer and a transducer possessing a thickness that varies from 1.4mm to 2.8mm. The considerable extension in bandwidth is clearly evidenced by the long low impedance minimum.

The major problem associated with this method of bandwidth extension is that the vibrating aperture is non-uniform across its surface for any given excitation function. However, for some applications this is not a significant disadvantage.

4.5 ii) Diverse pillar configurations

The wave longitudinal velocity in the thickness direction of a composite element is *dependent on the element's width to height ratio*. This dependence has been investigated using finite element analysis in section 4.3 ii). Figure 4.9 illustrated the dependence of longitudinal wave velocity on ceramic pillar width to height ratio for a 20% transducer. Unfortunately if the pillar aspect ratio exceeds a critical value then parasitic lateral modes give rise to severe degradation in the thickness coupling coefficient. These effects have already been fully investigated in section 4.3 ii). Therefore, the viable range of longitudinal wave velocities, within the PZT pillars of a composite transducer, varies from approximately 3250 to 3750ms^{-1} .

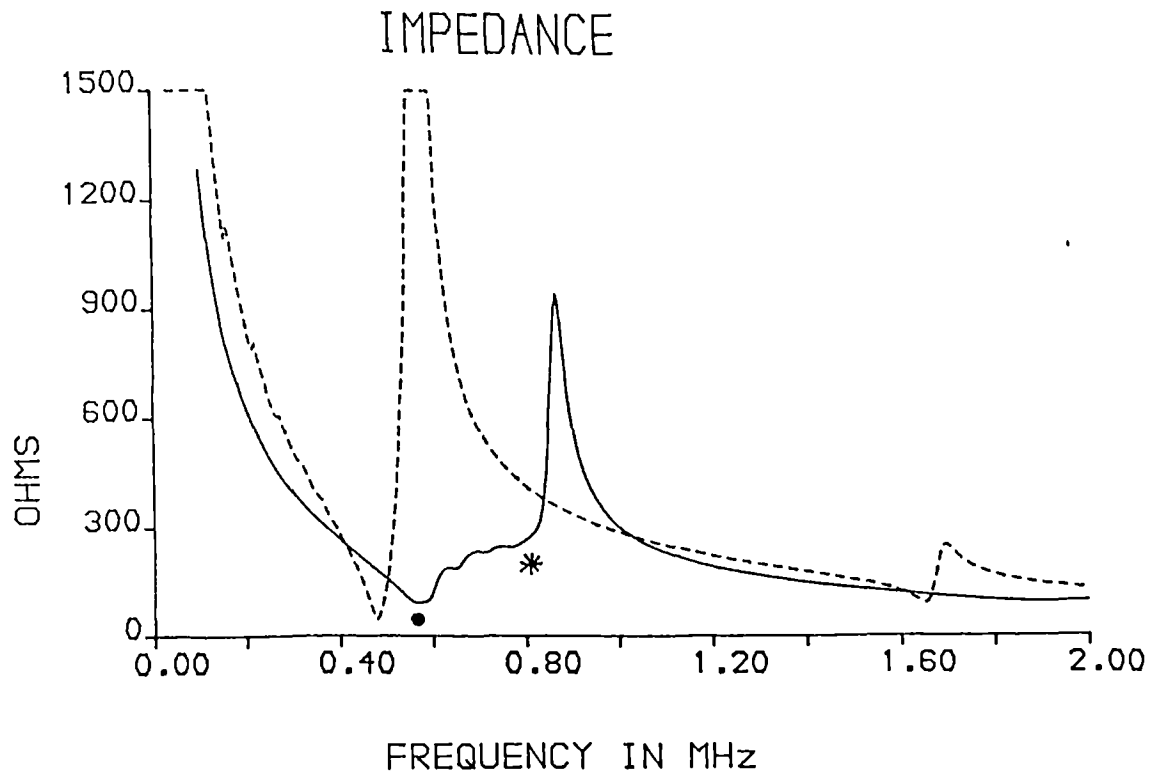


Figure 4.40 Impedance magnitude characteristic of a prototype 40% 500kHz (nominal) composite transducer.

Uniform thickness -----

Thickness varying from 1.4 to 2.8mm —————

1.4 mm thick portion at electrical resonance *

2.8 mm thick portion at electrical resonance ●

A composite may be manufactured comprising of pillars with varying aspect ratios and hence varying resonant frequencies. This may be achieved using the configuration illustrated in Figure 4.41. The configurations of the pillars are 0.44 x 0.44mm, 0.44 x 0.78mm and 0.78 x 0.78mm and 1.35mm thick. The mechanical resonant frequencies of these pillars were determined using finite element analysis to be 1.118, 1.019 and 0.978MHz respectively. Figure 4.42 illustrates the impedance magnitude profile of this device and the response of an approximately equivalent device with uniform thickness which is included for comparison. The transducer with varying pillar dimensions possesses a wider impedance minimum and hence demonstrates bandwidth extension.

Unfortunately, although the method described is elegant in concept, the actual increase in bandwidth is very limited due to the small range of velocities which are physically realisable.

CERAMIC PILLARS

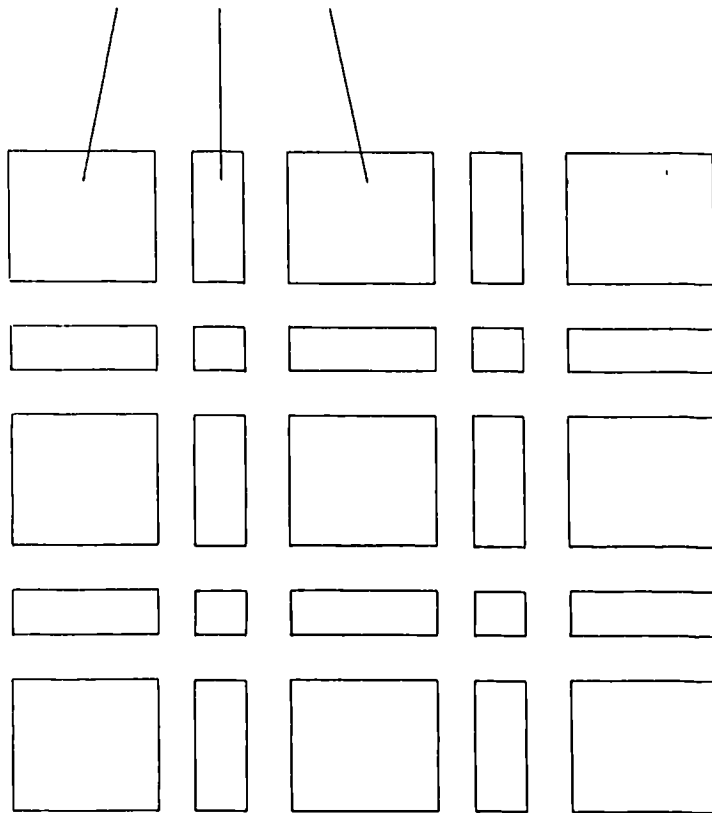


Figure 4.41 Typical configuration of a composite containing diverse pillar configurations.

IMPEDANCE

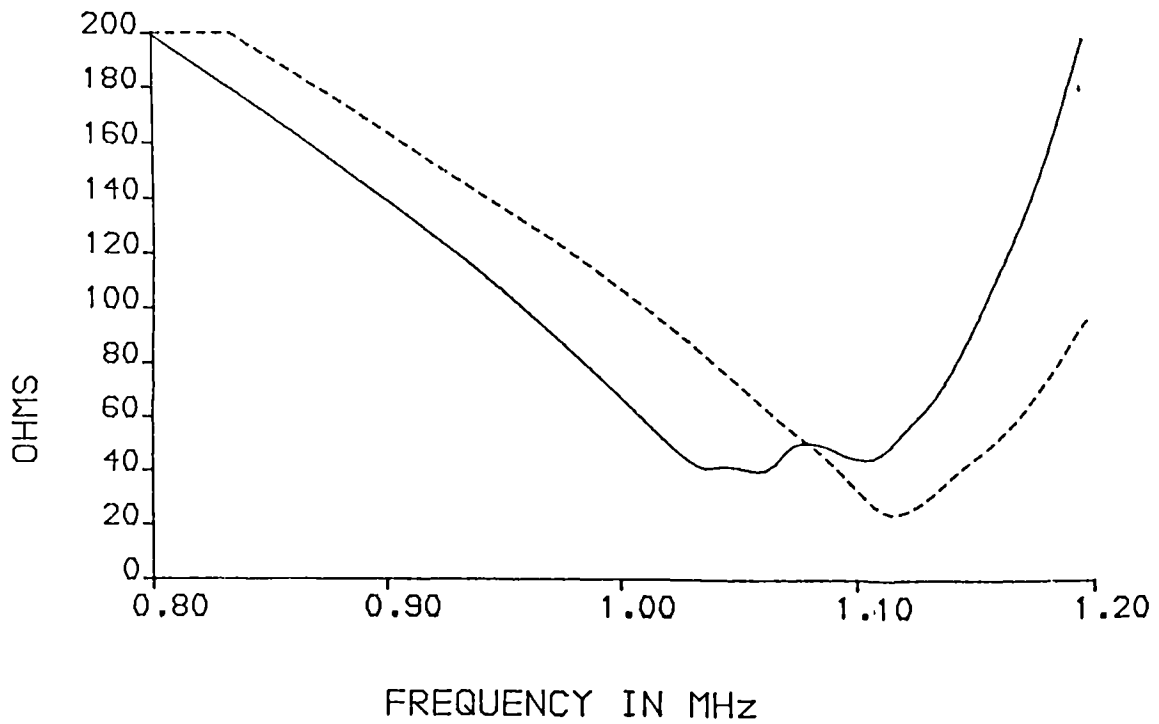


Figure 4.42 Impedance characteristics, in the vicinity of electrical resonance, of 50% 1MHz composites.
 Various pillar geometries —————
 Uniform pillar geometries - - - - -

4.6 CONCLUDING REMARKS

The influence of the selection of constituent materials on final composite transducer performance has been investigated. It is concluded that, for the manufacture of active composite transducers, only Lead Zirconate Titanate (PZT) materials are appropriate. The choice between PZT specifications will depend partially on the required application and geometry. The selection of the polymer is more complex. Light, compliant polymers result in the highest measured coupling coefficients in composites comprising of small aspect ratio pillars. However, the degree of energy transfer between ceramic and polymer is unknown. Furthermore, since the longitudinal and shear wave velocities are lower in compliant polymers, the range of geometries for which the frequencies of inter-pillar resonances are far higher than the fundamental thickness mode, is more limited. Particle loaded polymers may be used to provide a limited increase in overall bandwidth.

A comprehensive analysis of the vibrational and electromechanical characteristics of a diverse range of geometries has allowed some important conclusions to be drawn. Degraded performance, caused by strongly coupled lateral, inter-pillar resonances, is normally only encountered in low ceramic volume devices possessing high pillar aspect ratios. Therefore, the simultaneous existence of low ceramic volume fraction and high pillar aspect ratio should be avoided. The extent of the coupling between thickness and lateral resonant modes is also a

function of the polymer's elastic properties, and hence these should also be borne in mind. Furthermore, the highest degree of vibrational uniformity is obtained in structures possessing the lowest pillar aspect ratios. It is also worth observing that provided that the pillar aspect ratio is less than approximately 0.25, then Smith's compact one dimensional model [3] provides a reasonably accurate prediction of the effective material parameters of the composite material.

As a result of the investigation performed here, it has become evident that simple square section geometries do not exhibit a performance substantially different from those obtained using more complex geometries - such as circular, triangular or rectangular pillar geometries. However, it is probable that the increased design versatility offered by the use of some of these alternative pillar geometries will be suited to specialised applications. In particular, the triangular element composite, illustrated in Figure 4.27, permits the use of relatively large pillars without adversely affecting vibrational uniformity. Hence relatively viscous polymers may be used in the construction of such a structure.

It is possible to extend device bandwidth by utilising diverse thickness or pillar geometries, but the extent of the enhancement is generally rather limited.

CHAPTER V

MODELLING THE CHARACTERISTICS OF COMPOSITE
PIEZOELECTRIC TRANSDUCERS

5.1 INTRODUCTION

This chapter presents a comprehensive modelling strategy for the simulation of the characteristics of composite transducers including the effects of electrical and mechanical loading. Mechanical loss is included in this model. Additionally, a simple model for the depolarisation encountered during the manufacture of 1-3 composite transducers is included. The transducer model used is capable of incorporating matching layer effects. The strategy used involves a combination of a slightly modified established thickness mode transducer model and a simple model for predicting the equivalent thickness mode parameters of a composite material.

5.2 REVIEW AND EXTENSION OF SMITH'S THICKNESS MODE PARAMETER MODEL FOR COMPOSITE TRANSDUCERS

As discussed in Chapter II, there are essentially two valid models for predicting the equivalent parameters of composite transducers. These are the models by Smith et al [3] and Hashimoto et al [25]. Smith's model is preferred on the grounds that it obtains equally valid results but is far simpler to implement than Hashimoto's model. The limitations of this model, in terms of the assumptions made regarding pillar shape, inter-pillar spacing and lateral stress/strain are important and should be borne in mind. These have already been discussed in Chapter II. However, for the majority of practical applications, any slight inaccuracies arising from these assumptions, will have a negligible impact on predicted device performance. For cases where Smith's model is insufficient, it is necessary to resort to finite element analysis to predict modal vibrational behaviour and piezoelectric efficiency. However, if finite element analysis indicates non-uniform vibration, then it is probable that the behaviour of the transducer cannot be modelled accurately using a thickness mode transducer model which assumes only undistorted thickness mode vibration.

The accuracy of Smith's model has been verified for a wide range of devices. Previously, emphasis has been on volume fractions up to 30%. However, the present work has

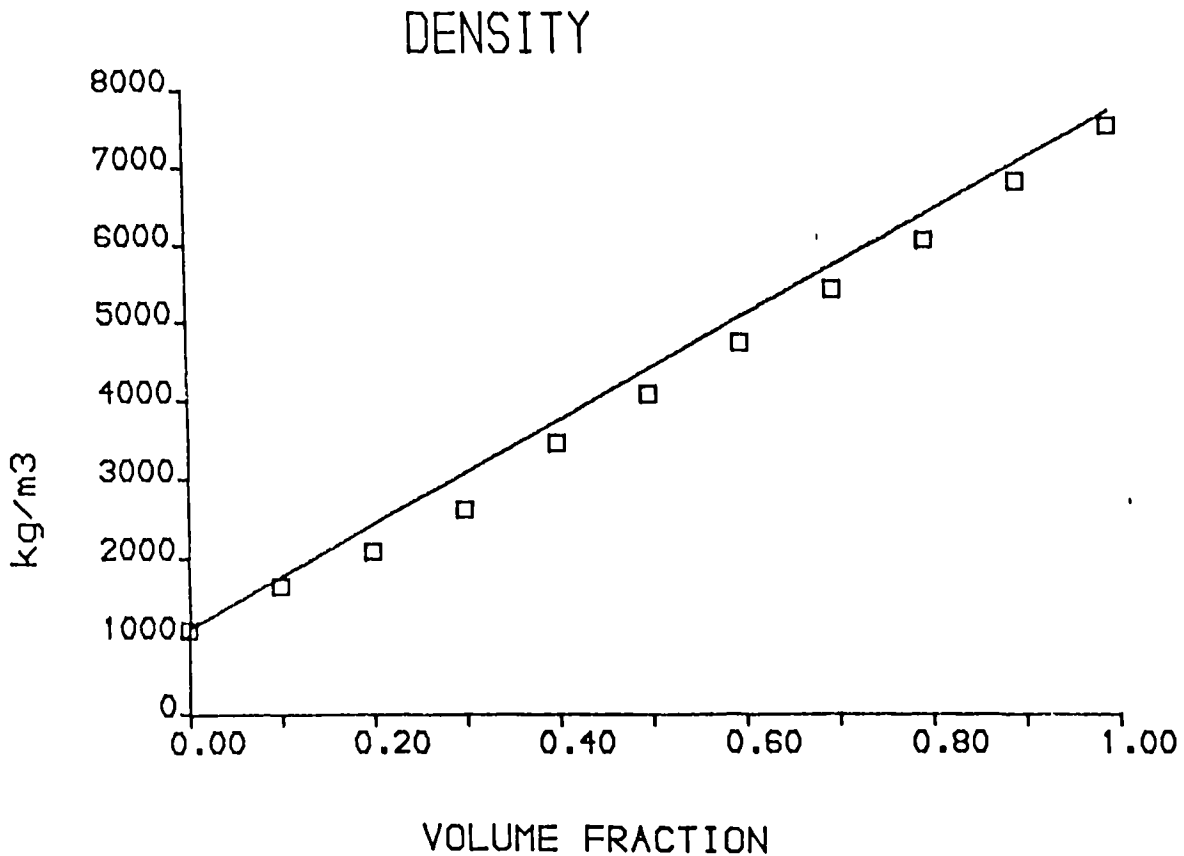


Figure 5.1 Comparison of theoretical and experimental composite density as a function of ceramic volume fraction.
 Experimental \square
 Theoretical —

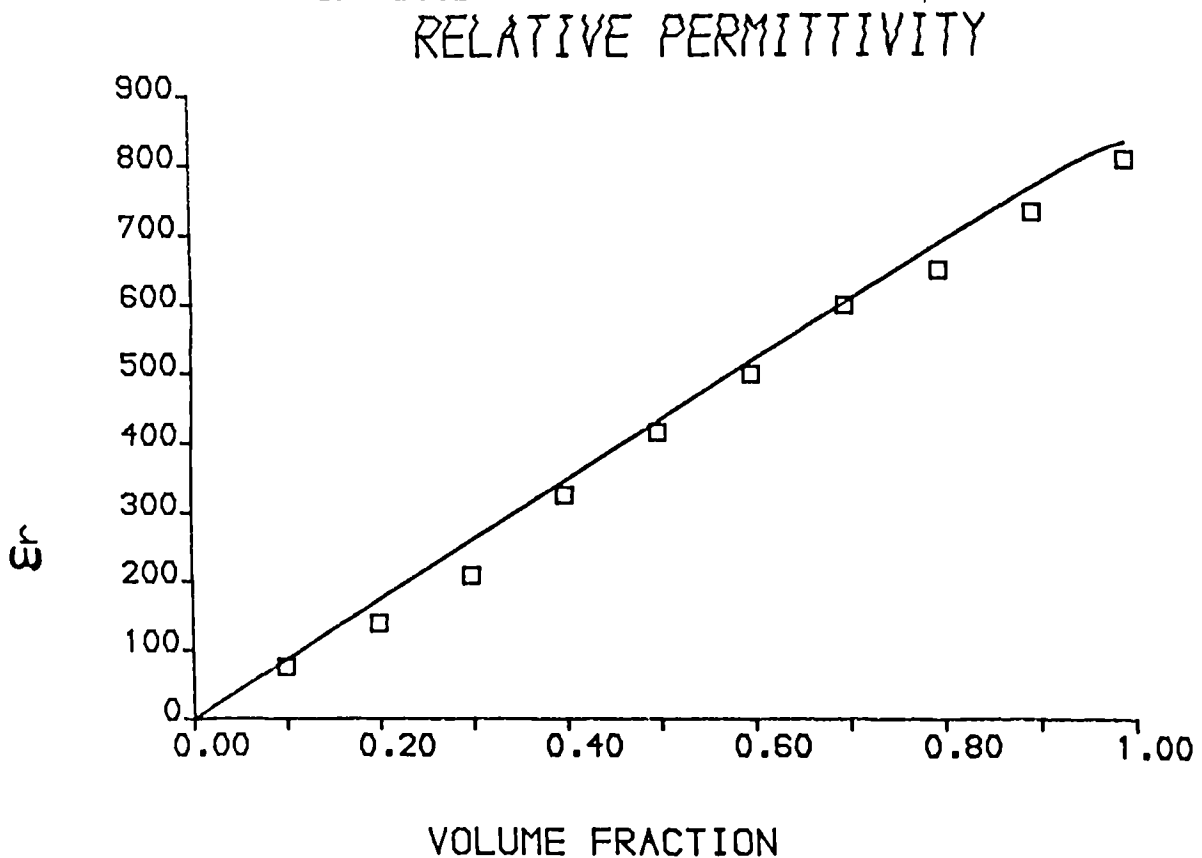


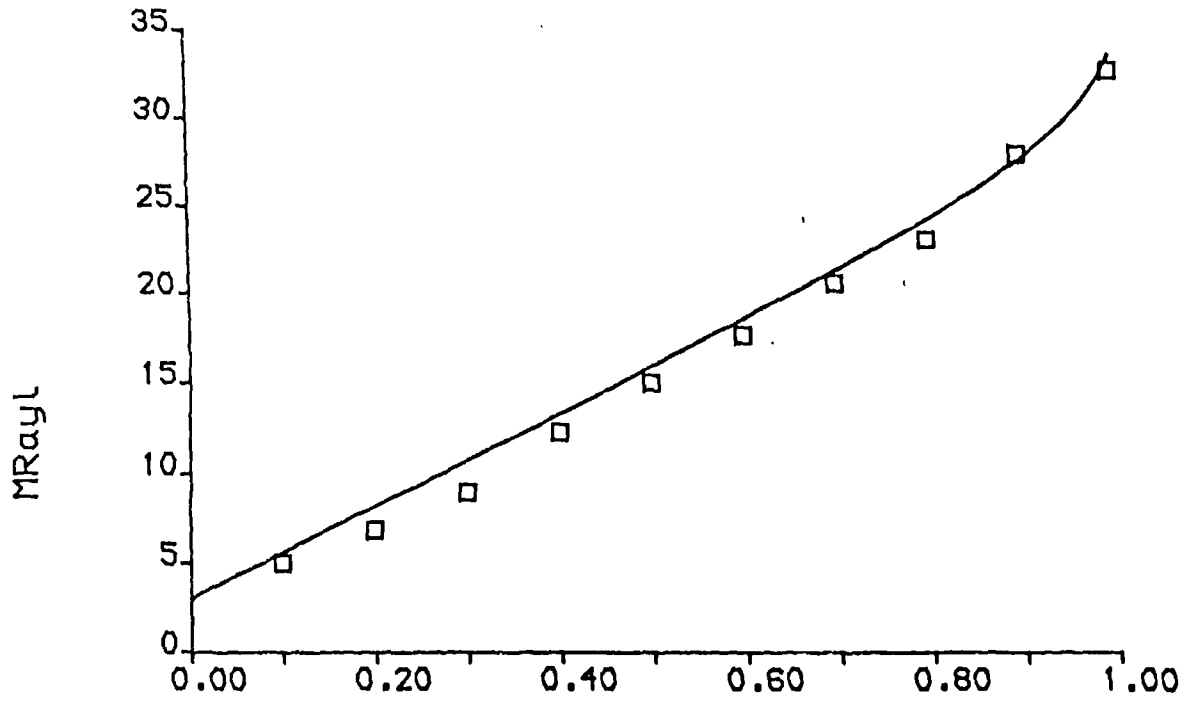
Figure 5.2 Comparison of theoretical and experimental composite permittivity as a function of ceramic volume fraction.
 Experimental \square
 Theoretical —

indicated the importance of composite transducers with ceramic volume fractions of up to 80%. Therefore, a range of devices, with volume fractions extending from 10% to 90%, and including a reference ceramic device (ceramic volume fraction = 100%) have been manufactured. EDO EC-65 ceramic, and CY1301/HY1300 epoxy were used. The material properties of these materials are described in Appendix A. The dimensions of the devices were 15 x 15 x 3mm. Therefore the centre frequency was approximately 500kHz. In all cases, except for the 80% and 90% devices, the ceramic pillars may be regarded as being tall and thin. Therefore, additional 250kHz 80% and 90% devices, with tall and thin pillars, were manufactured.

The accuracy of Smith's model was verified by comparing modelled density, permittivity, acoustic impedance, velocity and the electromechanical conversion coefficient, k_t , with measured results. Figures 5.1, 5.2 and 5.3, illustrating density, permittivity and acoustic impedance respectively, indicate excellent correlation between modelled and measured results. The trends are essentially linear and are therefore in accordance with intuitive expectation. The accuracy of these results verifies the quality of the manufacturing process which is described in Appendix B.

The correlation between measured and modelled velocity in Figure 5.4 is also good. The mathematical complexity, and the influence of the fundamental assumptions made in Smith's model are far more significant in this case.

ACOUSTIC IMPEDANCE

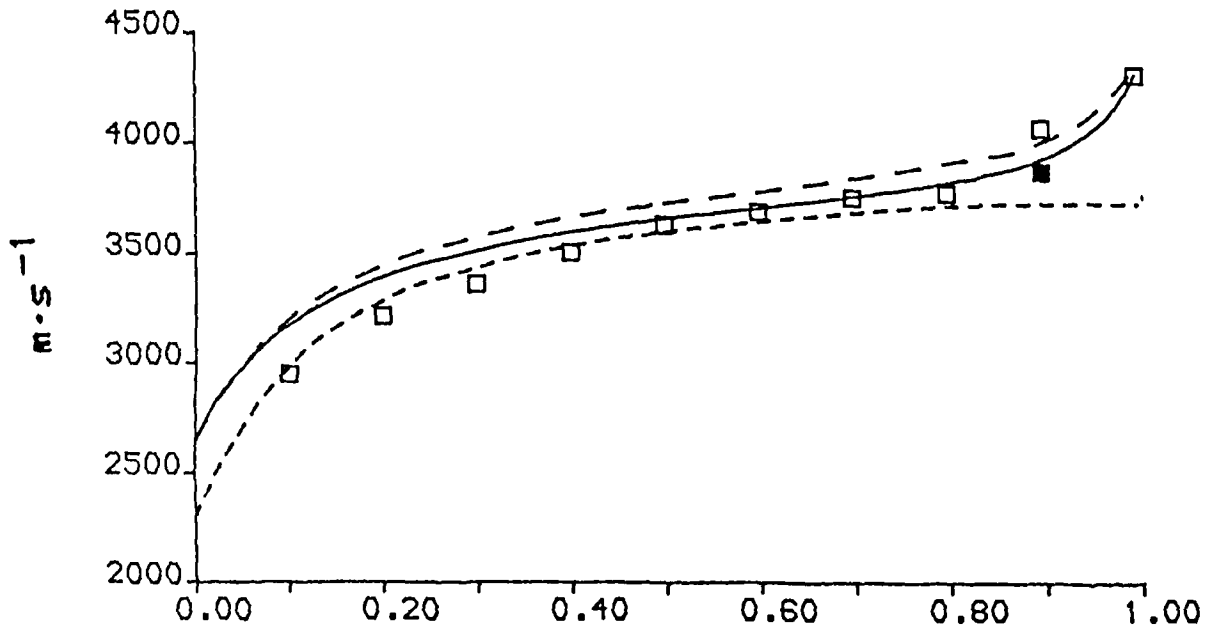


VOLUME FRACTION

Figure 5.3 Comparison of theoretical and experimental composite acoustic impedance as a function of ceramic volume fraction.

Experimental \square
 Theoretical —

VELOCITY



VOLUME FRACTION

Figure 5.4 Comparison of theoretical and experimental longitudinal velocity as a function of ceramic volume fraction.

Experimental 15:15:3mm \square
 Experimental 15:15:6mm \blacksquare
 FEM 'laterally free' - - - -
 FEM 'laterally clamped' - . - .
 Smith's model [3] —

Smith's model is perfectly adequate. The value denoted by the black square, for the 90% device corresponds to the thicker 250kHz device. Clearly, in the case of the 90% 500kHz transducer, the pillars are not tall and thin, and hence the pillars are laterally clamped and therefore possess an increased stiffness. Finite element analysis has been used to predict the thickness mode velocity of this complex structure. The predicted value, indicated by a circle, serves to emphasise that finite element analysis can be used successfully to predict thickness mode values for cases where Smith's model is not valid.

Figure 5.5, illustrating measured and modelled thickness coupling coefficient, indicates that Smith's model has consistently overestimated coupling efficiency in the low volume fraction composites. This feature has been observed by Smith and has been attributed to either mechanically induced depoling during the sawing process, or to poor electrical contact. The electrical contact in the devices described here has been tested and are of a perfectly adequate quality. Typically, the resistance across the transducer electrode is less than 1Ω over a frequency range up to 5 MHz. It is hypothesised that depoling is occurring during the sawing process. The shape of the coupling coefficient curve, indicating that most depoling occurs in low volume devices, which have undergone more sawing, supports this hypothesis.

It has been postulated that the extent of depolarisation is proportional to the ratio of sliced surface area to

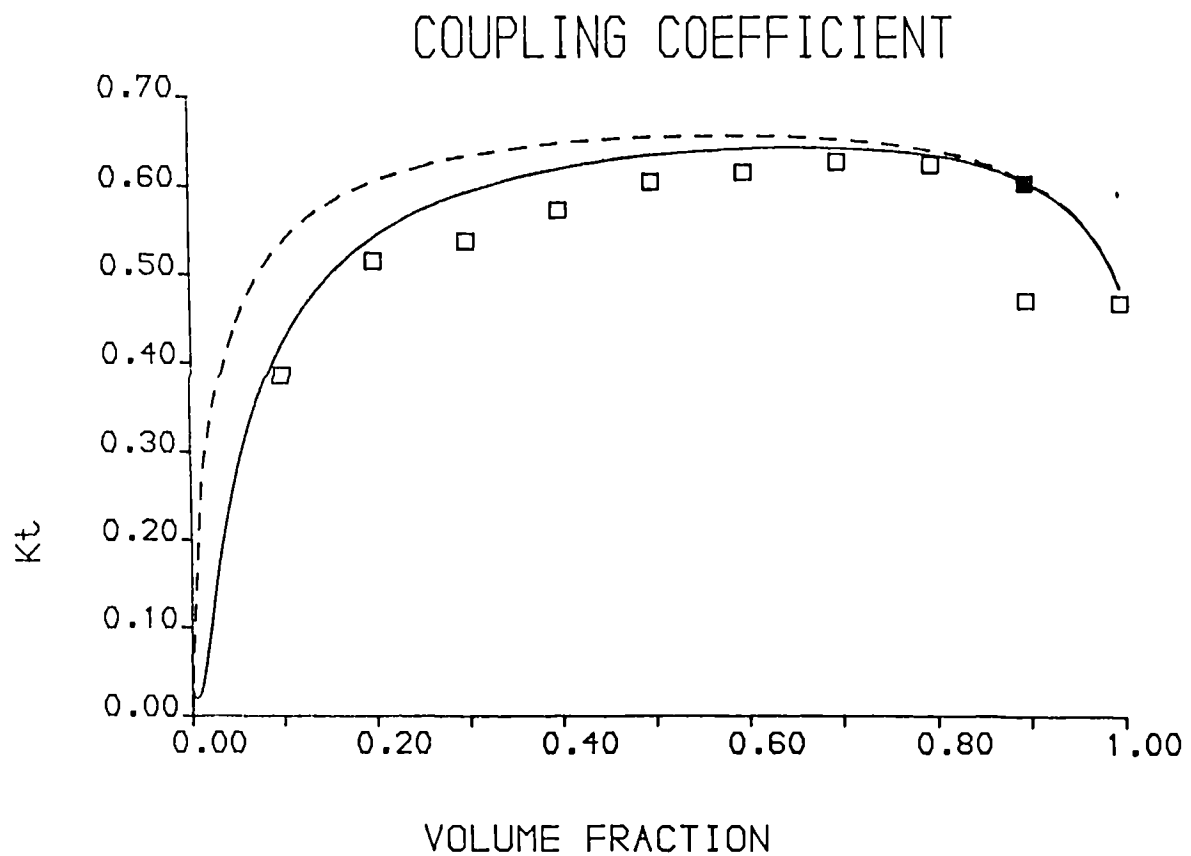


Figure 5.5 Comparison of theoretical and experimental composite thickness coupling coefficient as a function of ceramic volume fraction.

Experimental 15:15:3mm □
 Experimental 15:15:6mm ■
 Smith's model - - - - -
 Smith's model, modified to take account of depolarisation —————

overall ceramic volume. Following the arguments outlined in Appendix D, a modified electromechanical coupling coefficient, which includes the influence of the cutting process may be expressed as described in Equation 5.1.

$$k_t' = k_t(1-k(1-v)/\sqrt{vW}) \quad 5.1$$

W is the inter pillar spacing, k is the experimentally derived constant of proportionality, and v is the ceramic volume fraction. The constant of proportionality, k , was determined to be 2.7×10^{-5} m, for the manufacturing process used for all the composite transducers described in this thesis. The lower curve in Figure 5.5, which is obtained from Smith's model, and modified using the above expression, illustrates the improvement in the prediction of coupling efficiency that may be obtained. In its modified form, Smith's model provides a sufficiently accurate prediction of the thickness mode parameters. However, the value observed for the 90% device illustrates again that the model is only accurate for devices comprising of tall, thin pillars. Thus, the predicted coupling coefficient for the 90% 250kHz device is accurate, whereas it is inaccurate for the 500kHz device. Finite element analysis has been used to predict the coupling efficiency of the 500kHz transducer and the result obtained is denoted by the circle in Figure 5.5. Again, the need to resort to finite element analysis for transducers possessing complex pillar geometries, is emphasised.

5.3 DEVELOPMENT OF A SUITABLE THICKNESS MODE TRANSDUCER MODEL

A number of transducer models are available which may be used, in combination with the model described in the previous section, to predict composite transducer performance. In order to maximise the versatility of the model, it is necessary that the transducer model exhibits the following features.

1. Includes the influence of the electrical loading circuitry, in both transmission and reception.
2. Equally valid for both wideband, transient operation and narrowband operation
3. Includes the effects of mechanical loading.
4. Capable of extension to include the effects of multiple layers, so that the influence of matching layers may be correctly modelled.
5. Includes the effects of mechanical loss (wave attenuation). Loss in certain composites is significantly higher than in pure ceramic devices.
6. Ideally, the model should be capable of extension so that the performance of multiple active layers may be modelled. Further, the excitation and the electrical loading of these layers may be independent. Frequently, low frequency devices consist of a stack of plates which are mechanically in series but connected electrically in parallel. A model of this type of structure would have important practical applications.

The Mason [5] and the KLM [6] models are normally described without the inclusion of matching layers and mechanical loss. Nevertheless, the KLM model may be extended to include the effects of matching layers by cascading transmission lines in the model [43]. Each of these lines possesses the correct delays. Also, because these two models are based on electrical circuit analogies, the inclusion of electrical loading impedances is straightforward. The KLM model has been extended to include the effects of mechanical attenuation by Ih and Lee [27].

The systems modelling approach, originally described by Hayward [7], offers the advantages of being more physically meaningful, as the individual stages of the transduction process are represented by distinct transfer function blocks. This model is unique amongst the three models, in that it does not employ obscure circuit analogies, such as transformers and negative capacitances, to represent the process of conversion between charge and displacement. Although the systems modelling approach is not suited towards multilayered structures, an acoustic lattice technique has been used to extend the modelling strategy to take account of multiple layers [44]. In this case, the transfer functions of the individual layers are assembled into a matrix formulation representing the complete system. Standard matrix manipulation techniques are used to obtain the output voltage, force or operational impedance. Unfortunately, the increased

mathematical complexity of these matrix problems results in a loss of the clarity associated with the systems approach.

The systems model has been selected for use in the modelling of composite transducers as it offers the greatest versatility, clarity and scope for extension to incorporate active multilayer operation and mechanical losses. Much of the development and features of the model are discussed in the published literature. However, the principal aspects of the model, and particularly those which have been developed for the analysis of composite transducers, will be described briefly.

The model is based on the fundamental piezoelectric equations for a thickness mode vibrating slab of piezoelectric material. The general set of elastic and piezoelectric equations, which relate interaction along, and rotation around, three mutually perpendicular axes, are reduced to a simple unidimensional set of equations [24]. It is implicitly assumed that, in a thickness mode vibrator, the strains in the two axes perpendicular to the axis of vibration are zero. Hence Equations 5.2 and 5.3 are obtained. All symbols are in accordance with the IEEE Standard [1] and are defined in the List of Symbols at the beginning of the thesis. Standard axis notation, as illustrated in Figure 1.0, is used.

$$T_3 = c_{33}^D S_3 - h_{33} D_3 \quad 5.2$$

$$E_3 = D_3 / \epsilon_{33} - h_{33} S_3 \quad 5.3$$

The second term in the first equation represents the modification, due to the piezoelectric effect, of Hooke's Law. The second term in the second equation represents the modification of the Maxwell equation, $D = \epsilon E$, due to the piezoelectric effect.

The strain, S_3 , can be related to the following Laplace wave equation, which defines the displacement within a thickness mode vibrating transducer [45].

$$u = A e^{-sT} + B e^{+sT} \quad 5.4$$

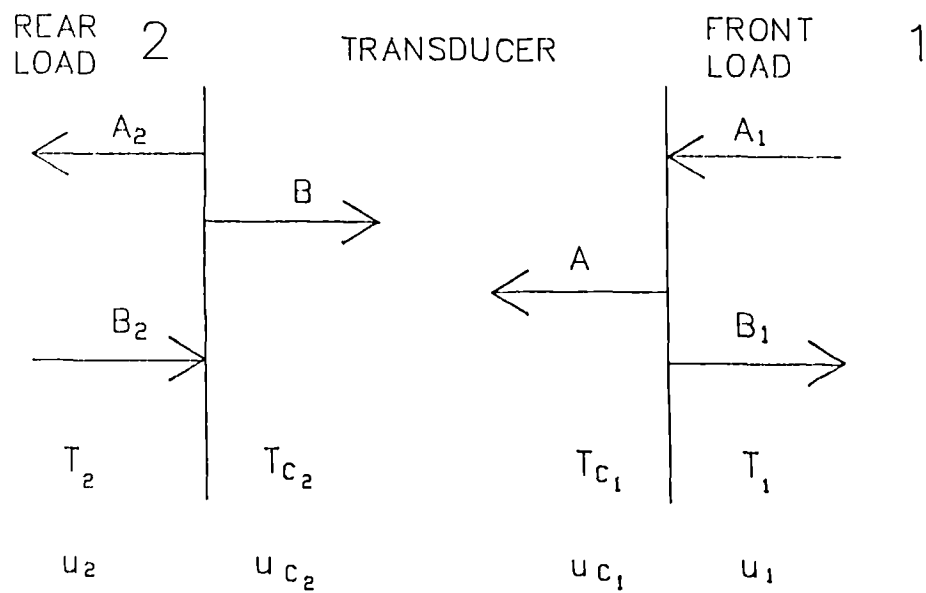
A and B are functions of mechanical displacement describing forward and backward wave propagation. T is the wave transit time across the thickness dimension of the transducer, and 's' is the Laplace operator.

The wave equation can be combined with Equations 5.2 and 5.3 to yield a general relationship for the transforms of force and mechanical displacement inside the transducer. Details of the algebraic manipulation required are described in the literature [44].

$$\bar{F} + h \bar{Q} = s Z_m (-A e^{-sT} + B e^{+sT}) \quad 5.5$$

$$\bar{V} = -h [A (e^{-sT} - 1) + B (e^{+sT} - 1)] \bar{U} \quad 5.6$$

A bar symbol ($\bar{\quad}$) denotes a Laplace quantity, \bar{Q} is the Laplace transform of electronic charge, and Z_m is the mechanical impedance of the transducer. \bar{F} corresponds to the force generated at the surface of the transducer



COMPATIBLE STRESS AND STRAIN AT BOUNDARIES

Figure 5.6 Boundary conditions associated with a single layer thickness mode transducer with front and rear loading.

to the force generated at the surface of the transducer and \bar{V} is the voltage across the electrodes. The practical value of this general expression is considerably enhanced by the inclusion of, \bar{U} , the electrical load factor, due to an arbitrary electrical load, \bar{Z}_E , connected in parallel with the electrodes of the transducer [46]. This is defined in Equation 5.7

$$\bar{U} = \frac{sC_o \bar{Z}_E}{1 + sC_o \bar{Z}_E} \quad 5.7$$

The boundary conditions of the system may be applied and hence expressions for A and B in Equations 5.5 and 5.6 obtained. At the boundary, continuity of particle displacement and normal stress must exist. This configuration is illustrated in Figure 5.6. Media 1 and 2 are semi-infinite and non-piezoelectric. Media 1 is adjacent to the front surface. Hence, the following expressions, for a receiver, relating voltage generated across the transducer electrodes to a particle displacement, A_1 , incident on the transducer front face may be derived. The algebraic manipulation required to derive this expression is detailed elsewhere [7,46].

$$\bar{V} = h \{ \bar{K}_F [\bar{A}_1(1-R_F) - h\bar{Q} /s(Z_m+Z_1)] - \bar{K}_B h(\bar{Q} /s(Z_m+Z_2)) \} \bar{U} \quad 5.8$$

Where K_F and K_B are the front and back reverberation coefficients respectively. K_F describes the difference in particle displacement, at opposite transducer faces,

arising from an incident impulse force function arriving at the front surface. R_F and R_B are the front and back reflection coefficients respectively.

$$\bar{K}_F = (1 - e^{-sT})(1 - R_B e^{-sT}) / (1 - R_F R_B e^{-2sT})$$

$$\bar{K}_B = (1 - e^{-sT})(1 - R_F e^{-sT}) / (1 - R_F R_B e^{-2sT})$$

$$R_F = \frac{(Z_m - Z_1)}{(Z_m + Z_1)}$$

$$R_B = \frac{(Z_m - Z_2)}{(Z_m + Z_2)}$$

Similarly, expressions relating force output to voltage input (transmitter) and transducer electrode voltage to excitation voltage can be evaluated. Each of these transfer functions can be manipulated and drawn in a block diagram format.

5.4 INCLUSION OF LOSS IN THE THICKNESS MODE MODEL

When a thickness mode transducer model is applied to a composite device, it would be preferable if mechanical wave attenuation could be included. Furthermore, the numerical values used in the simulation of the attenuation process should relate to the wave attenuation which can be measured experimentally. This can be achieved either directly using Selfridge's experimental technique [47], or indirectly from the values of impedance minimum, or maximum, at the resonant frequencies [1,28].

The resonant characteristics of the transducer are governed by the reverberation factors \bar{K}_F and \bar{K}_B . These are formed by summing to infinity the resultant surface displacements due to a wave propagating back and forth within the transducer cavity.

When losses are considered, the wave may be assumed to experience attenuation during each transit interval. If the wave attenuation, a , is defined in the conventional units of dB/cm, then the actual attenuation per transit interval may be calculated in the following manner.

1. Convert the loss in dB/cm (a_{dB}) to loss nepers/m (a_n)
ie from $20 \log_{10} (a)/\text{cm}$ to $\log_e (a)/\text{m}$
Loss, a_n (N/m) = $100/20 \times \log_e (10) \times a_{dB}$ (dB/cm)

2. The original wave, propagating over a distance, d , is modified by the following factor:

$$a = e^{-a_n d}$$

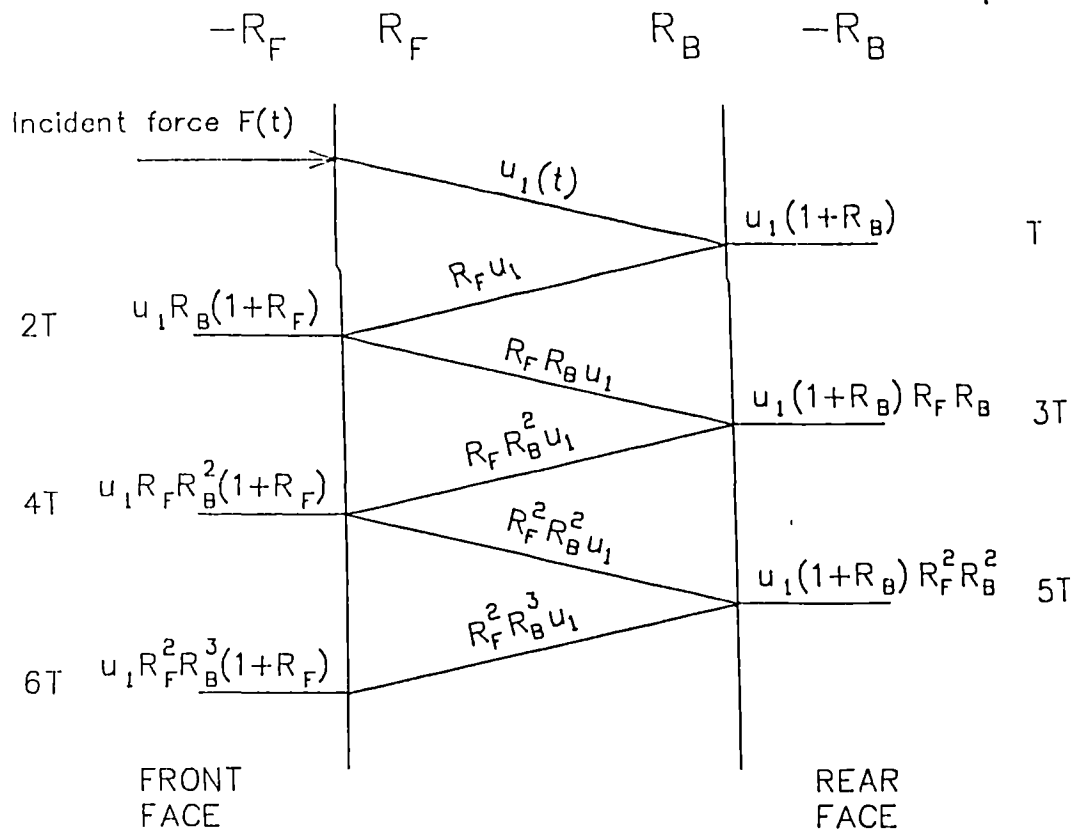


Figure 5.7 Effect of reverberation on an incident wave of force in a loss free thickness mode receiver.

3. Furthermore, for the purposes of including attenuation effects in a model, it is normally assumed that loss is a linear function of frequency [47]. Hence, the loss can be modified to take account of the frequency of operation. If the loss is specified in terms of dB/cm @ 1MHz, then the attenuation per transit interval is modified accordingly.

$$a = e^{-a_n df/f_0}$$

a_n = loss in nm^{-1}
 d^n = transducer thickness
 f = operating frequency
 f_0 = 1MHz

It is worth emphasising that it is conventional to assume that in certain materials, for example, most polymers, the loss is proportional to the square, or other power, of frequency [47]. In this case the above equation may be modified to take account of this. For the sake of simplicity, it will be assumed that the loss of composite transducers is a linear function of frequency. This approximation is adequate, provided that the loss has been calculated, or measured, at a frequency in the vicinity of the fundamental operating frequency of the transducer.

Consider the receiver transducer configuration illustrated in Figure 5.7. A wave of force, incident on the front face, gives rise to a particle displacement $u(t)$, which reverberates between the transducer faces. At each reflection, a proportion of the signal is lost to the load medium, and the remaining portion is determined by the reflection coefficient. During each transit interval, the

displacement is delayed by an interval defined by e^{-sT} , and is attenuated by the factor e^{-a} . Therefore, the total particle displacement, u' , at the transducer front face is given by Equation 5.9.

$$\begin{aligned} \bar{u}' &= \bar{u}_1 [1 + R_B(1 + R_B)e^{-2sT - 2a} + R_F R_B^2(1 + R_F)e^{-4sT - 4a} \\ &+ R_F^2 R_B^3(1 + R_F)e^{-6sT - 6a} + \dots] \end{aligned} \quad 5.9$$

Where: $a = a_n df/f_o$

R_F is the front face reflection coefficient

R_B is the rear face reflection coefficient

Hence:

$$\bar{u}' = \bar{u} [1 + R_B(1 + R_B)e^{-2(sT+a)} \left(\sum_{n=0}^{\infty} (R_F R_B)^n e^{-2n(sT+a)} \right)] \quad 5.10$$

Summation of the geometric progression results in:

$$\bar{u}' = \bar{u} \left[\frac{(1 + R_B)e^{-2(sT+a)}}{(1 - R_F R_B)e^{-2(sT+a)}} \right] \quad 5.11$$

The particle displacement at the rear surface is given by:

$$\bar{u}' = \bar{u} \left[\frac{(1 + R_B)e^{-(sT+a)}}{(1 - R_F R_B)e^{-2(sT+a)}} \right] \quad 5.12$$

Hence, the difference between front and rear particle displacements, which represents \bar{K}_F , is given by:

$$\bar{u}_F = \bar{u} \left[\frac{(1 - e^{-(sT+a)})(1 - R_B e^{-(sT+a)})}{(1 - R_F R_B e^{-2(sT+a)})} \right] \quad 5.13$$

$$\bar{u}_F = \bar{u} \bar{K}_F(s)$$

\bar{K}_B may be determined in an analogous manner. Also, the reverberation factors may be determined similarly for the transmission case, and precisely the same equations for K_F and \bar{K}_B result [46].

Fabulated values for the wave attenuation in certain materials exist. However, wave attenuation in a piezoelectric ceramic can be determined from the mechanical Q factor of the material. The Q factor may be determined using the IEEE Standard [1]. Mason has related attenuation per unit wavelength, to the quality factor via Equation 5.19 [5].

$$a = \frac{\pi}{Q} \quad 5.14$$

It is hypothesised that the attenuation in a composite may be estimated from the volume weighted sum of the attenuation coefficients of the two constituent phase materials. Thus Equation 5.15 is obtained.

$$a = va^C + (1-v)a^P \quad 5.15$$

Where:

v is the ceramic volume fraction.

a^C is the attenuation per unit length in the ceramic

a^P is the attenuation per unit length in the polymer

The approximate validity of this expression has been verified on an experimental basis. The manufacturer's value of the Q_m of PZT 5A is 75. Hence, the attenuation is calculated to be 0.836 dB/cm @1MHz. The attenuation in the

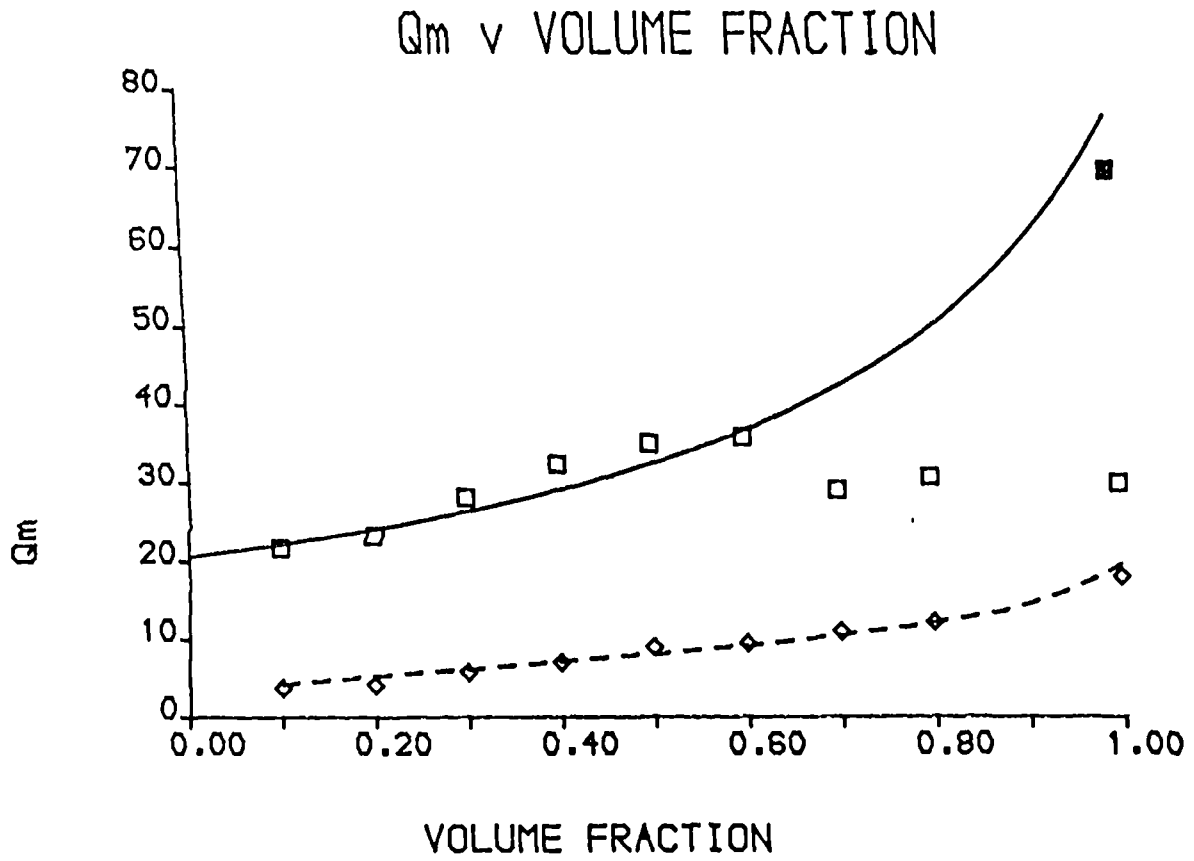


Figure 5.8 Comparison of theoretical and experimental composite mechanical Q factor as a function of ceramic volume fraction.

Experimental - air loaded 15:15:3mm	□
Experimental - air loaded 30:30:3mm	■
Theoretical - air loaded	—————
Experimental - water loaded 15:15:3mm	◇
Theoretical - water loaded	- - - - -

polymer has been determined experimentally using Selfridge's technique [47]. This involves measuring the reflected pulses from a large, thick block of the material when suspended in water. The measured reflected pulse amplitude is compared to the theoretical (lossless) value, and hence the attenuation is calculated. This test was performed on a 25mm thick block at 1MHz. The experimentally observed attenuation coefficient was 5.0 dB/cm @1MHz, and this value has been used throughout. A complete, thorough model for loss would be extremely complex and the improvement in accuracy that could be expected in practical simulations is considered marginal.

The mechanical Q value for a range of composites with ceramic volume fractions ranging from 10% to 90% were calculated using the above expressions. The mechanical Q of experimental 500kHz composite devices were calculated using the IEEE method and are shown superimposed on the theoretical curve in Figure 5.8. A close correlation is observed for volume fractions of up to 60%. Beyond that point, the Q_m factor reduces, instead of increasing as predicted by the theory. This error is caused by the presence of additional extraneous modes in the vicinity of the electrical resonant frequency preventing accurate measurement of Q_m . This results in an underestimate of the mechanical Q_m , as the theory used is derived for a pure, undistorted, unidimensional resonator. It is significant that the measured Q_m of the 15 x 15mm reference ceramic device is approximately 30, which is markedly degraded

from the manufacturer's nominal value of 75. However, the Q measured for a larger ceramic slab, with dimensions of 30 x 30mm, which did not possess significant extraneous resonant activity in the vicinity of the thickness resonance, was 70. This is in far better agreement with the predicted value, and serves to explain the deviation between results obtained for the high volume fraction composite devices. Figure 5.8 also illustrates the modelled and measured Q_m values for transducers loaded on one face with water. This has the effect of smoothing out the resonances. A steady increase of Q_m with increasing volume fraction is evident, and for this case, excellent correlation between experimental and modelled results is observed.

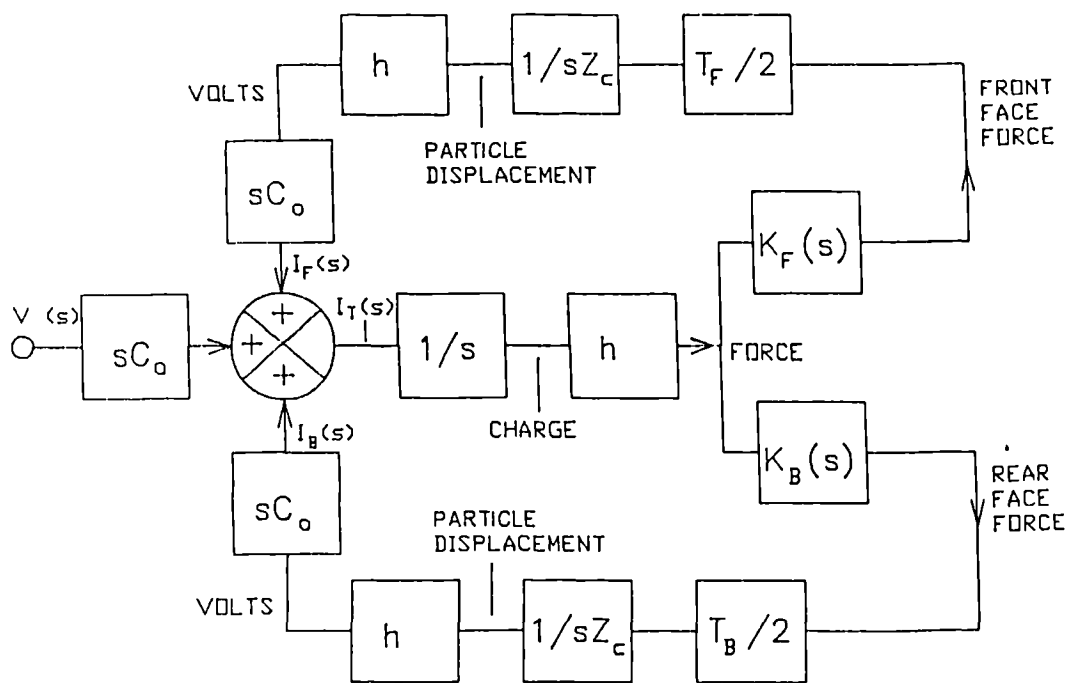


Figure 5.9 Admittance model in block diagram format

5.5 MODELLING THE OPERATIONAL IMPEDANCE OF A COMPOSITE PIEZOELECTRIC TRANSDUCER

The operational impedance of a transducer is determined by its dimensions, permittivity, piezoelectric coupling efficiency and mechanical loading. For practical applications, it is important to establish the magnitude and phase of the impedance in the vicinity of the resonant frequency so that a suitable matching circuit may be designed. Clearly, impedance is of prime importance in determining the transmission and reception performance of a transducer. The value of an accurate model for predicting transducer impedance is therefore evident.

The systems model described in section 5.3 may be configured as illustrated in Figure 5.9. This represents the admittance function of a transducer. The admittance, and hence impedance, is represented by a capacitance modified by two positive feedback loops. T_F and T_B are transmission coefficients at the front and back surfaces respectively, and are defined in Equation 5.16.

$$T_F = \frac{2Z_m}{Z_1 + Z_m} \qquad T_R = \frac{2Z_m}{Z_2 + Z_m} \qquad 5.16$$

The extent of the positive feedback, which gives rise to a maximum in admittance, is determined by h , the piezoelectric charge constant, the mechanical impedance of the transducer, Z_m , and the loading conditions which determine the transmission and reverberation functions.

The accuracy of the combined model, encompassing the modified material parameter model, and the extended thickness mode model, has been verified for a wide range of devices. The ten devices, described in section 5.2, with volume fractions ranging from 10% to 100%, were modelled. The experimental and simulated values for the frequencies and impedance magnitudes at the electrical and mechanical resonance are compared in Table 5.1. The clamped capacitance, C_0 , measured at twice the mechanical resonant frequency is also tabulated. The clamped capacitance corresponds to the capacitance of the transducer in the absence of any piezoelectric activity. Therefore, it is measured at a high frequency, typically at twice the mechanical resonant frequency, where net piezoelectric resonant activity is virtually non-existent.

IMPEDANCE

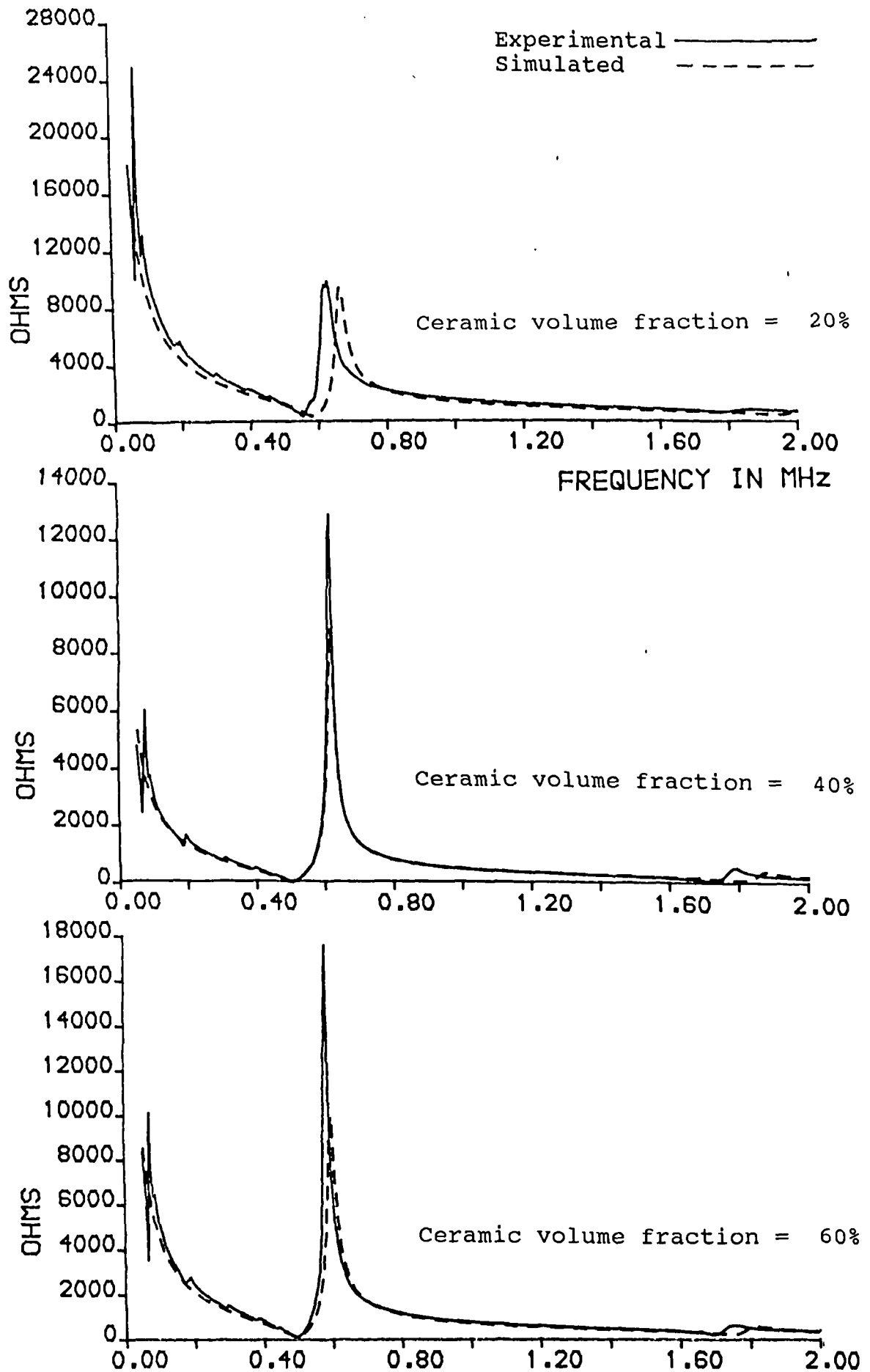


Figure 5.10 Theoretical and experimental impedance magnitude characteristics of 15 x 15 x 3mm composite transducers

TABLE 5.1

Comparison of experimental and modelled impedance characteristics

v	f_m (kHz)		$Z@f_m$ (Ω)		f_n (kHz)		$Z@f_n$ (K Ω)		C_o (pF)	
	EXP.	MOD.	EXP.	MOD.	EXP.	MOD.	EXP.	MOD.	EXP.	MOD.
0.1	575	619	1116	1015	623	672	11.6	10.0	69	72
0.2	551	582	323	307	631	666	9.8	9.4	114	135
0.3	531	542	163	169	615	642	14.3	9.3	159	188
0.4	494	494	96	121	585	599	17.3	10.0	213	229
0.5	508	503	54	77	616	620	15.3	9.0	284	291
0.6	505	499	42	56	618	620	13.2	8.9	334	343
0.7	524	520	37	38	648	649	21.7	8.2	411	399
0.8	513	516	32	30	632	640	4.6	8.6	432	454
0.9	659	542	37	24	678	657	2.8	8.4	486	505
1.0	670	654	39	26	725	730	5.1	5.5	539	551

Plots of the impedance spectra for the 20%, 40%, 60%, 80%, 90% and the 100% devices are illustrated in Figure 5.10. Generally, correlation is good, but it is best for the mid range region of 30% to 70%. At the higher volume fractions, especially in the case of the 90% device, the presence of additional extraneous modes becomes apparent. There are some discrepancies between modelled and measured values for the impedance maximum. The value of the modelled impedance maximum is very sensitive to changes in the loss characteristics. However, when the transducer is modelled for a practical loaded case, the effect of the load dominates the effect of internal loss and a superior

IMPEDANCE

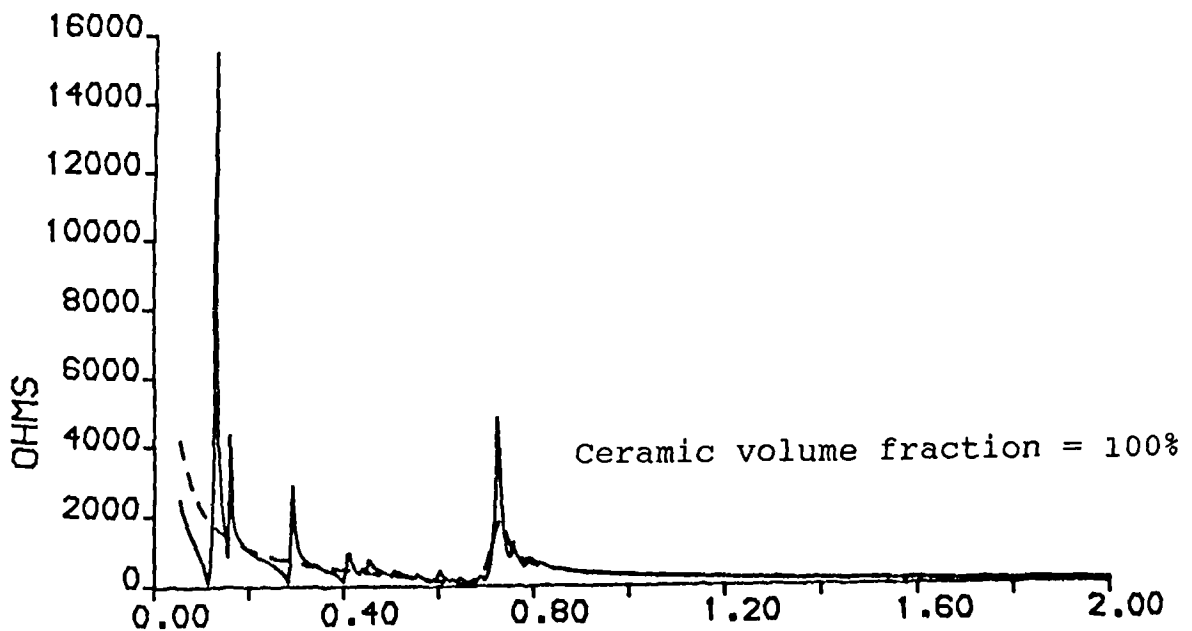
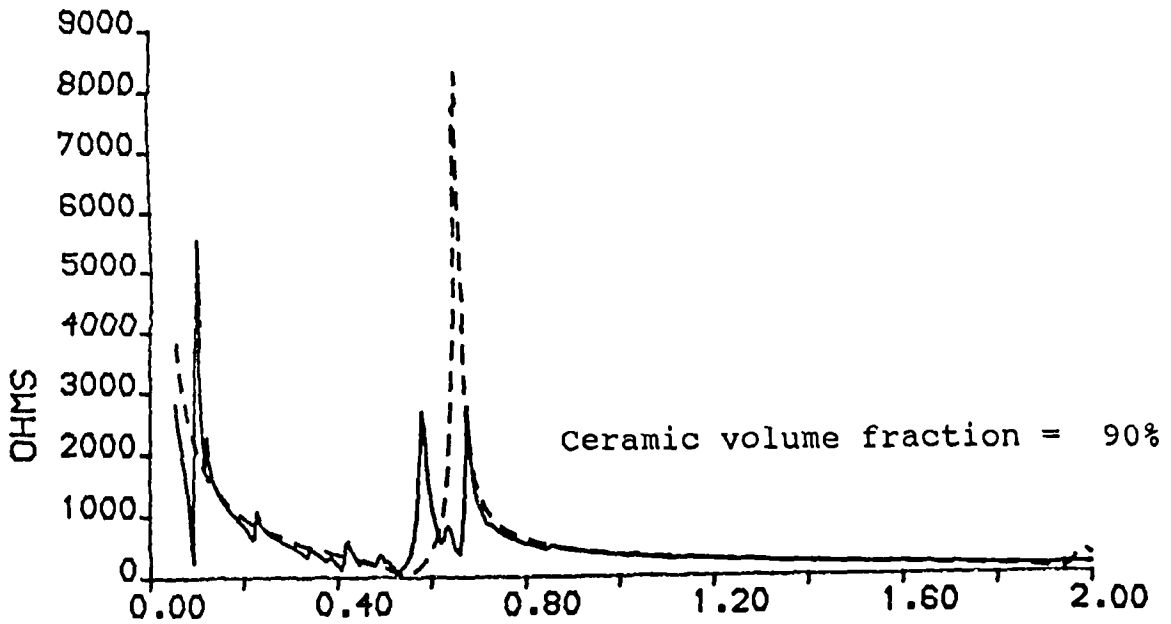
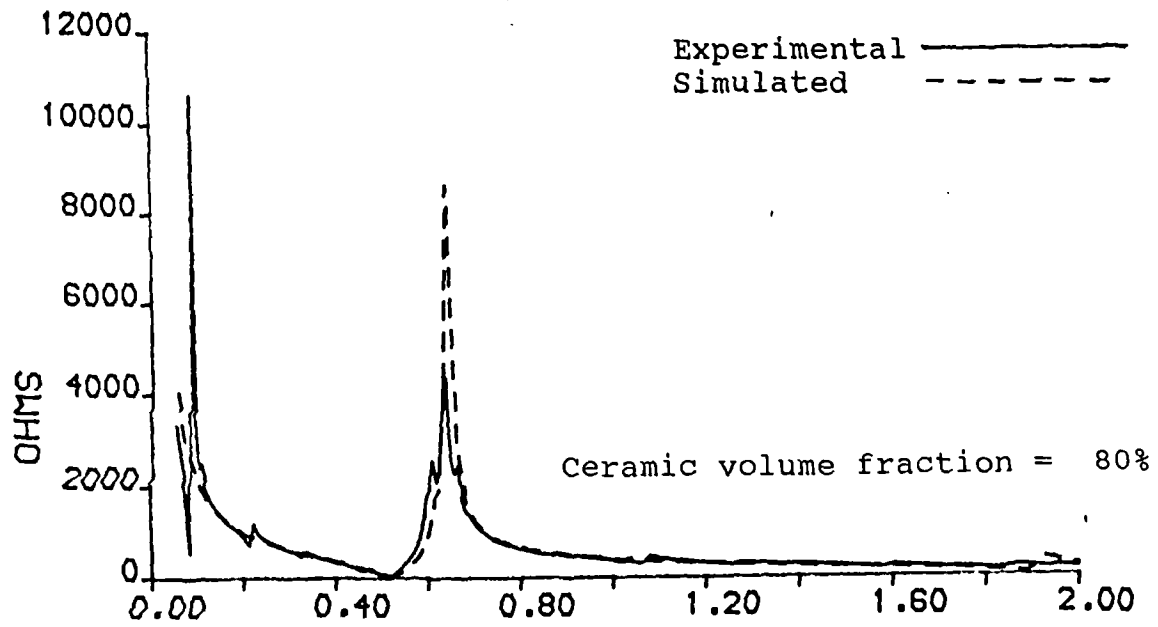


Figure 5.10 /continued

FREQUENCY IN MHz

correlation in impedance values is observed. This will be demonstrated in sections 5.3 iii) and 5.3 iv). In the 90% device, a parasitic mode is evident in the vicinity of the thickness resonant frequency. Clearly, this complex resonant activity may not be adequately modelled using the simple unidimensional approach adopted here.

The result for the 100% transducer is significant since the strength of the fundamental planar mode of the ceramic plate is plainly evident, and actually dominates the thickness resonance. Again, a thickness mode model is limited in that this mode of vibration is not included. However, at lower volume fractions, the planar mode becomes progressively weaker. This has important practical consequences since the composite material is behaving more as a pure thickness mode device. However, if a PZT transducer possesses a strong planar mode, then its transmitted/ received pulse response will contain a significant spectral content at the lower planar mode, in addition to that at the thickness mode frequency. In practice, this means that the geometry of PZT devices must be chosen so as to minimise the planar mode. This normally involves using a ceramic plate with a width to height ratio greater than ten or less than a half. These restrictions are normally not necessary when a composite material is being used. For the majority of practical cases, it is evident that the thickness mode dominates and hence a thickness mode model is entirely appropriate to the analysis of composite transducers.

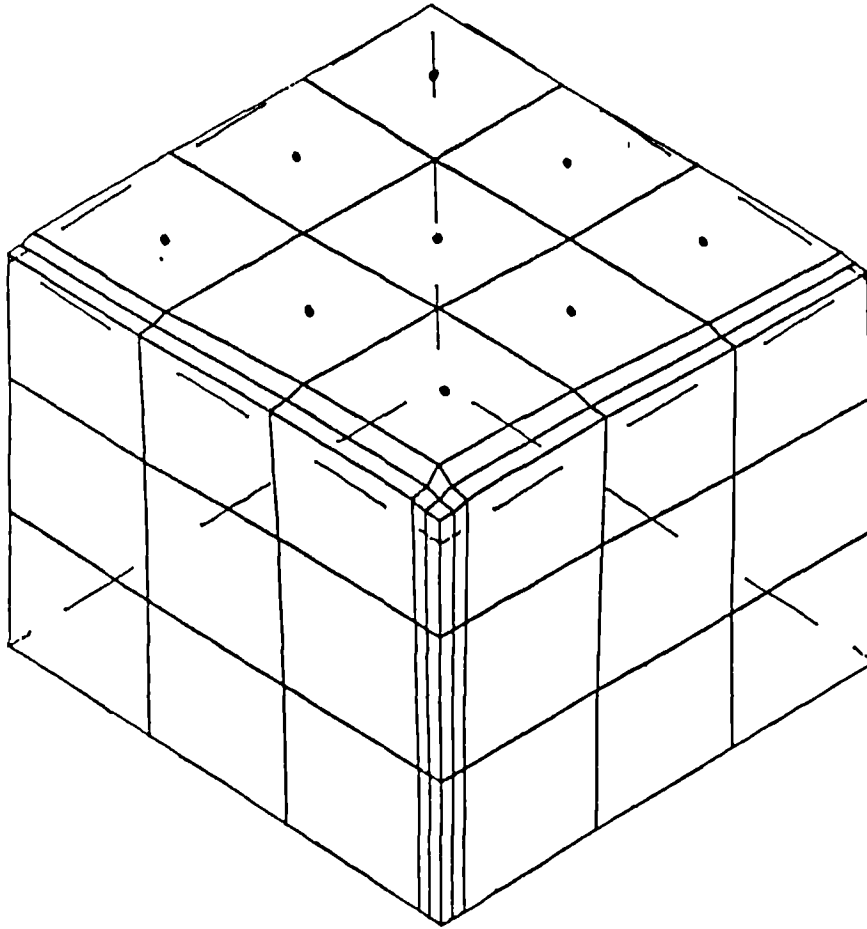


Figure 5.11 Thickness resonant mode of a 90% 3mm thick composite. (641kHz)

TABLE 5.2

Comparison of theoretical and measured lateral and thickness resonant frequencies in a 15x15x3mm PZT plate.

	LATERAL		THICKNESS	
	Exp.	Theor.	Exp.	Theor.
f_m (kHz)	110	112	670	683
f_n (kHz)	126	134	725	752

The 90% device has been analysed using finite element analysis. The thickness mechanical resonant mode of this device has been determined to occur at 641kHz, which is in reasonable agreement with the experimental value of 679kHz. This mode is depicted in Figure 5.11. As the pillar expands in the thickness direction, it contracts in the lateral direction. This lateral motion in the ceramic has the effect of drawing the polymer inwards. Clearly, the assumptions made in Smith's model regarding uniformity of strain in the thickness direction are not valid in this case.

Finite element analysis has also been used to predict the lateral and thickness modes of the pure ceramic device. The values for electrical and mechanical resonant frequencies are compared with the experimental values in Table 5.2. Finite element analysis has predicted these resonant modes with acceptable accuracy. Thus, finite element analysis is an invaluable tool in the modelling of composite, and conventional, transducers which cannot be considered using any other simpler method. However, as this example has illustrated, the majority of practically useful configurations are designed so that they conform to relatively pure thickness mode operation.

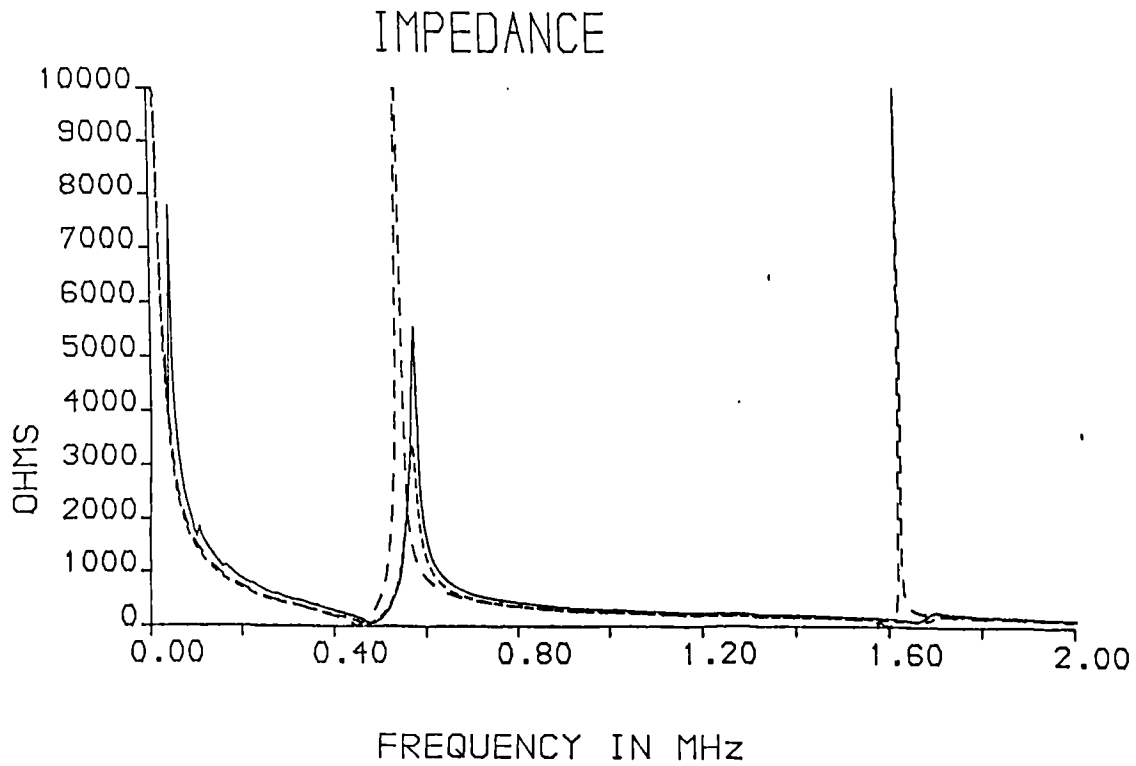


Figure 5.12 Theoretical and experimental impedance magnitude characteristics of a 40% 500kHz composite transducer in air.

————— Experimental
 - - - - - Simulated including loss of 2.61dB/cm @1MHz
 - . - . - Simulated excluding all loss

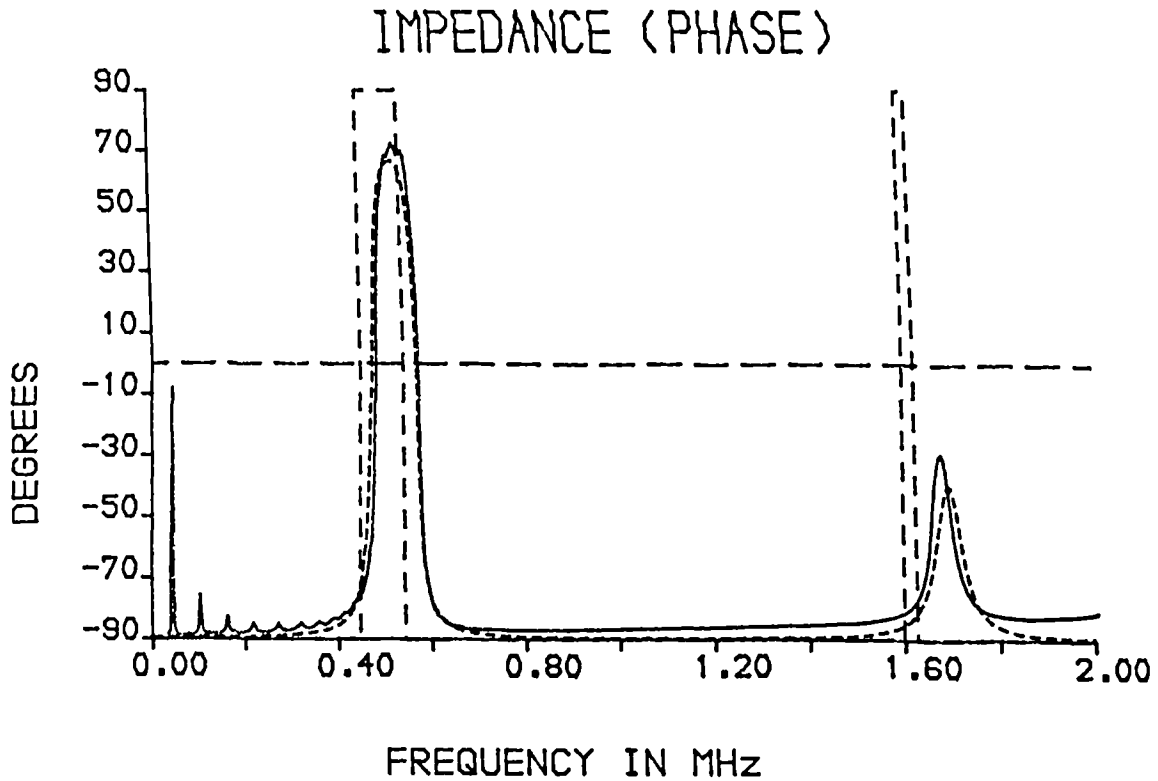


Figure 5.13 Theoretical and experimental impedance phase characteristics of a 40% 500kHz composite transducer in air.

————— Experimental
 - - - - - Simulated including loss of 2.61dB/cm @1MHz
 - . - . - Simulated excluding all loss

5.5 ii) Influence of internal loss on modelled impedance

The influence of internal mechanical loss on the modelled impedance of a typical composite resonator, operating in an air backed configuration, has been examined. Figure 5.12 illustrates the magnitude characteristics for a 30 x 30mm 40% 500kHz composite transducer. Curves corresponding to a loss free simulation, a simulation including losses and an experimental result are shown. Figure 5.13 illustrates the corresponding phase characteristics. The thickness of the transducer simulated for the loss free case was 5% greater than that of the prototype device. A modified thickness was used so that the distinction between the loss free and lossy simulations would be clear. Notice that at electrical resonance, the impedance is virtually zero. This is because the feedback current due to secondary piezoelectric action, is exactly in phase with the applied current. Thus, the net impedance tends towards zero. Conversely, at mechanical resonance, the feedback current is exactly antiphase and a virtually infinite impedance results. Notice that the phase response, in the case of the loss free simulation is exactly -90° except between the electrical and mechanical resonant frequencies where it is exactly $+90^\circ$.

Figures 5.12 and 5.13 also illustrate the actual measured responses and simulated response, assuming a wave attenuation of 2.61dB/cm @1MHz. This attenuation figure has been determined using Equation 5.15, described in section 5.3. The improved correlation between experimental

and simulated responses is readily apparent. It is evident that the phase response is more critically dependent upon the loss mechanism and hence provides a more precise indication of the quality of the simulation. Notice, that in the lossy case, the phase response never attains $+90^\circ$, and the transition from -90° , pure capacitance, to its peak positive value has become less pronounced. The numerical value of the measured impedance minimum was 46Ω at 483kHz and the corresponding simulated figure was 44Ω at 472kHz . The measured and simulated figures for the impedance maximum were $5.57\text{K}\Omega$ at 577kHz and $3.41\text{K}\Omega$ at 572kHz respectively. The correlation between results at the electrical resonant frequency is excellent. As discussed in the previous section, the difference between impedance values at the mechanical resonant frequencies is due to the extreme sensitivity of this value to deviations in the loss mechanism.

5.5 iii) Influence of a matching layer on modelled impedance

The practical importance of matching layers in transducer design are well established [20]. The material is normally selected to operate as an acoustic transformer, providing an optimised match between, typically a low impedance load and a relatively high impedance transducer. The optimum acoustic impedance of a single matching layer is given by the square root of the product of impedances of the transducer and the load media. More complex equations are available for determining the optimal impedances for

multilayer matching systems [48]. Furthermore, for the typical example of a transducer operating into a low impedance medium, via one or more matching layers, the layer, or layers, should be one quarter of an acoustic wavelength thick [20]. The consequence of this is that waves, not transmitted out of the matching layer, are reflected and inverted, in such a way that they remain in phase with subsequently transmitted waves from the transducer. A matching layer system, optimised in terms of material and thickness will result in improved bandwidth and sensitivity in a practical transducer system.

However, this argument does not take account of the acoustic attenuation which may occur in the matching layer. In practice, it is difficult to obtain a low loss material of a specific acoustic impedance. In the case of PZT 5A, the optimum impedance for matching into water, is 7.1 MRayl, which is difficult to obtain in a homogeneous material.

However, a composite transducer, with its lower acoustic impedance, is far easier to match satisfactorily to water. A typical composite transducer, possessing an acoustic impedance of 12 MRayl, requires a matching layer impedance of 4.2 MRayl for optimal matching to water. This value of impedance may be obtained in a homogeneous polymeric material without the necessity for a filler.

It is evident, that the practical aspects of designing matching layers would benefit from a comprehensive

modelling technique which incorporated the characteristics, and in particular attenuation, of a matching layer. A model would provide useful information regarding the practical influence of using sub-optimal materials and thicknesses of matching layer. Frequently, for example in steered arrays, it is desirable to use a matching layer considerably thinner than a quarter of a wavelength.

The Laplace transform method of modelling may be simply extended to include multiple matching layers, as demonstrated by Lewis [49]. The transforms relating displacement and force in the layer, are assembled into a large system matrix. The boundary conditions at the interfaces, which must be satisfied, are that stress and displacement are continuous. Solution of the system equations requires a matrix solution technique, which may become numerically cumbersome when several layers are included. The model used here, is an extension of the systems model described in section 5.3, and may include multiple active layers. It also includes the capability for different mechanical losses in each of the layers of the entire system. Therefore, the model is perfectly suited to a comprehensive analysis of composite transducers coupled to matching layers.

Figure 5.14 illustrates the measured and simulated impedance magnitude profile of a 60% 500kHz composite transducer coupled to a 1.52mm epoxy quarter wavelength matching layer. This configuration is air backed on both

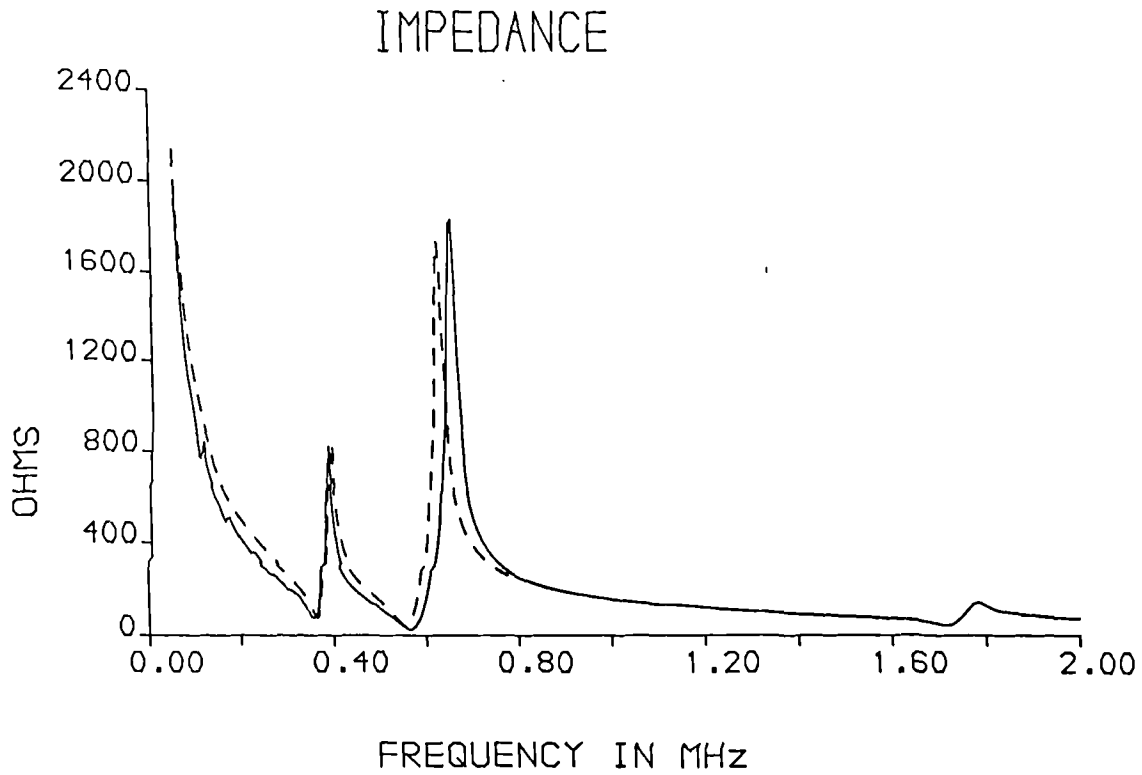


Figure 5.14 Theoretical and experimental impedance magnitude characteristics of a 60% 500kHz composite transducer, with a 1.52mm epoxy matching layer, operating into air.
 Experimental —————
 Theoretical - - - - -

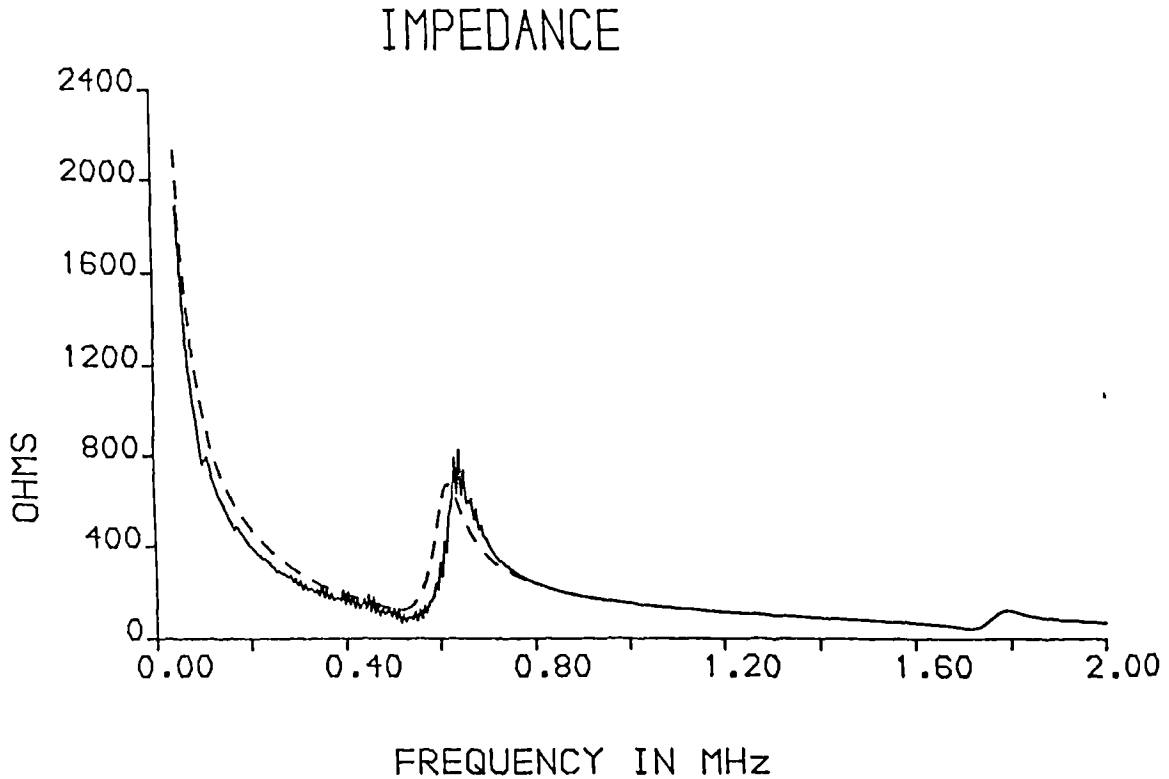


Figure 5.15 Theoretical and experimental impedance magnitude characteristics of a 60% 500kHz composite transducer, with a 1.52mm epoxy matching layer, operating into water.
 Experimental —————
 Theoretical - - - - -

front and rear surfaces. It is evident that the model has correctly predicted the two principal modes of vibration in the structure. The lower frequency mode corresponds to half wavelength resonance in the coupled structure. The higher frequency resonance corresponds to half wavelength resonance within the piezoelectric composite portion alone. The matching layer is not operating into the medium for which it was designed, and hence reverberation in the structure is complex.

In Figure 5.15 the measured and simulated impedance magnitude profiles of the same transducer with a water loading on the front face, is illustrated. The matching layer is now operating as an effective impedance transformer, and hence only one mode of vibration results. The response is clearly well damped and the extent of this damping is a result of the high quality acoustic match to the load media. The distortion apparent on the measured response is an artefact resulting from standing waves set up between the transducer face and the base of the beaker in which the experiment was performed.

5.5 iv) Influence of acoustic backing on modelled impedance

The acoustic backing of active transducers forms an important aspect of their design. For the applications under consideration here, heavy backing is applied to reduce reverberation within the transducer cavity to a minimum, and consequently maximise transducer bandwidth.

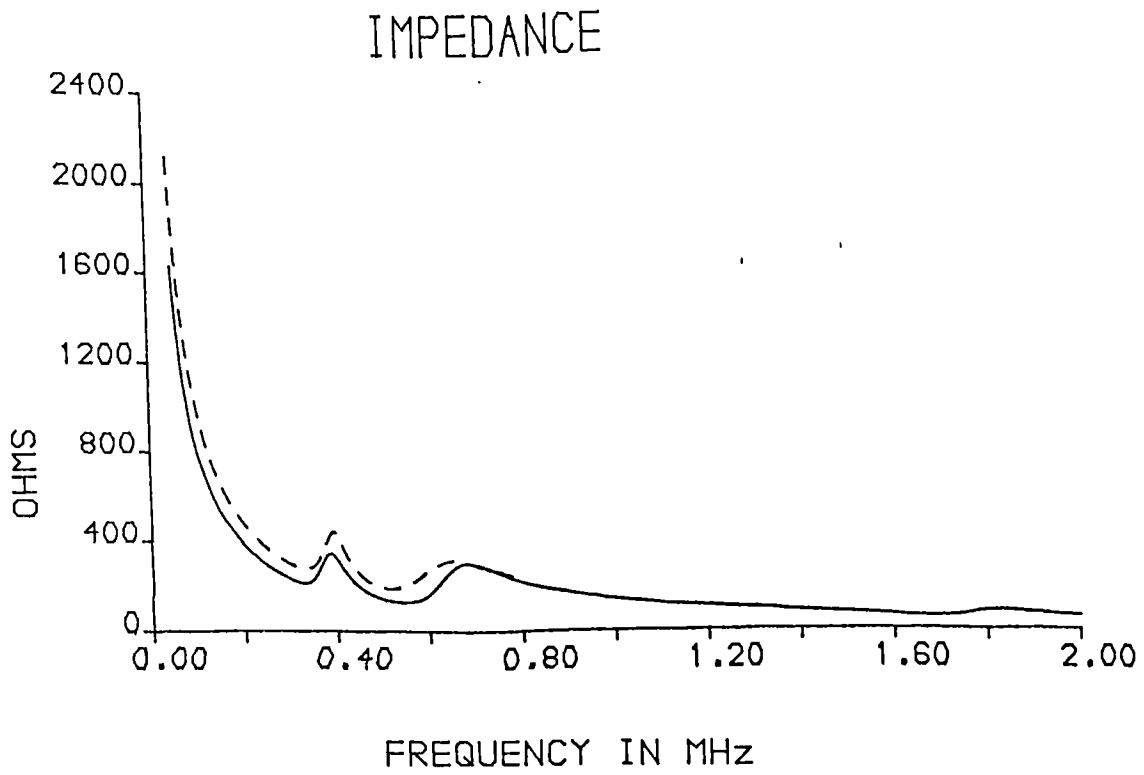


Figure 5.16 Theoretical and experimental impedance magnitude characteristics of a 60% 500kHz composite transducer, with a 1.52mm epoxy matching layer and a 10MRayl backing, operating in air.
 Experimental —————
 Theoretical - - - - -

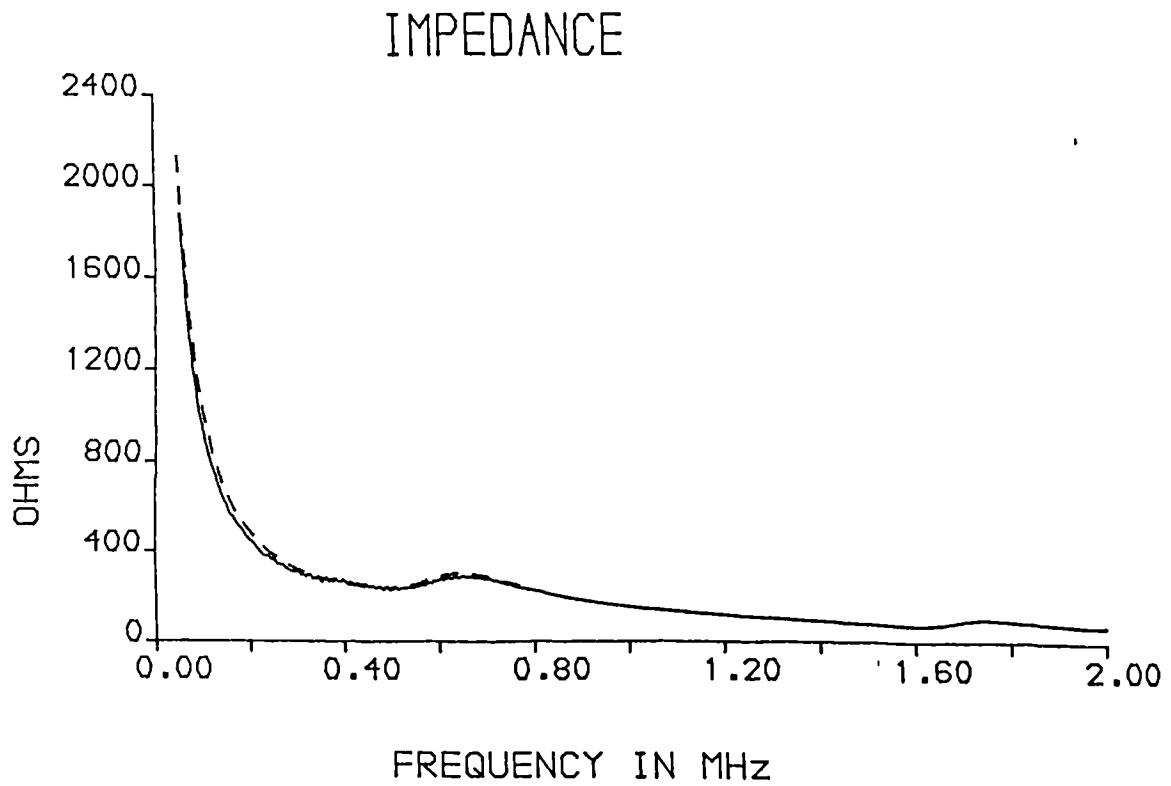


Figure 5.17 Theoretical and experimental impedance magnitude characteristics of a 60% 500kHz composite transducer, with a 1.52mm epoxy matching layer and a 10MRayl backing, operating into water.
 Experimental —————
 Theoretical - - - - -

Since, the front face load material is determined by the operating medium, then only the backing impedance is within the control of the designer.

Figure 5.16 illustrates the 'measured and simulated impedance profiles for a 60% backed and matched transducer operating into air'. The backing material is a soft setting epoxy polymer loaded with tungsten particles, possessing a measured acoustic impedance of 10 MRayl. Full details of its characteristics are described in Appendix A. The acoustic impedance of the transducer is 18.9 MRayl and therefore a reasonable acoustic match has been obtained. A transducer model is useful for assessing the viability of designs incorporating differing, suboptimal backing impedances.

The simulated and measured profiles in Figure 5.16 indicate excellent agreement. Again, a double resonant feature is evident due to the non-ideal acoustic match on the front face. However, when the same experiment was repeated with a water loaded face, the resulting impedance profile, as illustrated in Figure 5.17, indicate excellent, highly damped unimodal operation. A high degree of correlation between the simulated and experimental results is evident.

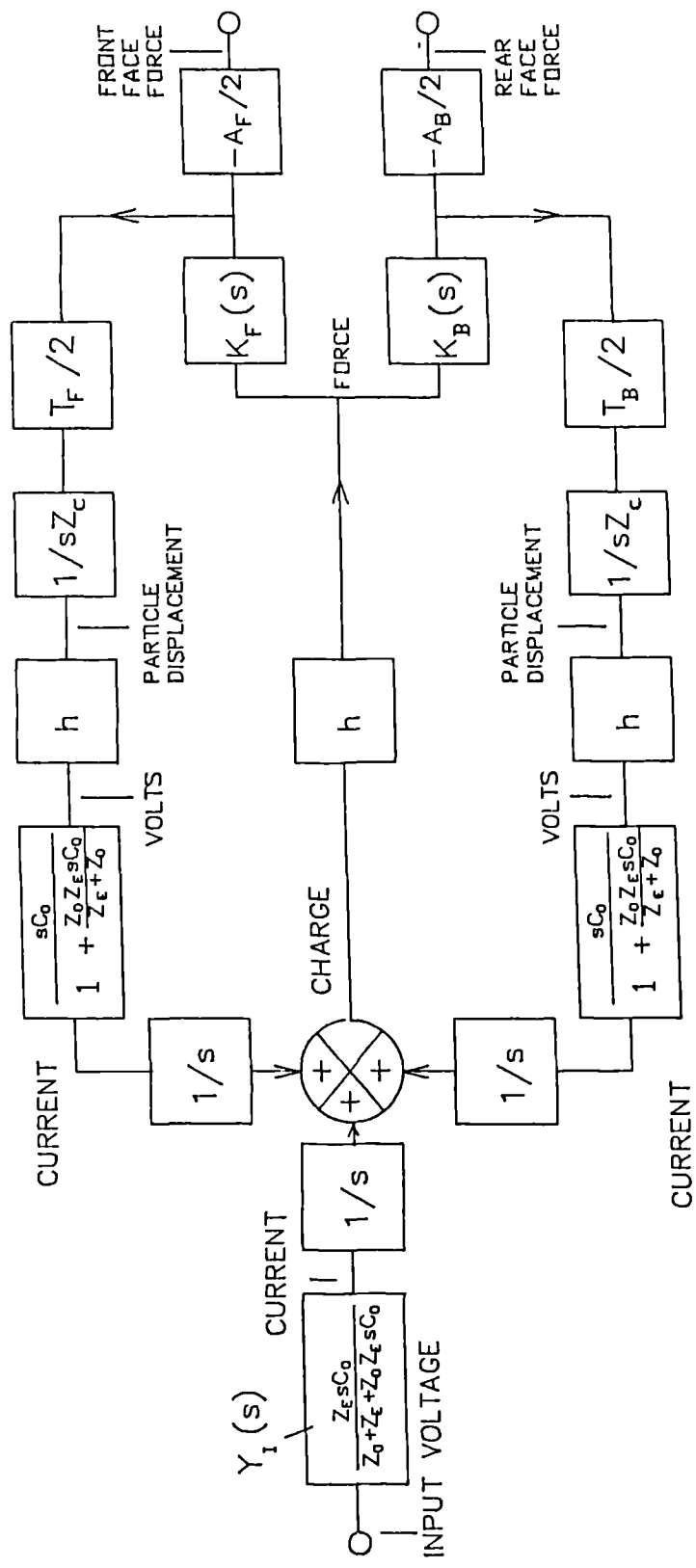


Figure 5.18 Transmitter transducer model in block diagram format

5.6 MODELLING THE TRANSMISSION CHARACTERISTICS OF A COMPOSITE PIEZOELECTRIC TRANSDUCER

5.6 i) General transmission model

The thickness mode transducer model may be configured as illustrated in Figure 5.18. This configuration matches the electrical excitation circuit depicted in Figure 5.19, which includes the series source output impedance, \bar{Z}_O , and an arbitrary load impedance, \bar{Z}_E , connected across the transducer electrodes. Hence, \bar{Y}_I , the input admittance block determines the current entering the transducer as a function of impedance sC_O , the parallel impedance, \bar{Z}_E , and the source impedance, \bar{Z}_O . Therefore, the influence of source impedance on output force may be analysed directly. The transducer current is converted to charge, and then to displacement, via the transduction transfer block (h). The reverberatory functions, \bar{K}_F and \bar{K}_B , determine the electrode displacement profiles. A proportion of the displacement is then transmitted outward into the load, or backing, while some gives rise to a secondary piezoelectric charge being generated across the electrodes via the feedback loops.

The model can be used with any arbitrary excitation. Continuous wave excitation, at a range of frequencies, will be used to determine the peak sensitivity and fractional bandwidth of a range of composite configurations. The aim is to identify the relative characteristics of different configurations of composite transducers. The model will then be applied to transiently

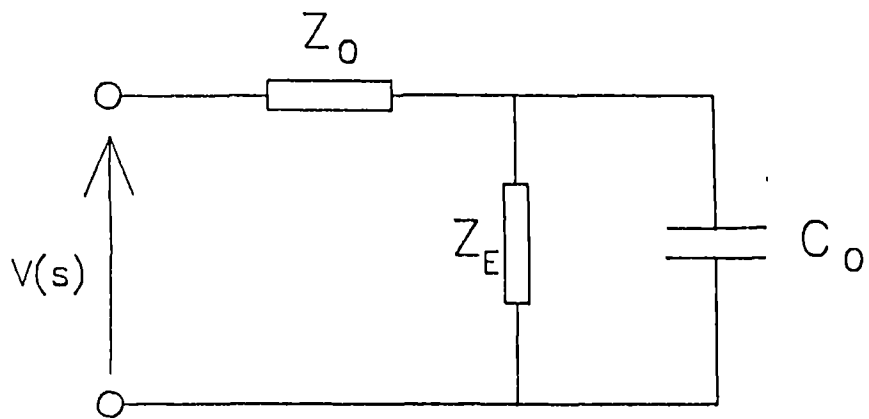


Figure 5.19 Electrical excitation circuit used with Figure 5.18

excited transducers and the resulting time domain outputs compared to experimentally obtained responses. It should be stressed that acoustic diffraction has a significant effect on both the amplitude and shape of the response at various points in the acoustic field. Diffraction will be discussed in Chapter VI and is not considered here. This is justified, since the measurements have been made at points where the influence of diffraction is minimal. During experimentation, the pressure was measured on axis in the far field, where diffraction induced fluctuations are minimal.

5.6 ii) Transmission characteristics of composite transducers under CW excitation

The ten 500kHz composite transducers described in section 5.2, were assembled into air backed, unmatched probes, as detailed in Appendix C. A short length of low loss coaxial cable was attached. The peak CW force output of these transducers, with ceramic volume fractions ranging from 10% to 100%, was measured using a wide band PVDF membrane hydrophone operating into a suitable high impedance amplifier. Details of the experimental apparatus are described in Appendix E. Only relative pressure responses are recorded because the hydrophone has not been calibrated with a reference acoustic projector. However, the response of the hydrophone and amplifier combination is known to be level to within ± 1 dB over the frequency range of interest. The frequency of the generator was varied and the -3dB frequencies recorded.

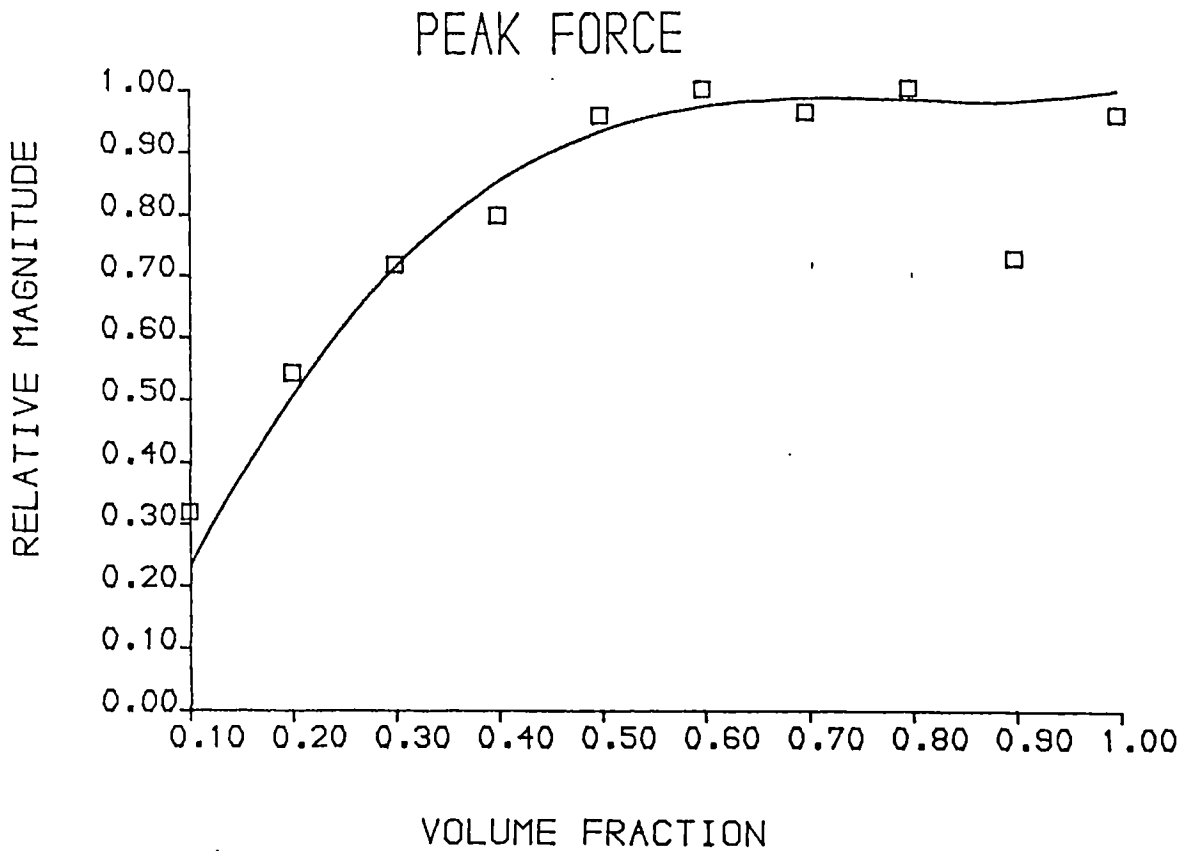


Figure 5.20 Normalised experimental and theoretical peak CW pressure output as a function of ceramic volume fraction (50Ω source impedance).
 Experimental \square
 Theoretical —

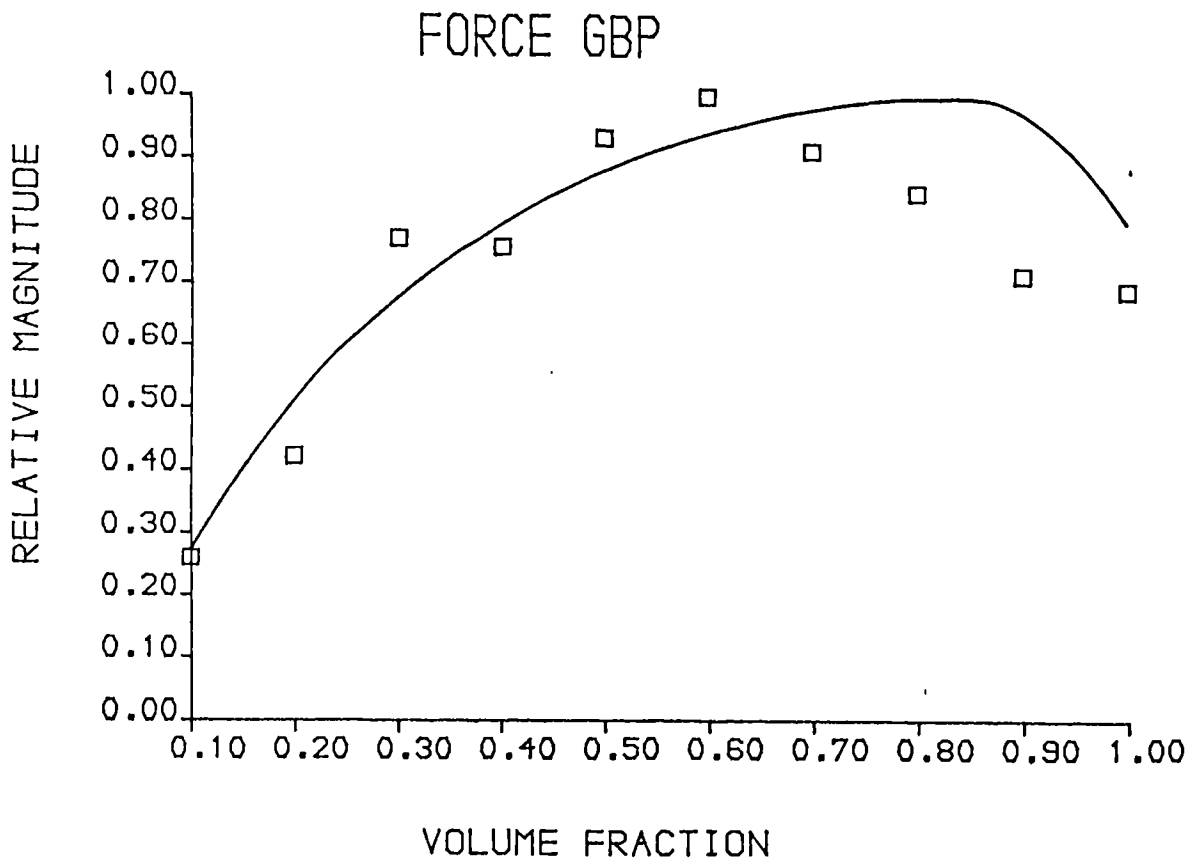


Figure 5.21 Normalised experimental and theoretical transmission GBP as a function of ceramic volume fraction (50Ω source impedance).
 Experimental \square
 Theoretical —

The experimental configuration has been simulated for each transducer using parameters predicted using the theory presented in section 5.2. The 50Ω source impedance of the generator and the 130pF capacitance in the connecting cables have also been included. The excitation level was 20V peak to peak and a twenty cycle sinusoidal burst used so that the steady state conditions could be obtained. Figure 5.20 indicates excellent correlation between the measured and simulated amplitude of CW force output at the frequency for which peak output is obtained. It is evident that volume fractions above 50% give the highest peak output. Although it is frequently assumed that lower volume devices are optimal, because they combine high coupling efficiency and low acoustic impedance, it is evident that their electrical characteristics reduce their output levels. The low capacitance and the improved acoustic match of low volume devices, results in high electrical impedance at resonance, which restricts the flow of current. The converse is true for the high volume devices. The inferior acoustic match of these transducers results in a sharply defined impedance minimum. They also possess an inherently higher capacitance which further reduces their electrical impedance.

The 90% device exhibits a disappointing response. This is because of the strong coupling of the thickness and lateral modes. This results in a complex, non-uniform vibrational characteristic and a consequent distortion of the impedance profile which restricts current flow, even

in the vicinity of the fundamental electrical resonant frequency. Therefore, the response of the 90% device is consistently poor for all the transmission, reception and pulse-echo tests. No further discussion of the poor response of the 90% transducer is made.

Figure 5.21 illustrates the force output Gain Bandwidth Product (GBP) of the transducers, plotted as a function of volume fraction. The GBP has been obtained from the product of peak CW force amplitude and the -3dB bandwidth, as a function of ceramic volume fraction. Transmission bandwidth is determined principally by the quality of the acoustic match to the load and therefore the low volume devices, with lower acoustic impedances, possess wider bandwidth for water loaded conditions. Hence, for increasing volume fractions, the peak CW force output increases, but the bandwidths reduce. Therefore, in terms of GBP, there is an optimum ceramic volume fraction which lies in the mid range. For the configurations examined here, the optimum is between 50% and 70% ceramic. There is a discrepancy between measured and simulated results at high volume fractions. This is probably due to experimental error associated with hydrophone alignment and the accuracy of the bandwidth measurement.

The peak force output was also measured and simulated for the case where the generator possesses a negligible output impedance. In practice, such a generator is impossible to realise because such a specification infers the ability to drive infinite currents. However, the 50 Ω output impedance

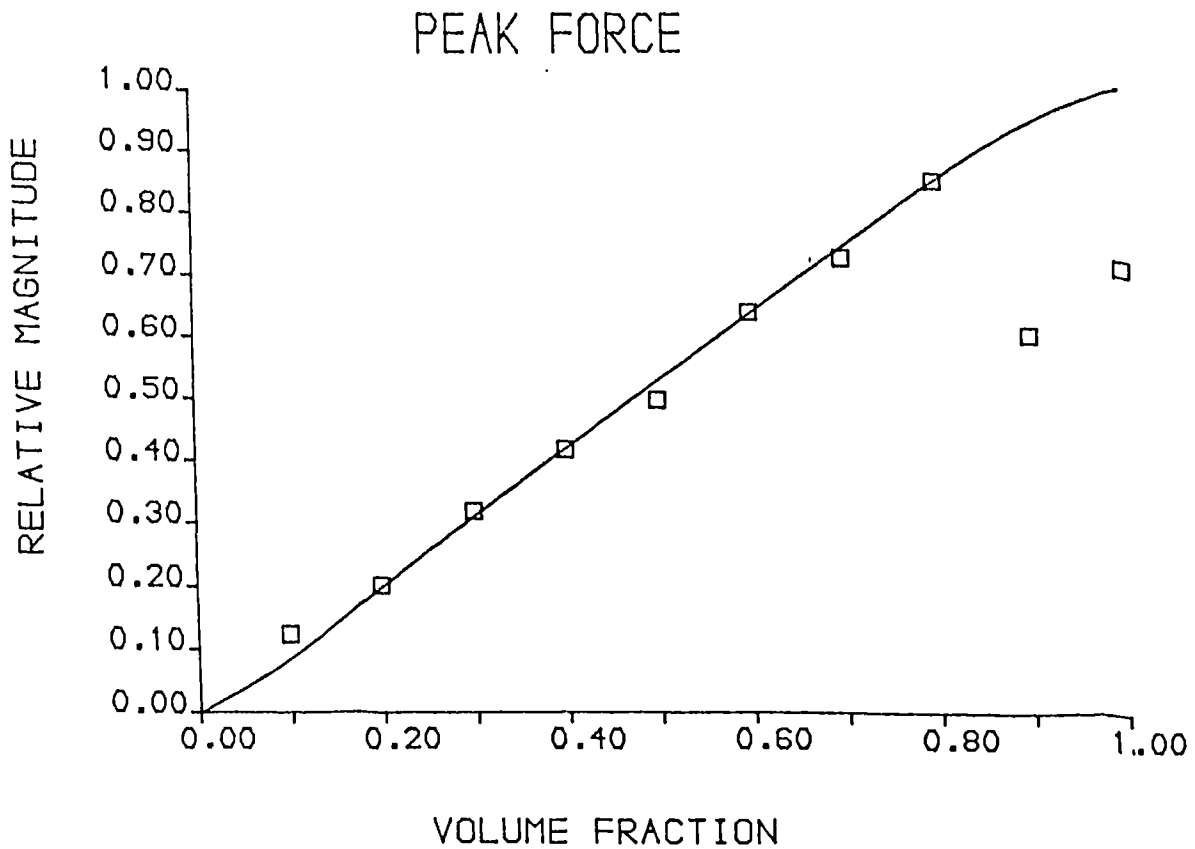


Figure 5.22 Normalised experimental and theoretical peak CW pressure output as a function of ceramic volume fraction (0Ω source impedance).
 Experimental \square
 Theoretical —

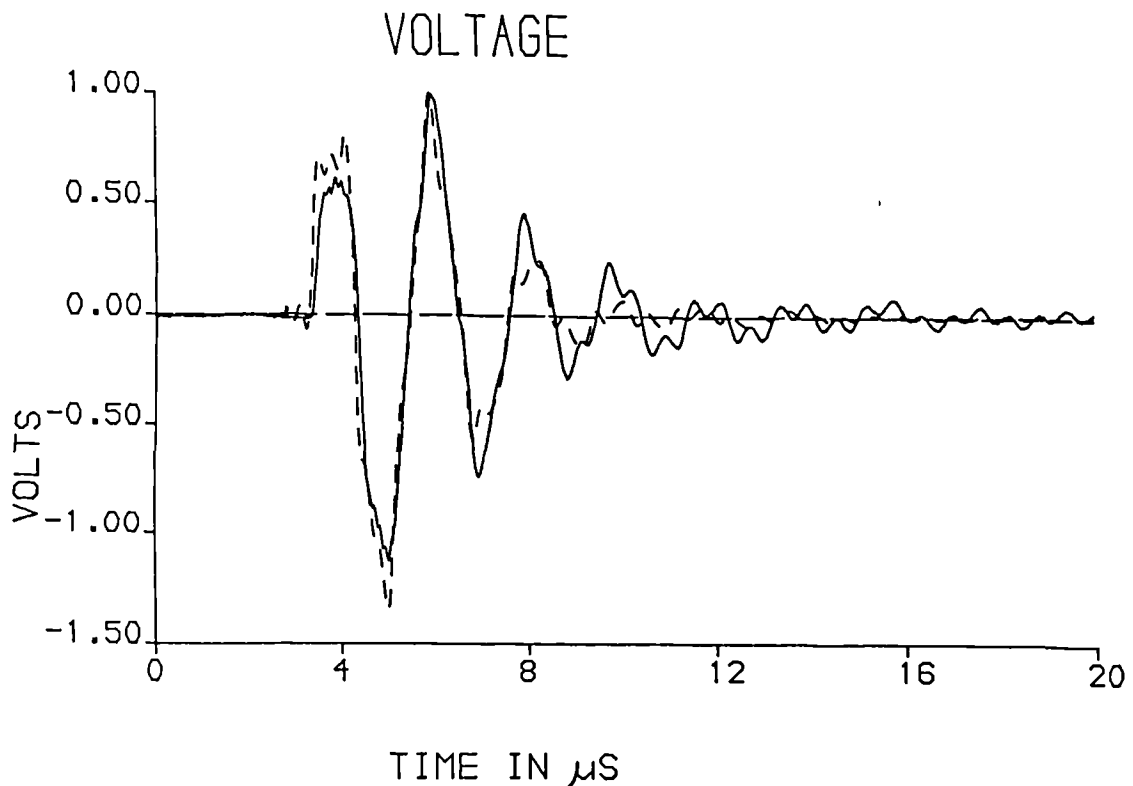


Figure 5.23 Normalised theoretical and experimental pressure response of a step excited, air backed, matched 60% 500kHz composite transducer operating into water.
 Experimental —
 Theoretical - - - - -

realise because such a specification infers the ability to drive infinite currents. However, the 50Ω output impedance of the generator can be effectively removed from the circuit by monitoring the voltage applied at the transducer terminals and adjusting the generator output control, and compensating for the voltage drop across the 50Ω output impedance. The simulated and measured results, for a 5V peak-peak excitation, are illustrated in Figure 5.22. In this configuration, the output level is essentially a linear function of volume fraction. In Figure 5.20, which is for a comparable configuration, except that the 50Ω output impedance is included, the peak force output levels off at higher volume fractions. This is because, at higher volume fractions, the impedance at resonance is less than 50Ω and therefore most of the available power is dissipated in the generator.

It is evident that the concepts of matched impedances and maximum power transfer are applicable to this type of configuration. The value of being able to model the influence of electrical source impedance on overall transducer operation is apparent.

5.6 iii) Transmission characteristics of composite transducers under transient excitation

For applications in ultrasonic imaging, transducers are normally excited via a rapid transient excitation step or impulse function. The spectrum of the pulse is sufficiently wideband that the pressure output of the transducer contains a combination of frequency components

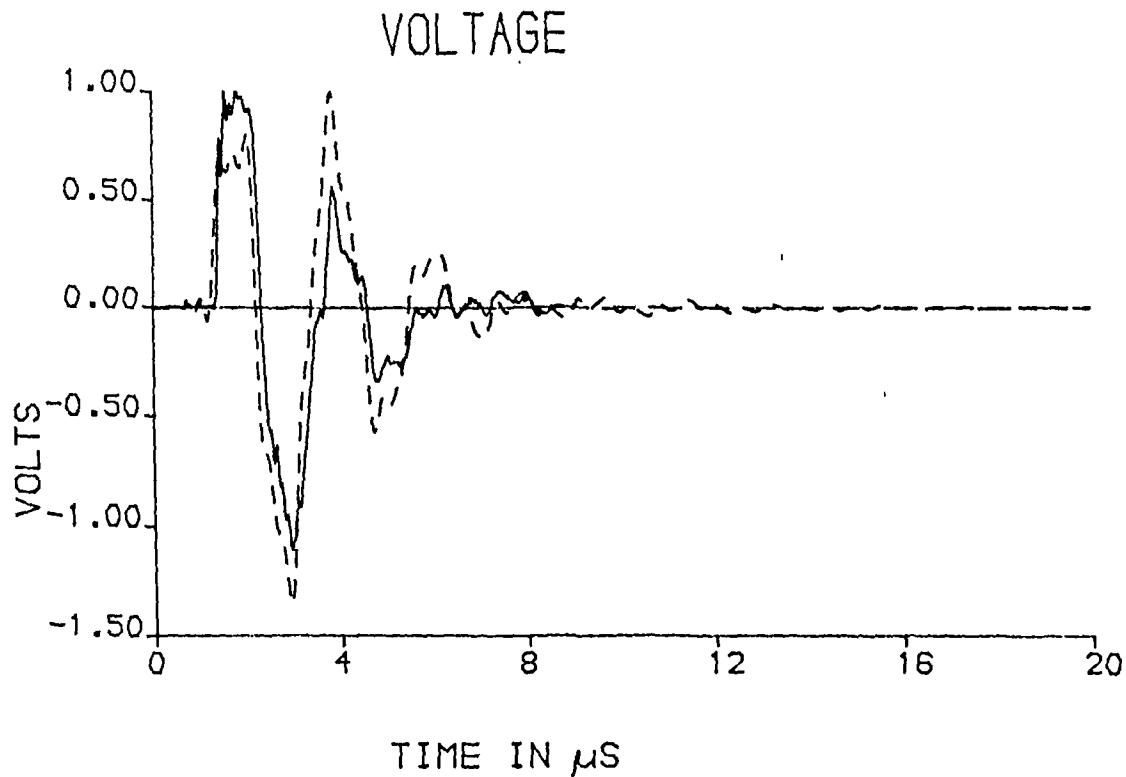


Figure 5.24 Normalised theoretical and experimental pressure response of a step excited, backed (10MRayl), matched 60% 500kHz composite transducer operating into water.
 Experimental —————
 Theoretical - - - - -

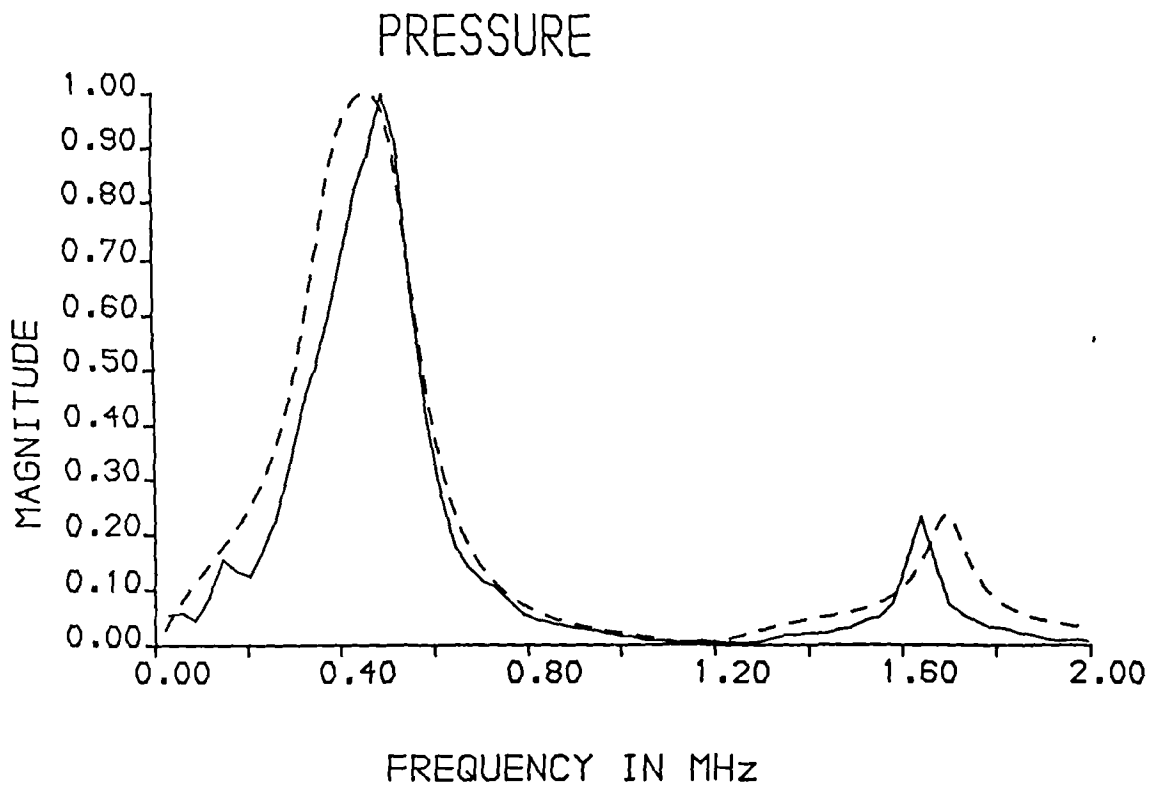


Figure 5.25 Normalised theoretical and experimental pressure response spectra of a step excited, backed, matched 60% 500kHz composite transducer operating into water.
 Experimental —————
 Theoretical - - - - -

determined by the response of the transducer. The pulse shape is also governed by the electrical and mechanical loading of the transducer. Therefore, a comparison between modelled and simulated time domain transiently excited responses represents a critical test of the accuracy of the transducer model. The specification of the pulser circuit used for this section is described in Appendix E.

Figure 5.23 illustrates the simulated and measured pressure output of an airbacked, matched 60% 500kHz transducer. In this, and in all subsequent figures illustrating measured or simulated wave profiles, the time scaling is respect to an arbitrary instant shortly before the arrival of the signal at the receiving probe. The excitation of the device normally occurs at an instant long before the arrival of signal at the receiver and hence it is not practical to use the time of excitation as the time origin in these plots. The correlation between the results indicates that the model has correctly simulated the physical phenomena occurring in this configuration. Figure 5.24 illustrates the correspondence of the measured and simulated responses of a 60% backed and matched transducer. As expected, both measured and simulated responses reveal an increase in the mechanical damping of the system due to the backing. This has resulted in more wideband, shorter response. The simulated and measured pressure output spectra of the 60% backed and matched transducers are compared in Figure 5.25. Again, good correlation may be observed.

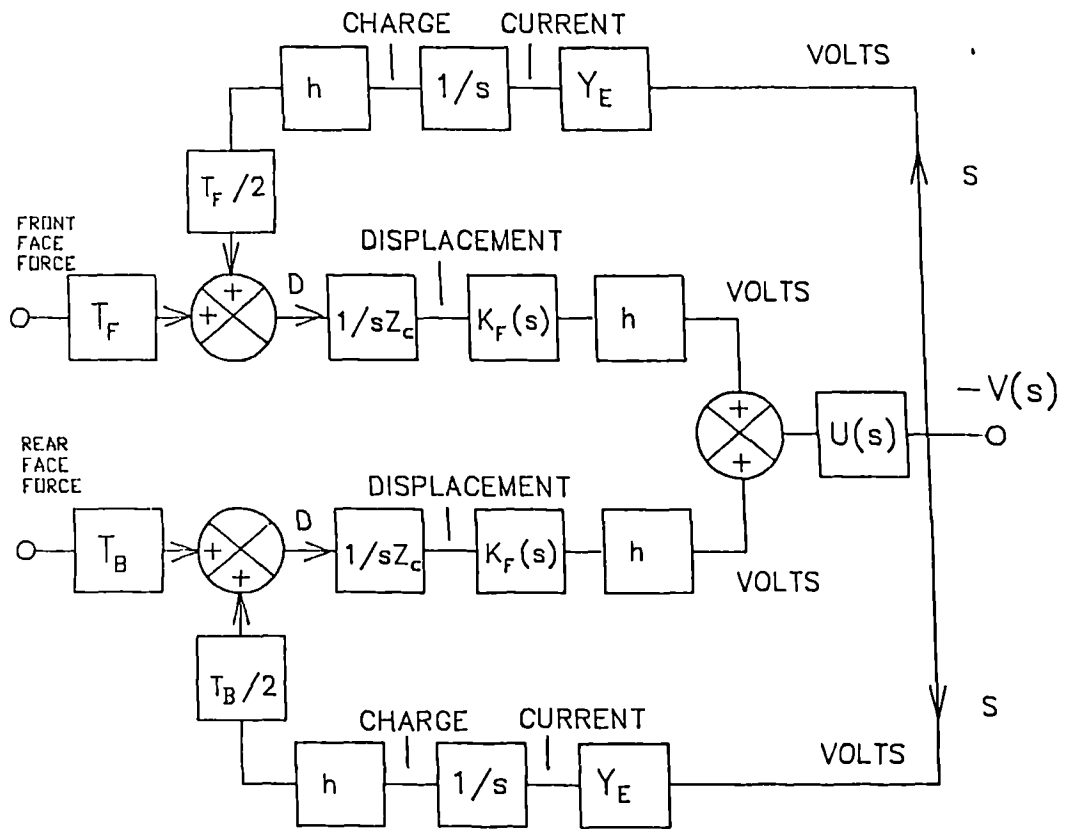


Figure 5.26 Receiver transducer model in block diagram format

5.7 MODELLING THE RECEPTION CHARACTERISTICS OF A COMPOSITE PIEZOELECTRIC TRANSDUCER.

5.7 i) General reception model

The thickness mode transducer model may be configured as illustrated in Figure 5.26. All symbols have the same physical definitions as those used in section 5.5. The paths marked 'D' represent the Direct piezoelectric effect from displacement to voltage. The electrical load factor influences both the actual output terminal voltage and the extent of Secondary action, which is described by the paths marked 'S'. As in the case of the transmitter, it is clear that the extent to which secondary action will influence the overall transfer function is governed by both electrical and mechanical loading and internal device characteristics. The model is equally valid for transient, wideband analyses and for CW analyses.

5.7 ii) Reception characteristics of composite transducers under CW excitation

The model has been used to investigate the reception characteristics of the ten different transducers described in section 5.2 for two different electrical loading conditions. A calibrated wideband matched and backed composite transmitter was used as the source. The calibration of this source, and the experimental apparatus employed for measuring the 'reception characteristics are described in Appendix E.

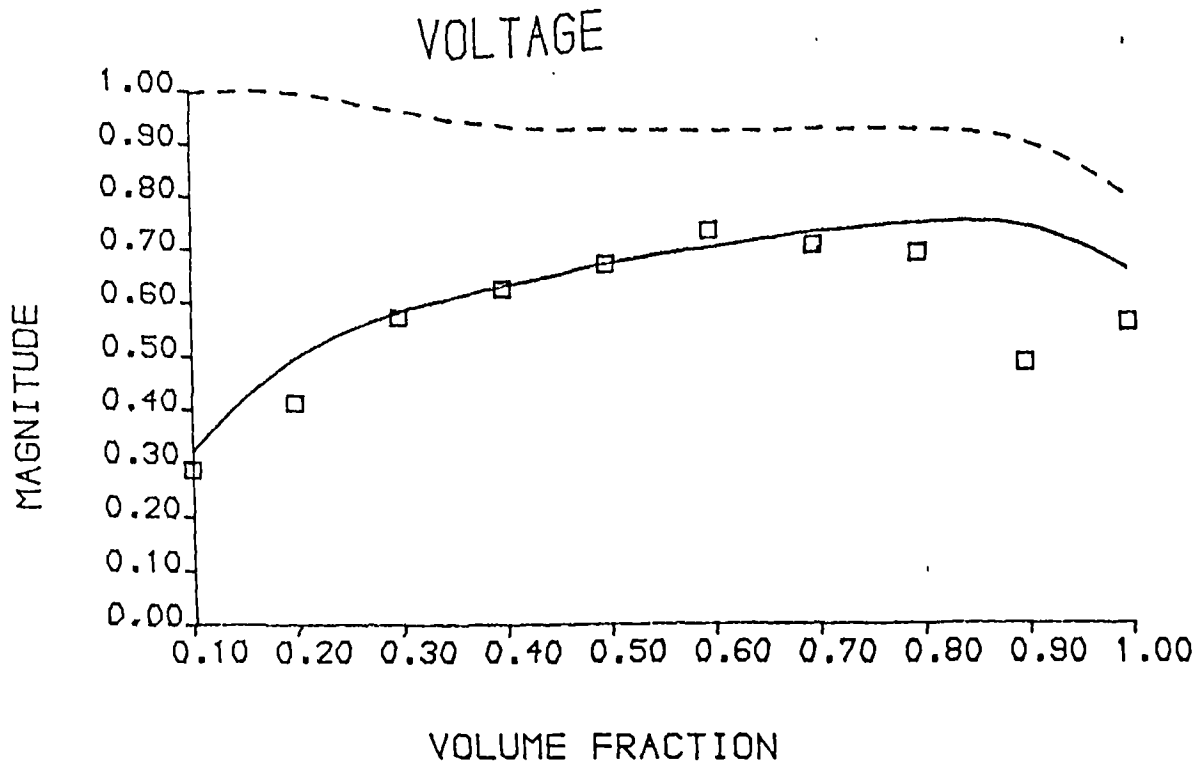


Figure 5.27 Normalised experimental and theoretical peak CW reception sensitivity as a function of ceramic volume fraction ($1M\Omega$ load).

Experimental □
 Theoretical - including cable effects - $130pF$ —————
 Theoretical - excluding cable effects - - - - -

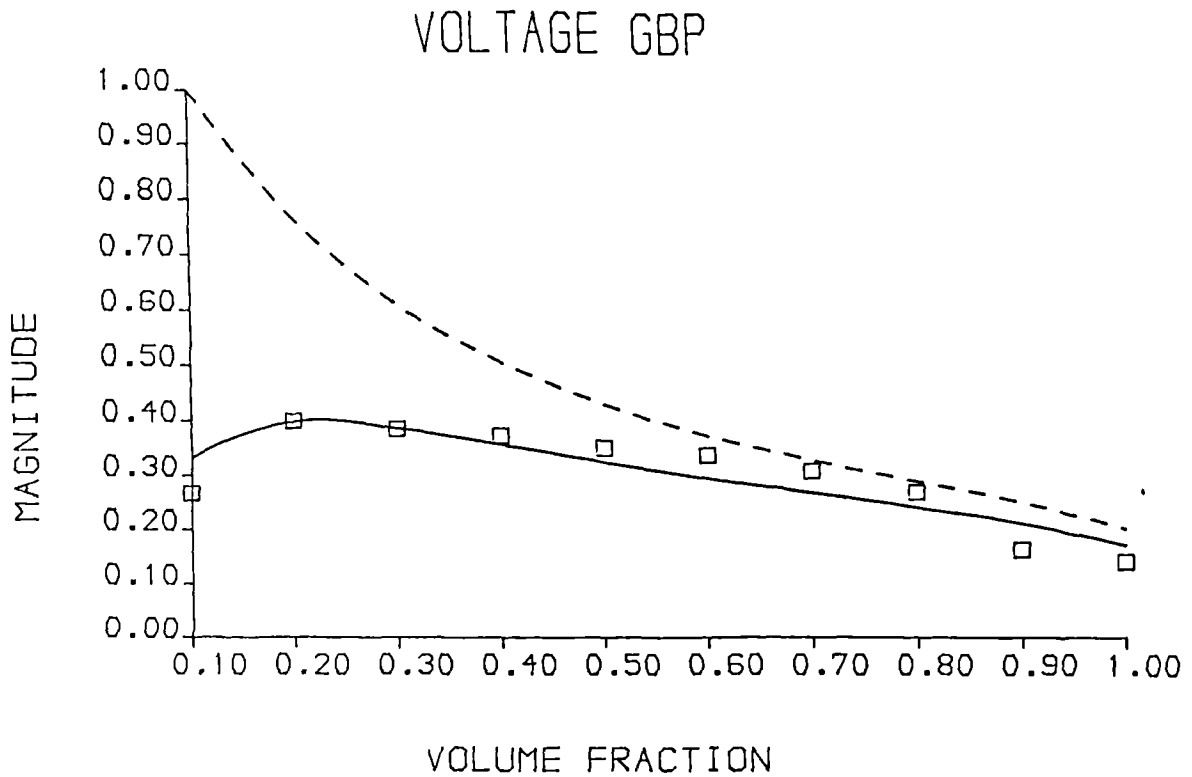


Figure 5.28 Normalised experimental and theoretical reception GBP sensitivity as a function of ceramic volume fraction ($1M\Omega$ load).

Experimental □
 Theoretical - including cable effects - $130pF$ —————
 Theoretical - excluding cable effects - - - - -

Figure 5.27 illustrates the measured and simulated peak CW reception characteristics of the ten transducers operating into a $1M\Omega$ impedance and including a measured cable capacitance of 130pF. The curve indicates reasonable correlation between measured and simulated results. However, it is surprising in that the lower volume fraction devices would be expected to exhibit the greatest sensitivity due to their lower acoustic impedance. The result shown here, with reducing sensitivity at low volume fractions, is caused by unavoidable electrical loading due to the cable. The dashed line indicates the response that could be expected in the absence of cable losses. As expected, the lower volume devices exhibit greater sensitivity in this case.

The measured and simulated reception gain bandwidth product is shown in Figure 5.28. Again, satisfactory experimental corroboration has been achieved. For increasing volume fractions, the degree of acoustic matching between transducer and load reduces and therefore bandwidth reduces. The simulated response, ignoring cable capacitance losses, indicates that more severe electrical loading is occurring in the lower volume devices. It is worth stressing that electrical loading influences bandwidth as well as sensitivity. In general, increased loading results in a greater bandwidth, achieved at the expense of reduced peak sensitivity.

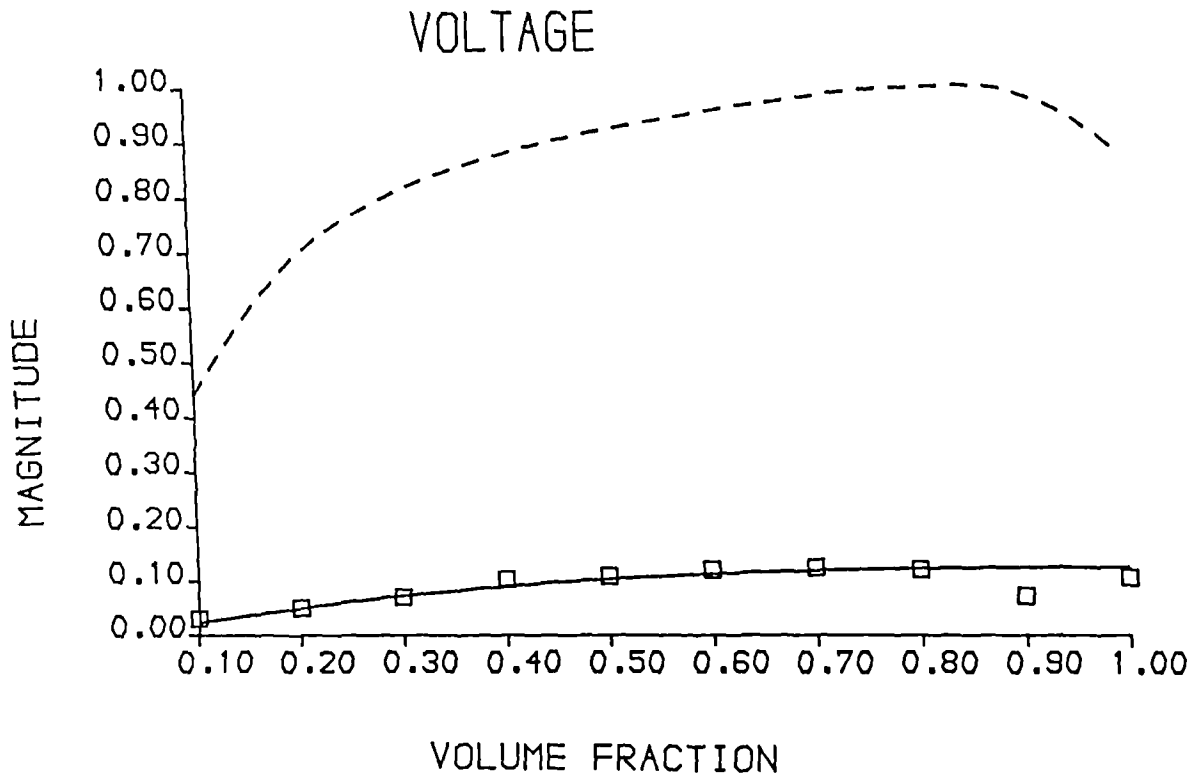


Figure 5.29 Normalised experimental and theoretical peak CW reception sensitivity as a function of ceramic volume fraction ($1M\Omega$ and 100Ω load).
 Experimental - 100Ω □
 Theoretical - 100Ω —
 Theoretical - $1M\Omega$ ---

The reception sensitivity of the transducers, operating into a 100Ω load, including also a cable capacitance of 130pF , is compared to the result for a $1\text{M}\Omega$ load in Figure 5.29. The loading effect is readily apparent and it should be noticed that, in this case, the pure ceramic device possesses a greater sensitivity than any of the composite transducers.

These results highlight the importance of minimising electrical loading effects when composite transducers are being used. They also serve to demonstrate the accuracy and versatility of the model. In particular, the effect of loading and matching components, on sensitivity and bandwidth, may be analysed.

5.8 PULSE-ECHO CHARACTERISTICS OF A COMPOSITE PIEZOELECTRIC TRANSDUCER

5.8 i) General pulse-echo model

The pulse-echo transducer configuration is the most important from a practical viewpoint. Obviously, it is defined by the combination of transmission and reception characteristics. It is therefore simulated by employing the model to firstly predict the pressure output for a given excitation, and then using this pressure function as the input to the same transducer operating as a receiver. There are number of important points which are worth emphasising.

1. A transducer may be optimised for transmission or reception. For pulse-echo operation, a compromise is required. Alternatively, but rarely implemented, separate source and receiver transducers should be used.
2. The electrical matching circuitry used in reception is completely different from the transmission circuitry. In practice, a high input impedance amplifier, protected from the transmission pulse by diodes, is commonly employed.
3. The frequencies of peak transmission and peak reception sensitivity rarely coincide. In the absence of loading, peak transmission occurs at the electrical resonant frequency (impedance minimum) and peak reception sensitivity at the mechanical resonant frequency (impedance maximum). Loading has the effect of reducing the difference between these two frequencies. However,

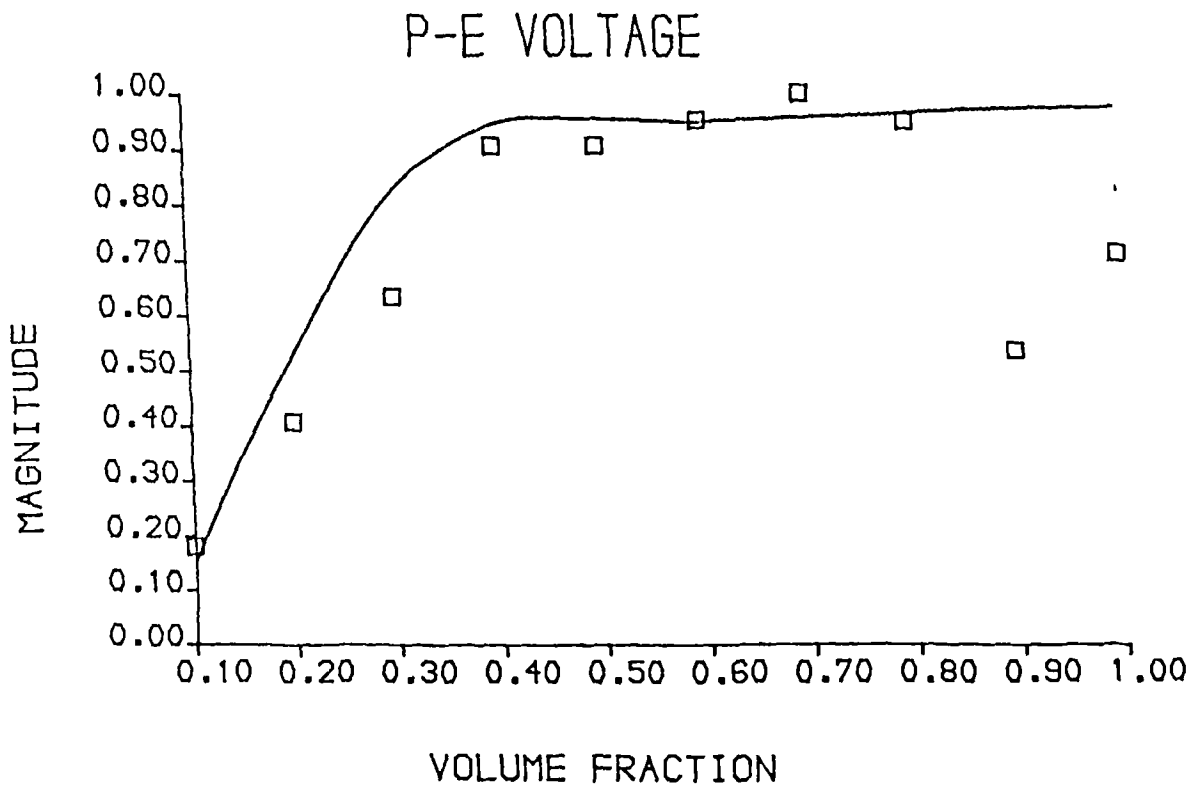


Figure 5.30 Normalised experimental and theoretical peak CW pulse-echo response as a function of ceramic volume fraction (50Ω source, $1M\Omega$ load and cable - $130pF$).

Experimental \square
 Theoretical —————

the effect of this loading depends on the transducer material and shape.

4. Acoustic diffraction may distort the pressure function in the field. These effects are discussed in greater detail in Chapter VI and in the literature. For the present, diffraction effects are neglected. This assumption is only valid if an ideal reflector, placed exactly perpendicular to the acoustic beam, and outwith the acoustic nearfield, is used. In the experiments a large, thick crown glass reflector was used.

5.8 ii) Pulse-echo characteristics of composite transducers under CW excitation.

The peak CW pulse echo sensitivity of the ten transducers is compared to the theoretical results in Figure 5.30. A cable capacitance of 130pF is included, but the excitation signal was monitored and the effect of the 50 Ω source compensated. That is, the excitation signal at the transducer terminals, was maintained constant. The experimental apparatus which was employed is described in Appendix E. The curve indicates that pulse-echo sensitivity, in this case, rises to a plateau level at around 40%. The experimental results for the 90% and 100% transducers are probably low because of complex parasitic vibrational activity, which is minimal in the lower volume devices. The results for transmission efficiency, and

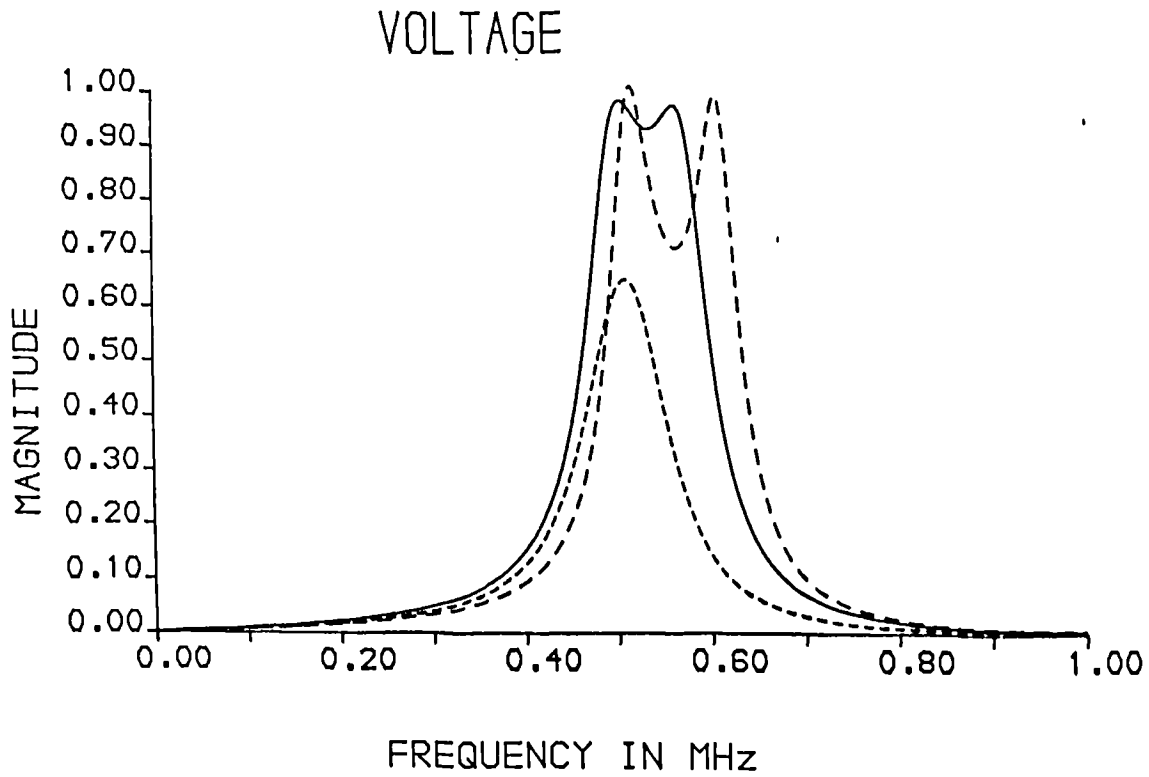


Figure 5.31 Normalised theoretical pulse-echo magnitude for three different composite devices
 Ceramic volume fraction = 20% -----
 Ceramic volume fraction = 50% _____
 Ceramic volume fraction = 80% - . - . - .

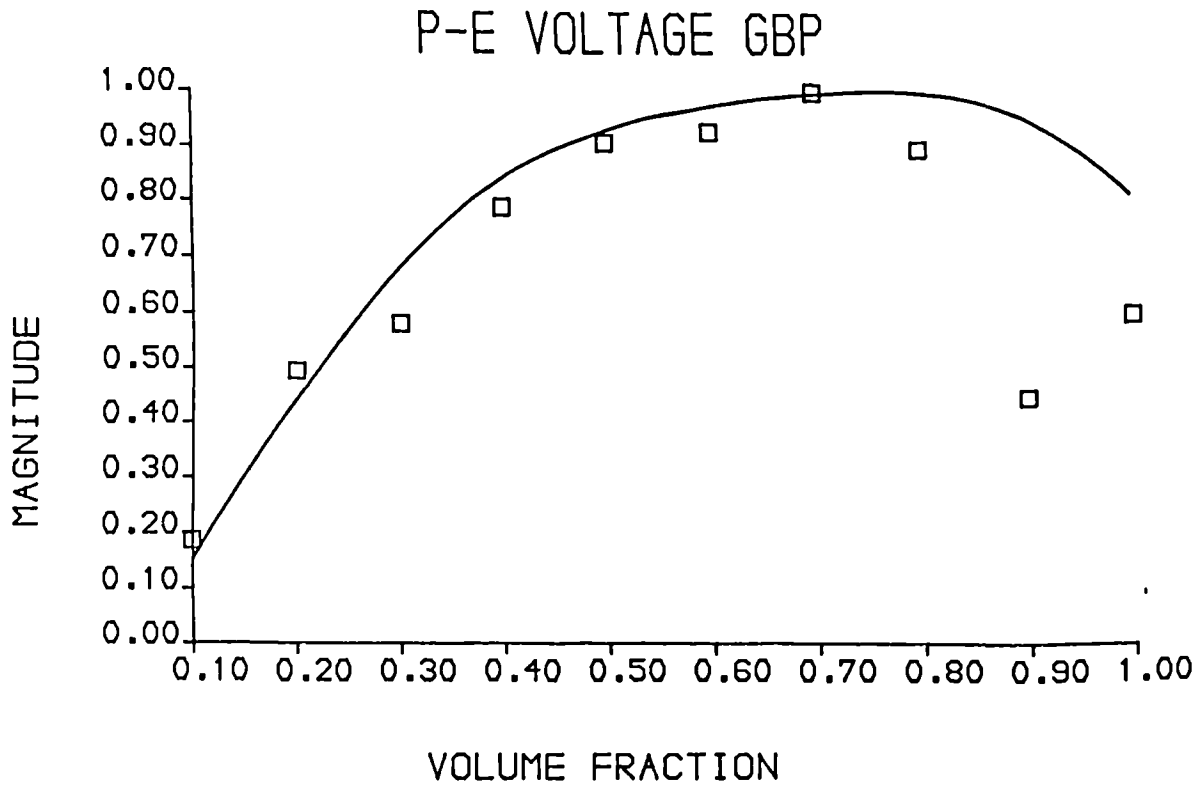


Figure 5.32 Normalised experimental and theoretical pulse-echo GBP response as a function of ceramic volume fraction (50Ω source, 1MΩ load and cable - 130pF).
 Experimental □
 Theoretical _____

reception sensitivity, considered separately, would suggest a curve which would rise steadily with increasing volume fraction. In fact, the frequencies of peak transmission and reception efficiency diverge, resulting in the curve shown. The pulse-echo magnitude spectra for the 30%, 50% and 70% transducers are shown in Figure 5.31. The 70% curve exhibits a distinct double peak, which is not apparent in the 30% curve. It is evident that these effects will also distort the measured bandwidth.

The pulse-echo gain bandwidth product curve for the ten transducers is illustrated in Figure 5.32. On the basis of Figure 5.30, which indicates that high sensitivity is obtained at a 40% ceramic volume fraction, it would be expected that the reducing bandwidth at higher volume fractions would imply that the optimal gain bandwidth product would occur at approximately 40%. However, this is not the case, because, as previously discussed, the distinct frequencies of peak transmission and peak reception efficiency distort the effective bandwidth. In fact, for this loading case, optimal pulse echo gain bandwidth product occurs at a 70% volume fraction.

The complexity of the actual pulse-echo sensitivities, and bandwidths, is apparent. Clearly, the effect of electrical source impedance and receiver input impedance may also be analysed. However, for the sake of brevity, and avoiding repetition of previous discussion, this work is not presented here. However, it is worthwhile briefly considering the pulse-echo characteristics of

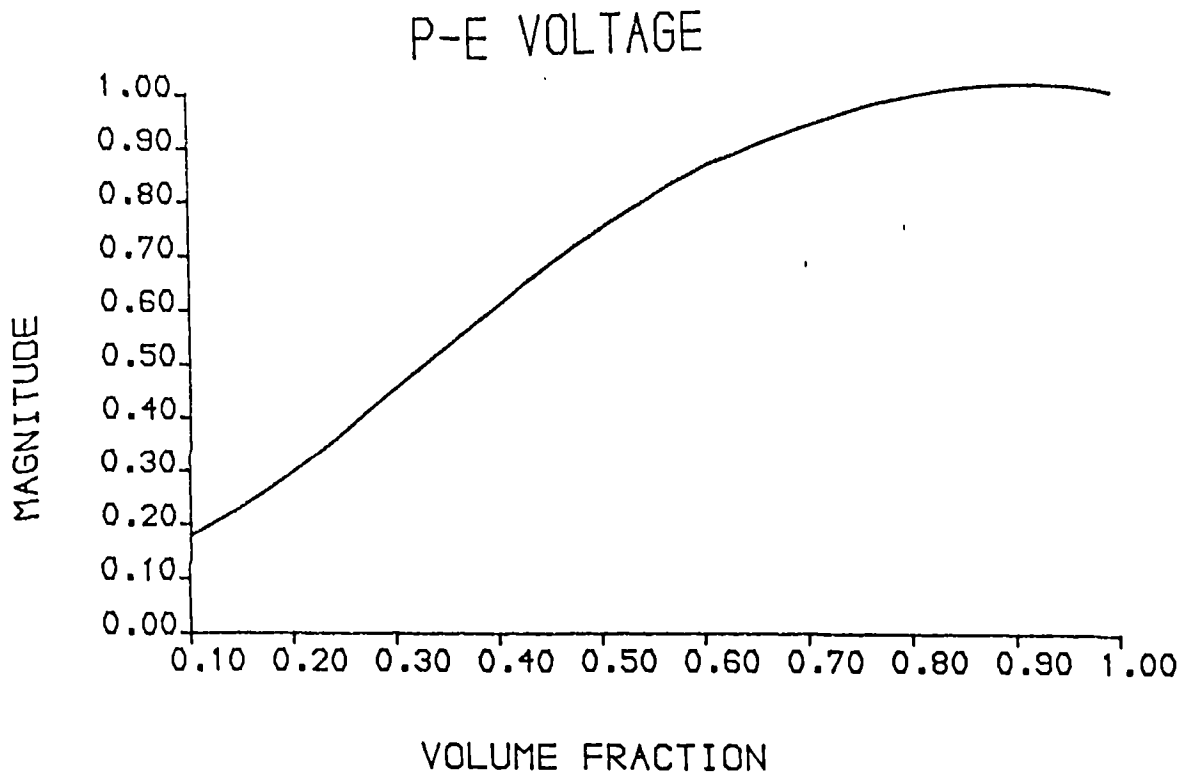


Figure 5.33 Normalised theoretical peak CW pulse-echo response as a function of ceramic volume fraction. Backing 7MRayl, 50Ω source/ 1MΩ receiver impedance.

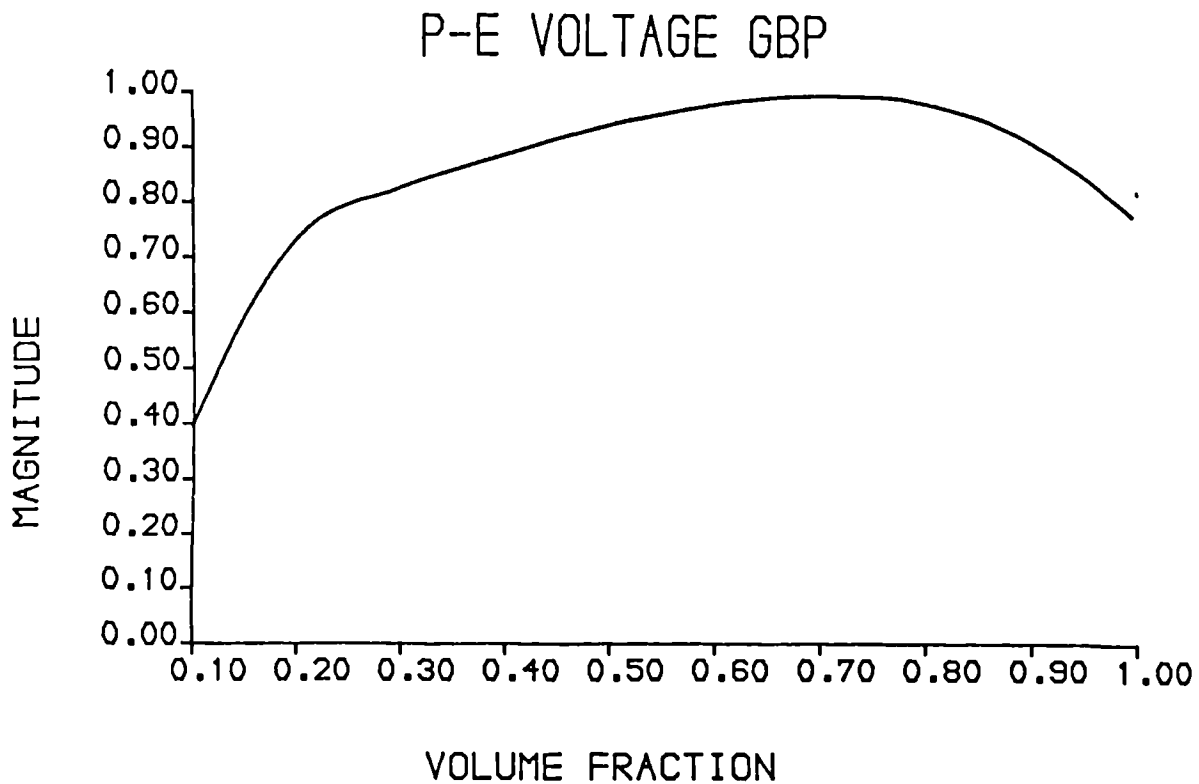


Figure 5.34 Normalised theoretical pulse-echo GBP response as a function of ceramic volume fraction. Backing 7MRayl, 50Ω source/ 1MΩ receiver impedance.

mechanically loaded transducers. Mechanical loading broadens the bandwidth to such an extent that the twin peaking in the pulse-echo spectral characteristics are effectively smeared out. Therefore, this undesirable variable is effectively removed from the design problem.

Figure 5.33 illustrates the simulated peak pulse-echo sensitivities of the ten transducers previously considered, except that in this case, a backing impedance of 7 MRayl is used, although, in practice, heavier backings are generally used. However, if the backing impedance is higher than the impedance of the transducer material, then quarter wavelength, rather than half wavelength, resonance results. Clearly, this will distort sensitivity and bandwidth measurements. These results were obtained for a source impedance of 50Ω and a receiver load impedance of $1M\Omega$. The effect of the 50Ω source impedance is negligible in this case, since the impedance of these backed transducers are greater than $1K\Omega$, even in the vicinity of resonance. Figure 5.33 indicates that peak CW pulse-echo sensitivity increases with increasing volume fraction, and is therefore similar to that which could be predicted from the transmission and reception characteristics taken separately. Figure 5.34, which depicts the pulse-echo gain bandwidth product for these configurations, indicates that the lower volume fraction devices have a greater bandwidth, and hence this is compensating, to a certain extent, for their lower peak sensitivity.

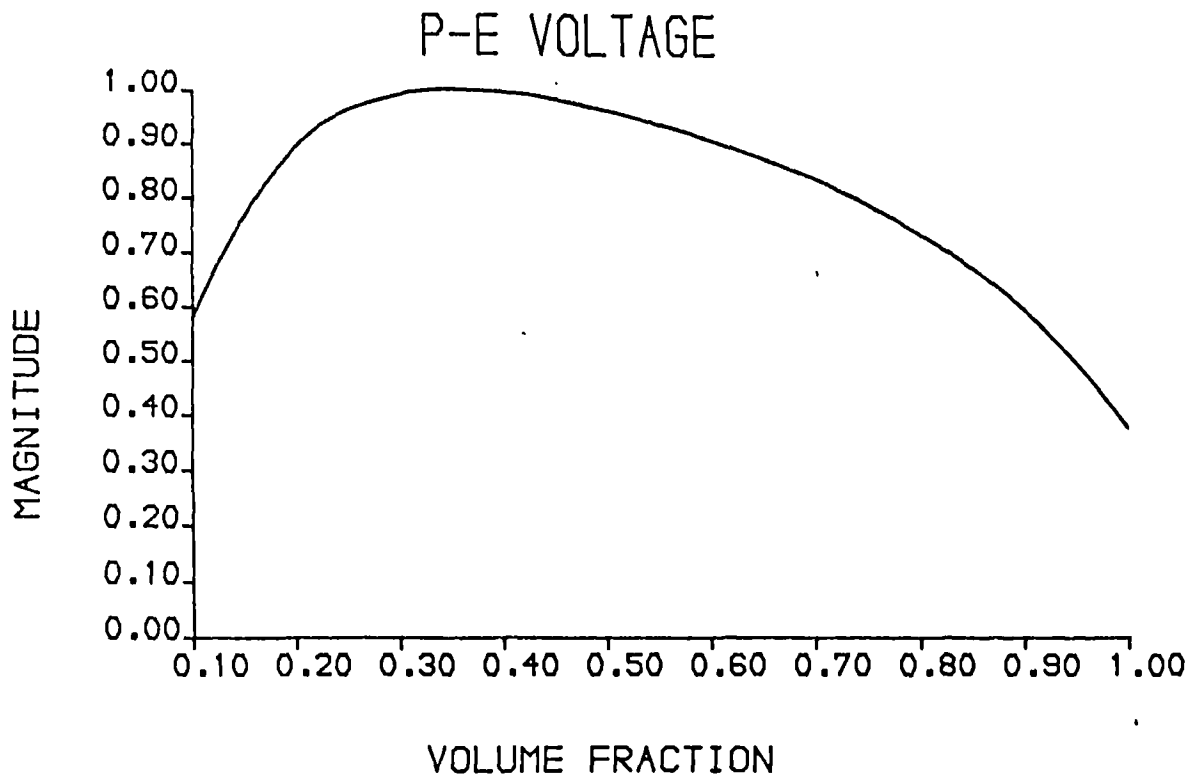


Figure 5.35 Normalised theoretical peak CW pulse-echo response as a function of ceramic volume fraction. Backing impedance = Transducer impedance, 50Ω source impedance, $1M\Omega$ receiver impedance.

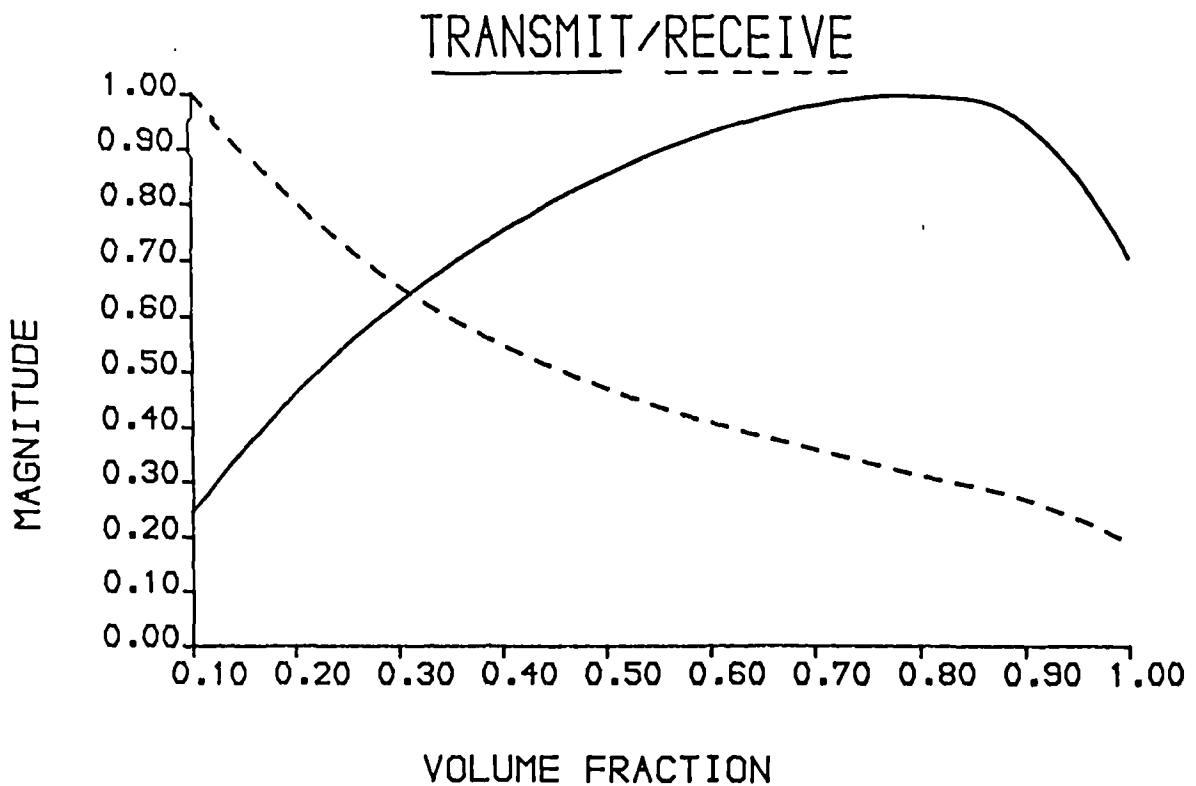


Figure 5.36 Normalised theoretical peak CW transmission/reception level as a function of ceramic volume fraction. Backing impedance = Transducer impedance. 50Ω source impedance, $1M\Omega$ receiver impedance.

Finally, the dependence of pulse-echo sensitivity on volume fraction for matched backed transducers is considered. In this case, each transducer is simulated with a backing impedance equivalent to its own impedance. In practice, it is difficult to produce well controlled, lossy backings with acoustic impedances higher than approximately 15 MRayl. Figure 5.35 illustrates the dependence of peak CW pulse-echo sensitivity on volume fraction. The gain bandwidth curve, which is not shown, is virtually identical because the bandwidths of all the transducers are very similar. Figure 5.35 indicates that the optimum volume fraction for these conditions is in the range 30% to 40%. This result may be explained by considering the transmission and reception characteristics for the same geometry and loading separately, as illustrated in Figure 5.36. Transmission efficiency increases with volume fraction, but decreases slightly at the upper end due to reducing coupling efficiency and acoustic matching. However, the reception characteristics indicate that low volume fraction transducers possess the highest sensitivity. Therefore, the compound effect of the two characteristics is as shown in Figure 5.35. Notice, that electrical effects are negligible in these cases because the source resistance is negligible and the receiver input impedance extremely high.

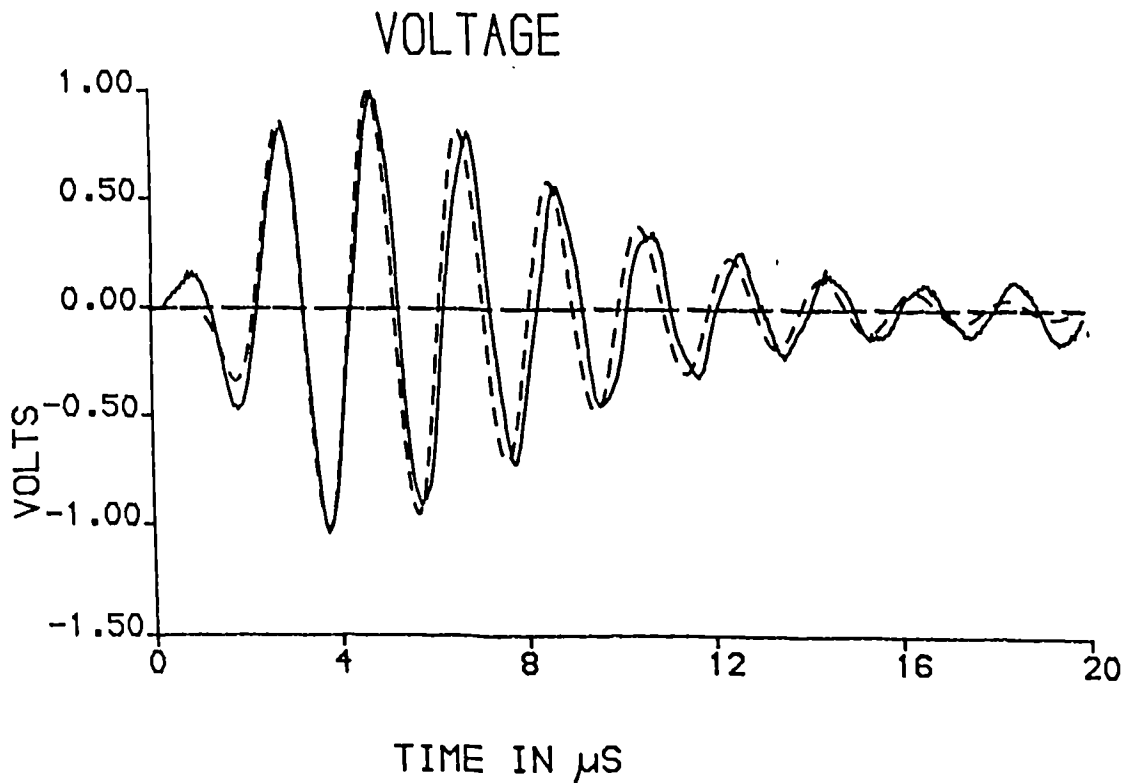


Figure 5.37 Normalised theoretical and experimental pulse-echo response of a step excited, air backed 40% composite operating into water. (No matching)
 Experimental —————
 Theoretical - - - - -

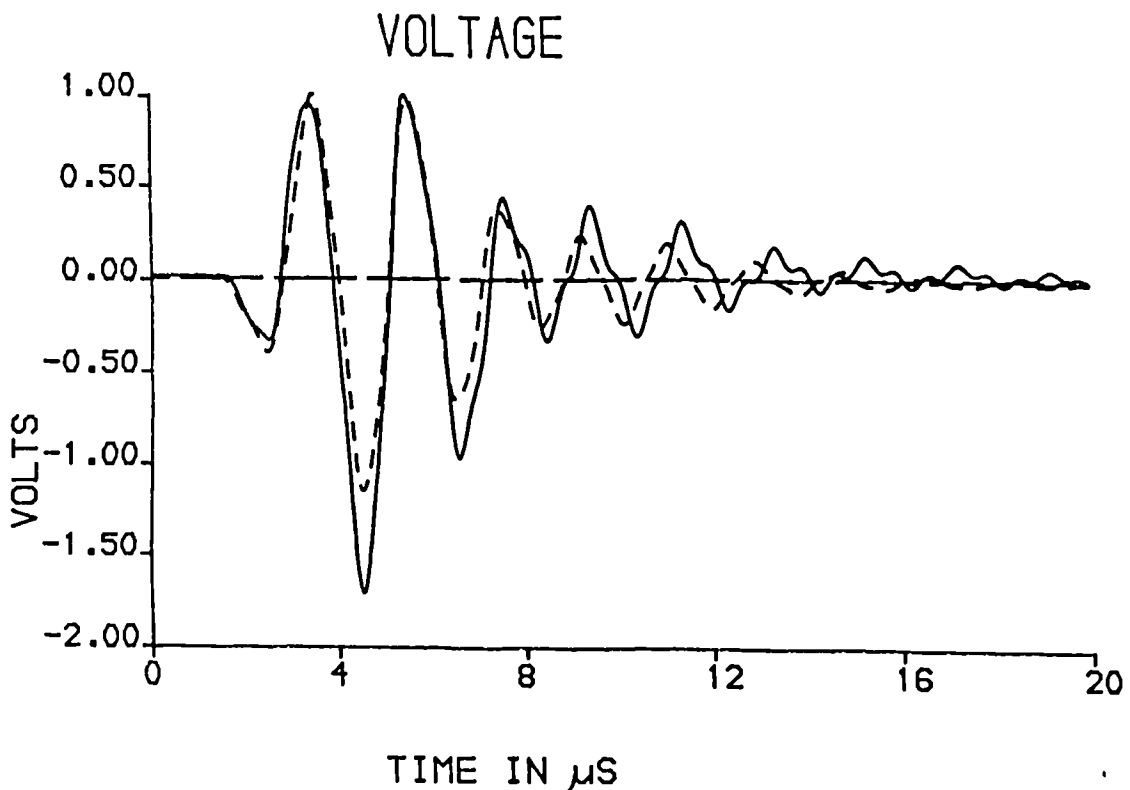


Figure 5.38 Normalised theoretical and experimental pulse-echo response of a step excited, air backed 40% composite operating into water via a quarter wavelength epoxy matching layer.
 Experimental —————
 Theoretical - - - - -

5.8 iii) Pulse-echo characteristics of composite transducers under transient excitation

The model may be employed to predict the pulse-echo waveform for a given impulsive excitation. The excitation circuitry and experimental apparatus described in Appendix E has been employed.

Figure 5.37 illustrates the measured and simulated response of a 40% transducer operating into water without either matching or backing. Excellent correlation between results may be observed. This experiment was repeated with the same transducer after a quarter wavelength epoxy matching layer had been applied, and the pulse-echo response shown in Figure 5.38 was obtained. Fortunately, epoxy possesses an almost ideal acoustic impedance for a matching layer in this case. Again, good correspondence may be observed and the effect of the widened bandwidth is apparent from the reduced pulse length of this pulse.

For optimum bandwidth, a heavy lossy backing should be provided. Figure 5.39 illustrates the measured and simulated response of the 40% volume fraction transducer after a lossy tungsten loaded backing had been moulded to the rear of the transducer. The acoustic impedance of this backing material is 10 MRayl. Figure 5.40 illustrates the measured and simulated pulse-echo responses of a 60% volume fraction backed and matched transducer. The reduced bandwidth of this device, caused by its inferior acoustic match to both backing and load medium, is evident.

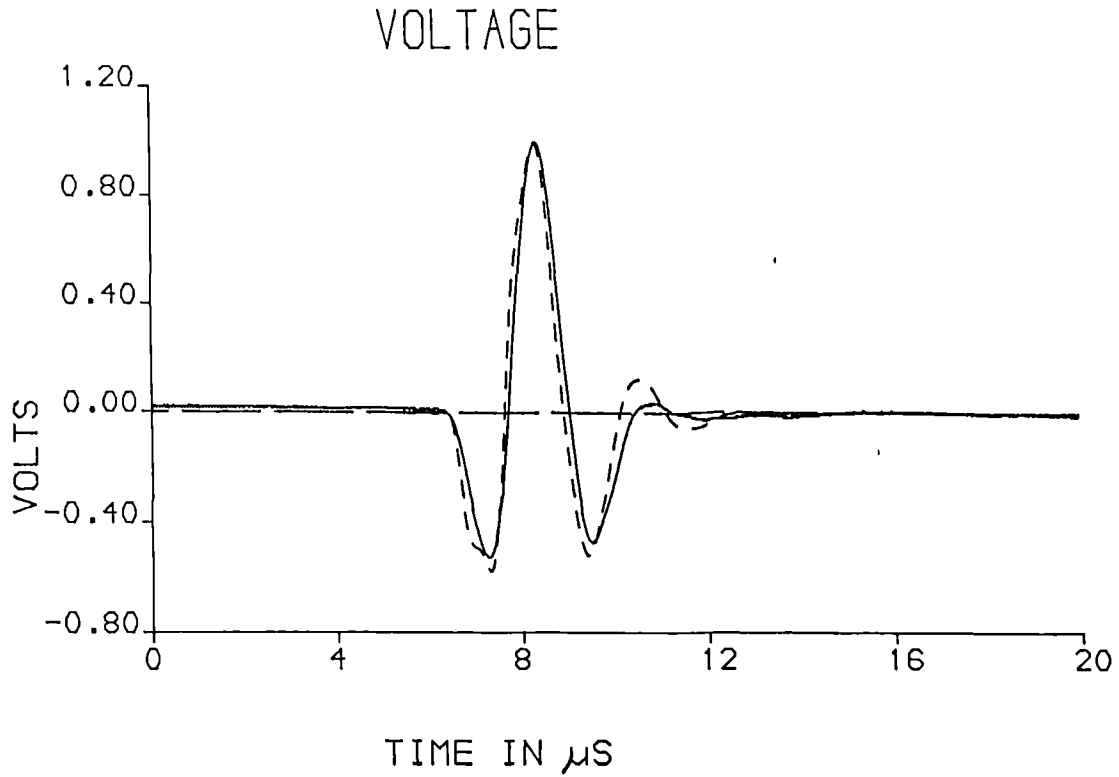


Figure 5.39 Normalised theoretical and experimental pulse-echo response of a step excited, backed (10MRayl) 40% composite operating into water via a quarter wavelength epoxy matching layer.
 Experimental —————
 Theoretical - - - - -

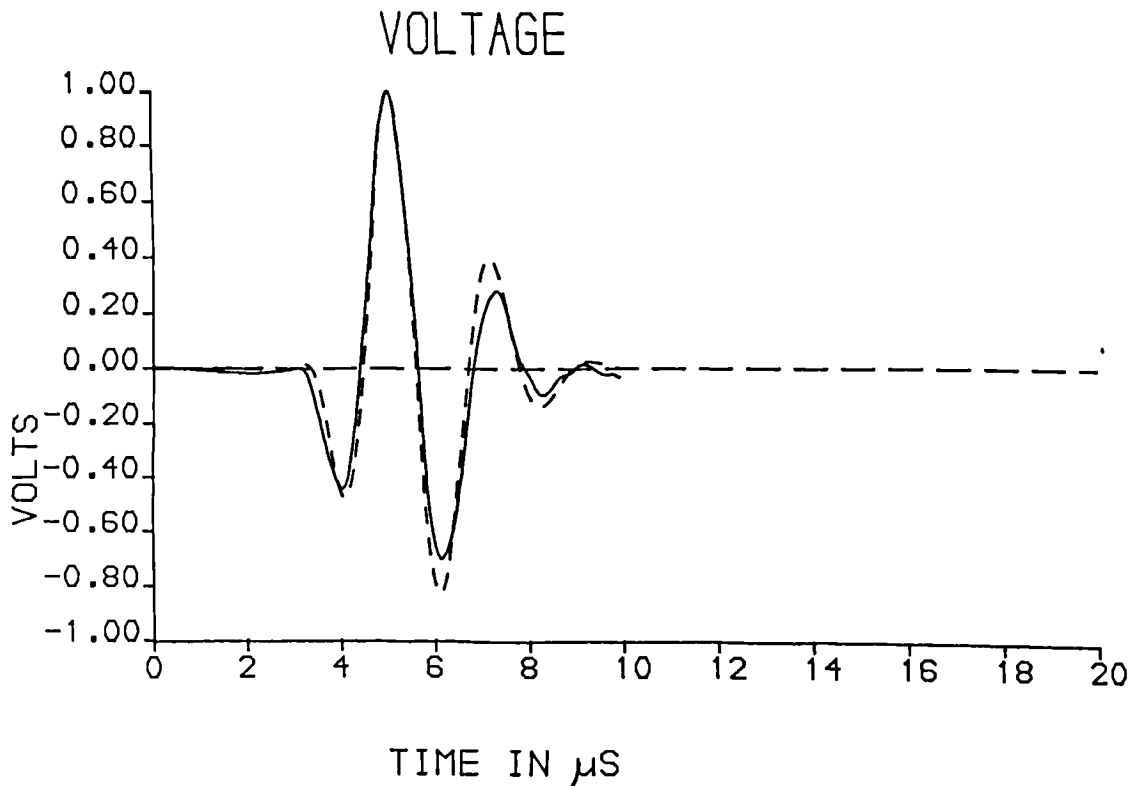


Figure 5.40 Normalised theoretical and experimental pulse-echo response of a step excited, backed (10MRayl) 60% composite operating into water via a quarter wavelength epoxy matching layer.
 Experimental —————
 Theoretical - - - - -

5.9 CONCLUDING REMARKS

A comprehensive model for predicting impedance, transmission, reception and pulse-echo characteristics of a composite transducer has been developed. It assumes that the transducer is behaving as a pure thickness mode resonator and this assumption should be verified by finite element analysis or by some other means. Propagation loss is included, as are the effects of electrical and mechanical loading. This model has been comprehensively verified and is therefore a valuable tool in the evaluation of new transducer designs. In particular, it has demonstrated that device performance is a highly complex function of transducer material, geometry, mechanical and electrical loading. Although, some general guidelines may be extracted, the work emphasises the value of analysing each design individually and completely.

CHAPTER VI

ELECTROMECHANICAL AND SPATIAL FIELD CHARACTERISTICS
OF COMPOSITE ARRAYS

6.1 INTRODUCTION

Ultrasonic transducer arrays are widely applied to imaging tasks in biomedicine, sonar and NDE. However, the capability of array imaging systems is frequently limited by the quality of the ultrasonic data produced by the transducers. Fortunately, composite materials possess a number of characteristics which make them, in some respects, superior to conventional ceramic materials. The limited amount of published literature on the use of composite materials in arrays [4,21] indicate that good spatial response may be obtained. However, it is apparent that the observed spatial field and electromechanical characteristics of composite array elements are a complex function of geometry and constituent materials. In certain cases, the spatial field performance of composite materials have been disappointing [22].

The objective of this chapter is to investigate comprehensively the dependence of both the spatial field and electromechanical characteristics of composite array elements. Ultimately, this will facilitate better design of practical composite arrays.

Initially, simple array imaging strategies are reviewed and the requisite characteristics of transducer arrays outlined. Thereafter, the theoretical and practical spatial characteristics of composite array elements are investigated. In particular, the presence of non-uniform vibration and laterally propagating waves are considered. A novel diffraction model is presented for efficiently,

and accurately, determining the near field characteristics of rectangular array elements. This model is particularly well suited to the analysis of the fields of two dimensional (2-D) array elements.

The dependence of the electromechanical parameters of composite array elements is thoroughly investigated as functions of constituent material, geometry of composite structure and the width of the element in terms of the number of active rows of pillars. These results will indicate which configurations are best suited to practical transducer arrays.

The electromechanical, spatial field and imaging performance of practical composite arrays are compared with those of conventional sliced ceramic and monolithic ceramic arrays. Finally, theoretical and practical results relating to a prototype 2-D composite array are presented. The characteristics of composite materials makes them particularly well suited to use in 2-D arrays.

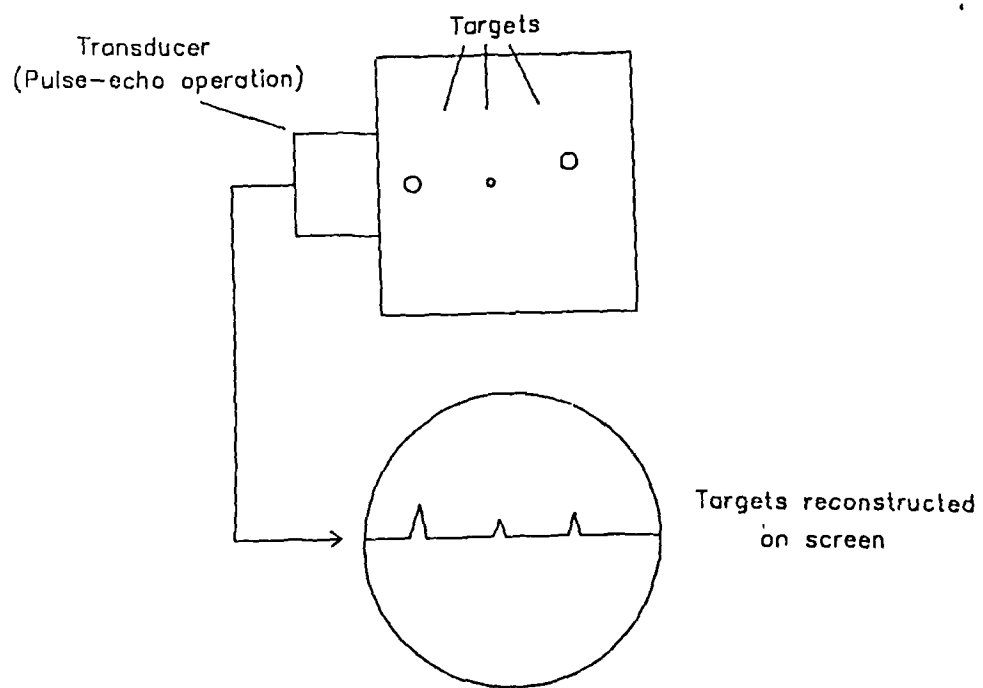


Figure 6.1 Schematic diagram of the A-scan

6.2 REVIEW OF IMPORTANT IMAGING STRATEGIES AND REQUISITE ARRAY CHARACTERISTICS

Pulse-echo techniques are the most useful in practical sonar, NDE and biomedical imaging and therefore tomographic methods are omitted in the present review. Tomography is applicable only to separate source/ receiver configurations where the target is placed between the source and receiver.

The simplest pulse-echo image is the A-scan. A single transducer is excited and its pulse-echo voltage response is plotted as a function of time. Since the velocity of sound in the medium is normally known, the time axis may be rescaled as a displacement axis. Thus, a target will give rise to a specific echo at a particular time, and hence displacement along the x-axis, on the A-scan. The size and position of the response may be interpreted readily by the user. A schematic diagram of the A-scan is shown in Figure 6.1. The A-scan, on its own, is of little use in imaging applications since it is one dimensional. However, even in this simplest example, the importance of high quality linear sensitivity and short pulse length is evident. Clearly, for maximum resolution, the highest practical frequency combined with the shortest possible pulse length is desirable. If an array of separate transducers are each used to generate A-scans, and these responses are placed side by side, in such a way that they reflect the geometry of the array, then a B-scan is formed. This is described schematically in Figure 6.2.

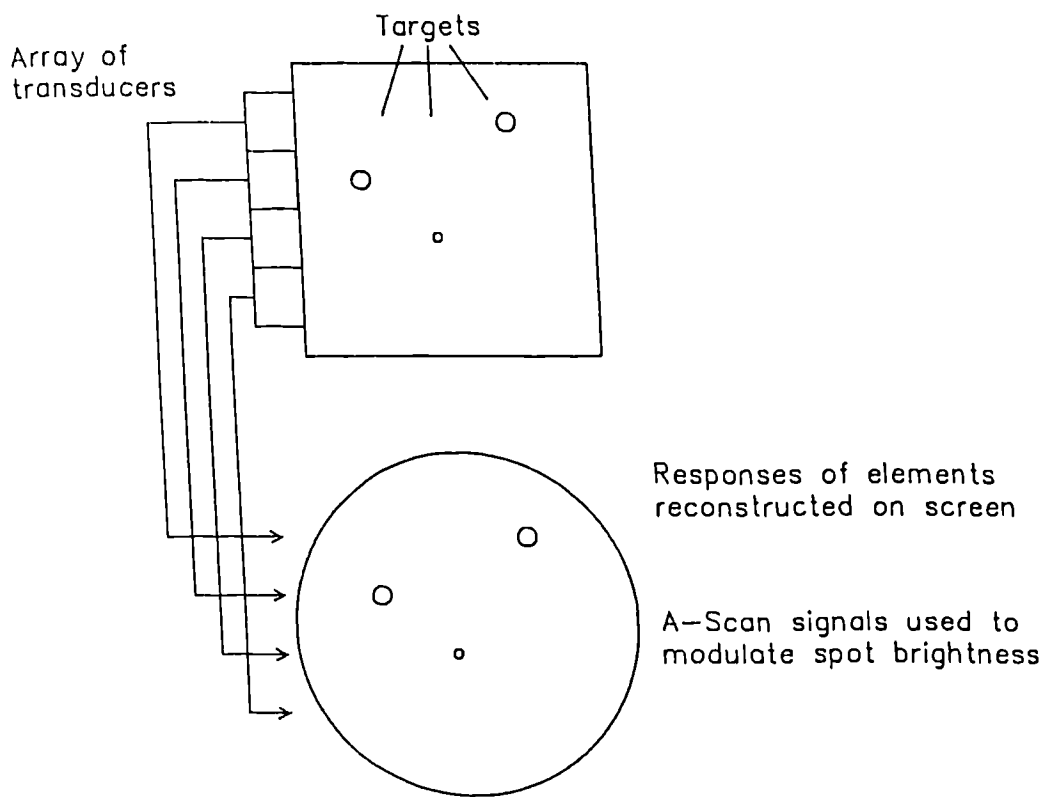


Figure 6.2 Schematic diagram of the B-scan

Normally the separate A-scans are peak detected, and this value used to modulate the brightness of a point on the screen.

It is evident that unless the transducers possess narrow directivities, then the target echo will be received on a number of elements at slightly delayed points in time. This will give rise to a blurred and distorted image. In medical ultrasonics, where the target is normally in the form of layers of tissue under the skin, the problem of target echo spreading is not significant. Highly directional elements are easily fabricated using relatively wide apertures. However, the aperture of a B-scan array is limited to the aperture of the array itself. It is evident that NDE and sonar applications generally require imaging properties beyond the capability the B-scan technique.

The third basic type of scan, the C-scan, is a development of the B-scan, and provides an image in the plane perpendicular to the direction of acoustic propagation. It is normally raster scanned mechanically and hence it is of limited practical value for real time applications.

A significant improvement in the quality of the image from a B-scan array may be obtained by focusing the received data. A target, at a specific point, will give rise to a signal in the responses of a number of array elements. However, the timing of this signal is related to the physical geometry of the target relative to the array. The

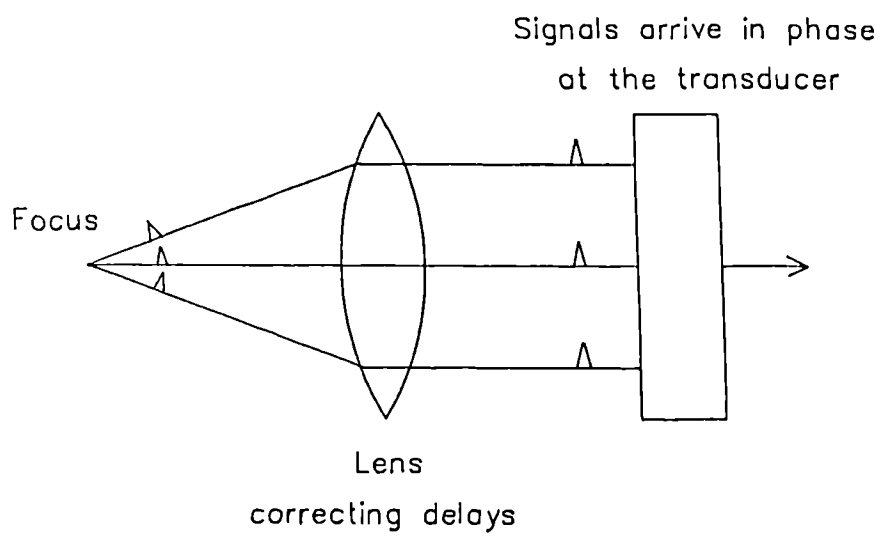


Figure 6.3 Concept of focusing using a physical lens

aim of focusing is to reconstruct the image of the target, using the responses of all relevant elements, and delaying them, so that for a particular target location, the responses are coincident and hence, upon summing, a high degree of focusing is achieved.

The concept of focusing is best illustrated by considering the use of a suitably shaped physical lens. This process is illustrated in Figure 6.3. Responses on elements furthest from the target, have travelled further and hence are delayed by the greatest amount. However, the lens corrects this by delaying central element responses more, so that on exit from the lens, all the responses are in phase and hence focusing is achieved.

Clearly, a physical lens has no versatility. However, if the delaying of the signals is achieved using electronic control, then virtually any focusing characteristic may be obtained. In practice, the responses of all the elements are normally digitised and stored in a computer memory. Thereafter, focusing is achieved under software control. Synthetic Aperture Focusing (SAF) involves the summation of the signals from several distinct positions which may be attributed to a common point in the field. If a scatterer is present at the point to which the array is being focused, then the backscattered signals will sum in phase after the appropriate element delays have been applied. The array is sequentially focused for all points of interest in the field and at points, other than those containing scatterers, the backscattered data will

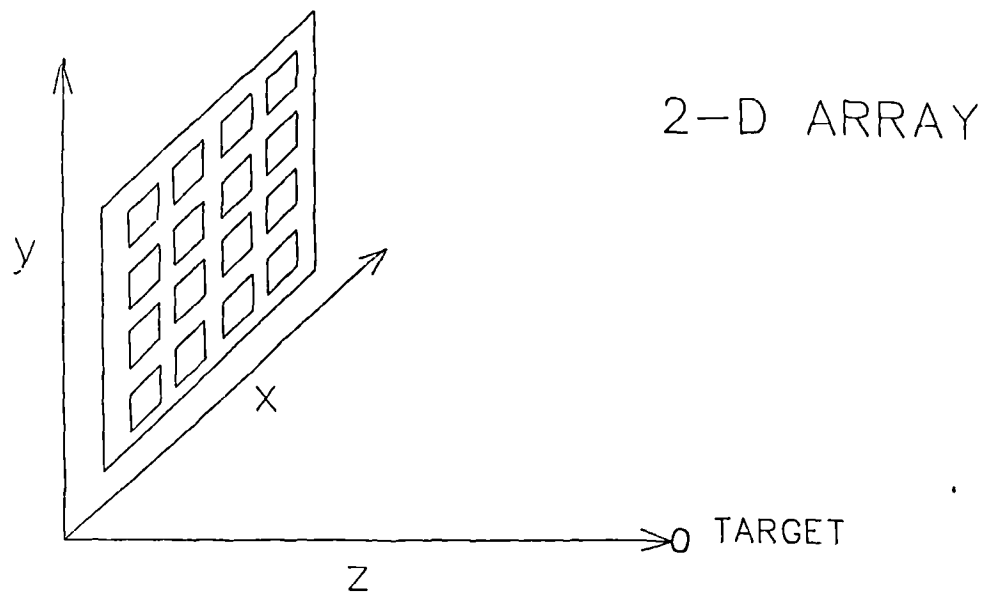
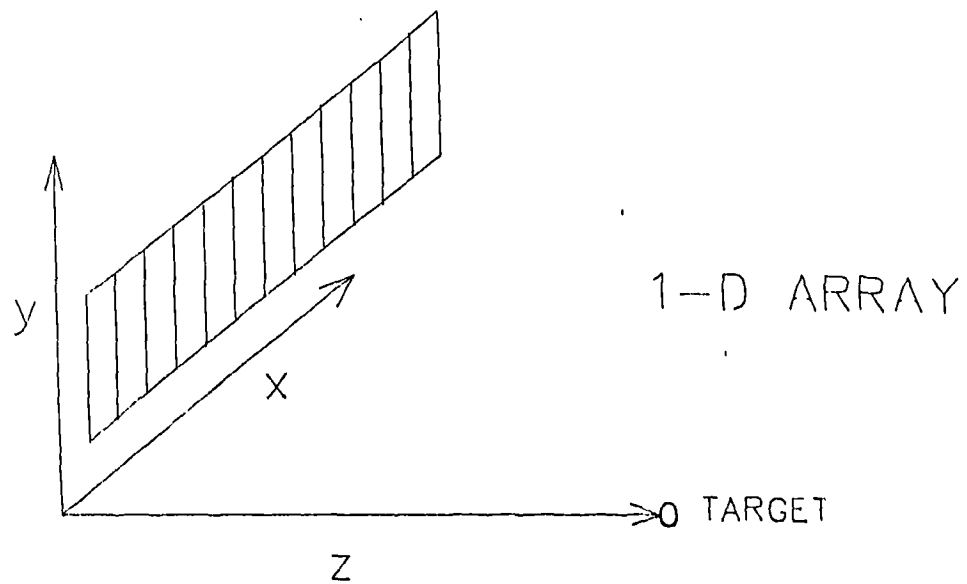


Figure 6.4 Axis notation for acoustic fields

- X : Direction along which the elements are spaced.
- Y : Direction perpendicular to 'X', but on the same plane as the active surface array. In a 2-D array, elements are spaced along this direction as well as along the X direction.
- Z : Perpendicular range from active 'array surface to target.

normally be uncorrelated and only a small net response is observed. However, certain array/ target geometries will exhibit spurious 'shadow' effects at non-scatterer points due to multipath reflections and similar phenomena.

Before considering the geometry of an array and target configuration, the general axis notation illustrated in Figure 6.4, is presented. Figure 6.5 illustrates the geometric configuration for the generation of a SAF image. The array possesses N elements, each with a response $S_i(t)$. The area to be imaged is divided into discrete pixels, with co-ordinates (x_j, z_j) . The transmit and receive time delay, t_{ij} , for each array element, i , is calculated for each specific pixel location, j . Therefore, the intensity at pixel, j , is defined by Equation 6.1.

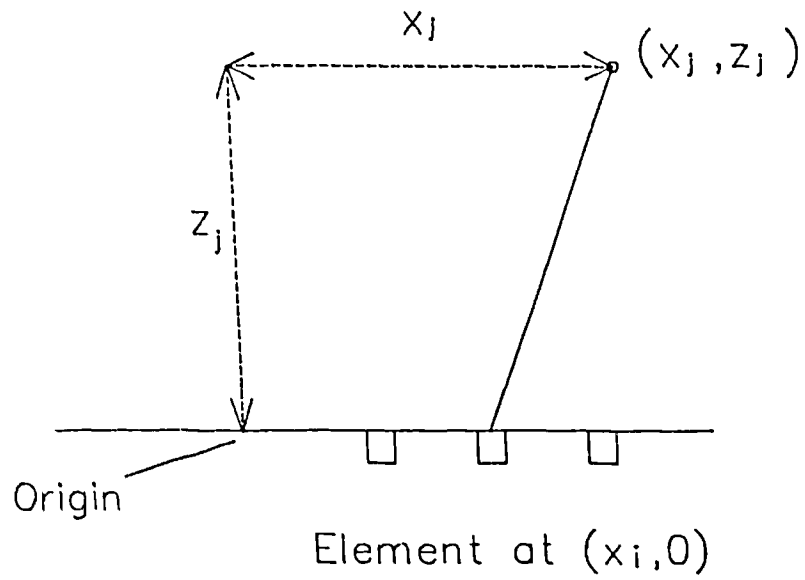
$$I(x_j, z_j) = \left| \sum_{i=1}^N S_i(t_{ij}) \right| \quad 6.1$$

Where,

$$t_{ij} = \frac{2}{c} \sqrt{(x_j - x_i)^2 + z_j^2}$$

It may be observed, that due to both transmission and reception delays, the time difference is twice that of a system which transmits a parallel beam and focuses in reception alone. Hence, the effective spatial resolution of SAF is twice that of such a system [50].

In the design of an array, the most important parameter, after the frequency of operation has been selected, is element spacing. If the spacing is greater than half a wavelength, then aliasing of signals from adjacent



$$t_{ij} = \frac{2}{c} \sqrt{(x_j - x_i)^2 + z_j^2}$$

Figure 6.5 Geometric configuration for generation of a SAF image.

elements will occur at high angles of incidence. The exact formulation for predicting these grating lobes and also the point spread functions has been analysed rigorously elsewhere [50]. Kino concluded that, in wideband systems, where the pulses are very short, the effects of both grating lobes and side lobes are considerably less than predicted theoretically for the narrowband case. In conclusion, the array spacing should ideally be no more than half a wavelength and high bandwidth pulses should be used. In practice, spacings of up to one wavelength are tolerable because practical element directivities limit the response at wide angles.

The above discussion allows the characteristics of an optimal array to be defined. These may be summarised as follows.

- 1) Omnidirectional element directivity. For optimal focusing, all elements should acquire signals which are independent of incident angle. In practice, this is impractical and therefore a smooth wide directivity, free of strong lobes, is desired. This aspect will be described more fully in section 6.4.
- 2) Wideband operation. Kino's work [50] indicates that ideally, the received echo signals should be as short as possible to permit maximum resolution with minimal side and grating lobes. In fact, Kino has proposed using inverse filtering methods to extract impulse type signal data from real responses. However, these techniques are omitted from the

current work. Instead, wideband operation will be obtained by using well matched transducer materials, heavy backing materials and, where appropriate, quarter wavelength matching layers.

- 3) Minimal inter-element coupling. If adjacent elements are excited, either mechanically or electrically, a serious degradation of spatial field response will occur. The actual response will be the result of a complex combination of several elements operating and a largely unpredictable effect on the imaging process will occur.
- 4) Uniformity. The requirement that all elements should have equal operating characteristics is obvious, but in practice depends on careful quality control during the manufacturing process.
- 5) High capacitance. Normally elements have a small area and hence their capacitance is low. This results in a high electrical impedance, making them difficult to drive. It is therefore essential that the element possess as high a capacitance as possible.
- 6) Ease of manufacture. It should be possible to manufacture the arrays simply, and without the requirement for expensive capital equipment, so that the arrays can be fabricated at a commercially viable cost.

6.3 THEORETICAL SPATIAL FIELD CHARACTERISTICS OF ARRAY ELEMENTS

Extensive study of the directivity of narrow strip array elements has been performed. Most of these assume that the element possesses a uniform displacement profile across its surface, is operated under CW excitation and only motion parallel to the array axis is considered. Clearly, these assumptions are not entirely valid for practical array elements. The spatial characteristics of a transducer are also modified partially by the relative mechanical impedances of the transducer and the medium. For the case of an infinite rigid baffle, wherein perpendicular displacement is zero outside the active area of the transducer face, the following approximate expression may be obtained [51]. This expression has been developed for an element whose length dimension is considerably greater than the width dimension, typical of those found in one dimensional arrays.

$$P = P_0 \frac{\sin(\pi W / \lambda \sin \theta)}{\pi W / \lambda \sin \theta} \quad 6.2$$

P_0 is the excitation pressure at the front surface of the aperture, W is the width of the aperture and λ is the acoustic wavelength. θ is the observation angle, with respect to a perpendicular axis emanating from the centre of the transducer aperture.

However, in the case of a pressure release baffle, wherein the pressure is zero outside the active area, a modified expression is obtained. This baffle condition more

accurately replicates the practical situation of a relatively low impedance composite transducer operating into water. The resulting expression is similar to that for the rigid baffle, except that a $\cos\theta$ term is included.

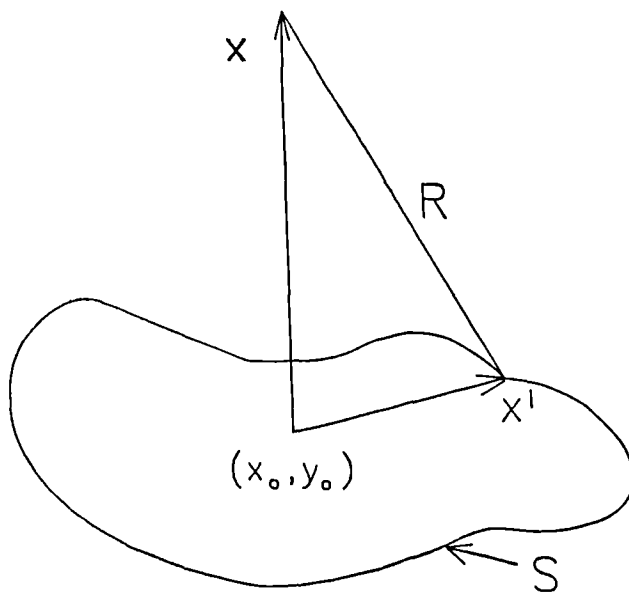
$$P = P_0 \frac{\sin(\pi W / \lambda \sin \theta) \cos \theta}{\pi W / \lambda \sin \theta} \quad 6.3$$

The accurate modelling of the practical configuration, in which non-uniform and wideband operation is to be considered, requires a more fundamental approach. The field profile of a transiently excited piston mounted in a rigid infinite baffle has been considered by a number of investigators. In particular, Stepanishen [52] has derived expressions for the field intensity at arbitrary points in the field of a circular piston. This technique has been extended by Lockwood and Willette for the analysis of the fields of rectangular sources [53]. In the present context, the general field expressions are briefly reviewed and a novel technique for evaluating the pressure responses at arbitrary points in the field of a rectangular source presented.

The pressure profile, $P(x,t)$, at an arbitrary point, x , is related to the velocity potential $\phi(x,t)$ by the following expression.

$$P(x,t) = -\rho \frac{\delta\phi(x,t)}{\delta t} \quad 6.4$$

ρ = density of the propagation medium.



$$R = |x' - x|$$

Figure 6.6 Geometry of an arbitrarily shaped source and observation point.

The velocity potential, for the general geometry, as illustrated in Figure 6.6, may be derived from the Rayleigh surface integral using a Green's function approach [52].

$$\Phi(\mathbf{x},t) = \int_S \frac{v(t-R/c) dS}{2\pi R} \quad 6.5$$

This expression is valid for a source embedded in an infinite rigid baffle. The modification necessary for a pressure release baffle will be considered subsequently. The versatility of the above equation is significantly enhanced by expressing the velocity potential as a convolution integral involving the velocity potential impulse response, $h(\mathbf{x},t)$, and the excitation velocity function, $v(t)$.

$$\Phi(\mathbf{x},t) = v(t) * h(\mathbf{x},t) \quad 6.6$$

Where

'*' denotes convolution,

and

$$h(\mathbf{x},t) = \int_S \frac{\delta(t-R/c) dS}{2\pi R} \quad 6.7$$

Consider the piston geometry illustrated in Figure 6.7, where R may be considered as the radius of a sphere centred on \mathbf{x} . The arc length, $L(R)$, is defined by the intersection of the piston with the surface of the sphere centred on \mathbf{x} . The angle, $\theta(R)$, is defined from the points of intersection on $L(R)$, and the normal to the X-Y plane passing through the point of interest, \mathbf{x} . Employing simple geometry, the incremental radial distance, δd , due to incremental increase, δR , of the radius of the sphere

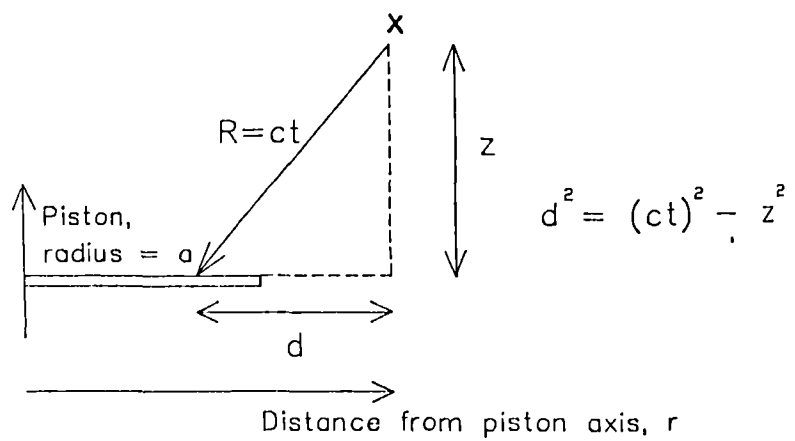
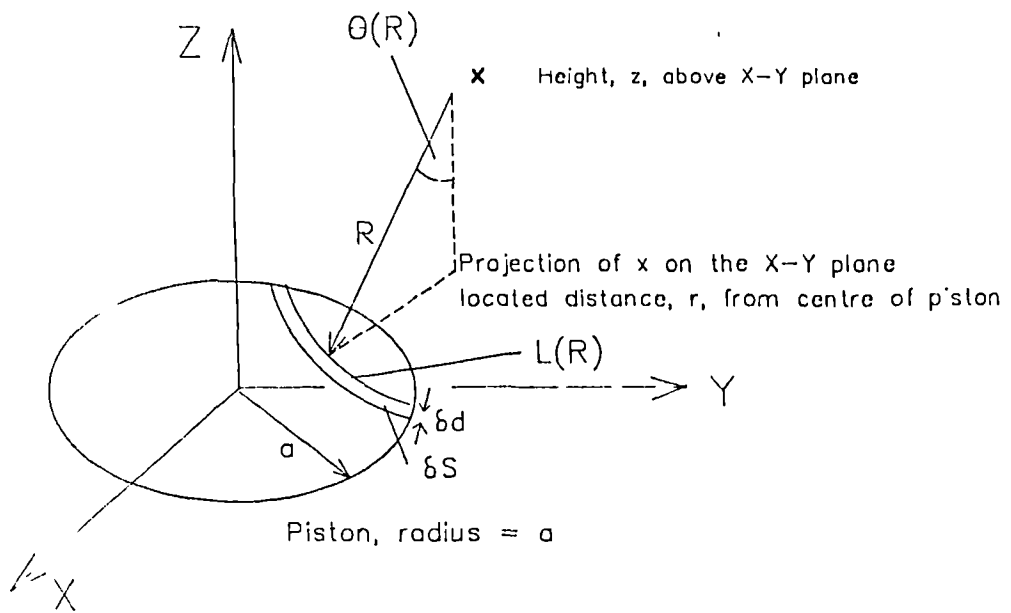


Figure 6.7 Geometry of circular piston source and observation point.

centred on \mathbf{x} , may be expressed as follows.

$$\delta d = \delta R / \sin\theta(R)$$

Also,

$$\delta S = L(R)\delta d$$

Hence:

$$\delta S = \frac{L(R)\delta R}{\sin\theta(R)}$$

Therefore Equation 6.7 may be transformed into Equation 6.8.

$$\phi(\mathbf{x}, t) = \int_0^{\infty} \frac{\delta(t-R/c)L(R)}{2\pi R \sin\theta(R)} dR \quad 6.8$$

Equation 6.8 may be further simplified to yield the following expression [52].

$$h(\mathbf{x}, t) = \frac{L(R)}{2\pi t \sin\theta(R)} \quad 6.9$$

Since $t-R/c$, and $\sin\theta(R) = d/R$:

$$h(\mathbf{x}, t) = \frac{c}{2\pi} \frac{L(R)}{d} \quad 6.10$$

Hence, the velocity potential, at an arbitrary point and time, may be evaluated from a calculation of angle, $L(R)/d$, corresponding to the intersection of the spherical wavefront with the portion of the plane which is of interest. Although the theory has been advanced from the viewpoint of the signal received on an arbitrary shape due to a point source, the derivation is reciprocal. That is, the same result is obtained for an arbitrarily shaped source projecting to a point in the field. Since the spatial point is general, the expression is equally valid for both near and far field.

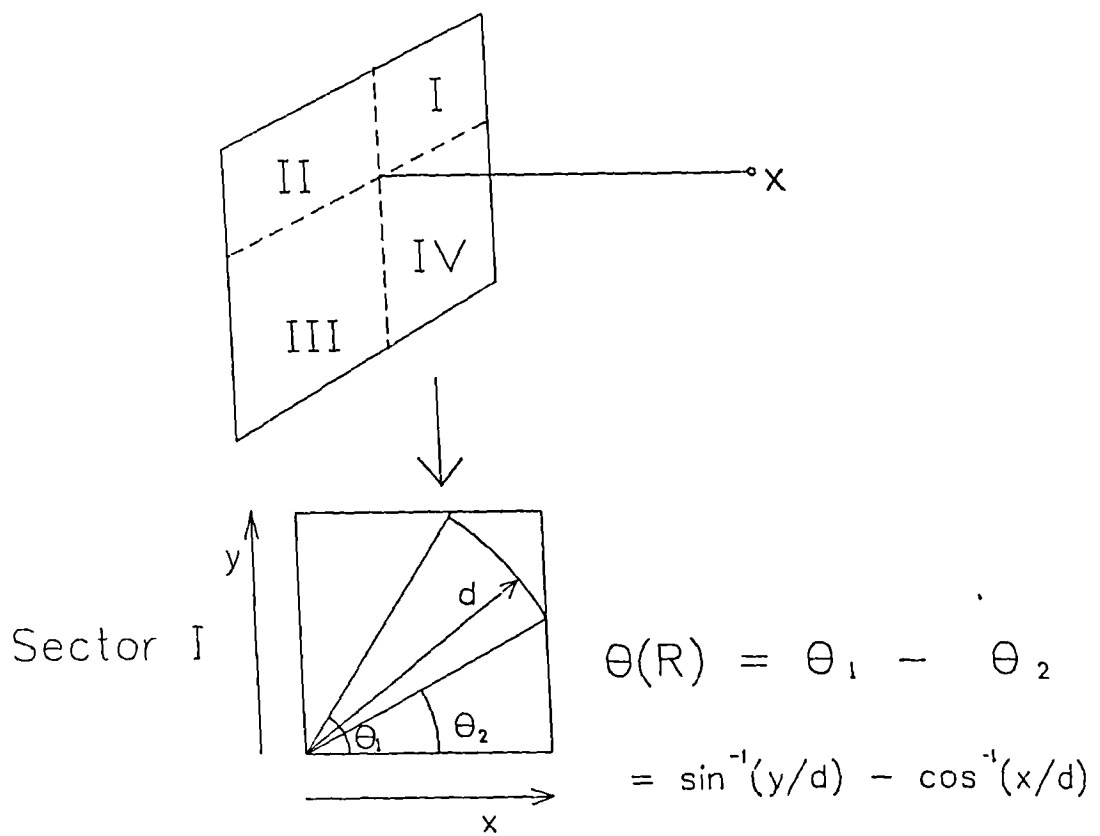


Figure 6.8 Concept for calculating arc lengths for a rectangular aperture.

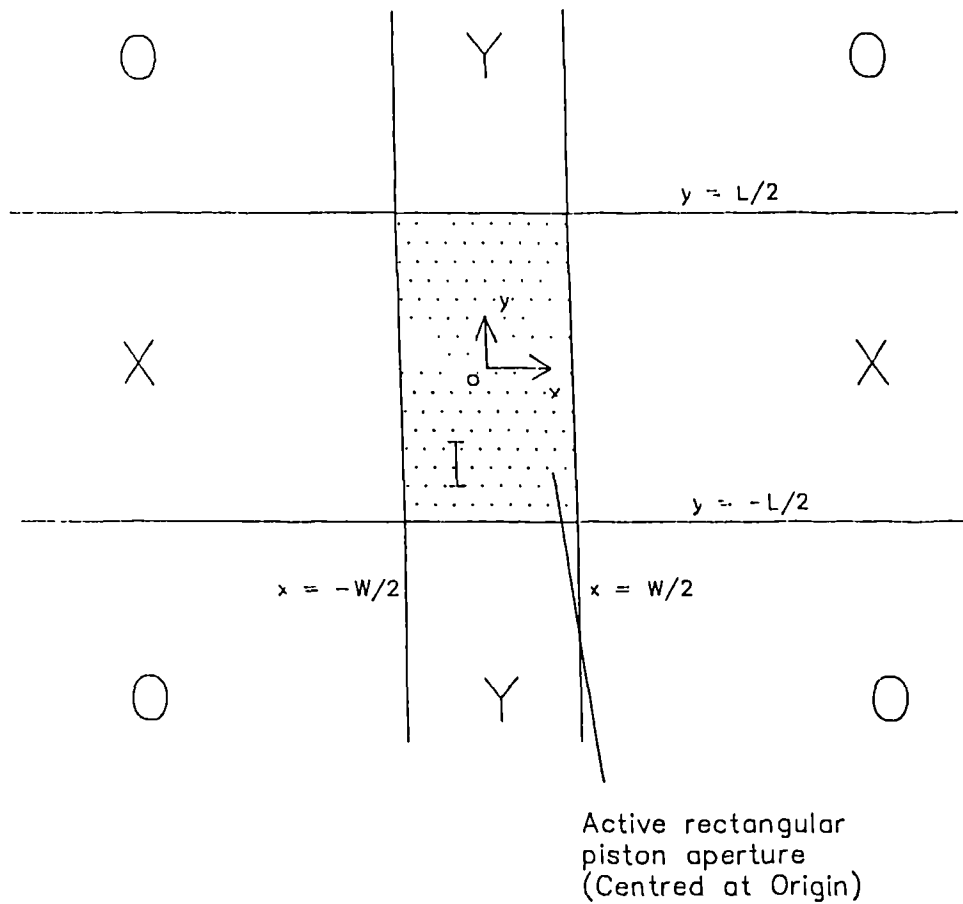
Although Stepanishen derived numerical expressions for disc sources, Lockwood and Willette [53] have described a method for evaluating the equivalent response of rectangular elements. Since, there can be as many as eight intersections between a curved wavefront and a rectangular frame, a versatile algorithm is required. Lockwood and Willette obtained an expression for the case in which the projection of the observed point, on to the plane of the source, lay within the area of the rectangular vibrating aperture. The rectangular element was split into four sub-elements, and the contributions of each of these calculated separately and finally summed. This concept is illustrated in Figure 6.8. The geometry for evaluating the intersected arc length is also illustrated. The situation for field points whose projection lies outwith the rectangular aperture is considerably more complex. The position of the rectangular element's corners with respect to the field point determines the number of intersections made. Lockwood and Willette proposed extending the rectangular element to include the projection of the field point. The velocity potential functions for the fields of the added rectangles are also calculated, and then these are subtracted to define the net velocity function of the rectangular element of interest. Therefore, this method requires redundant calculations for the regions outside the plane of interest. Furthermore, no algorithm is presented for defining which portions of the complete rectangle should be subtracted for the arbitrary point in the field of a source possessing arbitrary dimensions. The

design of such an algorithm, suitable for computer implementation, is not a trivial undertaking. The method described by Lockwood and Willette is normally adequate for calculating the fields of the elements typical of those found in conventional linear arrays. As illustrated in Figure 6.4, the length of the element is generally many times greater than the width and the observation point is almost invariably on the X-Z axis. These characteristics allow assumptions to be made regarding the number and location of the intersections between the wavefront and the edges of the aperture. However, the method is less satisfactory for the evaluation of the fields of the elements found in 2-D arrays, where the geometry of the intersections are more complex [54]. Although the calculation of the field response across a 2-D plane is generally sufficient for a 1-D array, it is frequently desirable to calculate the 3-D response of a 2-D array. Recently, Gomez-Ullate et al [55] have developed a method for the efficient calculation of the diffracted pressure response for the case that the projection of the observation point is outwith the vibrating aperture. However, the usefulness of this work is limited by this geometric constraint. The growing importance of two dimensional arrays necessitates the development of a more versatile algorithm.

Figure 6.9 Description of the zones, on the X-Y plane, associated with a rectangular aperture. The projection of the observation point, onto this plane, will determine which zone, and consequently, which mathematical expression is appropriate.

- I : Inner zone
- Y : Y axis zone
- X : X axis zone
- O : Outer zone

Projected field point at (x_o, y_o) .



A new algorithm for determining the velocity potential at arbitrary points due to a rectangular aperture is presented. The observation point, x , is projected perpendicularly onto the X-Y plane, as illustrated in Figure 6.6, and is assigned co-ordinates (x_0, y_0) . It is necessary to associate this projected point with the particular zone (I, X, Y, O - illustrated in Figure 6.9) in which it lies. The co-ordinates of the projected field point are compared with the X and Y limiting dimensions of the rectangular element. It is assumed that the centre of the element is the origin. The selection procedure is achieved in the following manner. The half-width dimension ($W/2$) is subtracted from the modulus of the x co-ordinate of the projected field point (x_0, y_0) to form x_1 . Similarly, y_1 is found by subtracting the half length dimension ($L/2$) from the modulus of the y co-ordinate.

$$\begin{aligned}
 x_1 &= |x_0| - W/2 \\
 x_2 &= |x_0| + W/2 \\
 y_1 &= |y_0| - L/2 \\
 y_2 &= |y_0| + L/2
 \end{aligned}
 \tag{6.10}$$

If both x_1 and y_1 are negative, then the field point lies within the area of the rectangular aperture. (Zone I in Figure 6.9)

If x_1 is positive and y_1 is negative, then the field point lies within the X axis region as illustrated Figure 6.9.

Figure 6.10 Geometry used for calculation of velocity potential when the projection of the field point lies within the aperture. (Inner zone)

For sub-rectangle I ($\tau_2 < \tau_3$)

$$t < \tau_1 \quad \theta(x_1, y_1, x_o, t) = 0$$

$$\tau_1 < t < \tau_2 \quad \theta(x_1, y_1, x_o, t) = \pi/2$$

$$\tau_2 < t < \tau_3 \quad \theta(x_1, y_1, x_o, t) = \sin(x_1/d)$$

$$\tau_3 < t < \tau_4 \quad \theta(x_1, y_1, x_o, t) = \sin(x_1/d) - \cos(y_1/d)$$

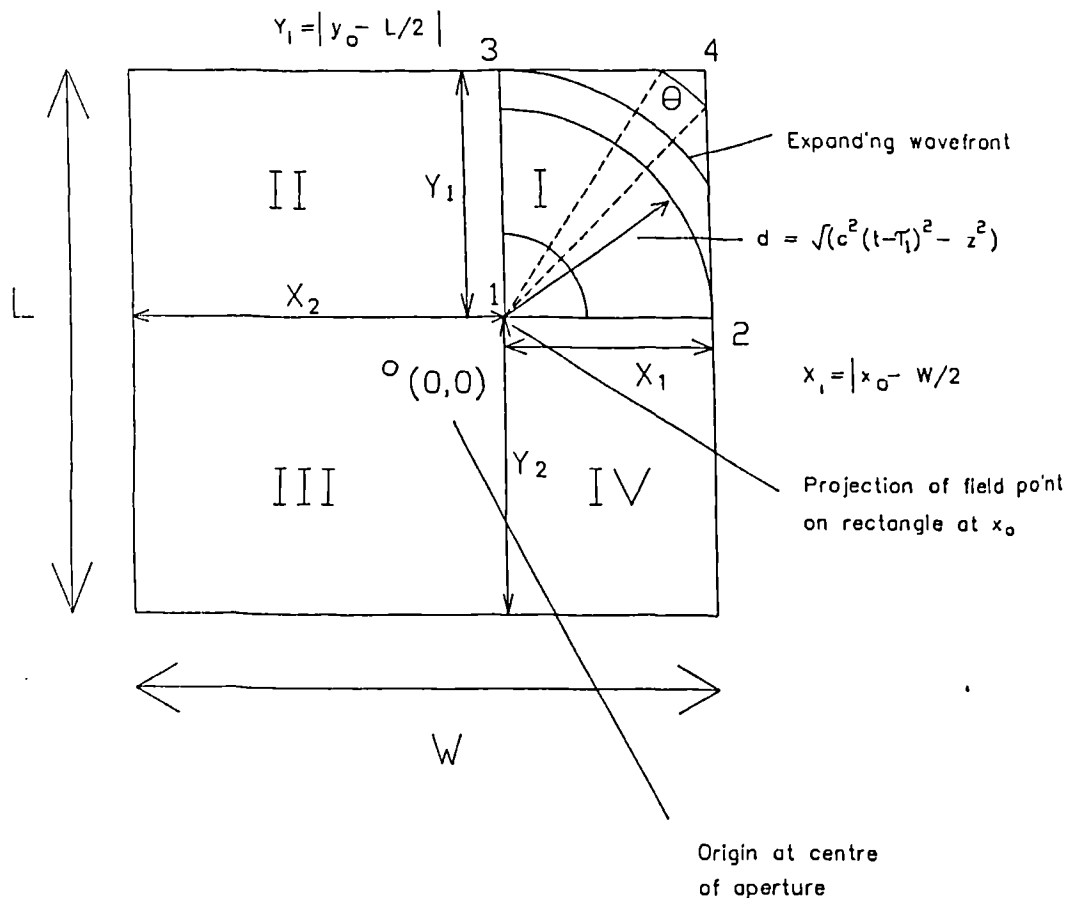
$$t > \tau_4 \quad \theta(x_1, y_1, x_o, t) = 0$$

Sub-rectangle I use x_1, y_1

Sub-rectangle II use x_2, y_1

Sub-rectangle III use x_2, y_2

Sub-rectangle IV use x_1, y_2



If x_1 is negative and y_1 is positive, then the field point lies within the Y axis region as illustrated Figure 6.9.

If both x_1 and y_1 are positive, then the field point lies in one of the outer regions. (Zone O in Figure 6.9)

i) Zone I (point inside aperture)

In a procedure similar to that employed by Lockwood and Willette, the aperture is split into four quadrants. Consider the top right corner, as illustrated in Figure 6.10. Before proceeding with the arc length calculation, the order in which the advancing wavefront encounters the sub-rectangle's corners must be determined. This will determine which edges are used in the calculation. It is known that in all cases, corner 1 is encountered first and corner 4 last. The order of reaching corners 2 and 3 must be determined. If corner 3 is reached before corner 2, then the times of arrival at the corners denoted 2 and 3 (τ_2 and τ_3 respectively) are interchanged and a modified integral for the interval τ_2 to τ_3 is used. After making minor geometric substitutions, from Figure 6.6, Equation 6.11 may be derived from Equation 6.9.

$$h(x,t) = \sum_{i=1}^2 \sum_{j=1}^2 \frac{c}{2\pi} \theta(x_i, y_j, x, t). \quad 6.11$$

Where, $\theta(x_i, y_j, x, t)$ is the angle, measured on the X-Y plane, associated with the arc due to the intersection of a sphere centred at the observation point, x , with the X-Y plane at a time, t . The variables, x_i and y_j , are the x

and y dimensions calculated using Equation 6.10. Thus the responses of the quadrants defined by (x_1, y_1) , (x_1, y_2) , (x_2, y_1) and (x_2, y_2) are summed. The field point is at a perpendicular range, z , and hence the times to reach the corners 1, 2, 3 and 4, from the observation point, for quadrant (x_i, y_j) , are evaluated as follows. Taking the moduli of lengths x_i and y_j in Equation 6.10, ensures that positive angles are always obtained and hence the equation is equally applicable for all four quadrants.

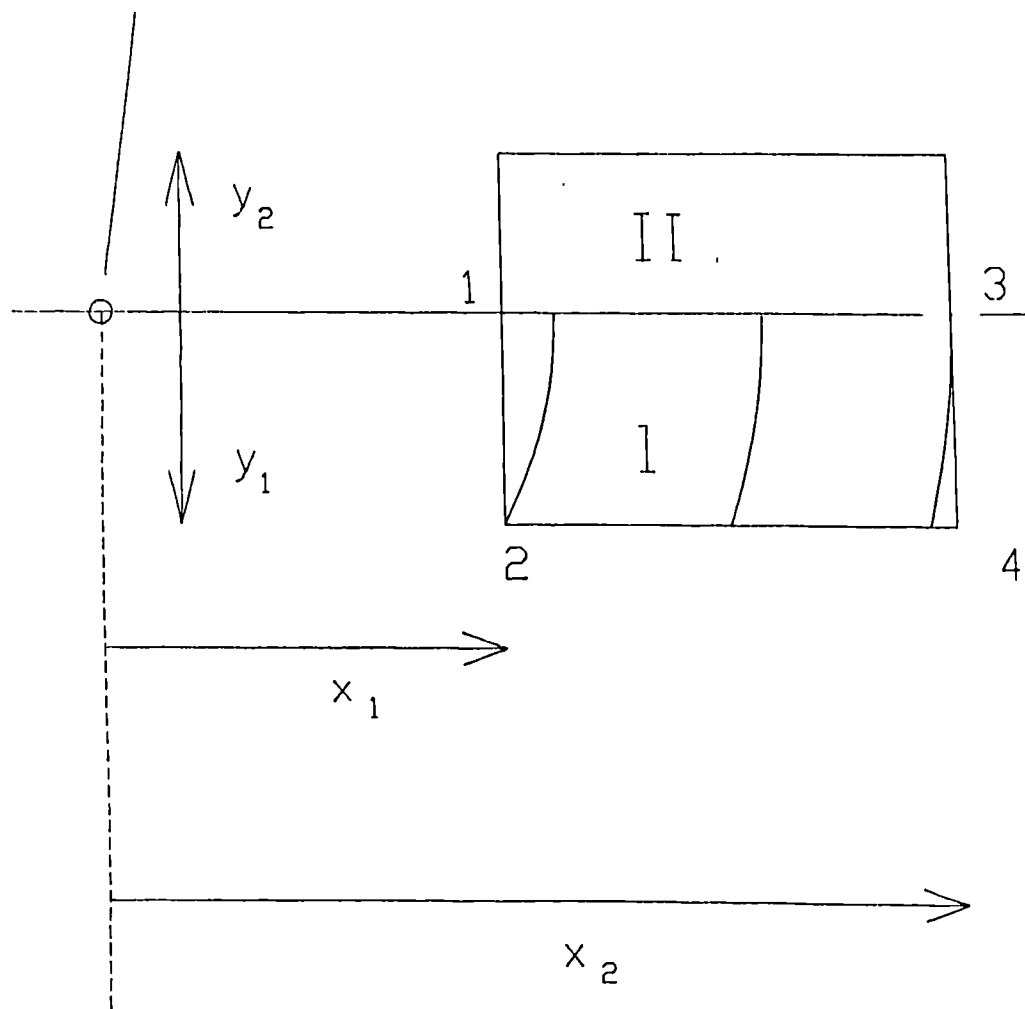
$$\begin{aligned} i &= 1, 2 \\ j &= 1, 2 \end{aligned}$$

$$\begin{aligned} \tau_{ij1} &= t - z/c \\ \tau_{ij2} &= t - \sqrt{(x_i^2 + z^2)} / c \\ \tau_{ij3} &= t - \sqrt{(y_j^2 + z^2)} / c \\ \tau_{ij4} &= t - \sqrt{(x_i^2 + y_j^2 + z^2)} / c \end{aligned} \quad 6.12$$

For the case that τ_{ij2} is less than τ_{ij3} , that is, corner 2 is encountered before corner 3, Equation 6.13 is applicable for evaluating the velocity potential.

$$\begin{aligned} h(x, t) &= \sum_{i=1}^2 \sum_{j=1}^2 \frac{c}{2\pi} \left[\int_{\tau_{ij1}}^{\tau_{ij2}} \frac{\pi}{2} \delta(\tau) d\tau \right. \\ &+ \int_{\tau_{ij}}^{\tau_{ij3}} \sin^{-1} \left[\frac{|x_i|}{\sqrt{(c^2(t-\tau)^2 - z^2)}} \right] \delta(\tau) d\tau \\ &\left. + \int_{\tau_{ij3}}^{\tau_{ij4}} \sin^{-1} \left[\frac{|x_i|}{\sqrt{(c^2(t-\tau)^2 - z^2)}} \right] - \cos^{-1} \left[\frac{|y_j|}{\sqrt{(c^2(t-\tau)^2 - z^2)}} \right] \delta(\tau) d\tau \right] \end{aligned} \quad 6.13$$

Projection of field point on plane



Sub-rectangle I use y_1

Sub-rectangle II use y_2

Figure 6.11 Geometry used for calculation of velocity potential when the projection of the field point lies in the x_1 axis zone.

If τ_{ij3} is less than τ_{ij2} , then the values of τ_{ij2} and τ_{ij3} are interchanged and the integral between τ_{ij2} to τ_{ij3} in Equation 6.13 is replaced by:

$$\int_{\tau_{ij2}}^{\tau_{ij3}} \sin^{-1} \left[\frac{|y_j|}{\sqrt{(c^2(t-\tau)^2 - z^2)}} \right] \delta(\tau) d\tau$$

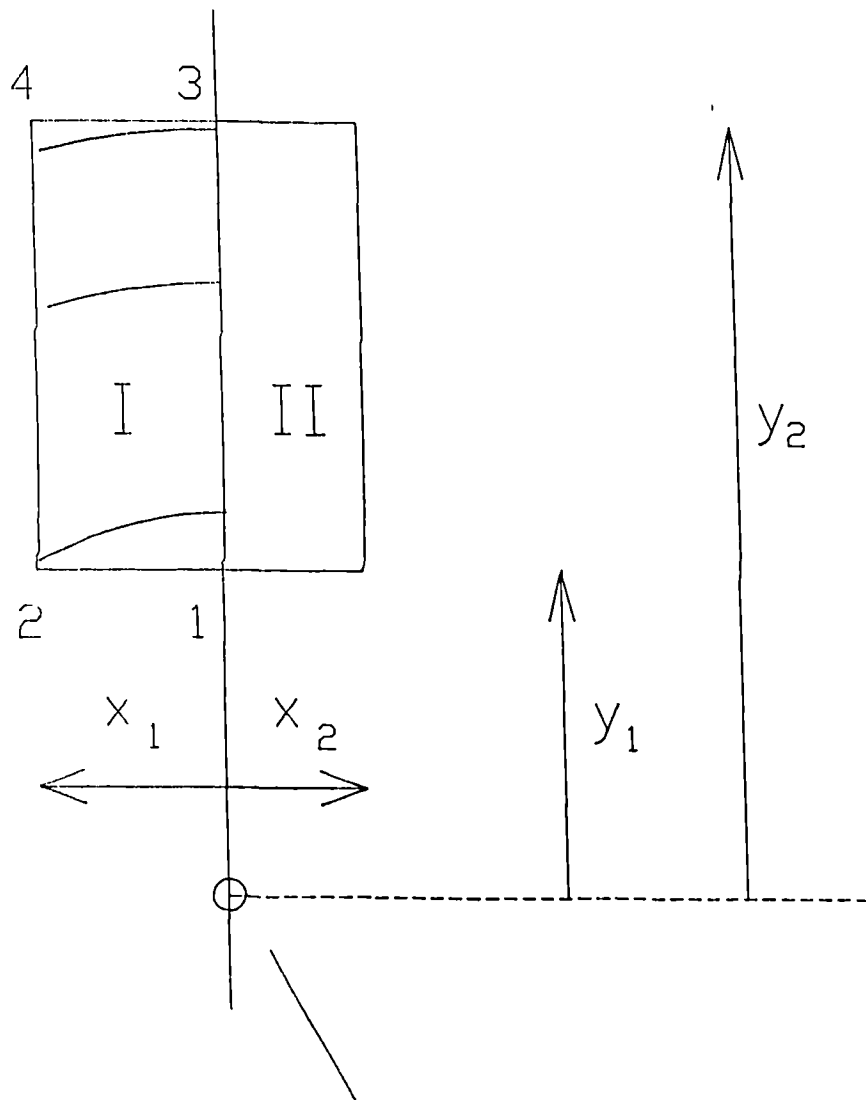
ii) Zone X (point in the X axis region)

In this case, the projection of the field point lies in the X axis region shown in Figure 6.9, and hence the geometry illustrated in Figure 6.11 is applicable. The complete velocity potential is calculated using two sub-rectangles. A summation is employed, with $j = 1, 2$, to obtain the net response of the upper and lower sub-rectangles. The wavefront arrival times at corners 1, 2, 3 and 4 are evaluated using Equation 6.14.

$j = 1, 2$

$$\begin{aligned} \tau_{j1} &= t - \sqrt{(x_1^2 + z^2)} / c \\ \tau_{j2} &= t - \sqrt{(x_1^2 + y_j^2 + z^2)} / c \\ \tau_{j3} &= t - \sqrt{(x_2^2 + z^2)} / c \\ \tau_{j4} &= t - \sqrt{(x_2^2 + y_j^2 + z^2)} / c \end{aligned} \quad 6.14$$

For the case that τ_{j2} is less than τ_{j3} , that is, corner 2 is encountered before corner 3, Equation 6.15 is applicable for evaluating the velocity potential. The derivation of this equation is similar to that used for Equation 6.13.



Projection of field point on plane

Sub-rectangle I use x_1

Sub-rectangle II use x_2

Figure 6.12 Geometry used for calculation, of velocity potential when the projection of the field point lies in the Y axis zone.

$$\begin{aligned}
h(x,t) = & \sum_{j=1}^2 \frac{c}{2\pi} \left[\int_{\tau_{j1}}^{\tau_{j2}} \cos^{-1} \left[\frac{x_1}{\sqrt{(c^2(t-\tau)^2 - z^2)}} \right] \delta(\tau) d\tau \right. \\
& + \int_{\tau_{j2}}^{\tau_{j3}} \sin^{-1} \left[\frac{|y_j|}{\sqrt{(c^2(t-\tau)^2 - z^2)}} \right] \delta(\tau) d\tau \\
& \left. + \int_{\tau_{j3}}^{\tau_{j4}} \sin^{-1} \left[\frac{|y_j|}{\sqrt{(c^2(t-\tau)^2 - z^2)}} \right] - \cos^{-1} \left[\frac{x_2}{\sqrt{(c^2(t-\tau)^2 - z^2)}} \right] \delta(\tau) d\tau \right]
\end{aligned}
\tag{6.15}$$

If τ_{j3} is less than τ_{j2} , then the values of τ_{j2} and τ_{j3} are interchanged and the integral between τ_{j2} to τ_{j3} in Equation 6.15 is replaced by:

$$\int_{\tau_{j2}}^{\tau_{j3}} \cos^{-1} \left[\frac{x_1}{\sqrt{(c^2(t-\tau)^2 - z^2)}} \right] - \cos^{-1} \left[\frac{x_2}{\sqrt{(c^2(t-\tau)^2 - z^2)}} \right] \delta(\tau) d\tau$$

iii) Zone Y (point in the Y axis region)

In this case, the projection of the field point lies in the Y axis region shown in Figure 6.9, and hence the geometry illustrated in Figure 6.12 is applicable.

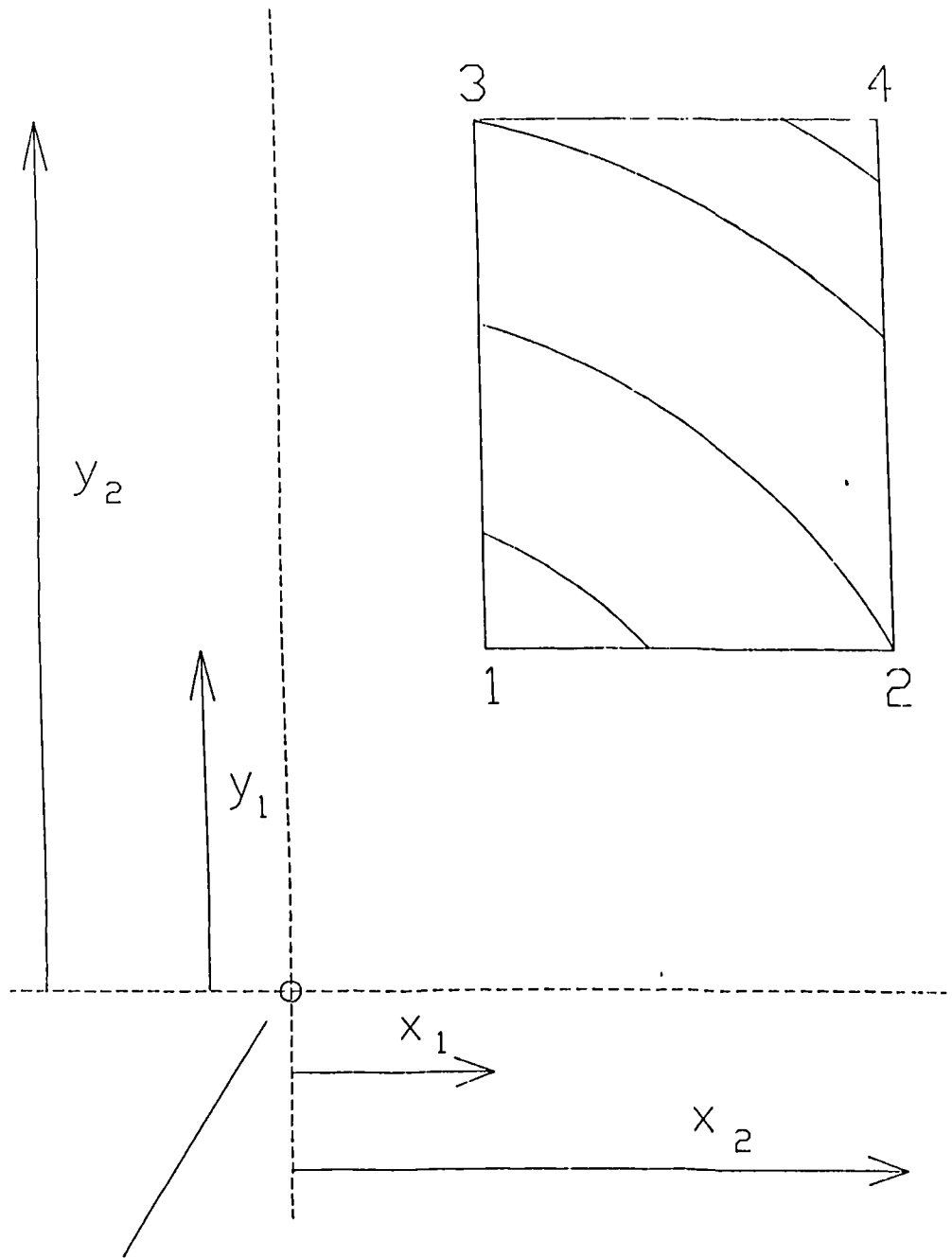
It is possible to reflect the geometry, of both the aperture and the target location, about the line $Y = X$, so that an equivalent diffraction problem in the X axis region is obtained. Thereafter, Equations 6.14 and 6.15

may be employed. Alternatively, the following equation may be used. The complete velocity potential is calculated from the sum of the responses from two sub-rectangles. The wavefront arrival times at corners 1, 2, 3 and 4 are evaluated using Equation 6.16.

$$\begin{aligned}
 i=1, 2 \\
 \tau_{i1} &= t - \sqrt{(y_1^2 + z^2)} / c \\
 \tau_{i2} &= t - \sqrt{(x_1^2 + y_1^2 + z^2)} / c \\
 \tau_{i3} &= t - \sqrt{(y_2^2 + z^2)} / c \\
 \tau_{i4} &= t - \sqrt{(x_i^2 + y_2^2 + z^2)} / c
 \end{aligned} \tag{6.16}$$

For the case that τ_{i2} is less than τ_{i3} , that is, corner 2 is encountered before corner 3, Equation 6.17 is applicable.

$$\begin{aligned}
 h(x,t) &= \sum_{i=1}^2 \frac{c}{2\pi} \left[\int_{\tau_{i1}}^{\tau_{i2}} \cos^{-1} \left[\frac{y_1}{\sqrt{(c^2(t-\tau)^2 - z^2)}} \right] \delta(\tau) d\tau \right. \\
 &+ \int_{\tau_{i2}}^{\tau_{i3}} \sin^{-1} \left[\frac{|x_i|}{\sqrt{(c^2(t-\tau)^2 - z^2)}} \right] \delta(\tau) d\tau \\
 &\left. + \int_{\tau_{i3}}^{\tau_{i4}} \sin^{-1} \left[\frac{|x_i|}{\sqrt{(c^2(t-\tau)^2 - z^2)}} \right] - \cos^{-1} \left[\frac{y_2}{\sqrt{(c^2(t-\tau)^2 - z^2)}} \right] \delta(\tau) d\tau \right]
 \end{aligned} \tag{6.17}$$



Projection of field point on plane

Figure 6.13 Geometry used for calculation of velocity potential when the projection of the field point lies in the outer zone.

If τ_{i3} is less than τ_{i2} , then the values of τ_{i2} and τ_{i3} are interchanged and the integral between τ_{i2} to τ_{i3} in Equation 6.17 is replaced by:

$$\int_{\tau_{i2}}^{\tau_{i3}} \sin^{-1} \left[\frac{Y_1}{\sqrt{(c^2(t-\tau)^2 - z^2)}} \right] - \sin^{-1} \left[\frac{Y_2}{\sqrt{(c^2(t-\tau)^2 - z^2)}} \right] \delta(\tau) d\tau$$

iv) Zone 0 (point in the outer regions)

If the projection of the field point lies outwith the X region, the Y region and the central region as illustrated in Figure 6.9, then the following equations are applicable. Consider the configuration illustrated in Figure 6.13. In this case, the response for the entire rectangular element is calculated in a single sequence. The wavefront arrival times at corners 1, 2, 3 and 4 are evaluated using Equation 6.18.

$$\begin{aligned} \tau_1 &= t - \sqrt{(x_1^2 + y_1^2 + z^2)} / c \\ \tau_2 &= t - \sqrt{(x_2^2 + y_1^2 + z^2)} / c \\ \tau_3 &= t - \sqrt{(x_1^2 + y_2^2 + z^2)} / c \\ \tau_4 &= t - \sqrt{(x_2^2 + y_2^2 + z^2)} / c \end{aligned} \quad 6.18$$

If τ_2 is less than τ_3 , Equation 6.19 is applicable for evaluating the velocity potential.

$h(x,t) =$

$$\frac{c}{2\pi} \left[\int_{\tau_1}^{\tau_2} \cos^{-1} \left[\frac{x_1}{\sqrt{(c^2(t-\tau)^2 - z^2)}} \right] - \sin^{-1} \left[\frac{y_1}{\sqrt{(c^2(t-\tau)^2 - z^2)}} \right] \delta(\tau) d\tau \right. \\ \left. \int_{\tau_2}^{\tau_3} \cos^{-1} \left[\frac{x_1}{\sqrt{(c^2(t-\tau)^2 - z^2)}} \right] - \cos^{-1} \left[\frac{x_2}{\sqrt{(c^2(t-\tau)^2 - z^2)}} \right] \delta(\tau) d\tau \right. \\ \left. \int_{\tau_3}^{\tau_4} \sin^{-1} \left[\frac{y_2}{\sqrt{(c^2(t-\tau)^2 - z^2)}} \right] - \cos^{-1} \left[\frac{x_2}{\sqrt{(c^2(t-\tau)^2 - z^2)}} \right] \delta(\tau) d\tau \right] \quad 6.19$$

If τ_3 is less than τ_2 , then the values of τ_2 and τ_3 are interchanged and the integral between τ_2 to τ_3 in Equation 6.19 is replaced by:

$$\int_{\tau_2}^{\tau_3} \sin^{-1} \left[\frac{y_2}{\sqrt{(c^2(t-\tau)^2 - z^2)}} \right] - \sin^{-1} \left[\frac{y_1}{\sqrt{(c^2(t-\tau)^2 - z^2)}} \right] \delta(\tau) d\tau$$

Thus, the velocity potential at arbitrary points are fully defined. Unlike the approach of Lockwood and Willette, there is no redundancy in any of the formulations. If the aperture consists of a pressure release baffle, as is generally the case for low impedance composite element operating into water, the response at each time instant is multiplied by a $\cos\theta$ factor. Referring to Figure 6.7, it is evident that this factor is defined by z/R , where $R=ct$. Hence the modification described in Equation 6.20 is employed.

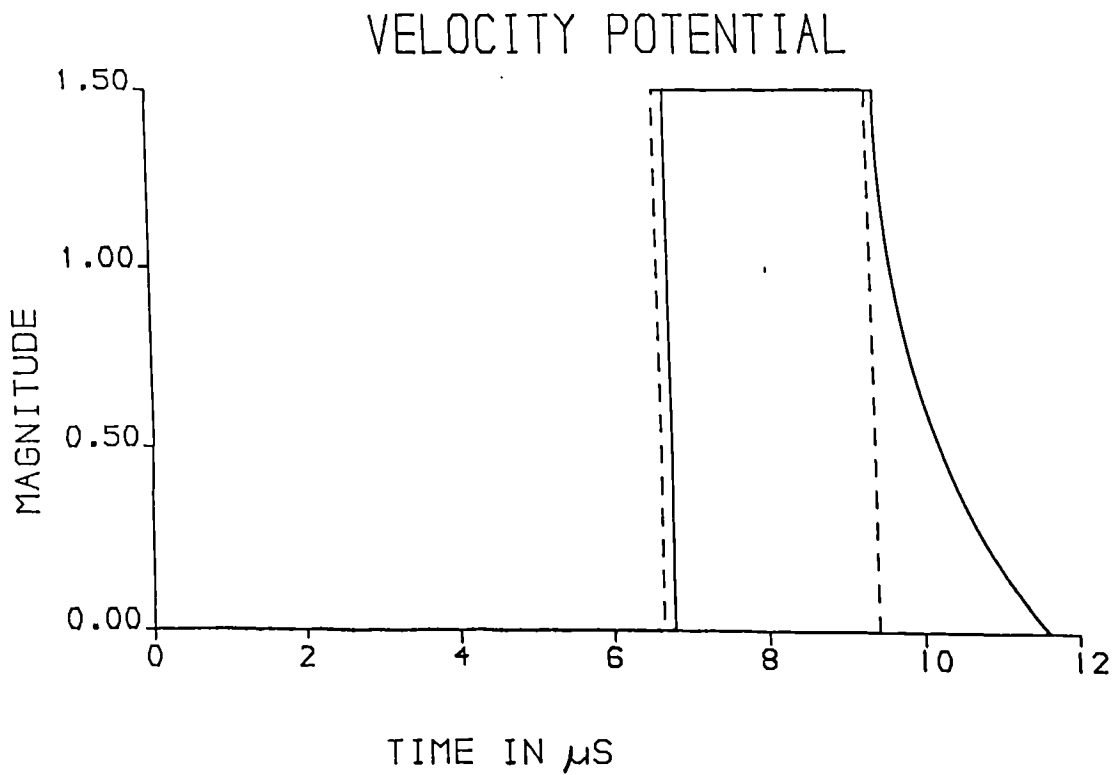
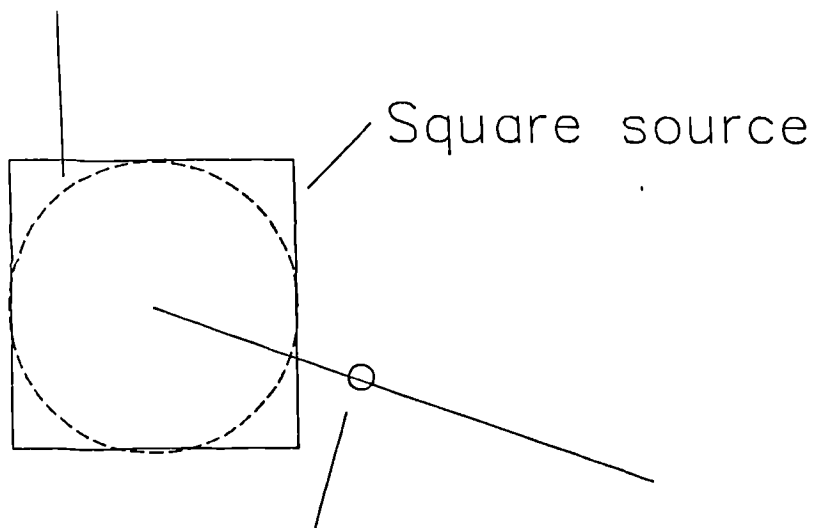


Figure 6.14 Velocity potential impulse response from circular and square apertures, on axis, at a range of $\sim 10\text{mm}$.
 Response of 20mm diameter circular source - - - - -
 Response of 20mm across square source _____

Circular source



Observation point

On axis, range = 10mm

Figure 6.15 Configuration of observation point with respect to source.

$$h'(x,t) = z/ct \quad h(x,t)$$

6.20

The expressions may now be used to compare the responses of circular and square sources. Figure 6.14 illustrates the on-axis velocity potential, at a range of 10mm from a square source with sides of length 20mm. The response of a 20mm diameter circular piston is illustrated for comparison. This configuration is illustrated in Figure 6.15. A step function is observed at the arrival time of the planar component in both cases. However, the downward step due to the radial edge of the circular source is far more pronounced than in the case for the square source. The interval over which this downward step occurs is related to the time difference between waves arriving from the centres of the sides, and the later arrival of waves emanating from the corners of the source. The corresponding pressure impulse responses due to the two sources are illustrated in Figure 6.16. These are obtained by differentiating the velocity potential responses. The response of the circular source exhibits a component due to the edges, which is equal in magnitude, but opposite in polarity, to that of the component due to the axial wave. However, the square source response exhibits only a very weak component due to smearing of the edge activity. Hence, if these responses are convolved with a CW excitation function, then the circular source will exhibit stronger near field interference between plane and edge wave components. Figure 6.17 illustrates the axial response of the above source geometries for a

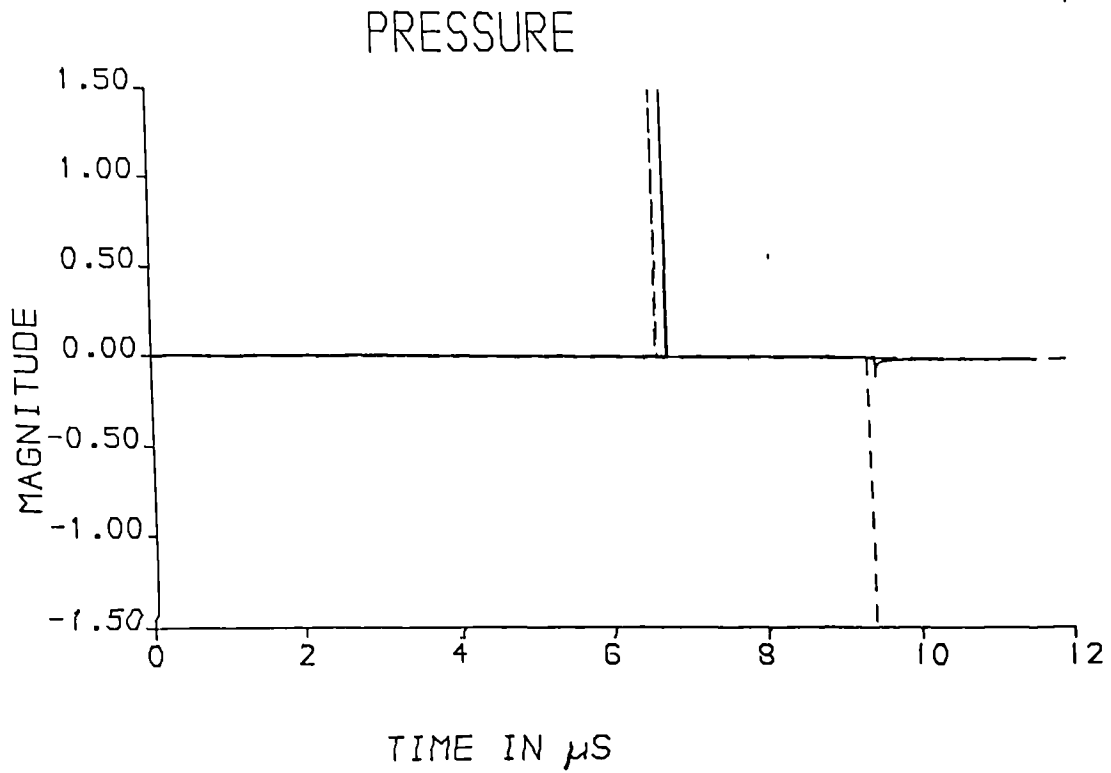


Figure 6.16 Pressure impulse response from circular and square apertures, on axis, at a range of 10mm.

Response of 20mm diameter circular source - - - - -
 Response of 20mm across square source _____

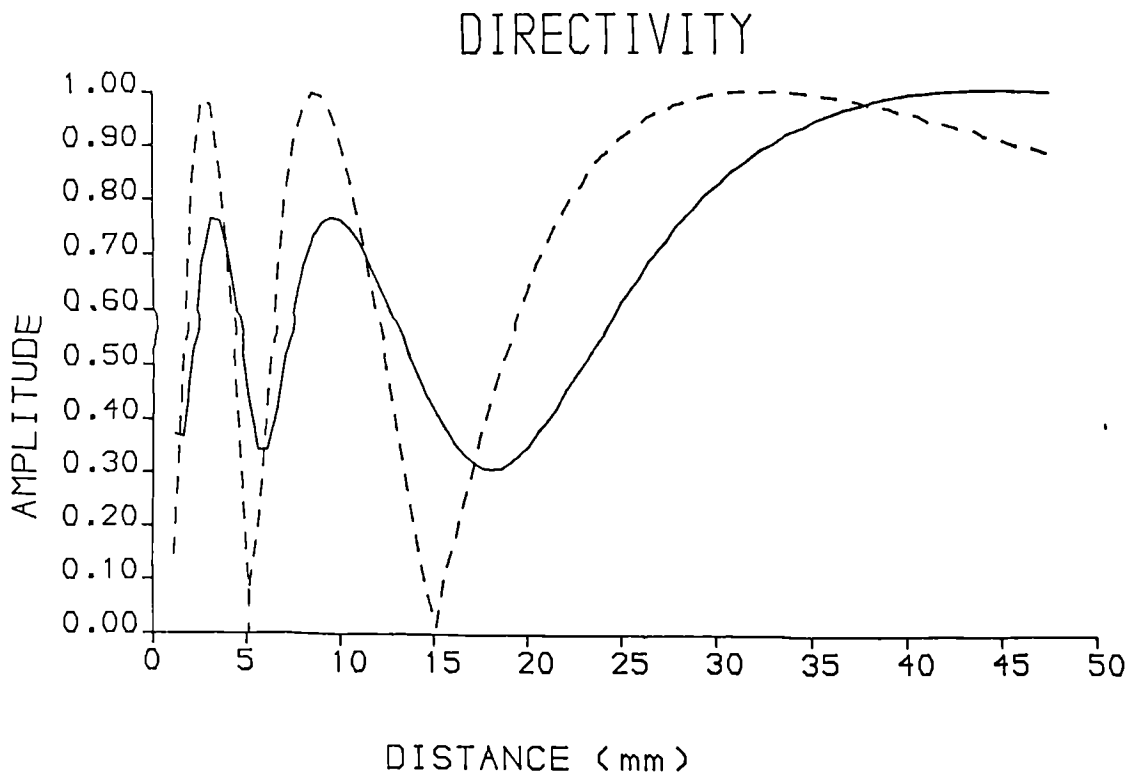


Figure 6.17 Axial 500kHz CW responses of the circular and square apertures.

Response of 20mm diameter circular source - - - - -
 Response of 20mm across square source _____

500kHz CW excitation. The variation in amplitude for the square source is half that encountered for the circular source.

The previous expressions are appropriate for uniformly vibrating apertures. A complex, non-uniformly vibrating aperture can generally be modelled by considering a stack of thin uniformly vibrating surfaces combined so that their cumulative response is representative of the non-uniform surface. Consider the configuration in Figure 6.18. For an aperture comprising of N sources, each with weighting, W_j . Equation 6.21 defines the net velocity potential. Notice, that if W_j is complex, then both amplitude and phase modulation of the surface may be modelled.

$$h(x,t) = \sum_{j=1}^N W_j [h_j(x,t) - h_{j-1}(x,t)] \quad 6.21$$

The appropriate aperture weighting function may be determined theoretically using finite element analysis. Although finite element analysis is capable of predicting diffraction directly, implementations for predicting field structures are computationally intensive. Therefore, finite element analysis is used only for determining the aperture weighting function, which cannot be achieved theoretically by any other method.

The diffracted pressure impulse response may now be convolved with the transducer aperture pressure function so that the diffracted response at any point due to an

PREDICTED SURFACE PROFILE



MODELLED AS:

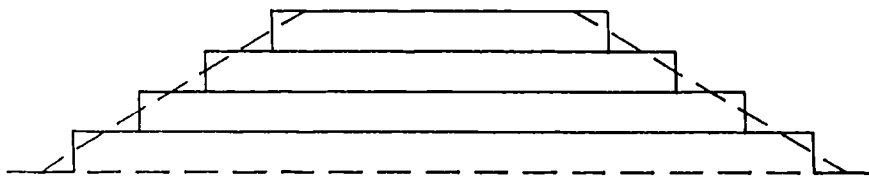


Figure 6.18 Modelling technique for non-uniformly vibrating apertures.

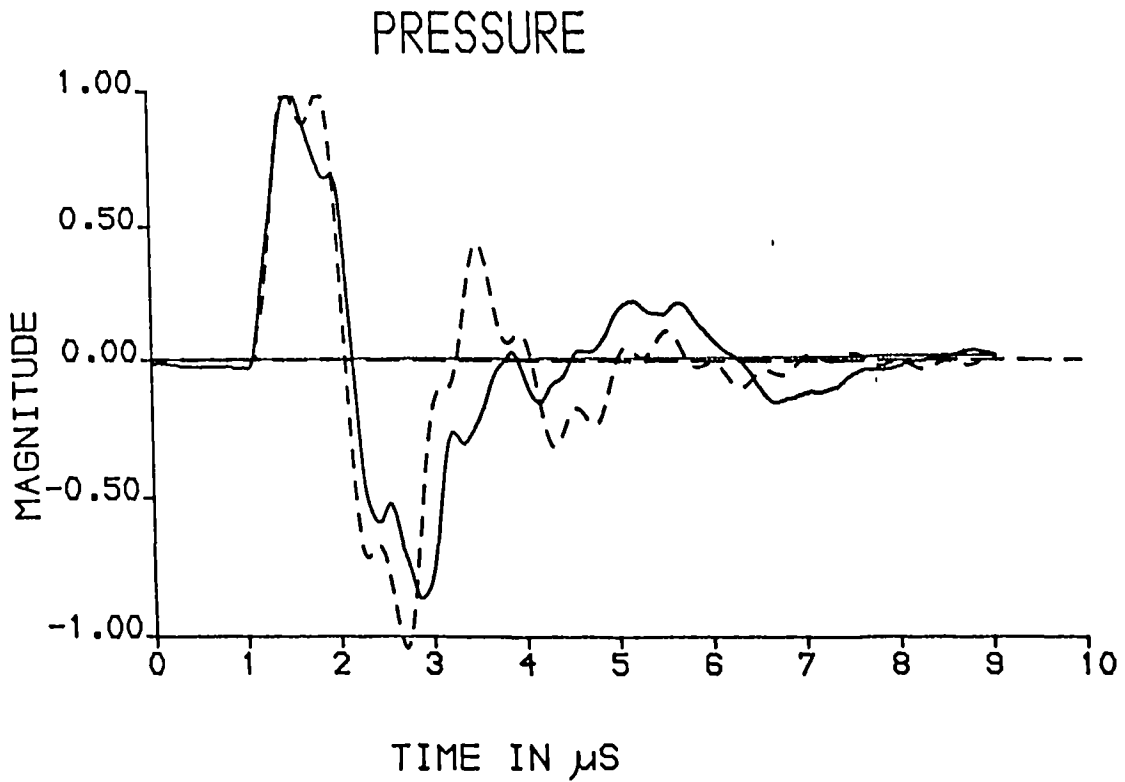
arbitrary transducer excitation function can be calculated. The complete system takes the form of Equation 6.22.

$$P(x,t) = - P_o(t) * \rho \frac{\delta}{\delta t} h(x,t) \quad 6.22$$

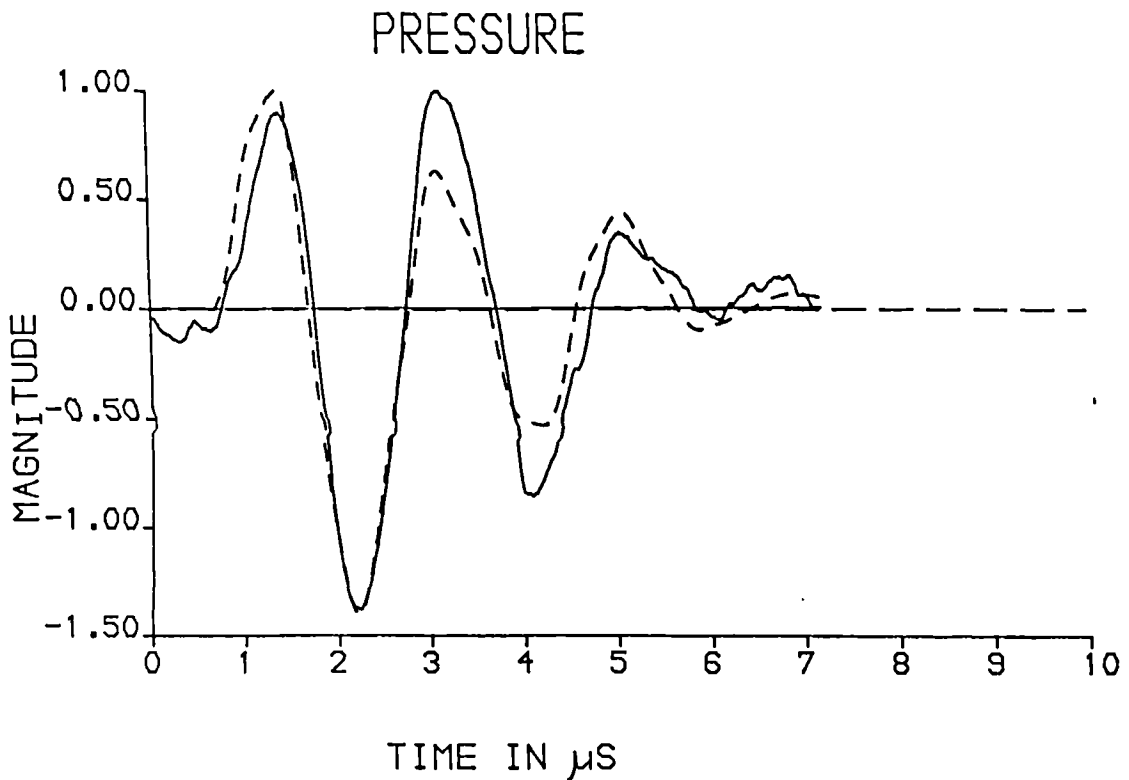
The versatility of this expression may be further enhanced if the aperture pressure function, $P_o(t)$, at the face of the transducer, can be determined by theoretical techniques. In general, any suitable thickness mode transducer model may be used to predict the transducer surface displacement as a function of the input excitation voltage and electrical and mechanical loading. If the voltage excitation function is $V_o(t)$ and the transducer thickness mode pressure transfer function is $w(t)$, then the entire system is described by Equation 6.23.

$$P(x,t) = - V_o(t) * w(t) * \rho \frac{\delta}{\delta t} h(x,t) \quad 6.23$$

Thus, a general model for the pressure response at an arbitrary point in the field is obtained. Using this model, the directivity characteristics of various structures may be derived, and compared with experimentally observed results.



Response at perpendicular range = 15mm.
 Experimental
 Simulated - - - - -



Response at perpendicular range = 15mm, 10mm off axis.
 Experimental
 Simulated - - - - -

Figure 6.19 Normalised theoretical and simulated pressure responses measured at two positions in the field of a 1.43 x 25mm 500kHz composite transducer.

6.4 FIELD CHARACTERISTICS OF PRACTICAL ARRAYS

6.4 i) Introduction

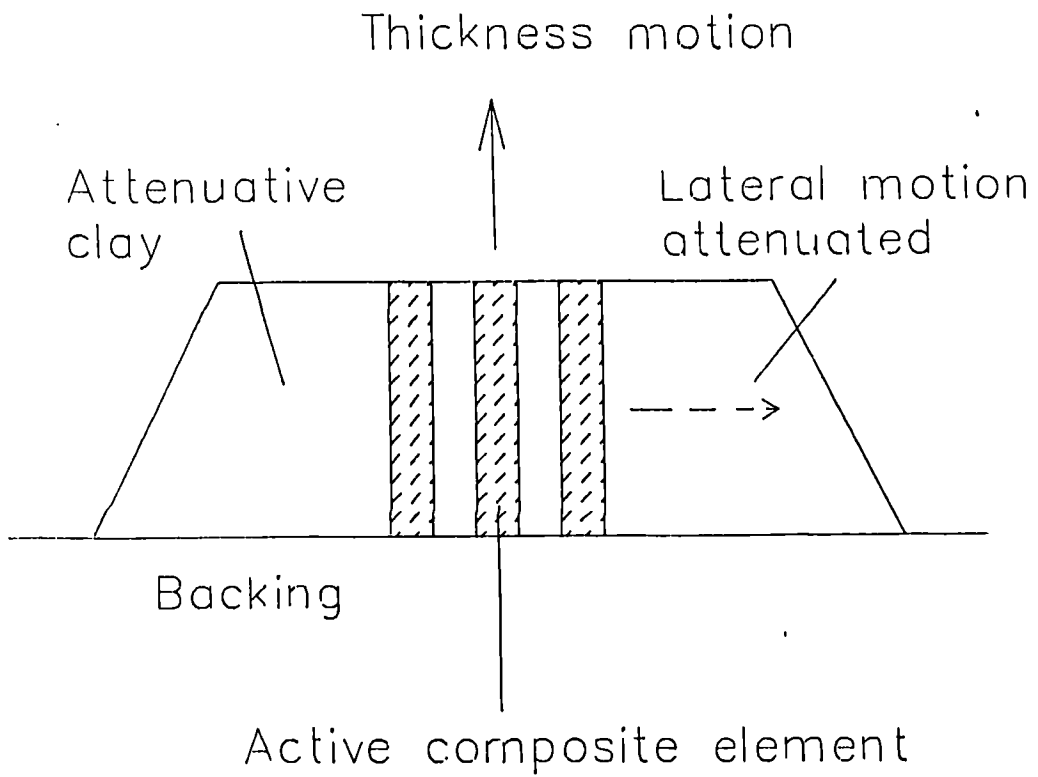
Previous work on the field characteristics of practical ultrasonic phased arrays has concentrated on sliced ceramic configurations. A number of conclusions, of relevance to the present discussion, are presented.

The directivity of elements is almost invariably inferior to that predicted due to non-ideal vibration of the aperture. In particular, Kino recommends that inter element electrical and mechanical coupling should not exceed -30dB, if a reasonable directivity is required [56]. It has also been observed that the correlation between theoretical and experimental directivity at wide angles, relative to the perpendicular direction, is exceptionally poor. Smith [57] suggested that as a thickness expanding element vibrates, the Poisson ratio effect gives rise to a significant anti-phase pressure component emanating from the sides of the elements. Smith used a simple model to generate significantly degraded, and more realistic, directivity characteristics.

6.4 ii) Field characteristics of isolated elements.

In view of the degradation in spatial response that is encountered in complete array structures, it is simpler to consider firstly the response of isolated array elements.

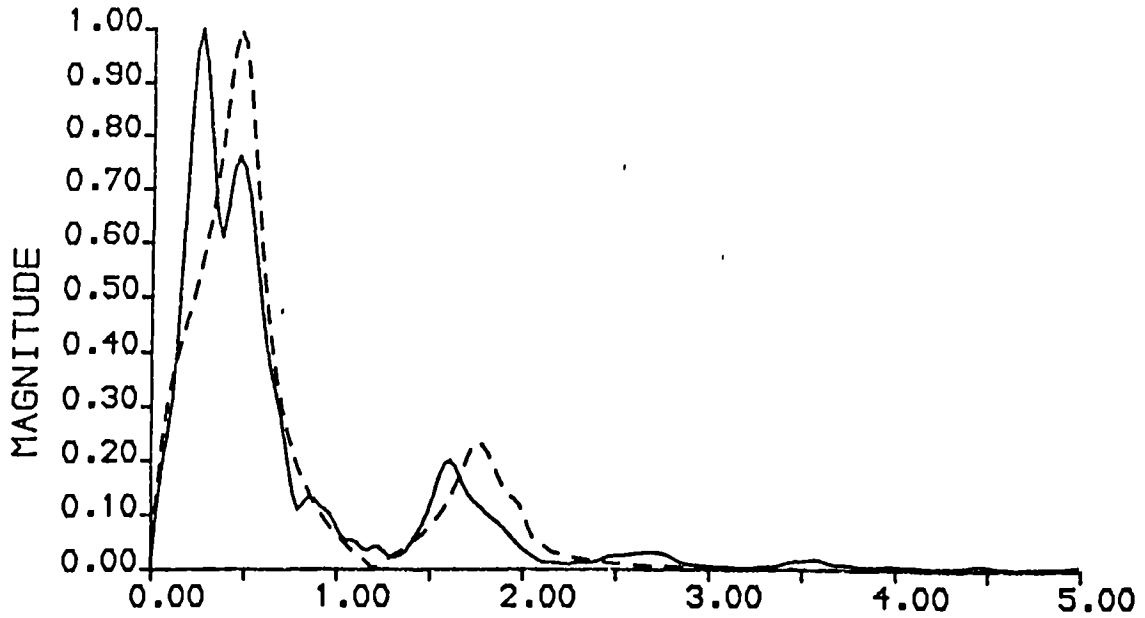
Figure 6.19 illustrates the measured and predicted pressure profiles for a backed and matched isolated



NB Clay removed at a later stage

Figure 6.20 Configuration of composite array element, including modelling clay and backing.

PRESSURE

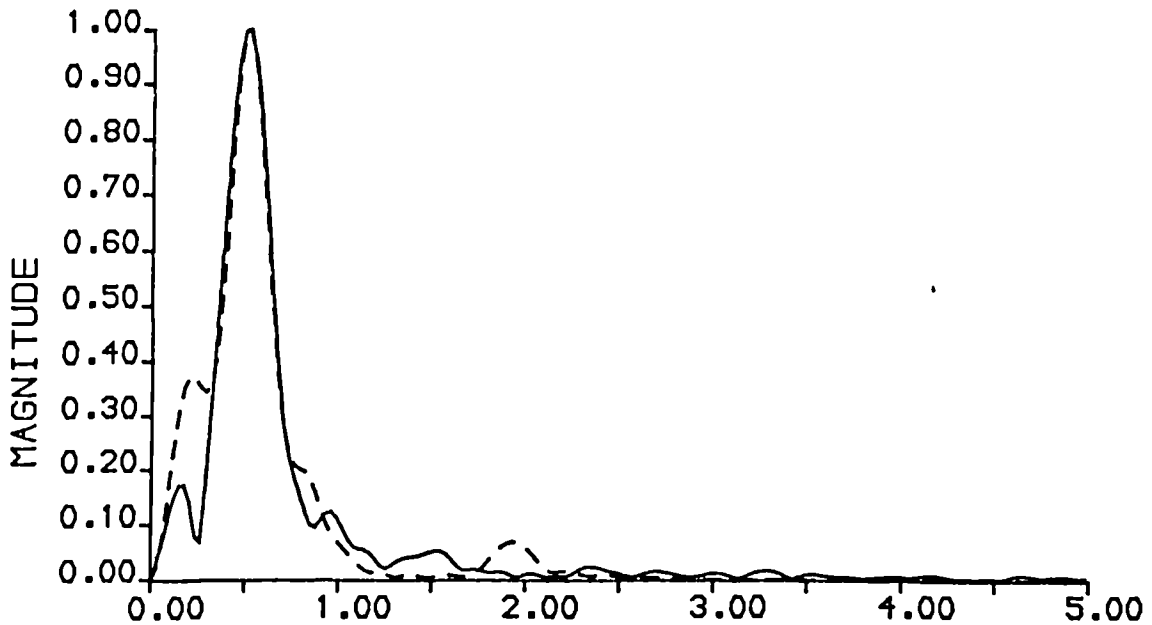


FREQUENCY IN MHz

Response spectra at perpendicular range = 15mm.

Experimental —————
Simulated - - - - -

PRESSURE



FREQUENCY IN MHz

Response spectra at perpendicular range = 15mm, 10mm off axis.

Experimental —————
Simulated - - - - -

Figure 6.21 Normalised theoretical and simulated pressure response spectra measured at two positions in the field of a 1.43 x 25mm 500kHz composite transducer.

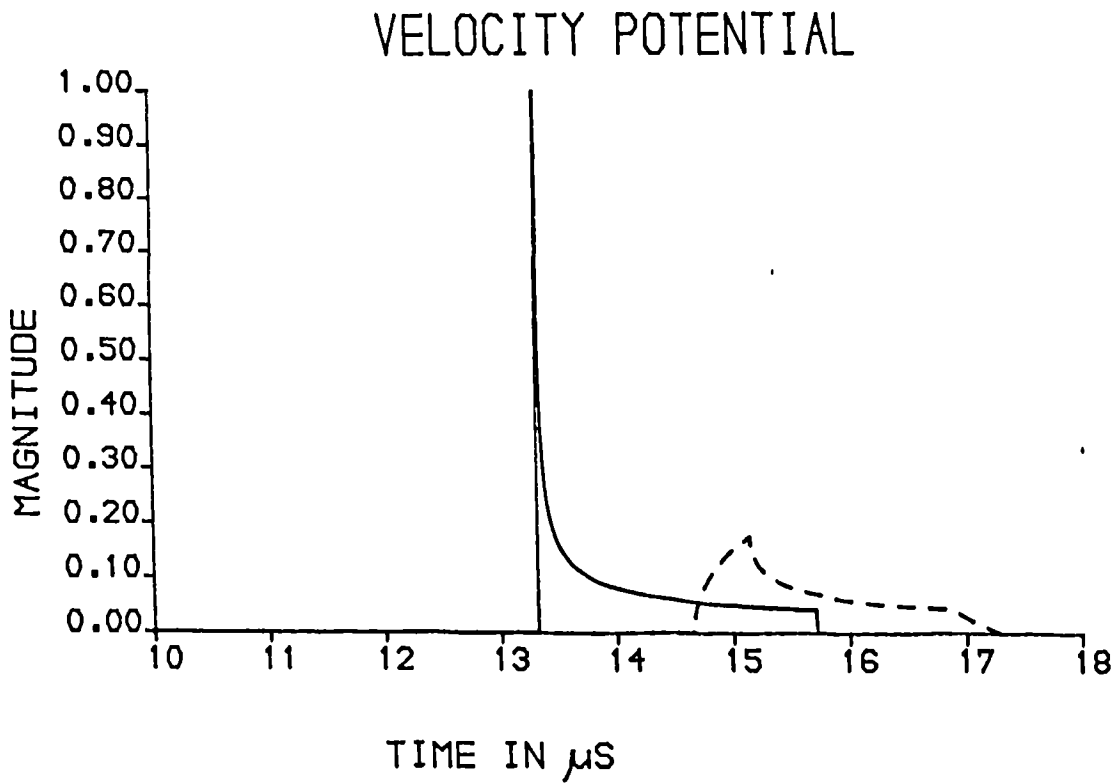


Figure 6.22 Velocity potential impulse response of 1.42 x 25mm aperture at two positions in the field.
 Response at perpendicular range = 15mm. ———
 Response at perpendicular range = 15mm, 10mm off axis. - - - -

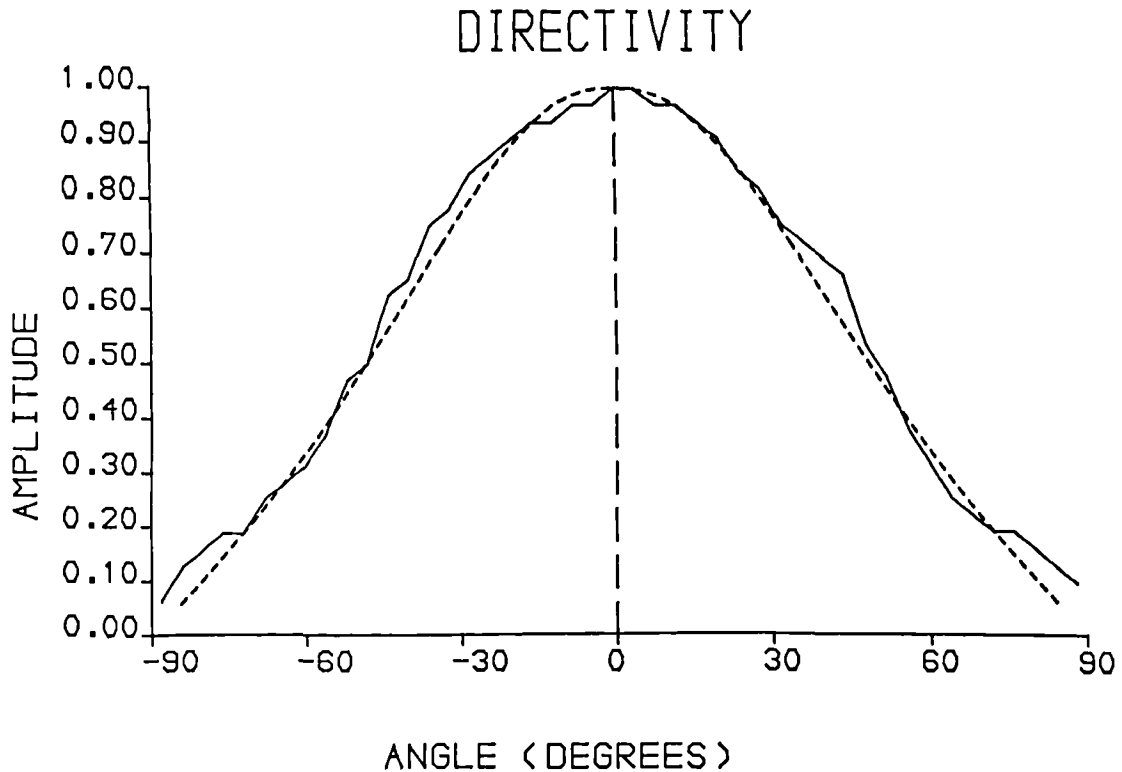


Figure 6.23 Theoretical and measured CW directivity characteristics of 1.43 x 25mm element. Operating at 500kHz and measured at a range of 120mm. Modelling clay included.
 Measured ———
 Theoretical - - - -

composite array element. The array element is 1.43mm wide by 25mm long and possesses three rows of ceramic pillars in the width direction. It possesses a 40% ceramic volume fraction and is 3mm thick. The element is unmatched, but is mounted on a tungsten loaded backing block. The transducer was excited with a step function from a standard pulser circuit - as described in Appendix E ii). The effect of energy propagating from the sides is not included in this case and hence it was necessary to suppress this energy in the practical element by applying a lossy modelling clay to the lateral faces. This successfully served the purpose of satisfactorily attenuating laterally propagating energy. The configuration is illustrated in Figure 6.20. The diffracted response on axis at a perpendicular range of 15mm, and also at 10mm off axis, at perpendicular range of 15mm are illustrated in Figure 6.19. The complete model, encompassing both the transducer model and the diffraction model, has provided reasonably accurate results. The principal features in the pressure responses have been replicated.

Figure 6.21 illustrates the spectral magnitude characteristics of the time domain responses in Figure 6.19. Again, reasonable correlation is observed between measured and simulated data. The effect of diffraction on the high frequency spectral component has been correctly modelled. When the observation point is off-axis, the corresponding velocity potential and pressure impulse

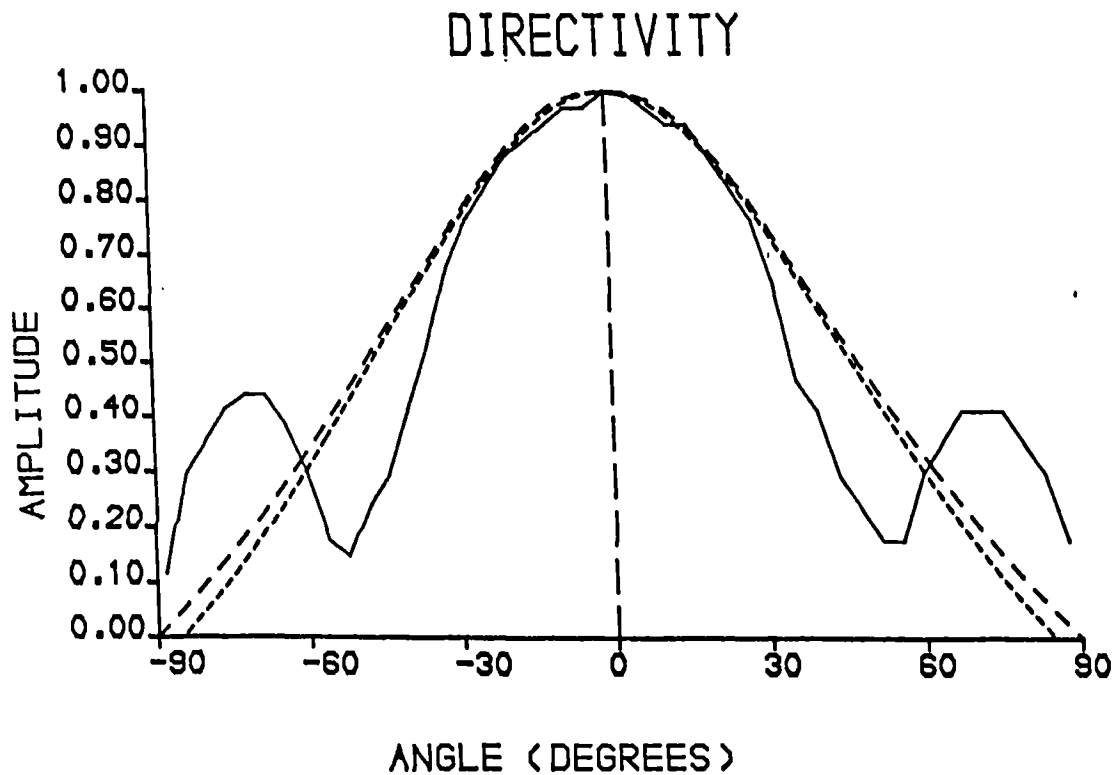


Figure 6.24 Theoretical and measured CW directivity characteristics of 1.43 x 25mm element. Operating at 500kHz and measured at a range of 120mm. Modelling clay removed.

- Theoretical CW model
- . - . - . Theoretical CW model, including the effect of anti-phase lateral motion.
- Measured

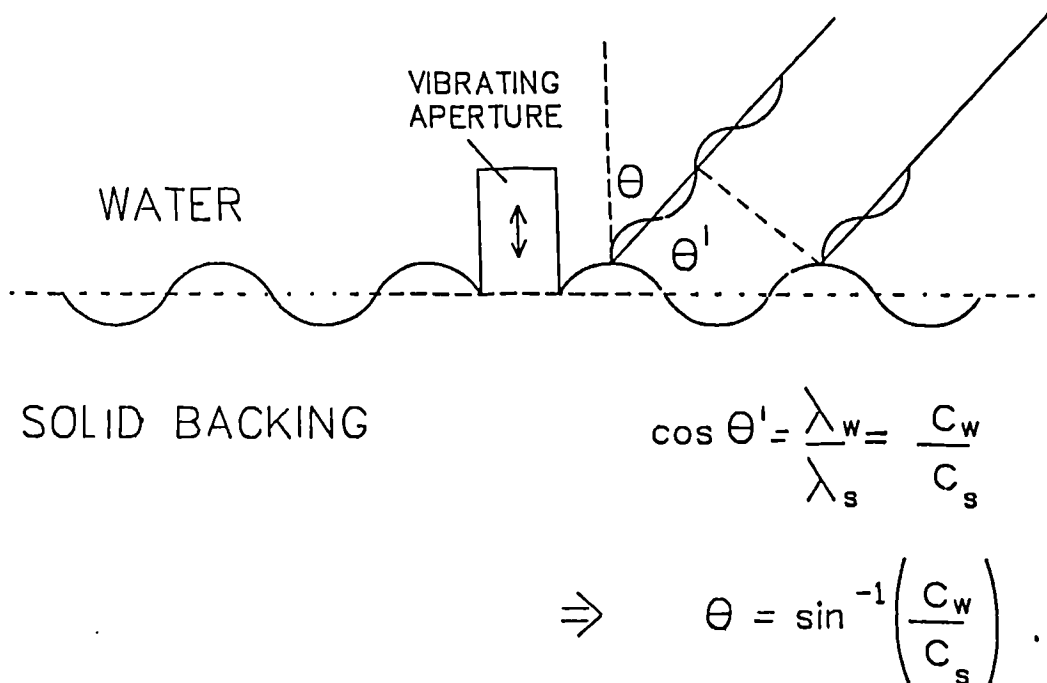


Figure 6.25 Relationship between transversely propagating surface waves and constructive interference, at a specific angle, in an adjacent fluid medium.

response contains few impulse type features. Hence, if the pressure impulse response is bandlimited, the resulting convolved transient pressure response experiences bandlimiting. The velocity potential impulse response associated with the two positions considered above, are illustrated in Figure 6.22. The off-axis response is clearly bandlimited.

The complete model may now be used to compute the element directivity characteristic. This characteristic defines the peak to peak amplitude of the diffracted response as a function of the observation angle with respect to an perpendicular axis emanating from the centre of the active element. Figure 6.23 illustrates the measured and simulated CW directivity of the same isolated element. Excellent correlation between the two results may be observed.

The response of the same element, but with the modelling clay removed from its lateral faces, is illustrated in Figure 6.24. A strong sidelobe feature is apparent at approximately 70° . Since this lobe is not evident in Figure 6.23, the lobe may be attributed to energy propagating from the sides of the element, or to energy propagating along the surface of the backing block. Finite element analysis has been performed for this configuration. The average lateral displacement was one twentieth of the thickness displacement. The diffraction model has been extended so as to permit the inclusion of several active apertures operating in perpendicular

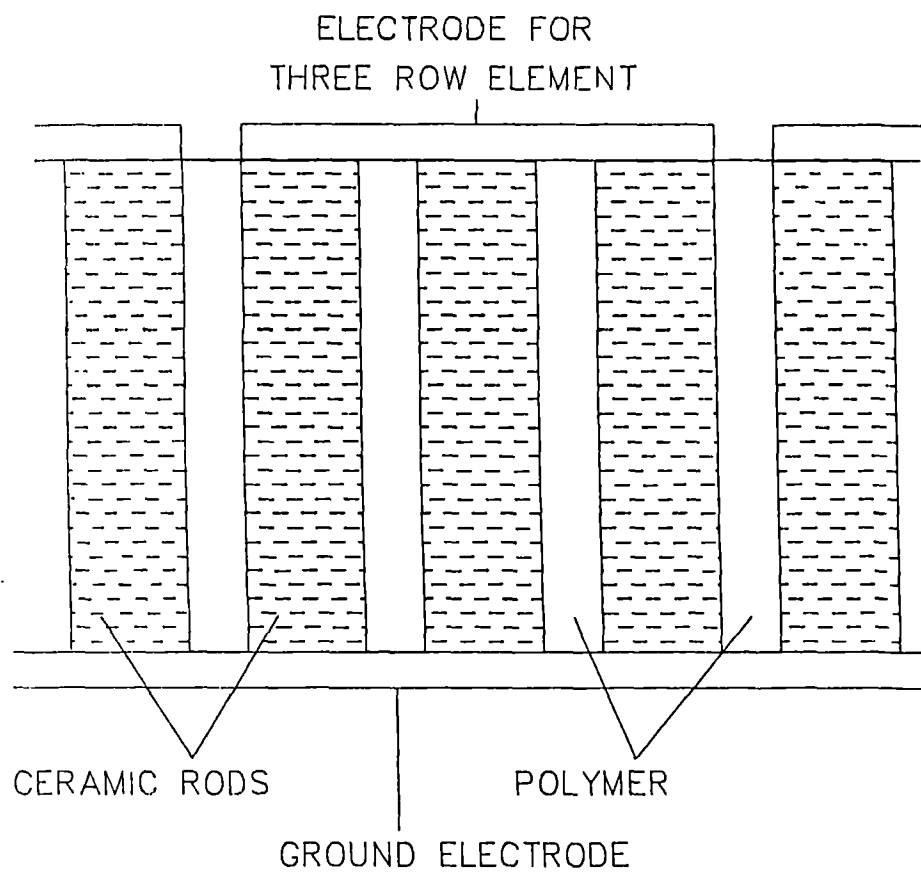


Figure 6.26 Cross-section of a typical composite array element.

directions. Phase differences are also included. The pressure contributions at the observation points in the field are summed and a net directivity function obtained. Figure 6.24 illustrates the modified directivity obtained when lateral activity is included. The lobe structure observed in the measured response has not been replicated and hence it is evident that laterally propagating energy from the element is not the major cause of the significant lobes. Instead, it is believed that these lobes are attributable to waves propagating outwards, along the surface. Referring to Figure 6.25, it is evident that an outward propagating surface wave gives rise to constructive wave interference at a particular angle. This angle is related to the ratio of wave velocities in the load and backing mediums. Using the measured value of the lobe angle, the estimated surface wave velocity in the tungsten load backing block is 1600ms^{-1} . Although an independent measure of this wave velocity has not been made, this figure correlates well with the transverse wave velocity of similar materials reported in the literature [58]. The velocity of these surface waves are typically approximately 95% of the wave velocity of the transverse wave velocity [50].

DIRECTIVITY

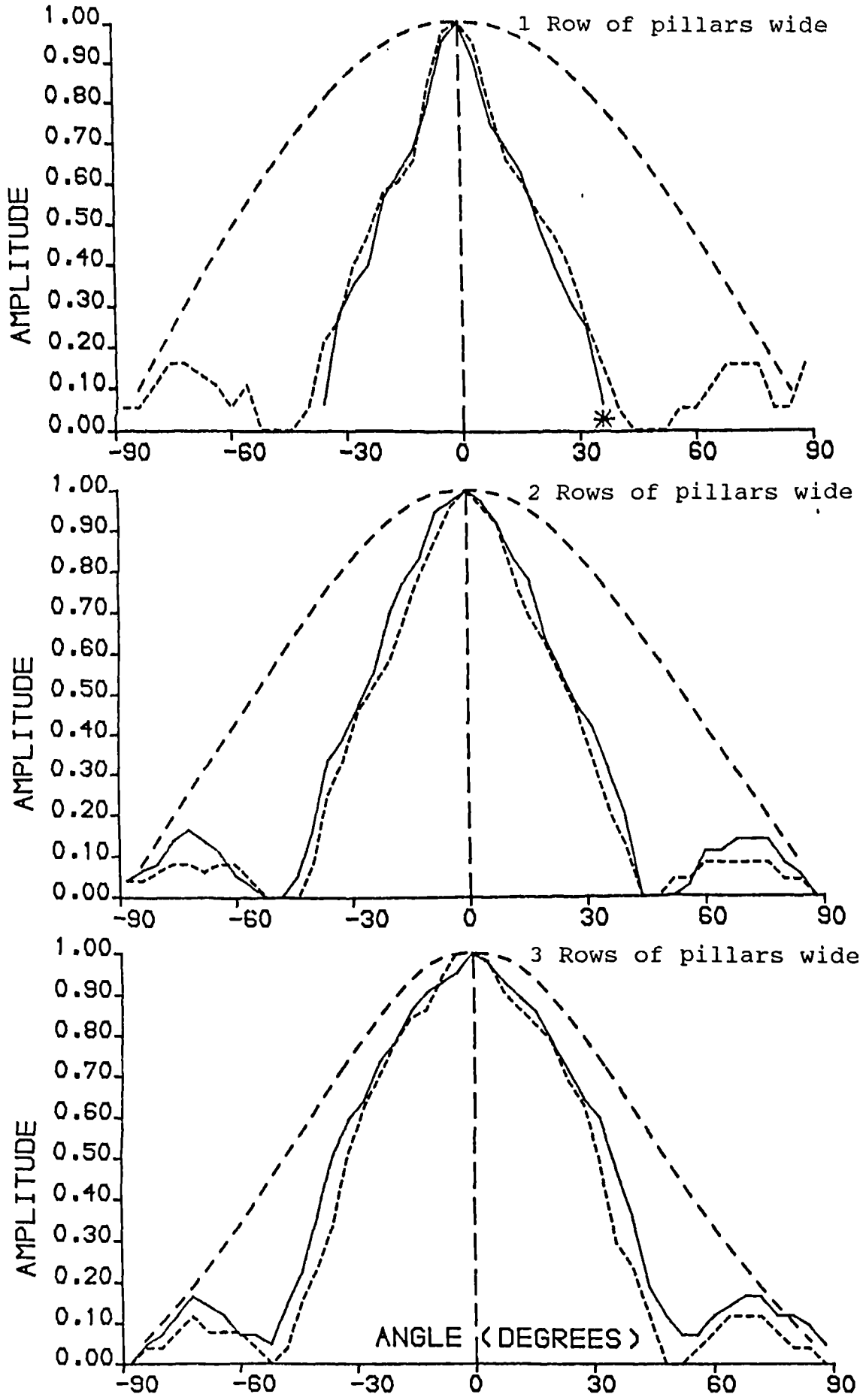


Figure 6.27 Measured and theoretical 500kHz CW directivity characteristics for three composite array configurations.

- Measured (air backed)
- Backed (3MRayl)
- - - - - Theoretical CW model
- * - Signals masked by noise beyond this angle

6.4 iii) Field characteristics of practical composite elements operating under CW excitation

The directivity characteristics of elements depends critically on the device geometry, rear loading, front face matching and the nature of the electrical excitation. These factors are considered briefly. Unless specified otherwise, the composite element is 3mm thick and possesses PZT 5A pillars, each 0.33mm across, and spaced at a centre to centre pitch of 0.55mm. This configuration is typical of that which may be found in a practical composite array, designed for 500kHz operation into water.

It has generally been assumed that inter-element isolation between composite array elements, which are defined by the electrode alone, is sufficient to merit that subdicing between elements is not necessary [4,21]. Therefore, a typical composite array element takes the form of that illustrated in Figure 6.26. The signal electrode typically excites two or more rows of pillars, depending on the design. A common ground electrode is employed.

Initially, an investigation of the influence of backing on directivity was performed. It would be expected that if a significant amount of energy is propagated laterally outwards from the excited element, then a backing medium would serve to absorb some of this energy. However, if the backing is excessively rigid, it might also provide a channel through which energy may be coupled to adjacent elements. Figure 6.27 illustrates the CW directivities of

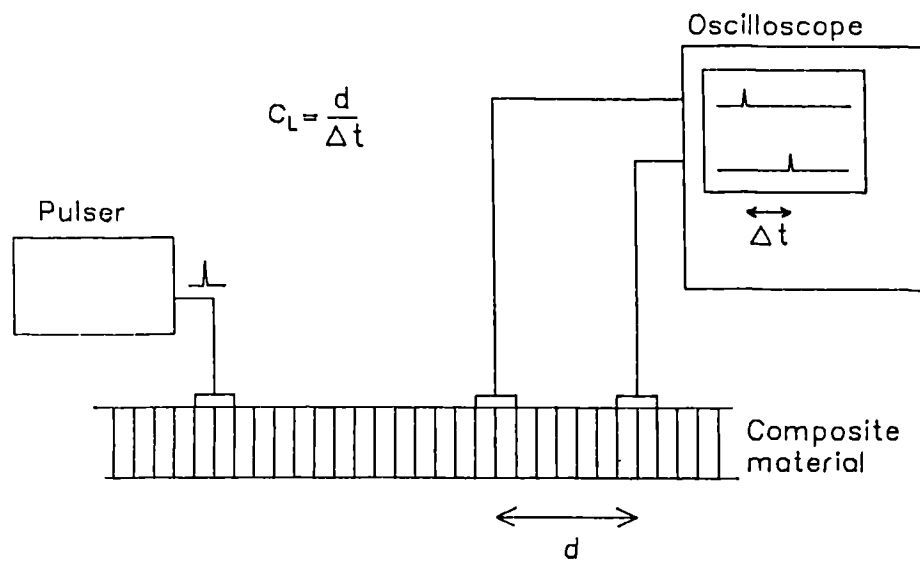


Figure 6.28 Experimental configuration employed for calculating Lamb wave velocity. Time interval between pulses, and distance between measured points, are monitored.

elements possessing one, two and three rows of active pillars, for both air backed and soft epoxy backed conditions. The theoretical CW directivity, assuming an ideal aperture, with no activity outwith the excited element, has also been superimposed. It may be observed that the backing has had the effect of slightly dampening the side lobe feature. However, the general shape of the experimental curves indicate that significant amounts of energy are still being propagated outwards from the active element. The narrowest element exhibits the narrowest directivity, relative to the theoretical curve, and hence this suggests that it emits the greatest amount of lateral energy in proportion to thickness propagating energy. This observation is satisfactory from an intuitive viewpoint since this element possesses the largest ratio of lateral surface area to thickness surface area.

Discussion of the field characteristics of composite elements in the literature is very limited. However, Shaulov [22] has recently observed similar lobe structures. These were attributed to Lamb waves propagating in the composite material. The presence of Lamb modes in array structures described has been verified using two methods.

Firstly, the Lamb wave velocity was calculated using the experimental apparatus illustrated in Figure 6.28. An impulse excitation was applied to one element and the interval between the times of arrival of the laterally propagating Lamb wave at two distinct, spaced elements

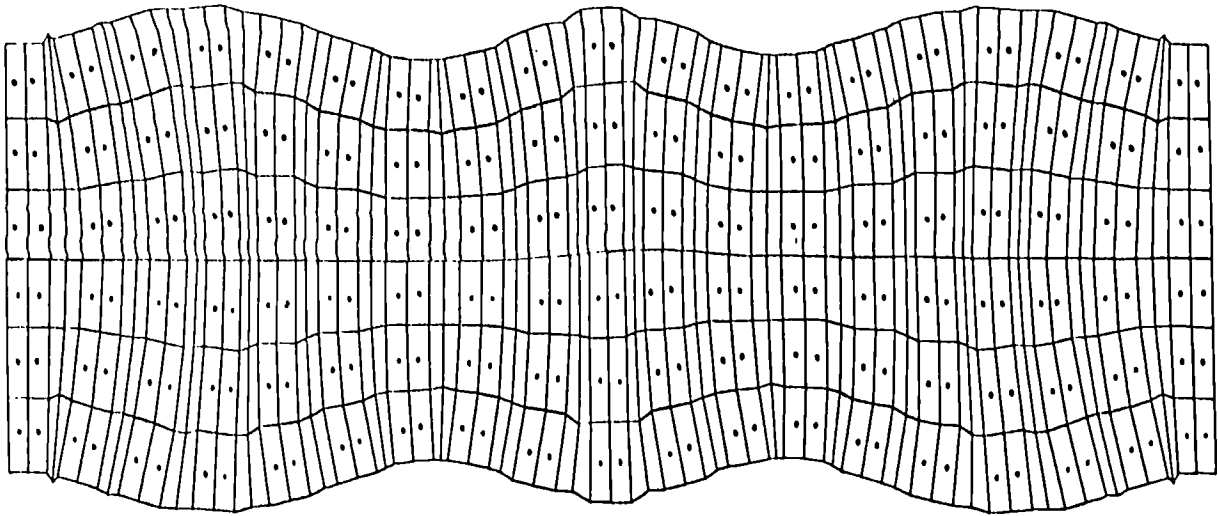


Figure 6.29 Lamb wave type displacement in a composite array determined using finite element analysis. This mode occurs at 610kHz.

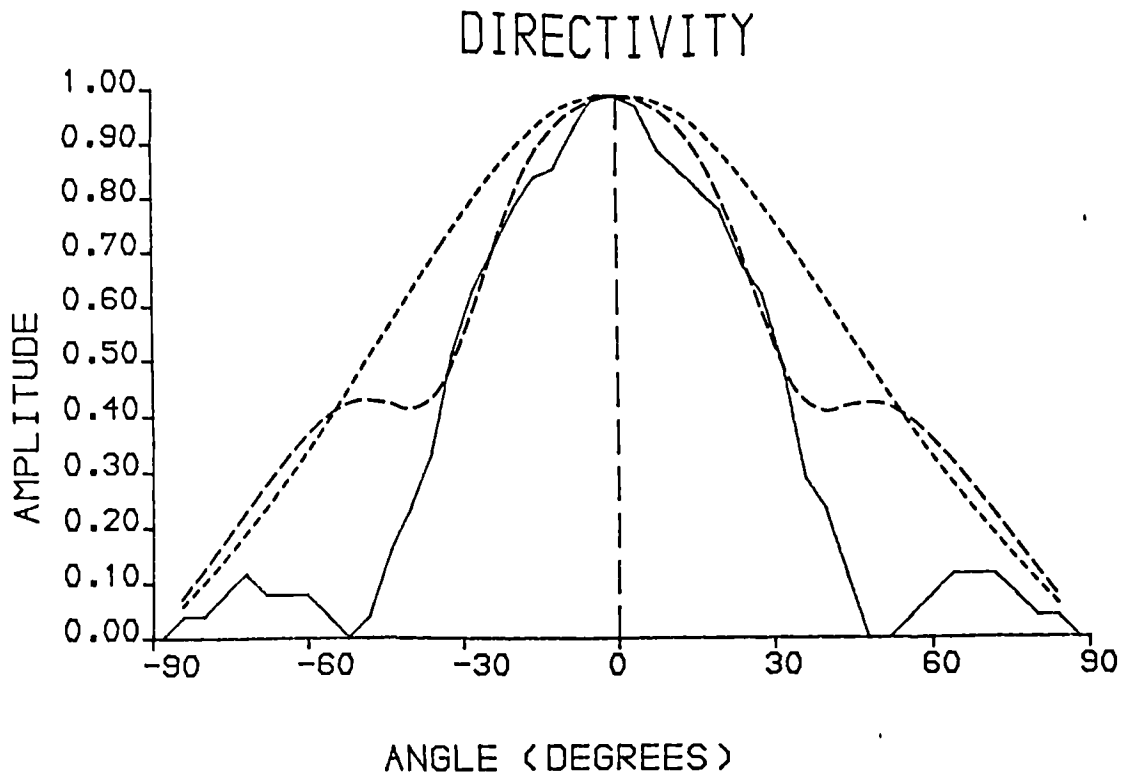


Figure 6.30 Measured and theoretical 500kHz CW directivity of a three row wide composite array element.
 Measured —————

 Theoretical, taking account of FEA displacement profile

-.-.-.-.-
 Theoretical, assuming uniform displacement

recorded. Using this time interval, and a knowledge of the spacing between the elements, the Lamb wave velocity was calculated to be 1660ms^{-1} . This wave velocity gives rise to a lobe at 65° , when the array is operating into water. This angle corresponds well with that observed experimentally.

Secondly, finite element analysis of the composite array structure was performed. Figure 6.29 illustrates a significant laterally propagating wave on the surface of structure adjacent to the excited element. The wavelength of this wave is 2.8mm at a frequency of 610kHz . This corresponds to a wave velocity of 1700ms^{-1} . The correlation between this result, and that presented above, is excellent.

The displacement profile, as determined by finite element analysis, has been used as the basis of a more accurate prediction of composite element directivity. This profile, illustrated in Figure 6.29, was simulated as an array of ideal elements, each possessing appropriate weighting and phasing. Figure 6.30 illustrates the new simulated directivity, the measured directivity, and the directivity predicted assuming only pure thickness vibration of the excited aperture. The improved simulated directivity has produced a very approximate estimate of the practical lobe structure. Clearly, this result could be further improved by extending the finite element mesh so that the entire array structure, and not just a small portion, is analysed. Furthermore, the finite element

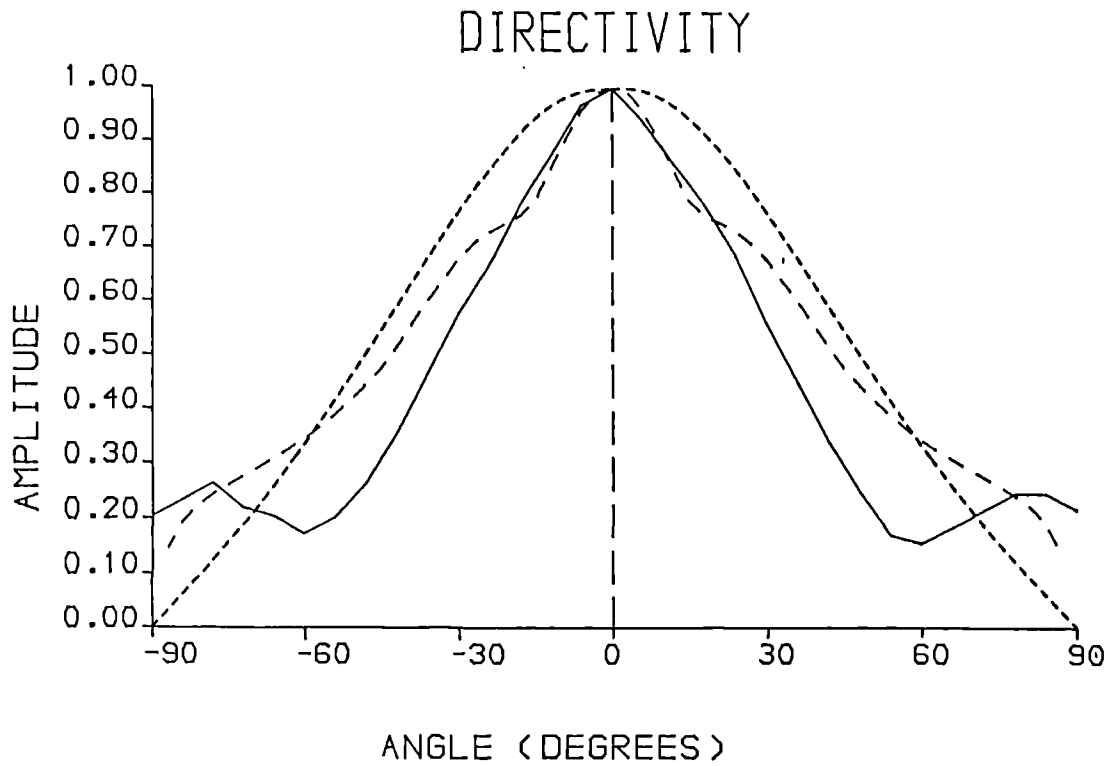


Figure 6.31 Measured and theoretical directivity characteristics of a three row wide composite array element for transient (step) excitation.

Measured —————
 Theoretical (Transient) - - - - -
 Theoretical (CW) - - - - -

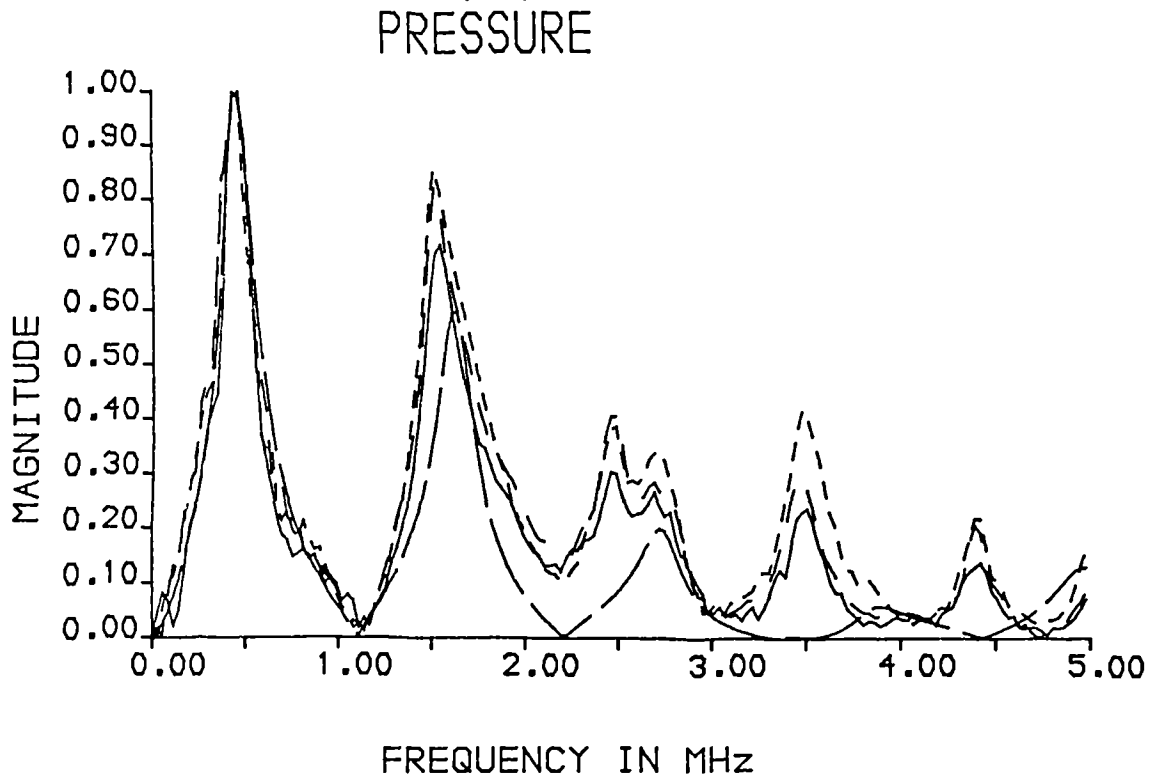


Figure 6.32 Measured and theoretical pressure output spectra of composite array elements possessing one, two and three rows of pillars.

————— Measured (1 row)
 - - - - - Measured (2 rows)
 - - - - - Measured (3 rows)
 ———— Theoretical (1 row)

(Theoretical results for 2 and 3 rows are not measurably different)

analysis has not included the effects of acoustic attenuation which occur in practice, but which are difficult to quantify.

6.4 iv) Field characteristics of practical composite elements operating under transient excitation

It is apparent that the directivity obtained when transient excitation is employed will be different from that observed when CW excitation is used. This is principally because a transiently generated pressure function contains a diverse range of spectral components, each of which is modified to a differing extent by the diffraction process. High frequency components tend to collimate along the axis, resulting in a narrower, and more peaked, directivity function. However, the extent of these effects can be modelled using the transducer and diffraction models previously described.

Figure 6.31 illustrates the measured and simulated directivity characteristic of a composite element possessing three rows of pillars operating under transient excitation. Again, the elements are backed with a soft setting epoxy. It is evident from the figure that transient excitation results in a narrower directivity than that obtained for CW excitation. However, the transient diffraction model has provided an approximate estimate of the practical directivity. It may be observed that the lobe structures caused by Lamb mode propagation are weaker when transient excitation is employed. Under CW

conditions, the composite structure is able to support a virtually steady state Lamb mode propagating along the plate. However, under transient excitation, the pulse decays before steady state Lamb mode propagation is established. It should be noted that the spectral content of the pressure response has been limited to approximately the third harmonic using a low pass R-C filter with a -3dB cut off frequency of 2MHz. The higher components result in added complexity and are of little practical consequence, except when the observation point is exactly on axis.

The foregoing results indicate that narrow elements possess relatively disappointing characteristics. It is necessary to establish definitively that this is due to the mechanical characteristics of the vibrating aperture and not the spectral content of pressure output wavelets. The magnitude spectra of the responses of elements possessing one, two and three active rows of pillars, are illustrated in Figure 6.32. These responses were not filtered and were measured precisely on axis at a range 120mm. A simulated response, taking account of diffraction has also been generated. The figure indicates extremely close correlation between the spectral content of the three elements. The simulated response is reasonably accurate up to the fifth harmonic. It would be unreasonable to expect the model to be accurate beyond this frequency due to the presence of further complicating factors. For example, the distinctive feature at 2.6MHz in the experimental curves is due to the fundamental

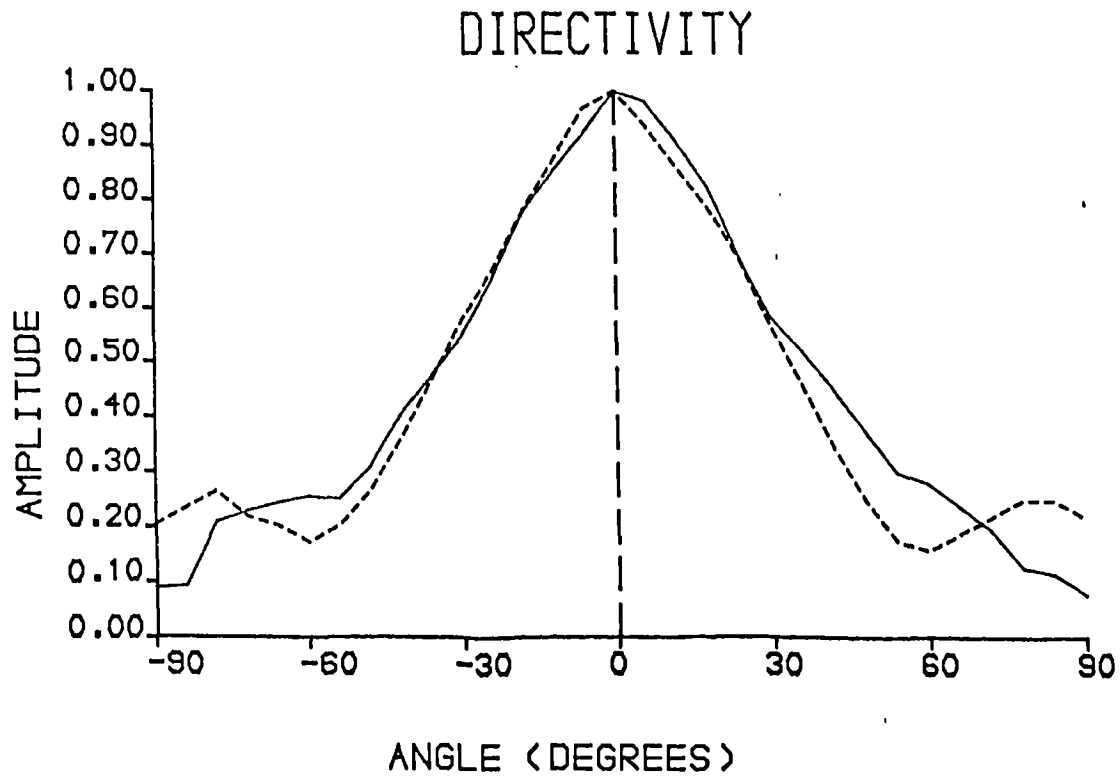


Figure 6.33 Measured and theoretical directivity (transient excitation) of three row wide composite array element.
 Conventional epoxy filler (CY1301/HY1300) -----
 Microballoon loaded epoxy filler _____

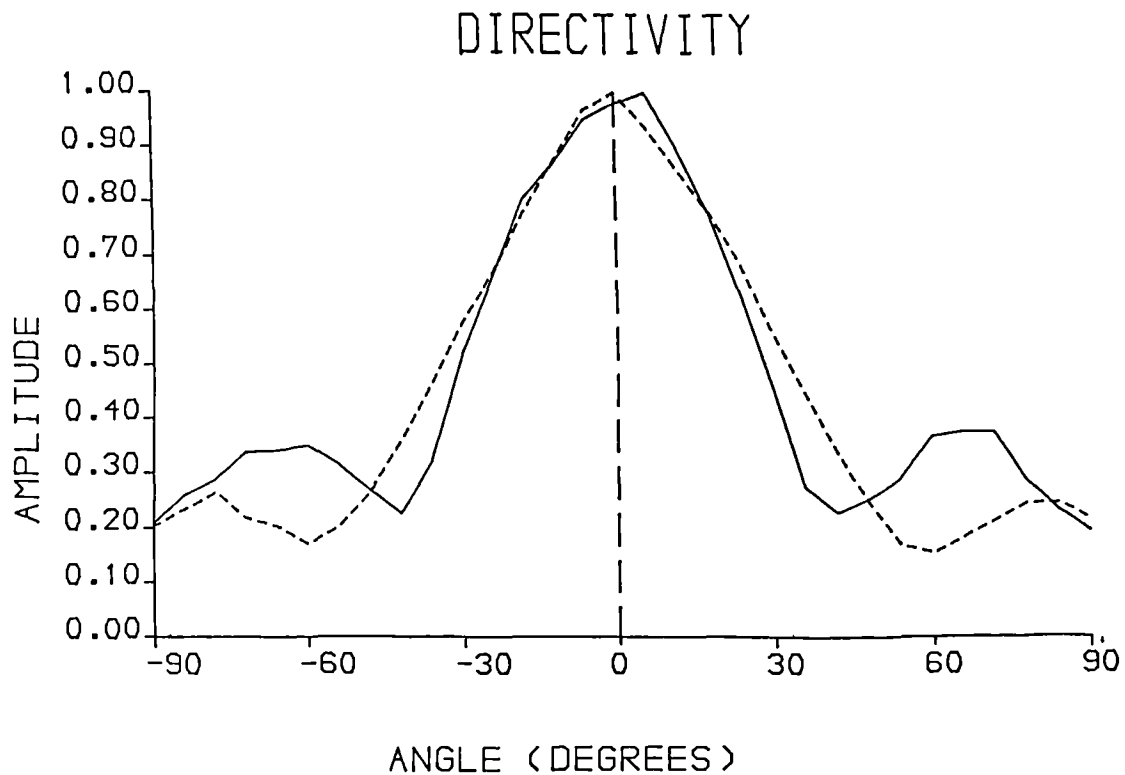


Figure 6.34 Measured and theoretical directivity (transient excitation) of three row wide composite array element.
 ----- Without matching layer
 _____ Including quarter wavelength epoxy matching layer

inter-pillar, polymer resonance which occurs at precisely this frequency. This resonance, which is well separated from the thickness fundamental, has a small but very distinctive influence on the pressure response of the device. The need to ensure that the inter-pillar resonance is well separated from the fundamental thickness resonant frequency is readily apparent. Ideally, this resonance should be located at one of the thickness mode nulls, and hence, the inter-pillar resonance would not be initiated by thickness activity.

Finally, the directivity characteristics of an element which was three rows wide, and has been partially isolated from its neighbouring elements by employing a lossy, microballoon loaded filler between the elements, are considered. It was believed that the lossy polymer would suppress some of the laterally propagating energy. Hence, an improved directivity characteristic was anticipated. The directivity of a prototype element, loaded on both sides with microballoon loaded epoxy, is compared with that of a conventional composite element in Figure 6.33. A modest improvement has been achieved, indicating that the laterally propagating energy has in fact been attenuated. Figure 6.34 illustrates the directivity characteristic of a conventional three row element incorporating a quarter wavelength epoxy matching layer. The matching layer was expected to widen the effective vibrating aperture and result in increased inter-element coupling. However, the figure indicates that the resulting degradation of the

DIRECTIVITY

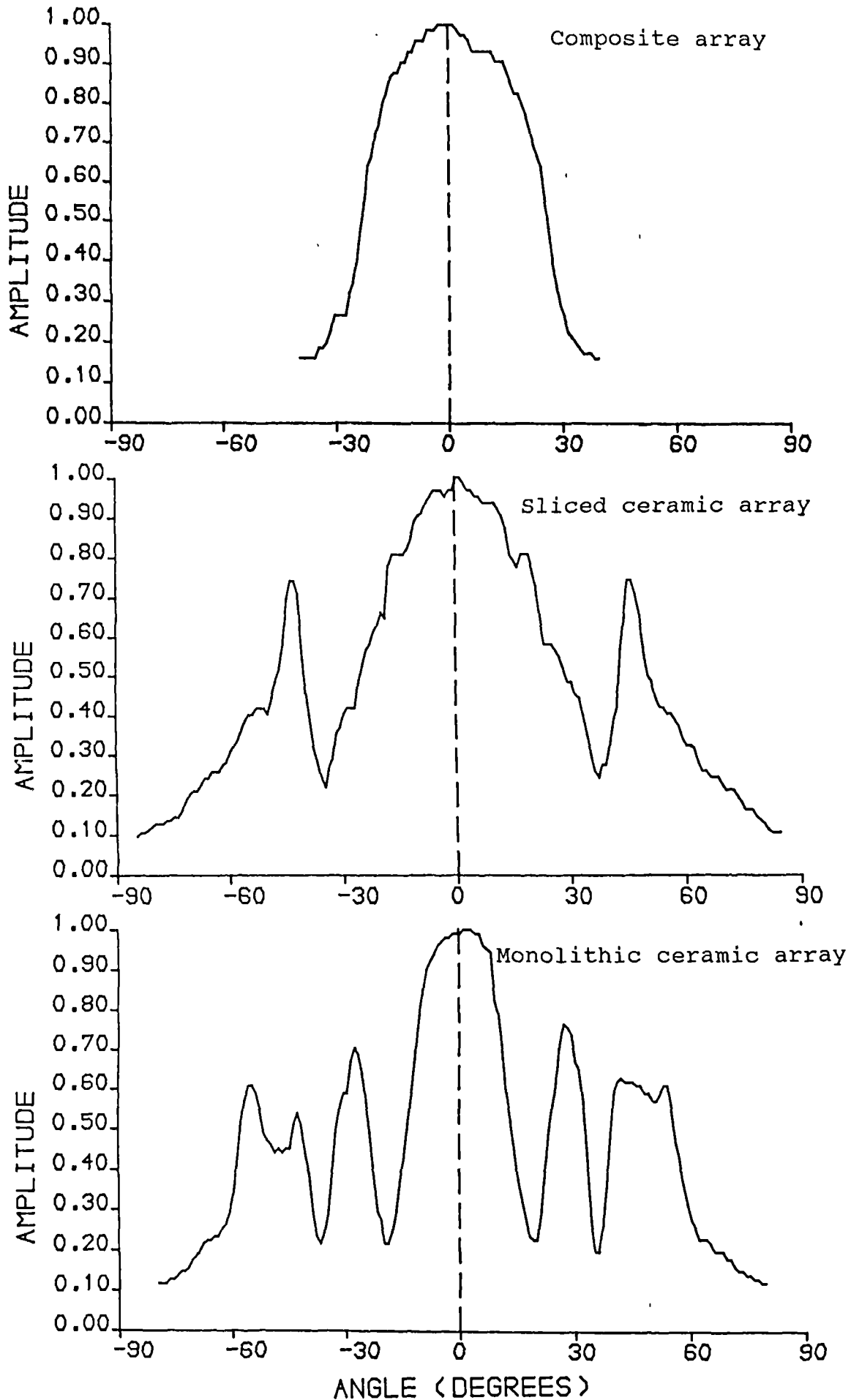


Figure 6.35 Transmission CW characteristics of practical 500kHz array elements.

* Signals masked by noise beyond this angle

main lobe directivity is modest, but sidelobe levels have increased significantly.

6.4 v) Comparison of the spatial characteristics of composite and conventional array elements

A brief comparison of the directivity characteristics of various array structures is made. Figure 6.35 compares the transmission CW single element directivities of complete composite, sliced and monolithic arrays. These arrays possess elements spaced with a 1.65mm pitch. Details of the manufacture and specification are described in Appendix C. The sliced array has a centre frequency of 350kHz, compared with 500kHz in the other arrays. This lower frequency explains why the sliced array possesses the widest main lobe. It is readily apparent that the sliced array possesses a major lobe at 45° . This lobe is probably the result of inter-element coupling occurring in the matching layer. Alternatively, Lamb type modes may exist within the matching layer. The directivity is clearly inferior to that obtained for the composite array. However, noise masked the response of the composite array when the angle of observation was more than 40° off axis.

The monolithic array demonstrates considerable lobe activity. Additionally, the main lobe is narrow indicating that the effective thickness vibrating aperture is considerably wider than a single element. The lobe at 30° is attributed to Lamb wave propagation extending from the excited element outwards through the ceramic plate. The

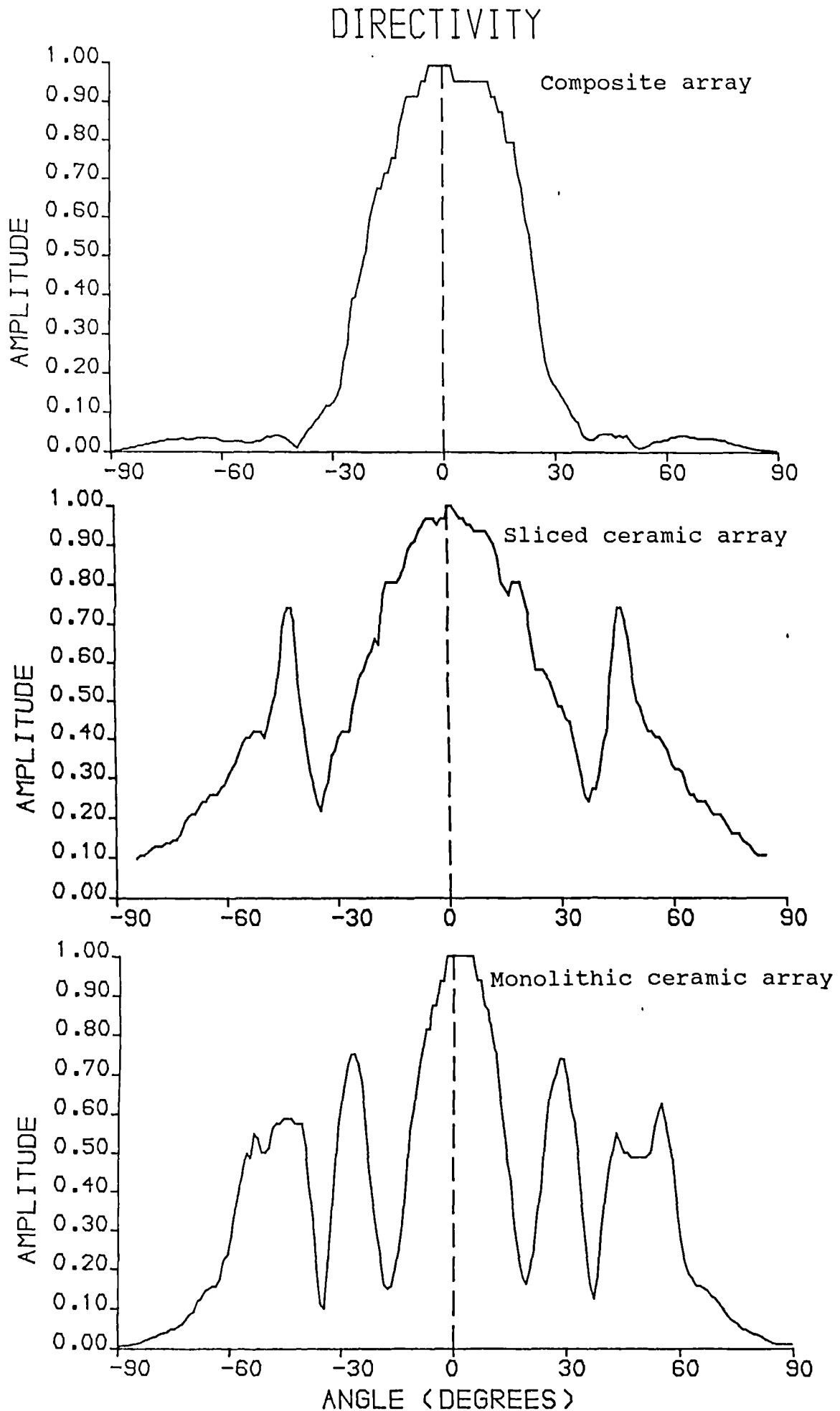


Figure 6.36 Reception CW characteristics of practical 500kHz array elements.

second lobe at 50° is also typical of those encountered by other investigators measuring the directivity characteristics of monolithic arrays in water [59].

The CW reception characteristics of the three arrays are illustrated in Figure 6.36. In this case, the response of the composite array at wide angles was not masked by noise. No significant lobes are apparent in this array. The transmission and reception characteristics demonstrate a high degree of reciprocity in terms of array element behaviour.

TABLE 6.1

Capacitance of array elements as a function of width in terms of rows of pillars

Number of rows	Experiment	Theory
1	16	16
2	33	31
3	47	47
4	61	63
5	76	78

Capacitances in pF. Smith's model has been used for the theoretical values. The elements are 40% PZT 5A ceramic, 25mm long and 2.8mm thick. The pitch between rod centres is 0.6mm.

6.5 ELECTROMECHANICAL CHARACTERISTICS OF COMPOSITE ARRAYS

The electromechanical characteristics of array elements may deviate from those encountered in thickness mode plates. Therefore, the extent of any modification of the thickness mode parameters, as used in the model, must be determined. In sliced ceramic arrays, the thickness mode parameters may require to be modified by as much as 20%. Virtually no investigation of the electromechanical characteristics of composite array elements has been performed. Three key electromechanical properties are now considered.

6.5 i) Permittivity

The permittivity of the element determines its capacitance, which in turn has a profound influence on transmitted/ received signal levels. The permittivity of the polymer is negligible in comparison to that of the ceramic and hence makes virtually no contribution to the overall permittivity of the composite structure. Table 6.1 illustrates the dependence of capacitance on the width of a composite array element expressed in terms of the number of active rows of pillars per element. The capacitance increases linearly with the number of rows of pillars, and thus the permittivity matches exactly that associated with the entire thickness mode plate. Excellent correlation with results obtained using Smith's material parameter model, described in Chapter V, has been obtained.

TABLE 6.2

Velocity of array elements as a function of width in terms of rows of pillars

Number of rows	Experiment	Smith's	FEM
1	3493	3603	3670
2	3487	3603	3670
3	3516	3603	3670
4	3481	3603	3670
5	3504	3603	3670

Velocities in ms^{-1} . The elements are 40% PZT 5A ceramic, 25mm long and 2.8mm thick. The pitch between rod centres is 0.6mm.

6.5 ii) Velocity

An element's thickness and wave velocity determine its frequency of operation. In sliced ceramic array elements, the lack of lateral clamping results in a significantly reduced thickness elastic stiffness compared to that found in a thickness mode plate. Therefore, wave velocity is also reduced since density is independent of geometry. Table 6.2 illustrates the dependence of wave velocity on element configuration, for the same geometries as considered in the previous section. Experimental figures are compared with results obtained using finite element analysis and Smith's composite parameter [3]. Good correlation between the results is evident. Velocity, and hence centre frequency, can thus be considered independently of the number of active connected rows of pillars. However, the conclusions obtained in Chapter IV indicate that velocity is a function of ceramic volume fraction, and to a lesser extent, pillar aspect ratio.

6.5 iii) Electromechanical coupling coefficient

Although, on the basis of the previous discussion of permittivity and velocity, it would appear reasonable to assume that electromechanical coupling efficiency is also largely independent of element configuration, this is, in fact, erroneous. The limited amount of published work on composite arrays has presented results indicating that the coupling coefficient is degraded in practical composite array elements. Shaulov and Smith obtained coupling

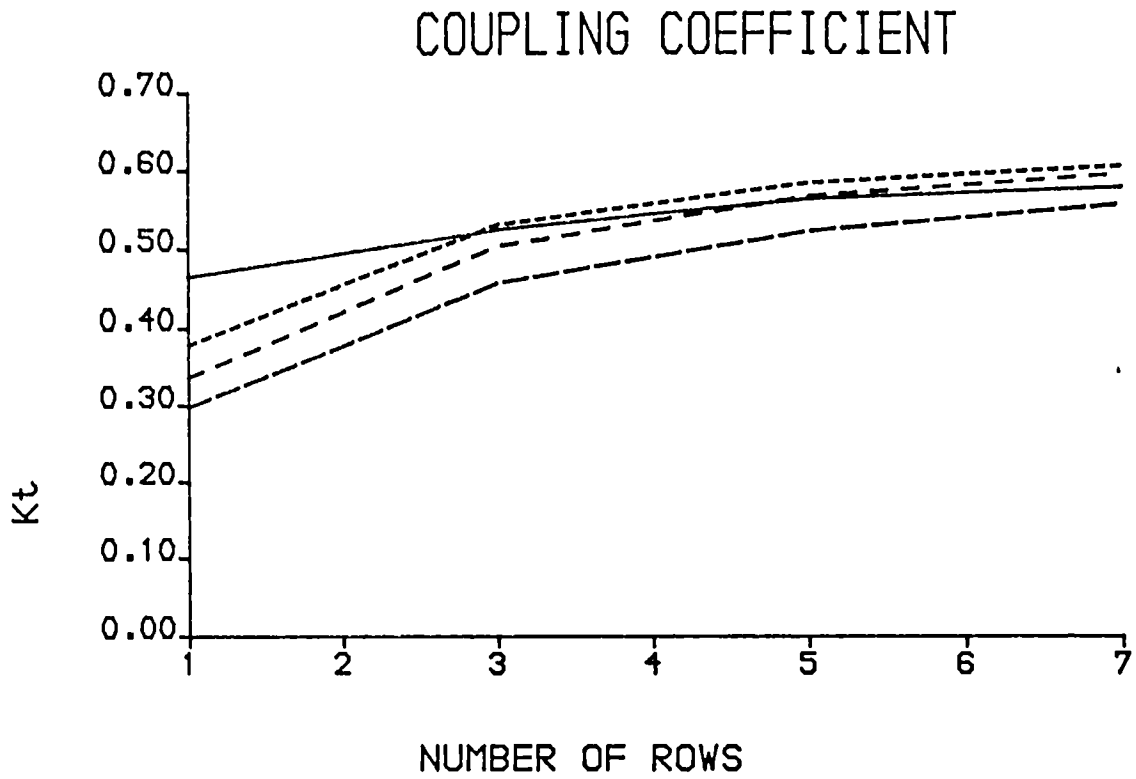


Figure 6.37 Theoretical dependence of thickness coupling coefficient on the number of active rows of pillars per array element, for four ceramic volume fractions. Pillar aspect ratio = 0.1.

Ceramic volume fraction = 20% —————
 Ceramic volume fraction = 40% - - - - -
 Ceramic volume fraction = 60% - - - - -
 Ceramic volume fraction = 80% — — — — —

coefficients of approximately 0.5 in their linear arrays [4]. This is significantly degraded from the coefficient that is encountered in a similar thickness mode composite plate ($k_t = 0.63$). The coupling coefficient is comparable to that obtained in a pure ceramic plate and is considerably inferior to that found in comparable sliced ceramic array elements ($k_t=0.68$).

Finite element analysis has been utilised to investigate the dependence of the electromechanical coupling coefficient of a composite array element on the element configuration. These results have been substantiated, where possible, using experimental data. The coupling coefficient is a function of the number of active ceramic pillars, ceramic volume fraction, pillar aspect ratio and constituent material parameters.

Figure 6.37 illustrates the theoretical dependence of thickness coupling coefficient on the number of active rows of pillars and the ceramic volume fraction. In each case, the ceramic pillars possess a width to height ratio aspect ratio of 0.1. A distinct reduction in coupling coefficient is observable as the number of active rows reduces. This trend is less marked for the 20% ceramic volume case. However, the results suggest that higher coupling coefficients are obtained using at least three rows of pillars and a volume fraction in the range 40% to 60%.

COUPLING COEFFICIENT

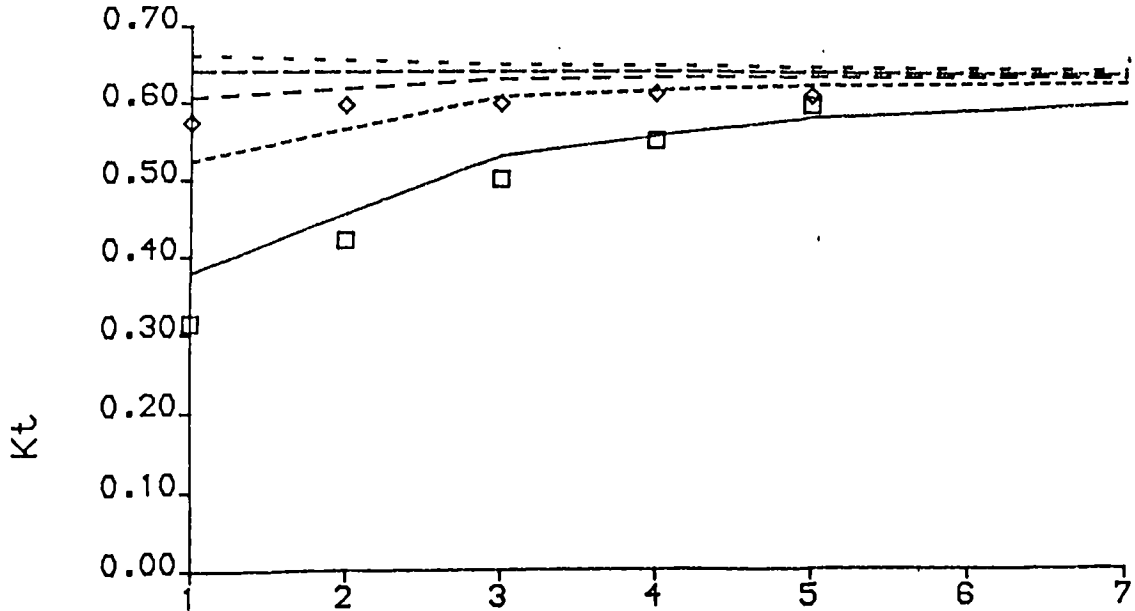


Figure 6.38 Theoretical dependence of thickness coupling coefficient on the number of active rows of pillars per array element, for five pillar aspect ratios. Ceramic volume fraction = 40%.

Theoretical : Pillar aspect ratio = 0.1 —————
 Theoretical : Pillar aspect ratio = 0.2 - - - - -
 Theoretical : Pillar aspect ratio = 0.3 - - - - -
 Theoretical : Pillar aspect ratio = 0.4 - - - - -
 Theoretical : Pillar aspect ratio = 0.5 - - - - -
 Measured : Pillar aspect ratio = 0.1 □
 Measured : Pillar aspect ratio = 0.3 ◇

COUPLING COEFFICIENT

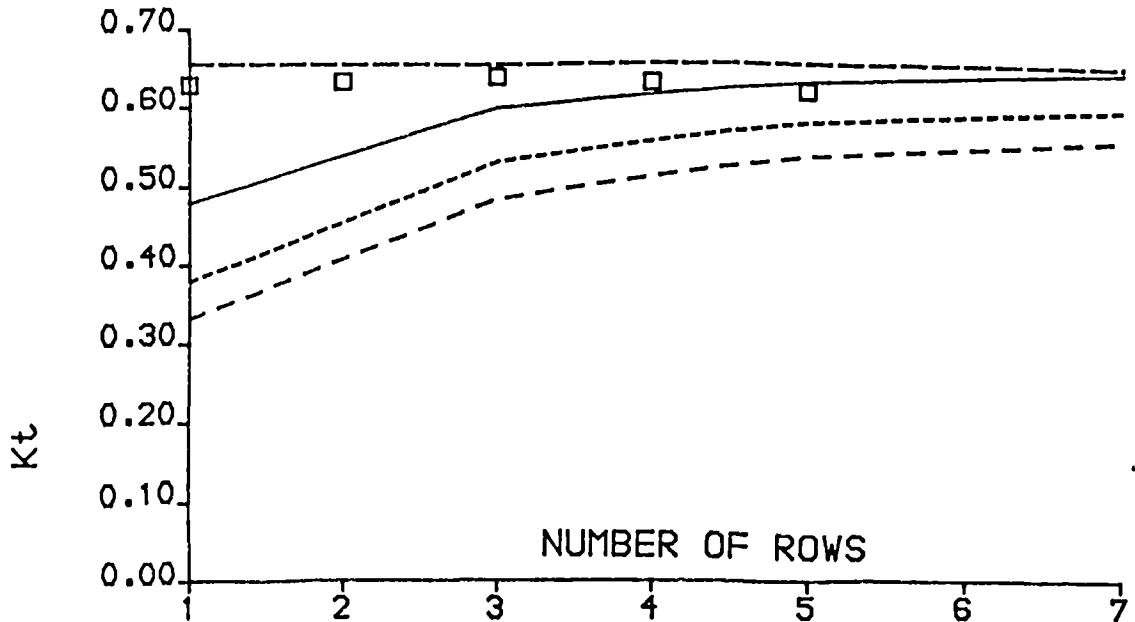


Figure 6.39 Theoretical dependence of thickness coupling coefficient on the number of active rows of pillars per array element, for four different polymer characteristics. Ceramic volume fraction = 40%. Pillar aspect ratio = 0.1.

Polymer modulus = 3GPa —————
 Polymer modulus = 6GPa - - - - -
 Polymer modulus = 9GPa - - - - -
 Microballoon Epoxy - Theoretical - - - - -
 - Measured □

The dependence of coupling coefficient on pillar aspect ratio and number of active rows is illustrated in Figure 6.38. A ceramic volume fraction of 40% has been employed in each case. Experimental data for two aspect ratios was obtained and these demonstrate a reasonable degree of correlation with the associated theoretical values. It is readily apparent that small aspect ratio elements are most susceptible to reducing coupling coefficient when only a small number of active rows of pillars are utilised. This is probably because energy is being lost via their lateral faces, which are relatively extensive in comparison to their thickness dimension. It would appear that when a high aspect ratios are employed, with only a limited number of active rows, the influence of lateral loading is negligible, and hence the coupling coefficient approaches that observed in isolated ceramic pillars ($k_{33} = 0.70$).

Finally, the influence of polymer material properties was analysed. Figure 6.39 illustrates the dependence of coupling coefficient on the number of active rows of pillars and polymer characteristics. Three conventional isotropic polymers have been analysed, possessing nominal elastic moduli of $3 \times 10^9 \text{Nm}^{-2}$, $6 \times 10^9 \text{Nm}^{-2}$ and $9 \times 10^9 \text{Nm}^{-2}$. The elastic modulus of CY1301/HY1300 epoxy corresponds to the middle of this range. This figure indicates that a similar trend regarding the dependence of the coupling coefficient, is observable for all three polymers, except that the highest coupling coefficients was obtained with the most compliant polymer. These

results are in agreement with those discussed in Chapter IV. Experimental and theoretical results have also been obtained for a lossy, compliant polymer. The polymer used was identical to the glass microballoon loaded epoxy resin discussed in Chapter IV. Since the polymer is both compliant and porous, it provides very little mechanical loading to the ceramic pillars. Hence, the coupling coefficient of array elements made using this material is virtually independent of electrode configuration. The coupling coefficient is observed to approximate to the value found in isolated free pillars, in both experimental and theoretical results.

6.5 iv) Comparison of electromechanical characteristics of composite, sliced ceramic and monolithic ceramic arrays

At this stage, it is worthwhile briefly comparing the electromechanical properties of similar composite, sliced ceramic and monolithic ceramic arrays. Although some ceramic array elements may be less efficient than similar composite array elements, they generally possess a higher net capacitance and this may compensate for their lower electromechanical efficiency.

The key electromechanical properties of composite (ceramic volume fraction = 36%), sliced and monolithic ceramic elements are presented in Table 6.3. In each case the active material is PZT 5A. These results are shown for elements which would comprise one, two and three rows of pillars, in the case of the composite array. The elements

are assumed to be 25mm long and their thickness corresponds to a 500kHz centre frequency. The parameters for the composite array were determined using finite element analysis, while the parameters of the sliced array were determined using a two dimensional linear systems model [60]. The parameters of the monolithic array elements were determined experimentally from prototype elements possessing the appropriate dimensions.

It is apparent that the wave velocities of the composite and sliced arrays, in the range 3000 to 3600ms⁻¹, are considerably lower than the thickness mode value for a pure ceramic plate (4350ms⁻¹). In the case of the monolithic array, the elements are laterally clamped, and hence the element is stiffened in the thickness direction via the Poisson ratio effect. Since a low acoustic impedance, and hence good matching and bandwidth, depends on a low product of velocity and density, it is evident that the composite will have the best match to low impedance media.

The coupling coefficients of the sliced array elements are significantly higher than for the others. As discussed previously, the coefficient in the composite is a function of the width of the element, but under no conditions will it be as high as that found in the sliced ceramic case. The monolithic array exhibits a very low coupling efficiency. It is likely that electric field fringing and significant lateral mechanical loading have degraded this coefficient from the thickness mode value of 0.486.

The effects of electric field fringing are most apparent in the measurements of capacitance in the monolithic array, which are considerably higher than for the case of the sliced array. This indicates that significant electrical cross coupling must occur between adjacent elements via the ceramic dielectric. The capacitance of the sliced array elements are also relatively high compared to the composite elements because, not only does the composite contain only 36% ceramic, but the sliced array elements are thinner due to their lower wave velocity.

The equivalent thickness mode parameters of these elements have been used in the transducer model, described in Chapter V, to determine the peak CW pulse-echo level, the pulse-echo GBP and Q of the responses. The elements are assumed to be operating into water via a quarter wavelength layer possessing the optimum impedance for matching each material to water. The impedance of the backing is half that of the transducer material. Therefore, this result does not take account of the fact that it is easier to provide a high quality backing for the low impedance composite than for the ceramic materials. The effects of source/ receiver impedance and cable capacitance were omitted from this simulation. The -6dB limits were used for calculating the GBP.

The results indicate that the highest peak, and GBP, pulse-echo response is obtained from a sliced array element. This is primarily because the coupling coefficients of these elements are higher than those of the composite and monolithic elements. However, the composite elements provide the lowest Q, on account of their superior match to the water load. Nevertheless, it is significant that the best GBP response of the composite is 73% of that obtained by the best sliced array. The response of the monolithic array is, in all respects, disappointing.

6.6 PERFORMANCE OF FOCUSED ARRAYS

6.6 i) Introduction

Section 6.2 briefly introduced the concept of focusing an ultrasonic array and some of the desirable characteristics of such an array. This section considers, from both a theoretical and practical viewpoint, the focusing of ultrasonic beams in transmission by employing suitable electronic control.

Figure 6.40 presents the geometry of a steered beam. Simple trigonometry determines the required delay between the sequential excitation of each of the elements in the array. The delay, for the i^{th} element, relative to the time that the first element is excited, is defined in Equation 6.24. The element delays are sequential and uniform and hence a suitable controller may be implemented with relative ease.

$$t_i = \frac{(i-1) d \sin \theta}{c} \quad 6.24$$

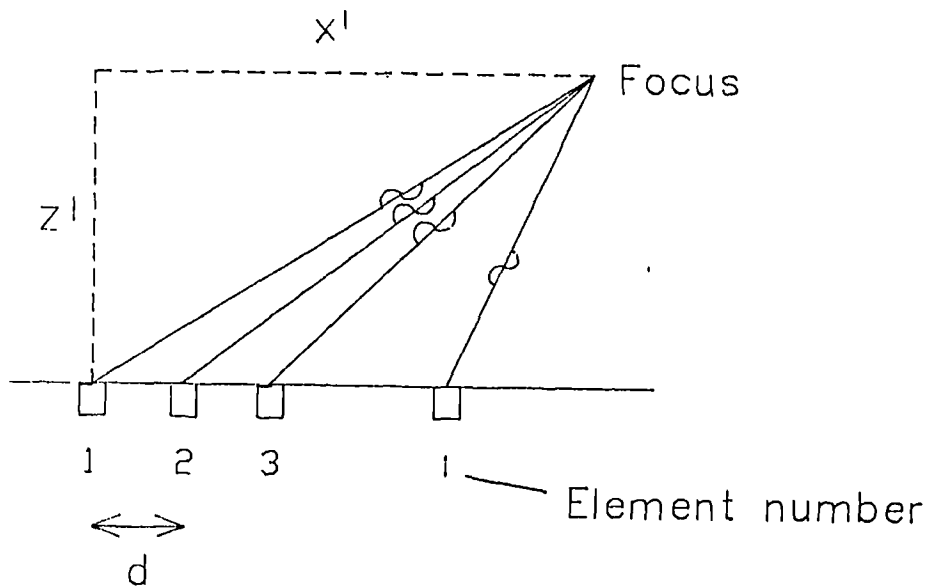
Where,

d = centre to centre pitch between elements

The geometry of a focused beam is illustrated in Figure 6.41. In this case the delays are non-uniform and the order in which the elements are excited depends on the geometry of the focus. This added complexity necessitates a more sophisticated design of array.

$$t_i = \frac{\sqrt{z'^2 + (x' - (i-1)d)^2}}{c} \quad 6.24$$

Target at (x', z')



$$t_i = \frac{\sqrt{z'^2 + (x' - (i-1)d)^2}}{c}$$

Figure 6.41 Geometry of a focused beam

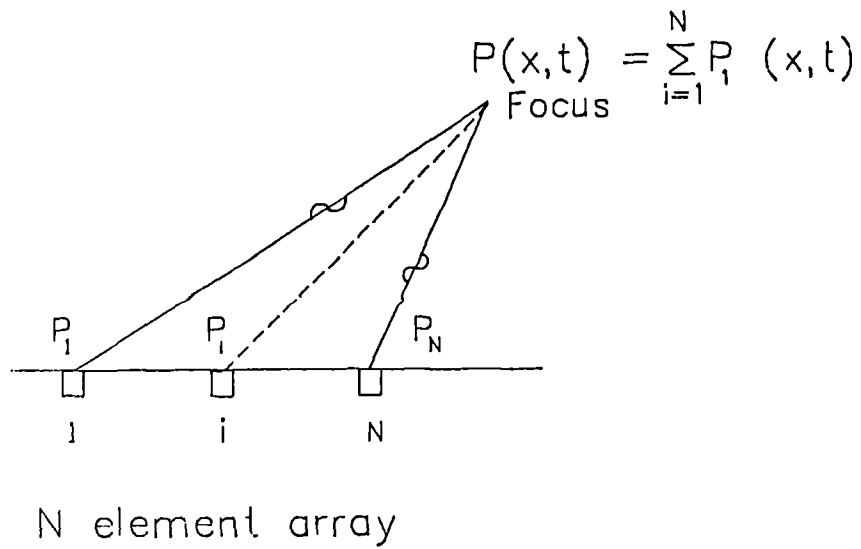


Figure 6.42 General geometry of a focused beam

It should be observed that these calculations are made assuming that the elements behave as point, or line, sources. A practical element possesses finite width and the peak response at an arbitrary point in the field may originate from one of the edges of the element and not from its centre. Therefore, imperfect focusing may occur where the elements possess significant width.

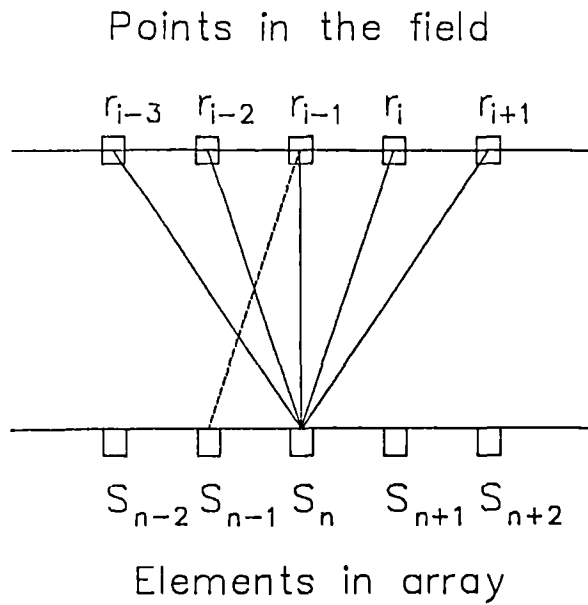
6.6 ii) Theoretical response of focused beam

The response at an arbitrary point in the field of a focused array is defined by the cumulative pressure response due to contributions from all the individual elements. For the sake of simplicity, it is assumed that the array is ideal in that it does not exhibit any inter-element coupling. Therefore, the response at point, x , for a N element array, is defined by Equation 6.26. This concept is illustrated in Figure 6.42.

$$P(x,t) = \sum_{i=1}^N P_i(x,t) \quad 6.26$$

Where $P_i(x,t)$ is the pressure response due to element 'i' at the point, x .

The element response may be assigned a weighting, or apodisation, in order to achieve a desired beam pattern. For example, a Gaussian weighting may be applied to the elements, with the strongest response in the centre, so that sidelobes are minimised. If each element is assigned a weight, $w(i)$, then Equation 6.27 may be developed.



Signal at r_{i-1} due to S_{n-1}
 = Signal at r_i due to S_n

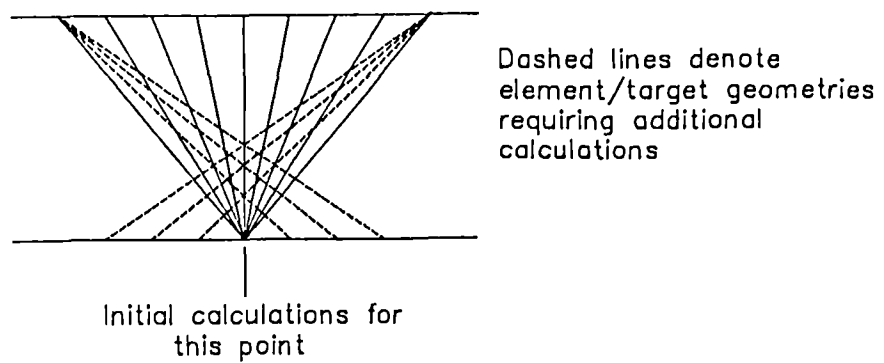


Figure 6.43 Use of common observation point/ array element spacing to achieve a substantial computational saving during field calculation.

$$P(\mathbf{x},t) = \sum_{i=1}^N w(i) P_i(\mathbf{x},t) \quad . \quad 6.27$$

The implementation of the model as defined above, is still intensive from a computational viewpoint, since it requires the calculation of the responses of all the elements at all the points of interest in the field. Frequently, the output directivity pattern of such a model indicates the peak signal magnitude at a regular array of positions in the x and z directions in the field. A vast reduction in the computational requirement may be achieved if the interval between x positions of the targets in the acoustic field corresponds with the inter-element spacing of the array. In this case the response of, typically, the centre element is calculated at all points in the field. The response, due to all the other elements may now be extrapolated using the transposition technique illustrated in Figure 6.43. For example, the signal at r_{i-1} , due to element $n-1$, is equal to the signal at r_i due element n . Likewise, the responses due to the other elements are evaluated. Clearly, a limited number of extra calculations are necessary at the edges of the field so that the responses of end elements at points at the opposite end of the field may be calculated. This is illustrated in Figure 6.43.

The response of each element, $P_i(x,t)$, is calculated using the method presented in section 6.3. Equations 6.26 to 6.27 have assumed that the net response may be calculated from the pressure responses of the individual elements. Alternatively, the net response may be calculated from the summation of the velocity potential responses or pressure impulse responses of the elements, as presented in Equations 6.28 and 6.29 respectively. The net responses are convolved with the pressure excitation function and the resultant pressure response obtained.

$$P(x,t) = - P_o(t) * \rho \frac{\delta}{dt} \left(\sum_{i=1}^N w(i) h_i(x,t) \right) \quad 6.28$$

$$P(x,t) = P_o(t) * \sum_{i=1}^N \left(w(i) P_{Ii}(x,t) \right) \quad 6.29$$

Where, $P_o(t)$ is the aperture pressure function, and $P_{Ii}(t)$ is the pressure impulse response.

$$P_{Ii}(t) = -\rho \frac{\delta}{\delta t} h_i(t) \quad 6.30$$

However, these latter two methods achieve only a limited improvement in computational efficiency and are more susceptible to numerical ill-conditioning due to the step and impulse type discontinuities in the velocity potential and pressure impulse responses. The proposed model uses bandlimited pressure signals and is therefore less susceptible to these problems.

6.6 iii) Practical implementation of a focused array

ARRAY

Taking account of the conclusions of Chapter IV and sections 6.4 and 6.5, two prototype forty element 500kHz composite array have been designed. The elements are 1.43mm wide and 25mm long. Each element comprises three rows of PZT 5A type ceramic pillars, with a centre-to-centre pitch of 0.55mm. The overall inter-element pitch is 1.65mm and is therefore marginally greater than half a wavelength at the operating frequency in water. The construction of the arrays is described in detail in Appendix A. A sliced ceramic array, and a monolithic ceramic array, were fabricated in addition to two composite arrays. Composite array #1 possesses a quarter wavelength epoxy matching layer, but has no backing medium. Composite array #2 possesses a tungsten loaded backing but has no matching layer. A thin polyurethane varnish layer protects the front face metallisation.

ARRAY CONTROLLER

A versatile computer controlled thirty two channel array controller has been developed. A very high temporal resolution was required so that the controller could be used with very high frequency arrays ($\approx 10\text{MHz}$) operating into metallic media. FAST TTL technology was selected in preference over ECL technology for reasons of 'cost and versatility. Four 74F191 devices are cascaded in each channel, resulting in a 16 bit counter operating at up to

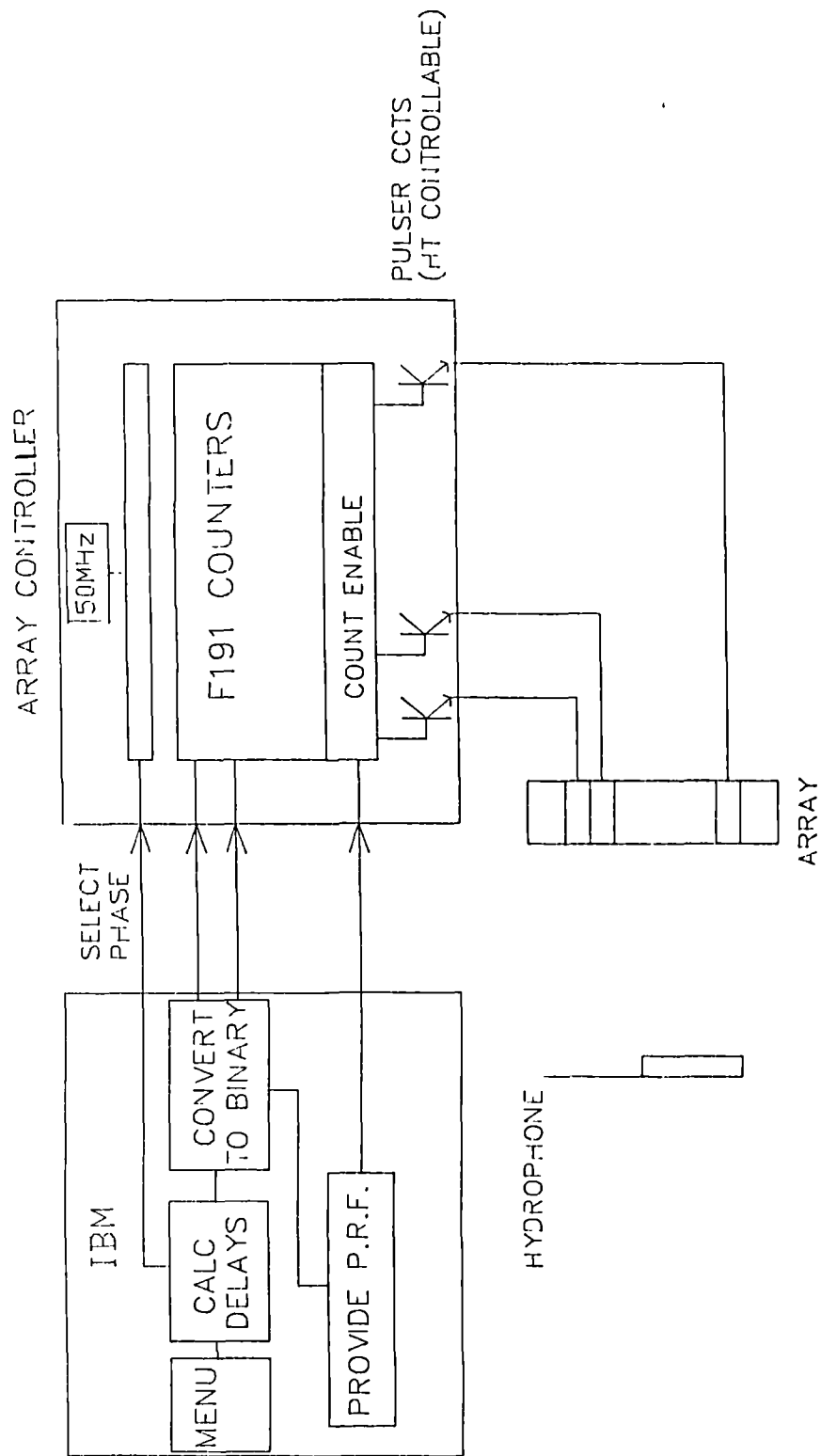


Figure 6.44 General configuration of array controller.

50MHz. The clock cycle is split into eight phases, permitting a maximum resolution of 2.5nS. An IBM PC-AT offers the user a menu type selection of suitable focusing characteristics. The IBM then calculates the required element delays, converts these to binary quantities and transfers these to the array controller. Thereafter, the IBM provides pulse repetition frequency (PRF) control of the array controller. This configuration is illustrated in Figure 6.44.

6.6 iv) Theoretical and measured field response of focused arrays

A comprehensive investigation of the field responses of the arrays which have been fabricated for a range of operating configurations would be extensive. Consequently, a single typical result is presented for each array. This is sufficient to permit the relative merits of each type of array to be assessed.

Figures 6.45 to 6.48 illustrate the measured and simulated directivity characteristics of composite array #1, composite array #2, the sliced ceramic array and the monolithic ceramic array. These results have been obtained at a range of 150mm for a steering angle of $+30^\circ$. Any misalignment in terms of the peak response is due to experimental positional error. Both composite arrays demonstrate good directional characteristics which are in general agreement with the theoretical response. There are no significant sidelobes and the signal levels observed at

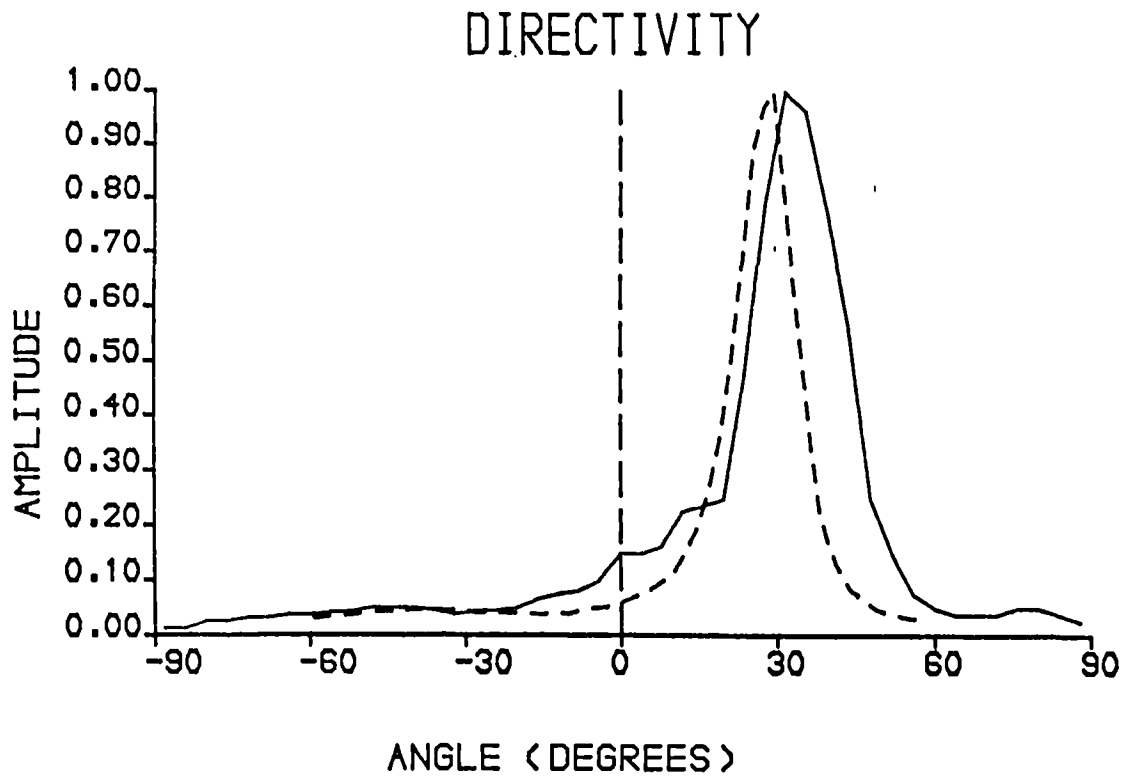


Figure 6.45 Theoretical and measured directivity of the composite array #1 (+30° steer).
 Theoretical - - - - -
 Measured —————

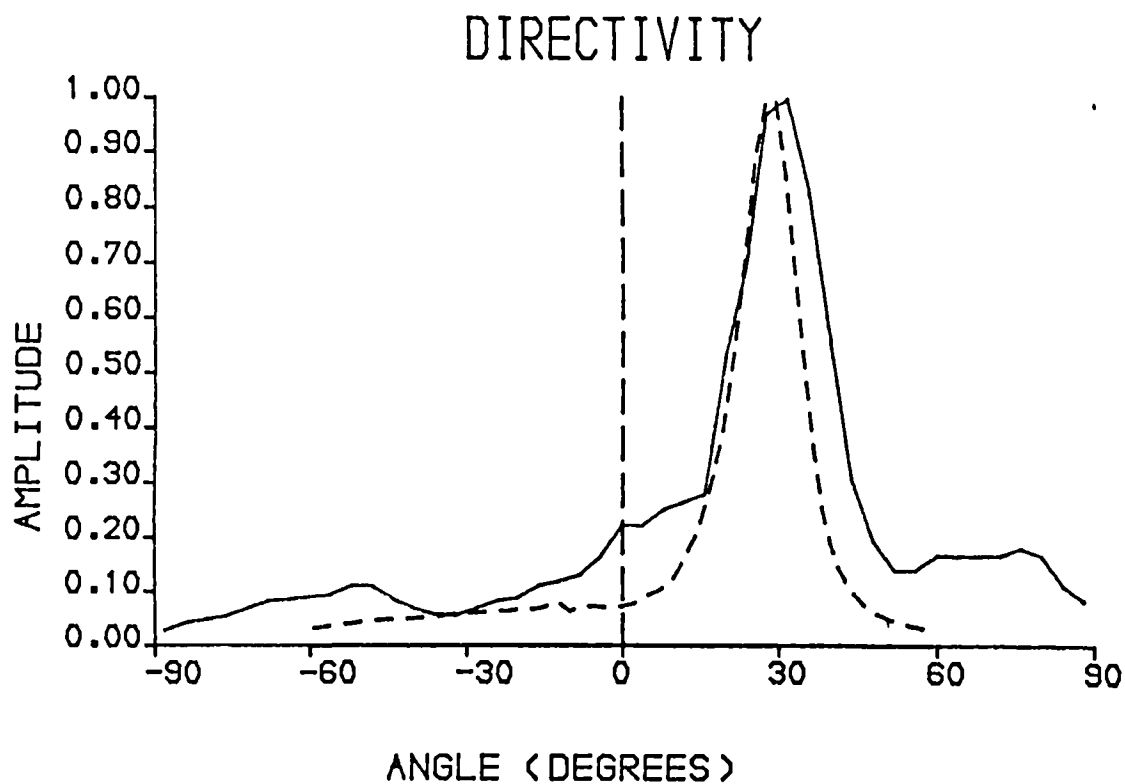


Figure 6.46 Theoretical and measured directivity of the composite array #2 (+30° steer).
 Theoretical - - - - -
 Measured —————

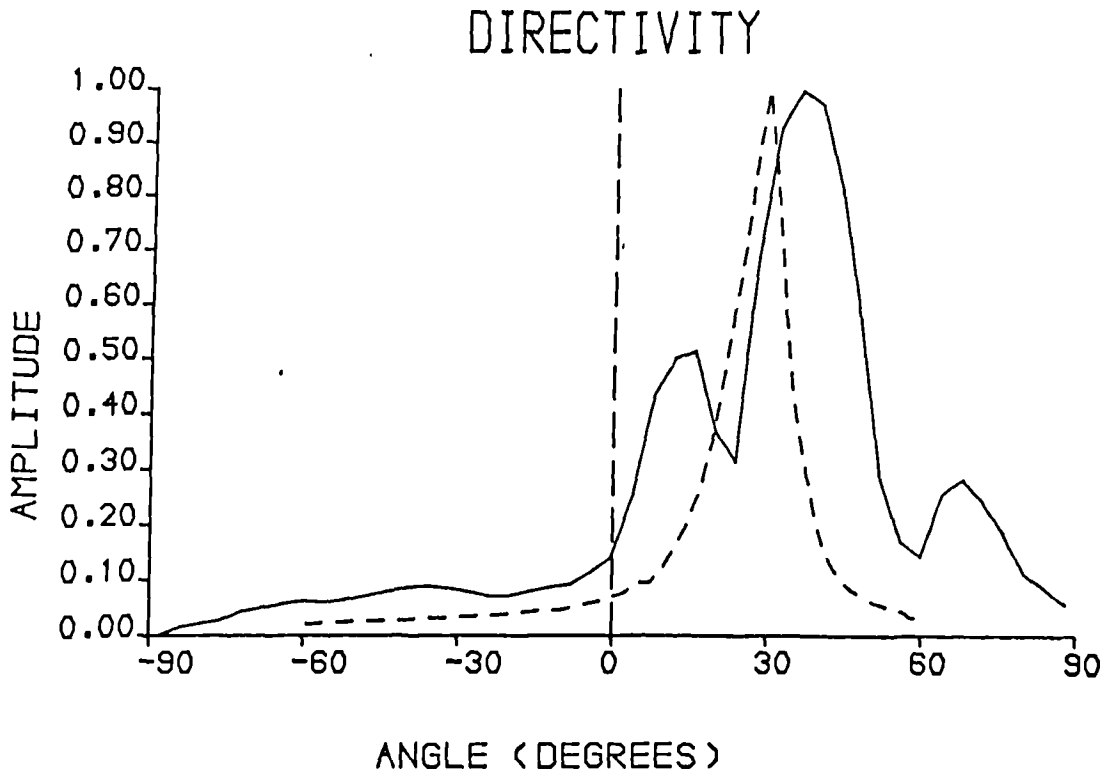


Figure 6.47 Theoretical and measured directivity of the sliced ceramic array (+30° steer).
 Theoretical -----
 Measured —————

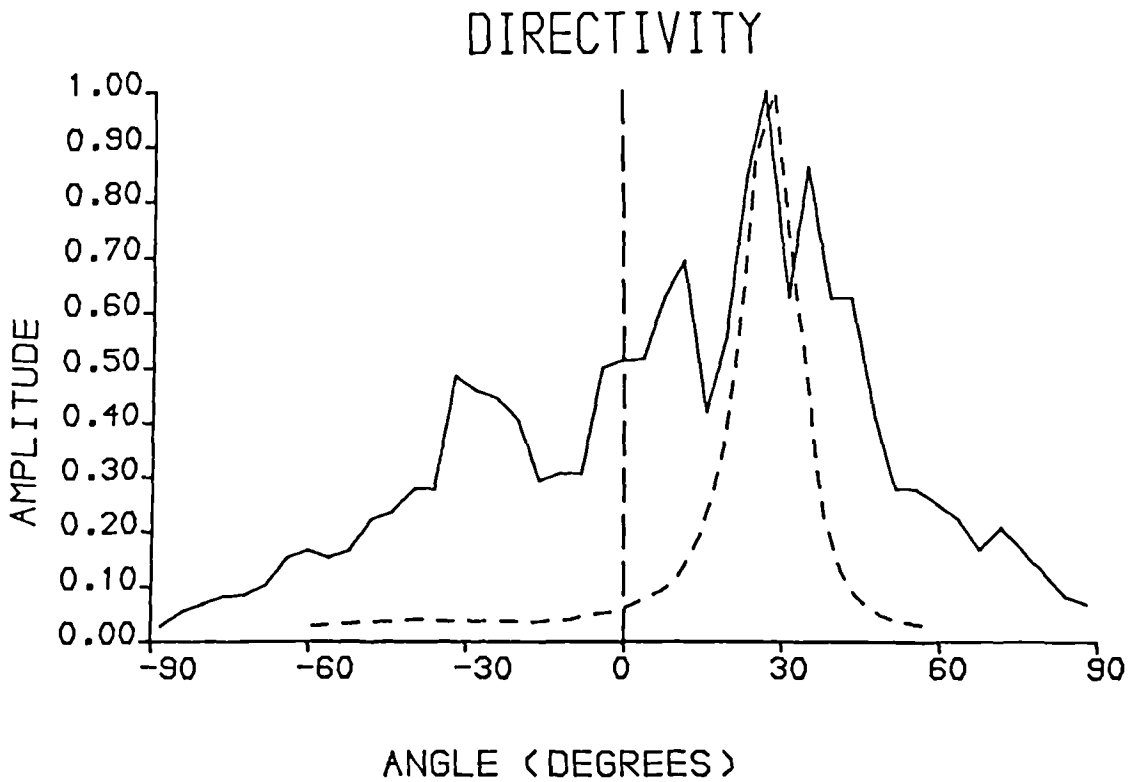


Figure 6.48 Theoretical and measured directivity of the monolithic ceramic array (+30° steer).
 Theoretical -----
 Measured —————

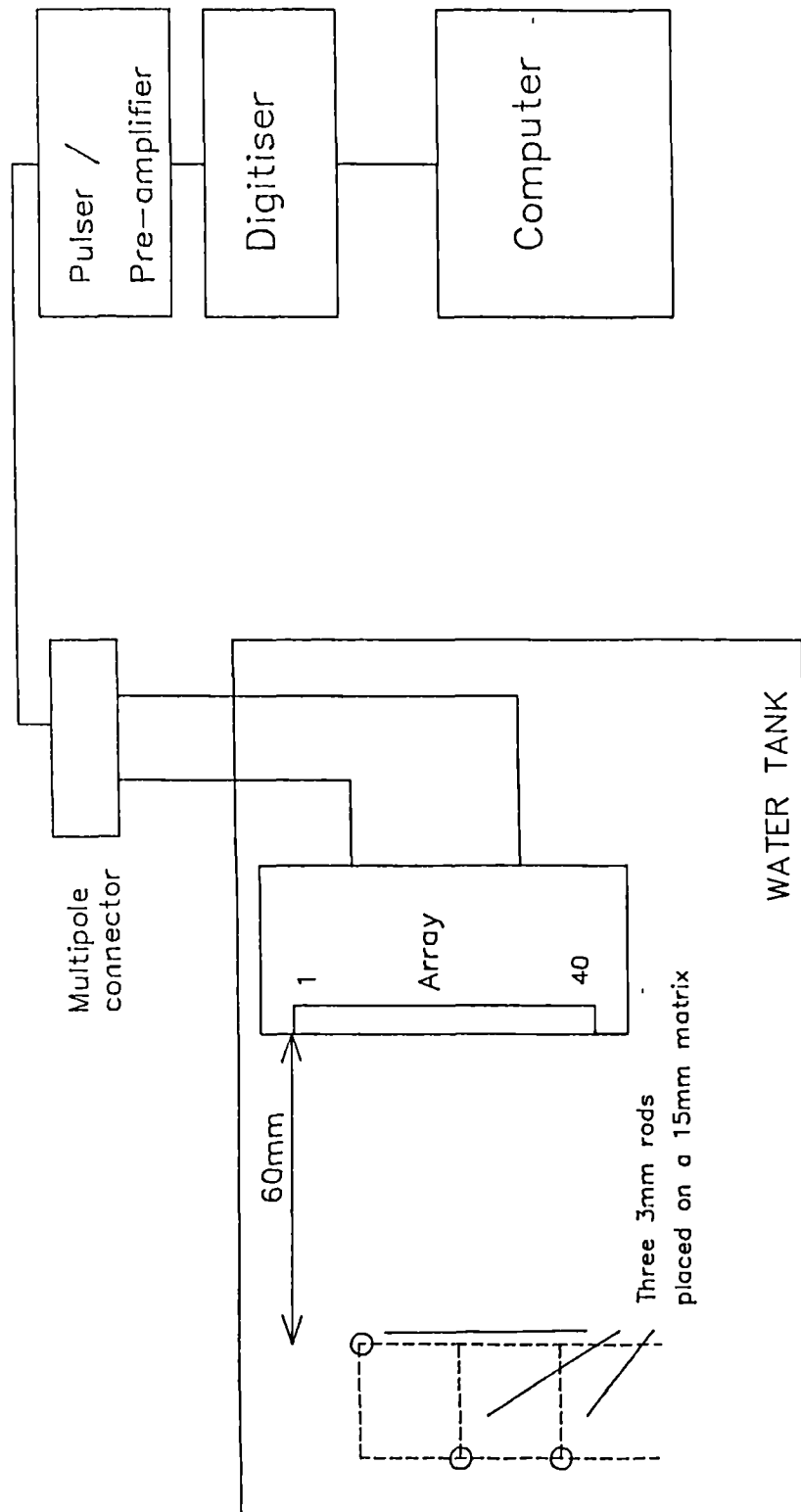


Figure 6.49 Experimental apparatus for acquisition of image data.

angles, away from the angle of steer, were barely measurable.

The directivity of the sliced array, illustrated in Figure 6.47, possesses strong sidelobe features. These are presumably due to the same relatively strong inter-element coupling as that observed in the single element directivities in section 6.4. However, this response is vastly superior to that demonstrated by the monolithic array in Figure 6.48. Strong responses are observed at a number of angles away from the angle of steer. The responses near $+30^\circ$ and -30° are probably attributable to Lamb mode propagation along the ceramic plate. Hence, this monolithic array exhibits a virtually useless directivity response.

6.6 vi) Synthetic focusing in reception

In contrast to transmission beamforming, reception beamforming can be accomplished entirely in software. A suitable synthetic focusing algorithm has already been discussed briefly in section 6.2. Synthetic focusing of the backscattered data from one target has been performed for all four transducer arrays described in the previous section.

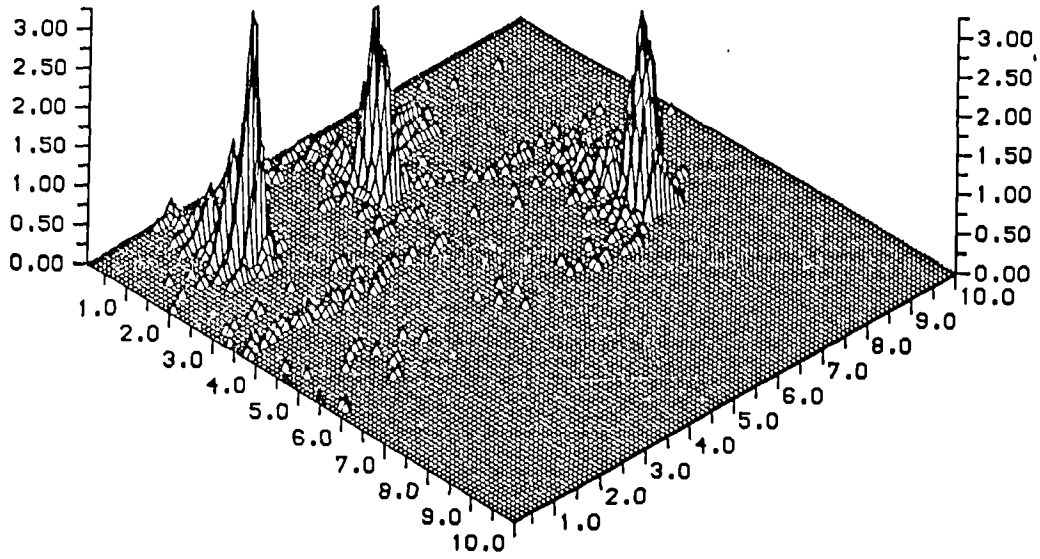


Figure 6.50 Isometric image of three rods obtained with composite array #1.

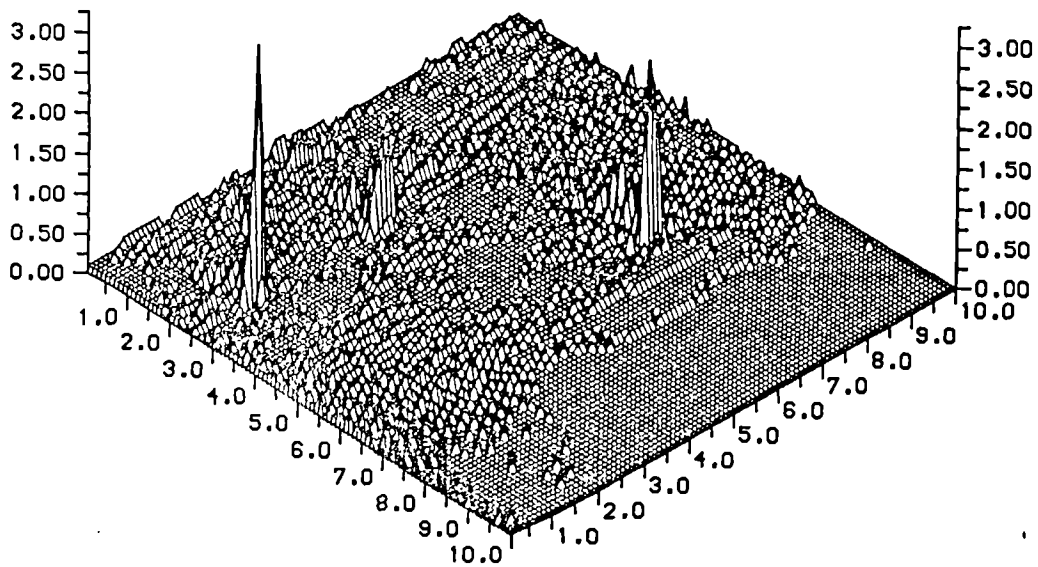


Figure 6.51 Isometric image of three rods obtained with composite array #2.

The target comprised of three 3mm steel rods placed approximately 60mm in front of the array's active surface. The elements were sequentially excited and the pulse-echo responses digitised at 20MHz and stored in computer memory. The experimental apparatus is described in Figure 6.49. The corresponding isometric image intensity plots are illustrated in Figures 6.50 to 6.53. All the images were obtained using the same quantisation and gain settings. The data was filtered with a R-C circuit possessing an upper cut-off -3dB frequency of 2MHz. No thresholding has been performed. Therefore valid comparison of the imaging characteristics of the four arrays can be made.

Composite array #1 has produced a reasonably good image with a high signal to noise ratio. The secondary peaks behind the main features are due to the pulse lengths being approximately four cycles long, which is because this array is airbacked and consequently possesses a relatively narrowband response. However, composite array #2, which is backed with tungsten loaded epoxy and possesses pulse lengths of approximately one and half cycles, has produced a far sharper image. However, the noise level is slightly increased because improved bandwidth has been obtained at the expense of reduced peak signal level. The sliced array has produced an image somewhat inferior to that obtained using composite array #1. The pulse lengths of this array were longer than those of the composite arrays and this has resulted in

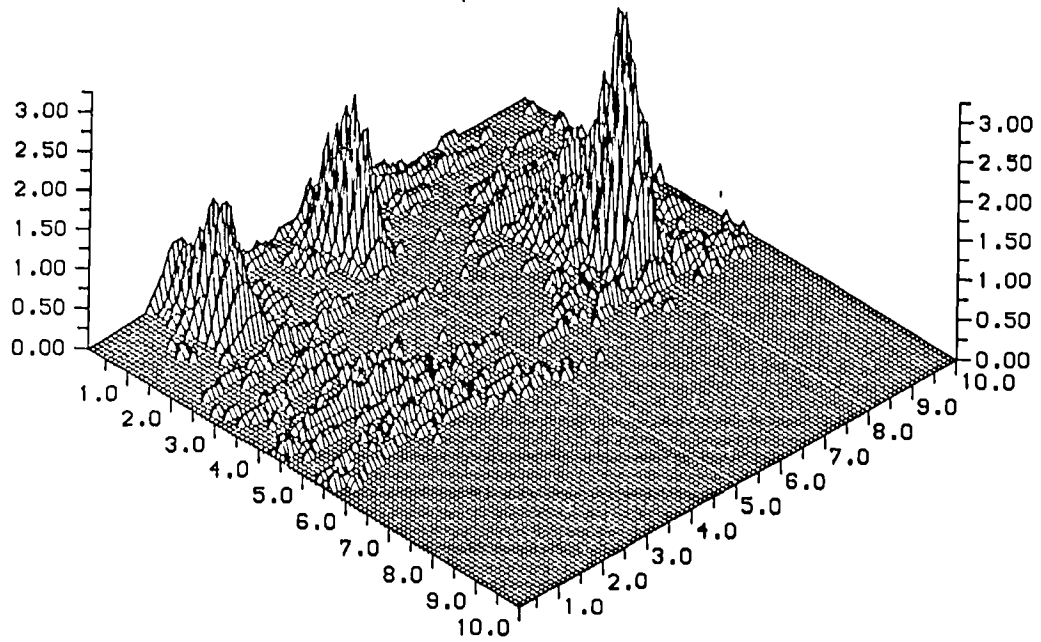


Figure 6.52 Isometric image of three rods obtained with sliced ceramic array.

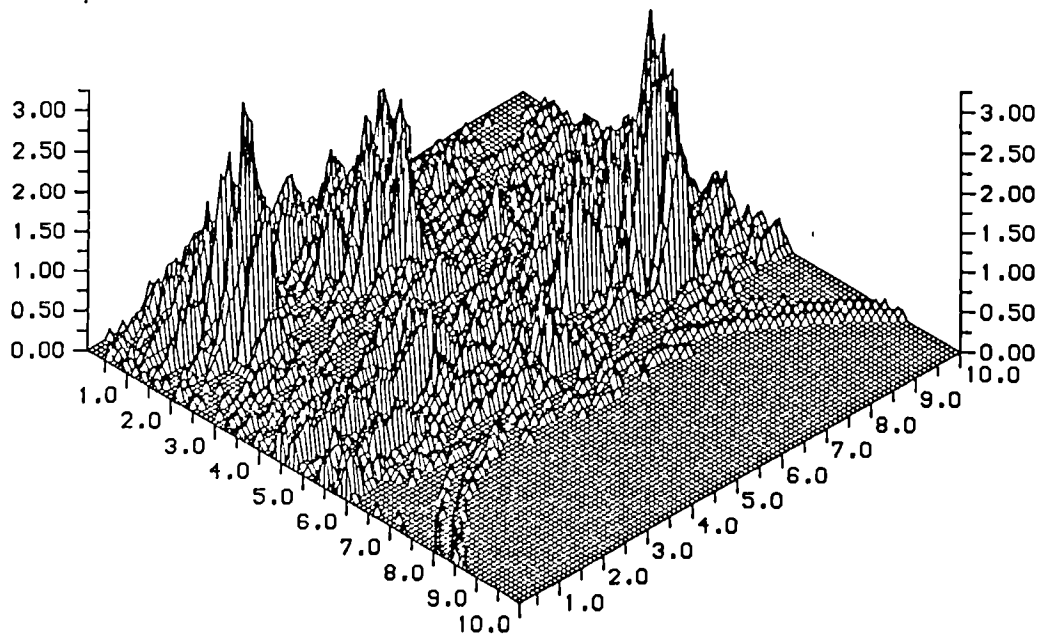


Figure 6.53 Isometric image of three rods obtained with monolithic ceramic array.

additional peaks in the image. The monolithic array has produced a virtually meaningless image. This is a result of the complex directivity functions of the individual elements, which has already been discussed in section 6.4. The quality of the image obtained using the monolithic array, and to a lesser extent for the other arrays, will depend to significant degree on the relative position of the array and target. The best imaging results are obtained using point-like scatterers in the near field of an array possessing elements with wide directivities.

The relative quality of the images obtained using the four arrays broadly correspond with the relative qualities of their single element characteristics and their steering characteristics. The composite arrays provide somewhat better results than the sliced array. However, the relative merits will depend on the precise configuration of the array. Without exception, the monolithic array exhibits very poor characteristics when it is operated into water.

6.7 CHARACTERISTICS OF TWO-DIMENSIONAL ARRAYS

6.7 i) Introduction

In recent years, there has been a growing interest in two dimensional (2-D) imaging arrays for NDE and medical diagnostics. This has been motivated by a requirement for the higher reliability, and quality, of information provided by a three dimensional (3-D) image. Recent advances in transducer and microelectronic technology has provided the basis for the rapid development in this field. In 1986 a 3.5 MHz 2560 element array was demonstrated by Kojima [61]. The mechanical Q of the elements was 2 and hence excellent wideband operation was obtained. Excellent element response was obtained by using a partial subdicing technique to eradicate undesirable modes.

Composite transducer technology has a place in current 2-D array design. The majority of the arrays described use relatively wide elements possessing narrow directivities. This permits a C-Scan image to be obtained rapidly. However, if synthetic focusing techniques are used, wider directivities and closer element spacings are required. This results in greater difficulty in obtaining satisfactory electrical connection. In addition to providing electrical connection at the rear of each element, it is necessary to employ a dense backing medium. Thus the manufacturing difficulties are compounded. However, a composite material, possessing a lower acoustic impedance, requires only a light backing to achieve the

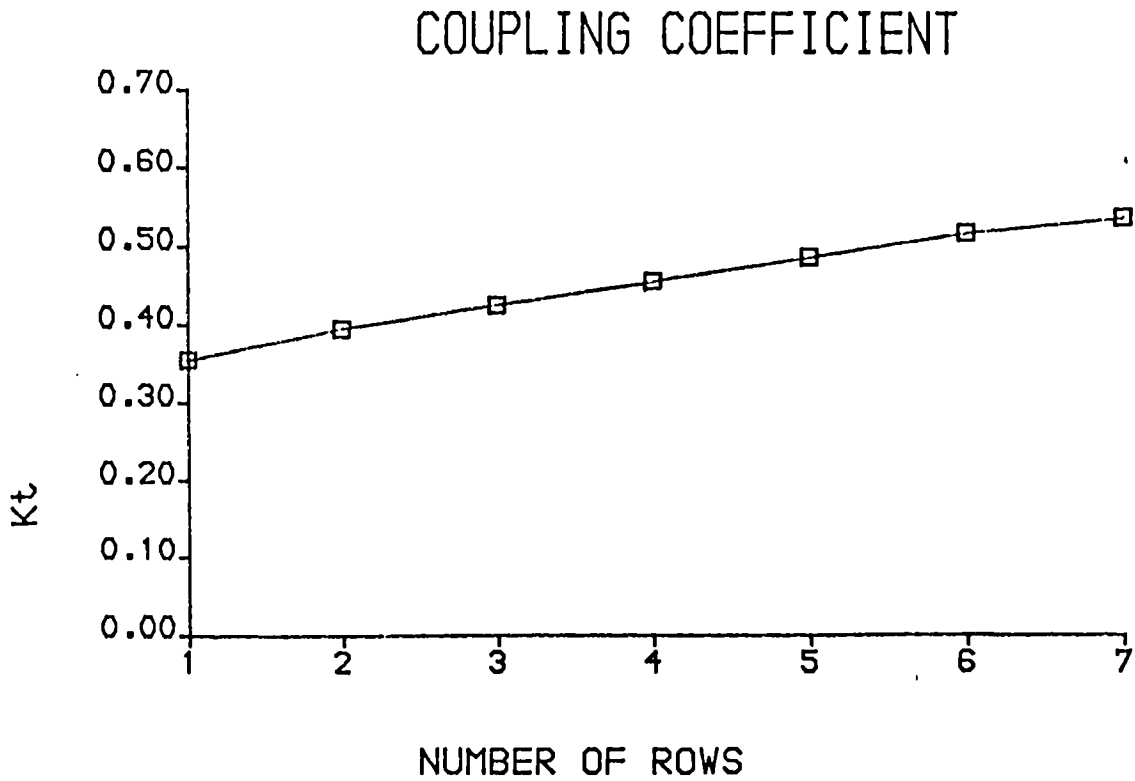


Figure 6.54 Measured dependence of thickness coupling coefficient on the number of rows of pillars, per side, of a 2-D composite array element. Ceramic volume fraction = 40%. Pillar aspect ratio = 0.14.

same bandwidths as those already demonstrated using backed ceramic elements.

A prototype 10 x 10 focusing 500kHz composite array has been designed and manufactured. The electronic technology for providing separate addressing, excitation and receiver amplification is not considered here since the complexity and cost of this technology places it beyond the scope of the current work. Instead, electrical connection to each element is brought from the active element to an integrated circuit socket. A miniature pulser/ receiver circuit is manually connected to each element and pulse/ echo data obtained. This data is transferred to a computer where 2-D synthetic focusing is performed on the A-Scan data.

6.7 ii) Electromechanical and spatial field characteristics of 2-D array elements

It is assumed that the principal conclusions relating to 1-D composite array elements also apply to 2-D array elements. These are outlined below.

1) The electromechanical coupling coefficient is lower than that obtained in a thickness mode plate. The larger the element, in terms of the number of rows wide, the higher the coupling coefficient. Figure 6.54 illustrates the measured dependence of coupling coefficient of a typical 2-D array element as a function of the number of pillars per side of each element. The increasing trend evident in the curve is similar to that obtained in

section 6.5 for the 1-D array element. Finite element analysis of these configurations was not feasible owing to the geometrical complexity of the required meshes.

2) The spatial field performance of relatively narrow composite array elements are considerably degraded from the theoretically predicted characteristic. The relationship between width and the effects of laterally propagating energy has been discussed at length in section 6.4. Clearly, the same conclusions apply to 2-D array elements.

On the basis of the above findings, it is suggested that a 2-D array element consist of at least a 3 x 3 matrix pillars.

6.7 iii) Design and manufacture of a 2-D composite array

Two prototype 500kHz 10 x 10 element arrays were constructed. An initial design used silver loaded epoxy for providing the electrical connections. The array was air backed. It was concluded that silver loaded epoxy was difficult to use and unreliable. It was also apparent that a modest backing was desirable in order to achieve the required bandwidth.

For the sake of simplicity, a 2.54mm pitch was selected, thus permitting the use of standard integrated circuit device mounting technology. Unfortunately, this pitch corresponds to 85% of a wavelength in water, and hence, is significantly greater than the desired half wavelength

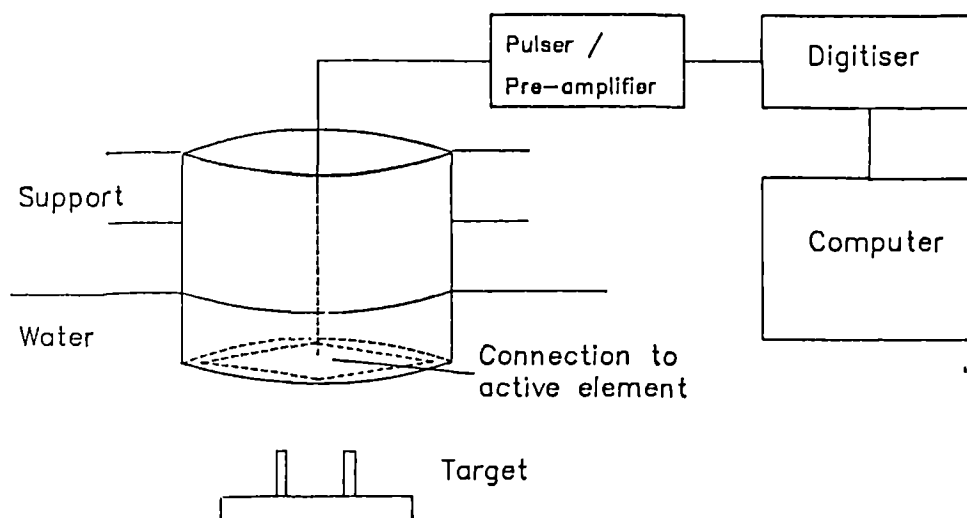
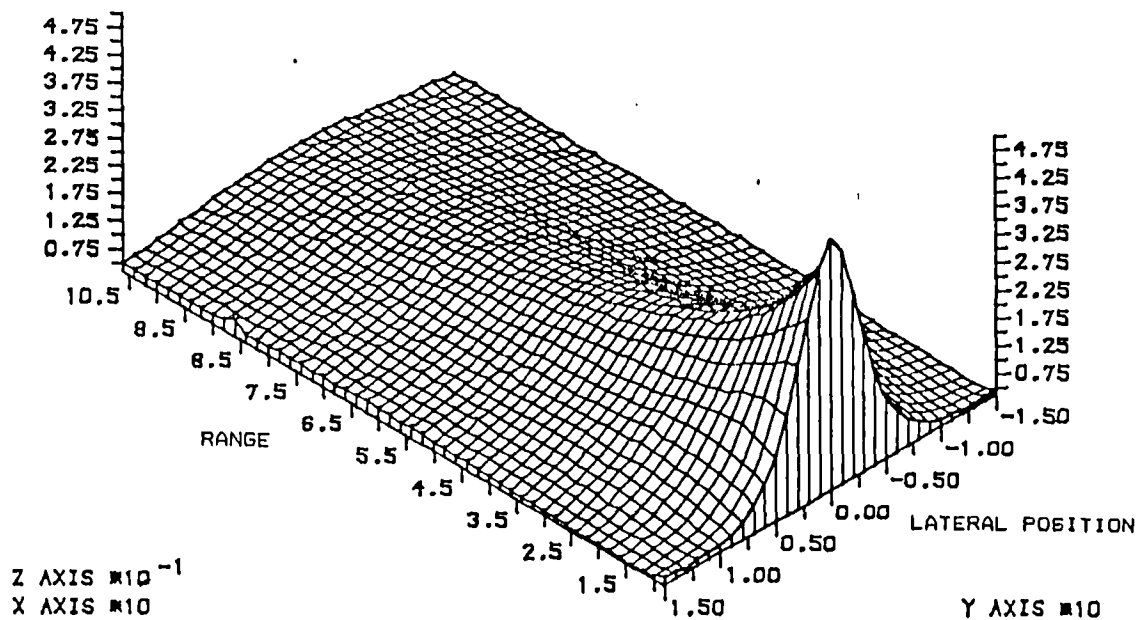
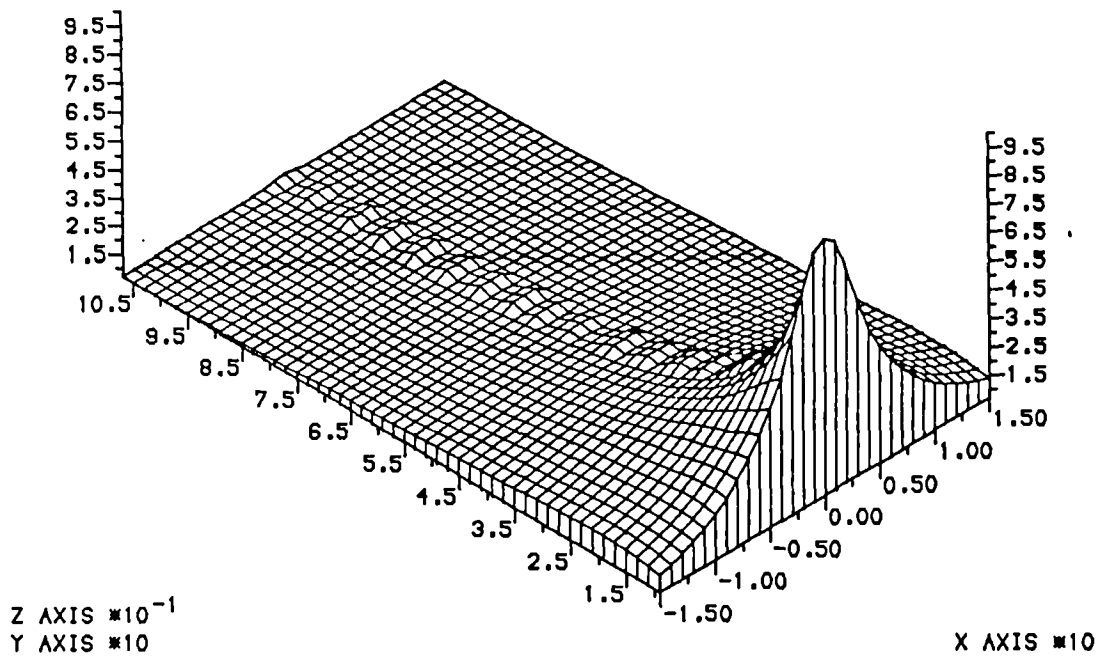


Figure 6.55 Acquisition of image data using the prototype 2-D array.

spacing. Taking account of the conclusions of Chapter IV, and of the earlier sections of this chapter, a 40% ceramic volume fraction was selected using PZT 5A ceramic and CY1301/HY1300 polymer. Each 2-D array element comprises a four by four matrix of pillars. The pillars possess an aspect ratio of 0.14 and hence uniform element vibration may be expected. The front face of the composite material has a common ground electrode and a quarter wavelength epoxy matching layer. On the rear surface a thin chromium/copper film was deposited. This was scribed to define the 100 elements. The tips of the wire wrapped sockets were aligned on the composite structure and then soldered to the electrodes. The resulting structure was reinforced by potting the volume around the wire-wrap pins with a soft epoxy resin. This material also provided the desired backing impedance. In the present prototype array configuration, the array is operated with an open back with the active array surface facing downwards into the water. This is illustrated in Figure 6.55. A miniature pulser/ receiver circuit is placed immediately above the array with a short interconnecting wire and pin sequentially addressed to each element via the 'wire-wrap connector. This geometry minimises electrical loading since parasitic cable capacitance is virtually eliminated. This is vital since the elements each possess a capacitance of 7pF and an impedance of 35K Ω at the centre frequency. The receiver employs a precision preamplifier stage possessing an input impedance greater than 10⁸ Ω .



Measured



Theoretical

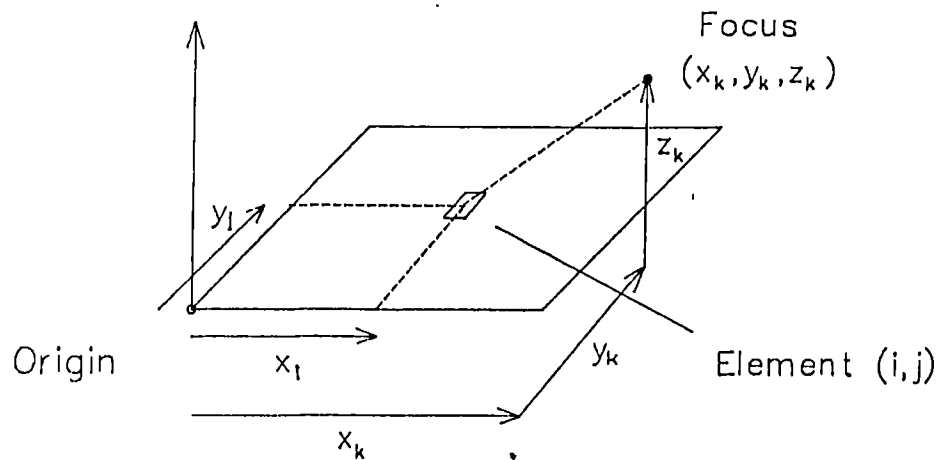
Figure 6.56 Theoretical and measured directivity of a single element in the 2-D array.

6.7 iv) Imaging performance of the prototype 2-D composite array

Prior to considering the imaging performance of the array, it is worthwhile briefly investigating the spatial characteristics of a single element. The measured spatial field characteristic of a single 2-D element is compared with the theoretical characteristic in Figure 6.56. The diffraction algorithm presented in section 6.3 was used to obtain the theoretical result. A reasonable degree of correlation between the two characteristics may be observed. However, the measured response possesses a stronger response along the axis, which suggests that the active aperture is relatively wide, and hence more directional.

A 2-D synthetic focusing algorithm has been implemented on computer [62,63]. This is an extension of a 1-D synthetic focusing algorithm and permits focusing throughout the volume adjacent to the array face. Naturally, since a 2-D array can produce a 3-D image, the processing requirement is considerably greater than that for 1-D array producing a 2-D image of a single plane.

The following expression for calculating the image intensity at a location (x_k, y_k, z_k) in the field of a 2-D array, may be obtained. This expression relates to the general geometry illustrated in Figure 6.57.



$$t_{ijk} = \frac{2}{c} \sqrt{((x_k - x_i)^2 + (y_k - y_j)^2 + z_k^2)}$$

Figure 6.57 Geometry associated with the formation of a 3-D image using a 2-D array.

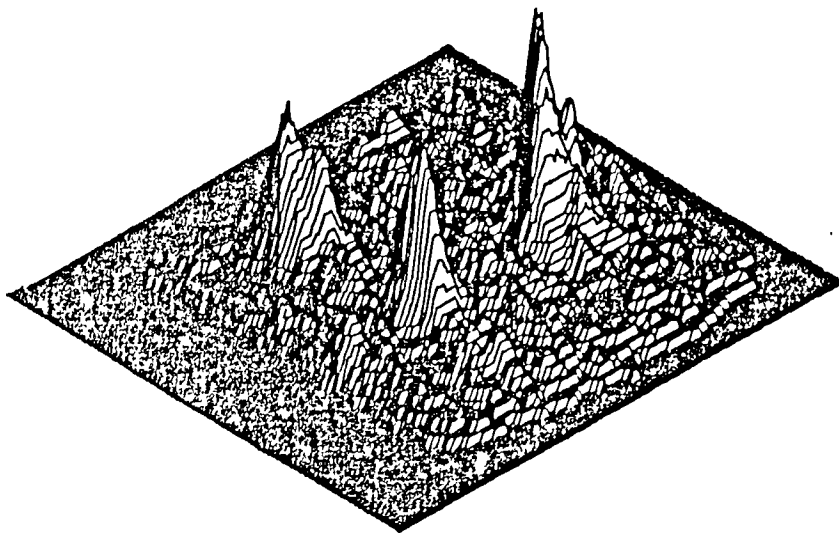


Figure 6.58 Thresholded image of three 5mm screw heads obtained using the prototype 2-D array.

$$I(x_k, y_k, z_k) = \left| \sum_{i=1}^M \sum_{j=1}^N S_{ij}(t_{ijk}) \right| \quad 6.30$$

Where,

$$t_{ijk} = \frac{z}{c} \sqrt{(x_k - x_i)^2 + (y_k - y_j)^2 + z_k^2}$$

Since the image generated is three dimensional and therefore cannot be represented on paper or screen, the user normally specifies a particular plane, or sequence of planes, of interest [63]. Figure 6.58 illustrates a thresholded image of three 5mm screw heads lying 50mm in front of the active face of the prototype 2-D array. Thresholding was necessary because of the relatively high noise levels associated with such low signal levels. Having regard to the small number of elements and the relatively low operating frequency, it is evident that a reasonably good quality image has been obtained. There is clearly scope for improvement in the design of 2-D arrays, although the manufacturing difficulties associated with closer spacings and higher frequencies are considerable.

6.8 CONCLUDING REMARKS

A comprehensive investigation of the electromechanical and spatial field characteristics of composite array elements has been performed. A novel, versatile and efficient algorithm for determining the pressure responses of rectangular elements, under arbitrary excitation, and at arbitrary field locations, has been developed.

The field characteristics of practical elements are influenced to a considerable extent by the presence of laterally propagating Lamb waves emanating from the excited element. These give rise to lobes in the directivity characteristics. The extent of this Lamb wave activity is difficult to quantify, although finite element analysis has provided a useful guide. The amplitude of these laterally propagating waves may be slightly reduced by employing a suitable backing material or by providing some isolation between individual elements by slicing between them and filling with a lossy material.

The electromechanical characteristics of practical array design have been considered using both finite element and experimental techniques. Although permittivity and velocity are largely independent of electrode configuration, the electromechanical coupling coefficient is a complex function of the number active rows of ceramic pillars, pillar geometry, ceramic volume fraction and constituent material characteristics. Generally, wide aperture elements possess the highest coupling coefficients.

The performance of practical composite, and conventional, steered arrays has been assessed. This has required the development of a versatile, efficient array directivity model and a high specification array controller. Although some of the characteristics pertaining to individual array elements are integrated out when an entire array is operated, it was still evident that the composite arrays provided a performance superior to that of the sliced array. In comparison, the monolithic array exhibited a virtually unusable characteristic owing to the presence of strong laterally propagating vibrational modes.

A prototype two dimensional array has been developed. The electromechanical, spatial and imaging characteristics of this array are in broad agreement with expectation. It was evident that a measurable increase in performance, in terms of increased frequency and reduced spacing, would require considerable resources.

CHAPTER VII

MODELLING THE CHARACTERISTICS OF STACKED
COMPOSITE TRANSDUCERS

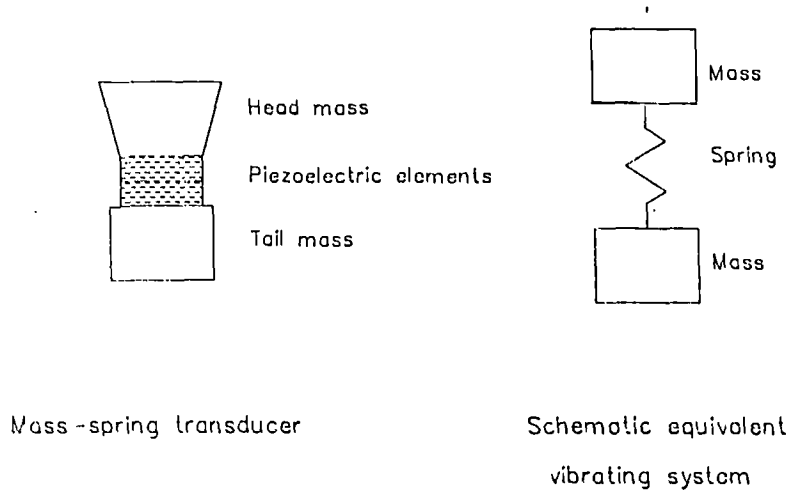


Figure 7.1 Configuration of the 'mass-spring' transducer

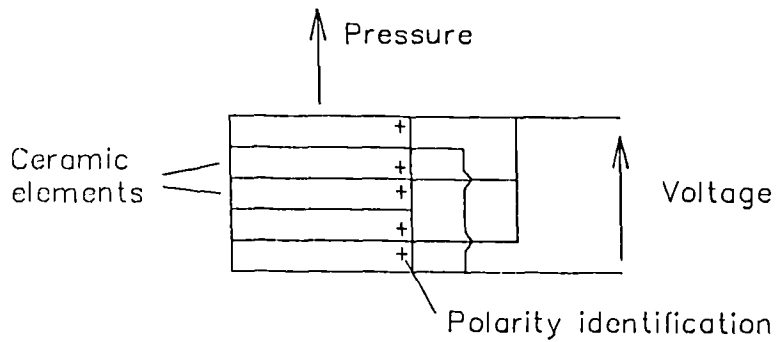


Figure 7.2 General configuration of a stacked, multiple active layer transducer

7.1 INTRODUCTION

Stacked transducer assemblies are frequently employed for low frequency active applications. The most immediate characteristic of low frequency active transducers is the relatively large size of the components. Unfortunately, piezoelectric materials are generally expensive and fragile. Therefore, a range of 'mass-spring' devices have been developed to overcome these problems for frequencies below approximately 50kHz. The operation of this type of transducer, illustrated in Figure 7.1, is determined by the natural resonant frequency of a system involving a head mass, tail mass and a relatively compliant piezoelectric 'spring' between them. The design is relatively cheap and capable of high power operation because the ceramic phase is mechanically biased in compression, but is generally narrowband.

If wide bandwidth is of prime concern in the design of a low frequency transducer, then a pure piezoelectric thickness mode resonator is generally required. Clearly, this type of design is prohibitively expensive at very low frequencies and is incapable of high power operation because of the lack of mechanical biasing. Low frequency thickness mode piezoelectric transducers are generally fabricated from a stack of layers bonded together, as illustrated in Figure 7.2. These layers are mechanically operating in series, but are generally connected electrically in parallel. Since the impedance of a thickness mode transducer is a linear function of its

thickness, then it is apparent that by slicing a thick piezoelectric plate into several layers, and reconnecting them electrically in parallel, then a significant reduction in impedance is obtained. A reduced impedance facilitates the use of a lower voltage to obtain a specified pressure output response. Furthermore, manufacturers experience considerable difficulty in obtaining satisfactory piezoelectric polarisation of ceramic blocks more than approximately 15mm thick.

On the basis of previous discussion of the properties of composite piezoelectric materials, it is evident that composites offer scope for providing high bandwidth, low frequency stacked transducers. In addition to their inherently wider bandwidth, when operating into low impedance media, they also permit the use of device geometries previously unobtainable. For example, if a stacked ceramic transducer possesses a width dimension similar to its thickness dimension, then serious cross coupling of lateral and thickness mode vibrational activity may occur. However, composite transducer materials generally possess only weak lateral modes of resonance and these are only weakly coupled to the thickness dimension. These aspects have been considered in Chapter IV.

It is also possible to design 'asymmetric' stacked transducers. In this context, 'asymmetry' occurs when any feature of a stacked structure gives rise to non-uniform vibrational activity. A 'symmetric' structure consists of

layers possessing uniform thickness and material characteristics, which are connected to a common electrical load, or loads. However, if any of the material properties, thicknesses or loads are changed then uniform excitation/ vibration is likely to be inhibited. An asymmetric transducer will typically possess multiple resonances not encountered in uniform symmetric structures. In theory, it should be possible to design novel wideband stacked transducers. Furthermore, by changing the nature of the electrical load, or excitation, a variety of characteristics may be obtained from a single physical design.

Wideband, low frequency composite transducers are well suited to a variety of NDE and sonar applications, for which conventional materials do not possess the requisite characteristics. These include the NDE of porous, low impedance media. Examples of such media include concrete, and stone, in the form of processed masonry or naturally occurring material within mines or quarries. It is conceivable that wood, both living and dead, could be inspected for thickness, porosity or rot. Additionally, since composite piezoelectric materials possess a relatively low impedance, it is also conceivable that NDE may be performed through an air gap [64]. It would also be possible to apply through air transmission, using low frequency composite transducers, to robotic vision/control in opaque environments. The requirement for improved imaging quality, at extended ranges, in both

civil and military sonar applications, has resulted in a motivation to develop advanced wideband acoustic signal processing and an appropriate transducer technology. The relative merits of composite materials, compared to conventional ceramics, in terms of potential bandwidths and sensitivities, are readily apparent.

This chapter investigates the performance of a wide range of stacked composite transducers, from both a theoretical and experimental viewpoint. The influence of the number of layers on transmission, reception and impedance are considered. This analysis includes the effects of attenuation attributed to bond layers. Finally, a brief analysis of some asymmetric stacked structures is presented.

7.2 DEVELOPMENT OF A STACKED TRANSDUCER MODEL

The foregoing discussion of the versatility of stacked transducers, in terms of geometry, number of layers, the nature of the bond layer and material characteristics, suggests that a general transducer model for these structures would be invaluable. Fortunately, Hayward et al [65] have recently developed a versatile stacked thickness mode transducer model based on a frequency domain matrix formulation similar to that originally proposed by Lewis [49]. However, Lewis' formulation included only the effect of passive layers. Prior to this, comparatively little modelling of stacked structures had been performed. Martin developed a model for stacked cylindrical tube vibrators similar to those encountered in standard mass-spring devices [66]. This method was based on Mason's electrical circuit analogy [5], and involved considering an array of 'T' type equivalent circuit models electrically connected in parallel. The derivation presented was for N identical stacked elements. In this case, a general wave function may be derived, and the entire 'T' network can be reduced to a single equivalent circuit. If the elements are not identical, the formulation becomes unwieldy and requires matrix manipulation. In conclusion, the formulation presented lacks versatility, and its implementation for the general asymmetric case is complex.

The new frequency domain formulation has been developed from the general equations for describing the behaviour of a single layer. Thus, it uses expressions similar to

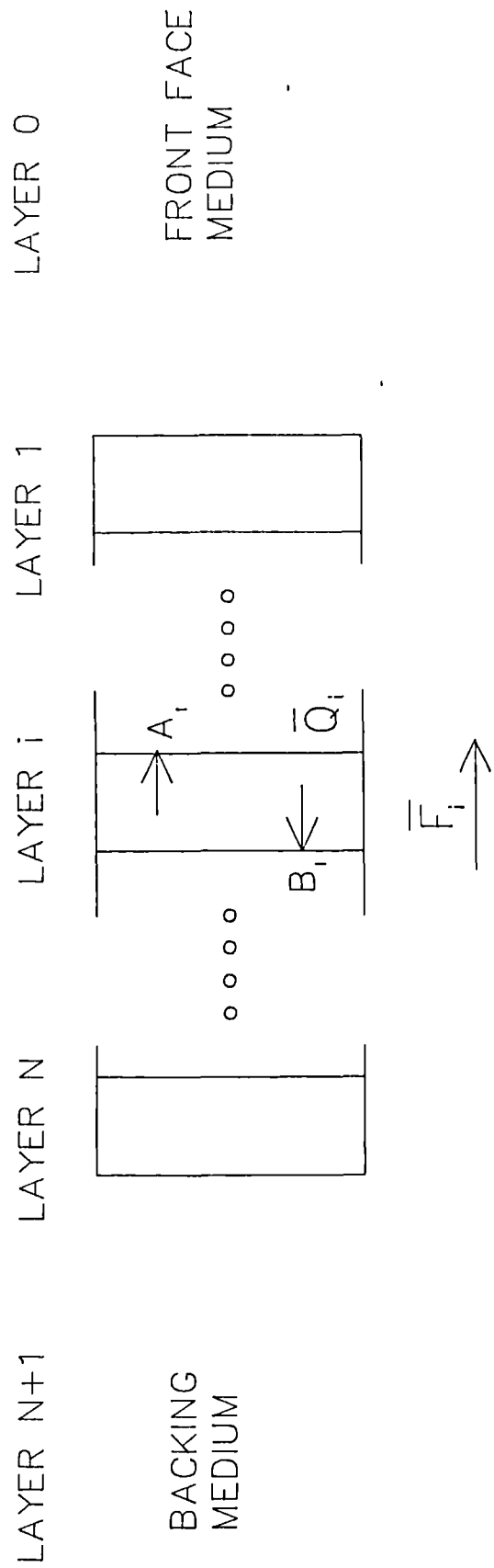


Figure 7.3 General, one dimensional, layered transducer system

those considered in Chapter V. It should be stressed that the model is one dimensional and therefore the dimensions of the complete stacked structure, and each component layer, should be such that non-thickness mode resonant activity is negligible. For the general one dimensional layered system, as illustrated in Figure 7.3, Equation 7.1 describes the relationships between forces, charges and displacements. A bar above a symbol denotes a Laplace quantity.

$$\bar{F} + h_i \bar{Q}_i = sZ_{mi} [-A_i e^{-sT_i} + B_i e^{sT_i}]$$

$$\bar{V}_i - \bar{Q}_i / C_i = -h_i [A_i (e^{-sT_i} - 1) + B_i (e^{sT_i} - 1)] \quad 7.1$$

\bar{F}_i is the total force travelling in the thickness direction in the i^{th} layer. \bar{Q}_i is the charge on the electrodes of the layer and \bar{V}_i is the voltage across layer 'i'. T_i is the wave transit time across layer 'i' and is derived from the layer thickness and wave velocity. A_i and B_i are functions of mechanical displacement describing forward and backward wave propagation.

7.2 i) Independent electrical excitation/ loading of the active layers

In this case, each active layer is connected via a Thevenin equivalent load impedance to the voltage source appropriate to that layer. This configuration is illustrated in Figure 7.4. The charge across the i^{th} layer may be expressed in terms of the source voltage, the voltage across the transducer, and the Thevenin load impedance.

$$\bar{Q}_i = (\bar{V}_S - \bar{V}_i) / s\bar{Z}_{Ei} \quad 7.2$$

This expression may be substituted directly into Equation 7.1 to yield versatile system equations containing functions of excitation voltages and load impedance rather than the charges across specific layers. The resulting expressions are detailed in the literature [65].

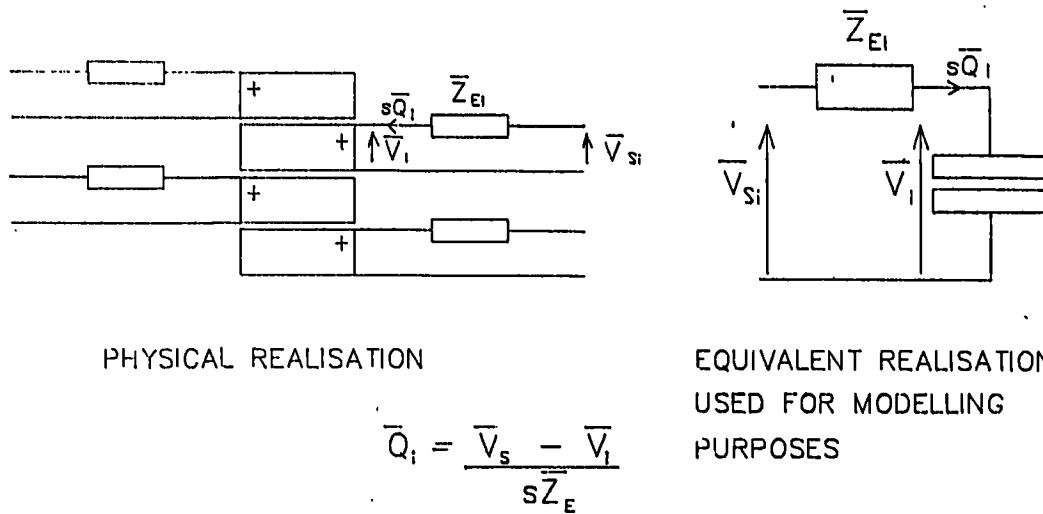


Figure 7.4 Configuration of a stacked structure composed of electrically isolated active layers

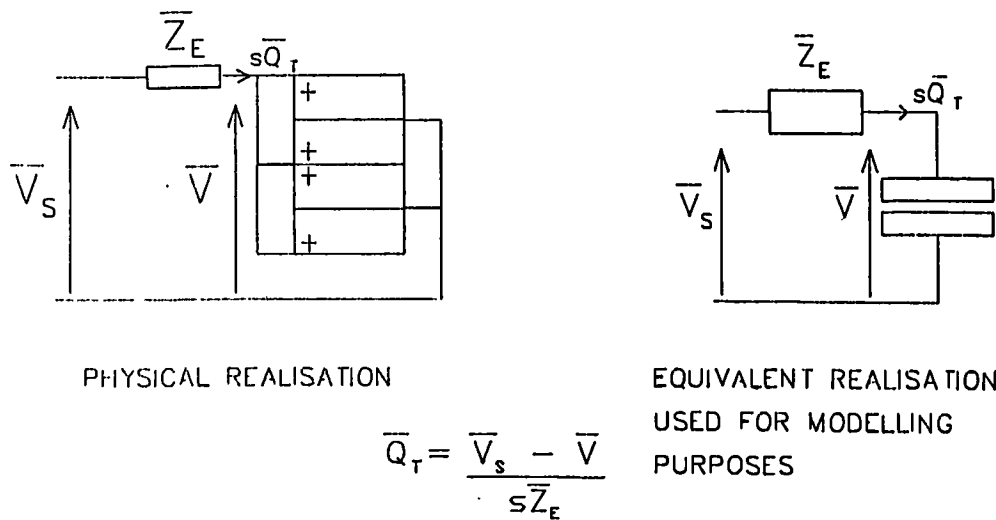


Figure 7.5 Configuration of a stacked structure composed of active layers connected in parallel

7.2 ii) Parallel electrical excitation/ loading of the active layers

This configuration, illustrated in Figure 7.5, is of more general interest than that considered above. The electric field across the layers is common, and therefore all are influenced simultaneously. Furthermore, any secondary field generated by one layer is applied simultaneously to all others. Thus, if the structure is asymmetric, complex secondary effects may be observed in each of the layers.

The total charge associated with the structure may be derived from the excitation voltage, transducer terminal voltage and Thevenin equivalent load impedance, as described below.

$$\bar{Q}_T = (\bar{V}_S - \bar{V}) / (s\bar{Z}_E) \quad 7.3$$

This expression may be substituted into Equation 7.1 to yield relationships for the i^{th} layer. The required substitutions and algebraic manipulation are described in the literature [65].

The expressions for all N layers are developed and solved simultaneously. This may be achieved efficiently in practice by representing the equations in matrix form. The unknown quantities are evaluated by solving the matrix equation using Gaussian elimination.

7.3 PERFORMANCE OF STACKED COMPOSITE STRUCTURES

7.3 i) Impedance as a function of the number of layers

In this, and subsequent sections, a brief comparison is made between the performance of stacked, and non-stacked structures possessing the same centre frequency, and hence overall thickness.

The impedance characteristics of a piezoelectric transducer are determined by its clamped capacitance and the extent to which this is modified by secondary piezoelectric activity in the vicinity of resonant modes. Therefore, the dependence of the overall impedance characteristics of a stacked transducer will reflect, to a large extent, the dependence of the capacitance on the stacking geometry. Equation 7.4 is the standard expression for determining the capacitance of a parallel plate capacitor where, A is the plate area, and d is the distance between them.

$$C = \frac{\epsilon_r \epsilon_0 A}{d} \quad 7.4$$

Hence, for a specific permittivity and area, the capacitance is inversely proportional to the distance between the plates. If a single transducer is sliced into 'N' equally thick layers, then the capacitance of each layer is increased by a factor of 'N'. If these 'N' layers are then connected in parallel, the overall capacitance of the structure is increased by a factor of 'N²'. In the vicinity of the electrical resonance, the impedance may

IMPEDANCE

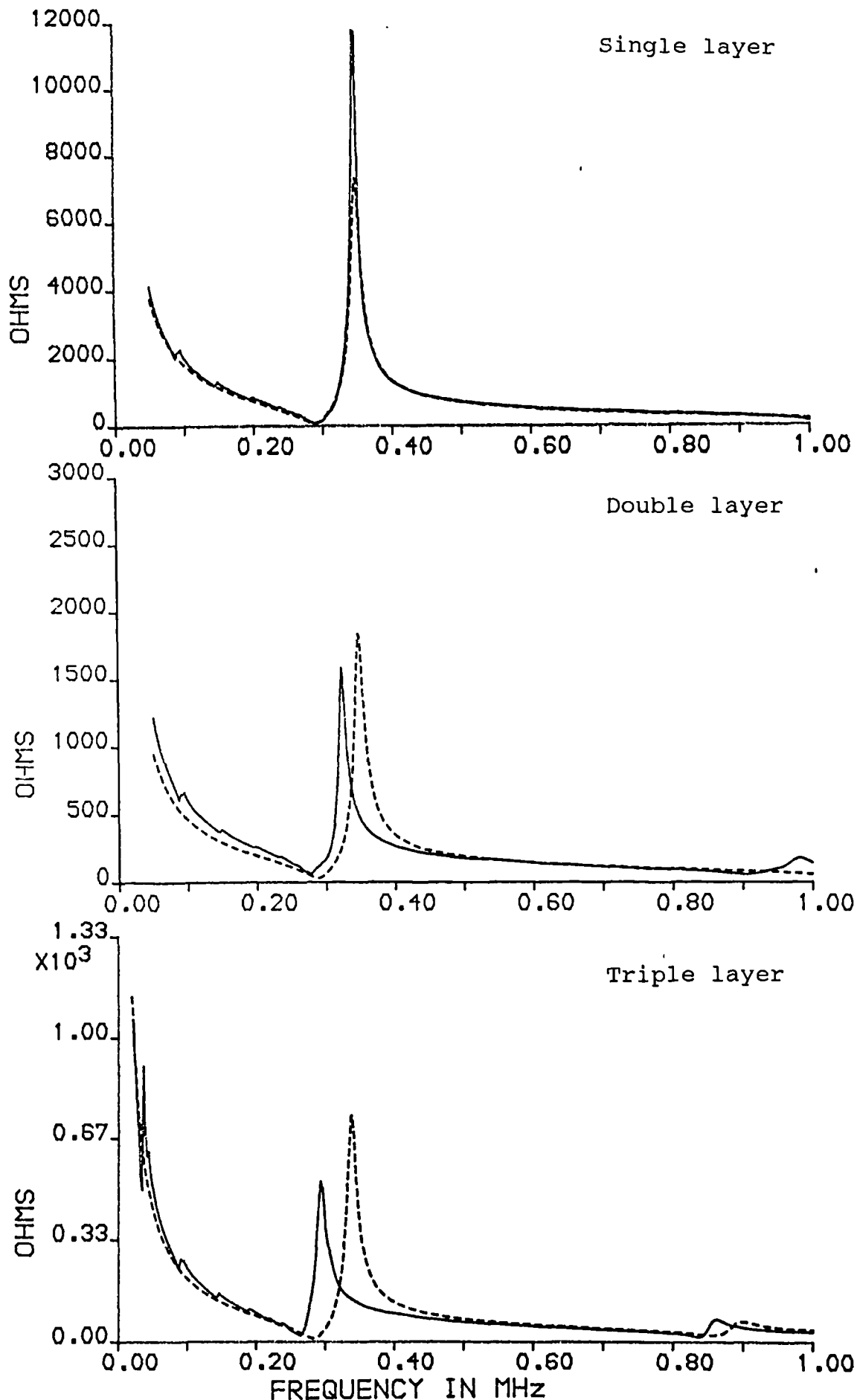


Figure 7.6 Impedance magnitude characteristic of a 30x30mm 250kHz 40% composite transducer for three layer configurations. Measured— Theoretical----

possess a significant resistive component, which depends on the mechanical loading conditions. However, it may be shown that the resistive component of impedance also decreases by a similar factor to that for the capacitive component. The resistance of a block, of area A , thickness d and volume resistivity, ρ , is defined in Equation 7.5.

$$R = \frac{\rho d}{A} \quad 7.5$$

If ρ and A are constant, then resistance is proportional to thickness, d . Hence, if a block is sliced into ' N ' layers, then the resistance of each layer is reduced by a factor of ' N ', and the parallel combination of these by a factor of ' N^2 '.

It should be stressed that these approximate relationships are less accurate for stacked transducers comprising of three or more layers, and for stacked transducers which are asymmetrically mechanically loaded. This is because the mechanical boundary conditions on each of the internal and external layers are different, and hence the quantity of secondary piezoelectric activity is different. More complex configurations must be analysed using the complete, comprehensive stacked transducer model.

The expected reduction in impedance of stacked transducers has been verified for 250kHz, 40% PZT 5A transducers. Figure 7.6 demonstrates moderate agreement between measured and simulated results for up to three layers. Notice that the impedance magnitude axis has been scaled down by a quarter and a ninth for the double and triple

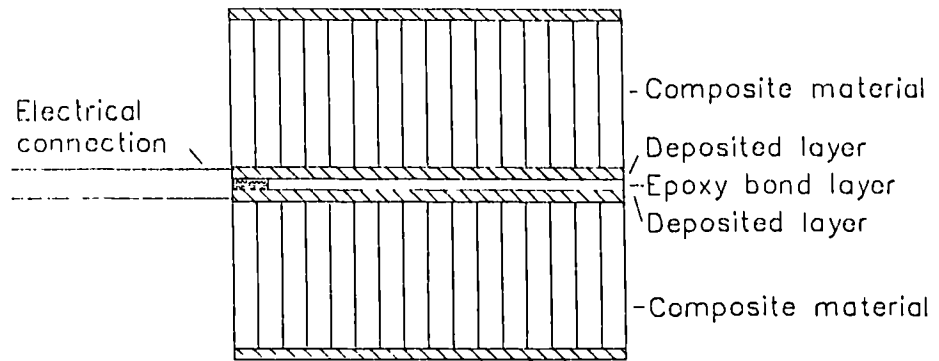


Figure 7.7 Stacked transducer with vacuum deposited electrodes

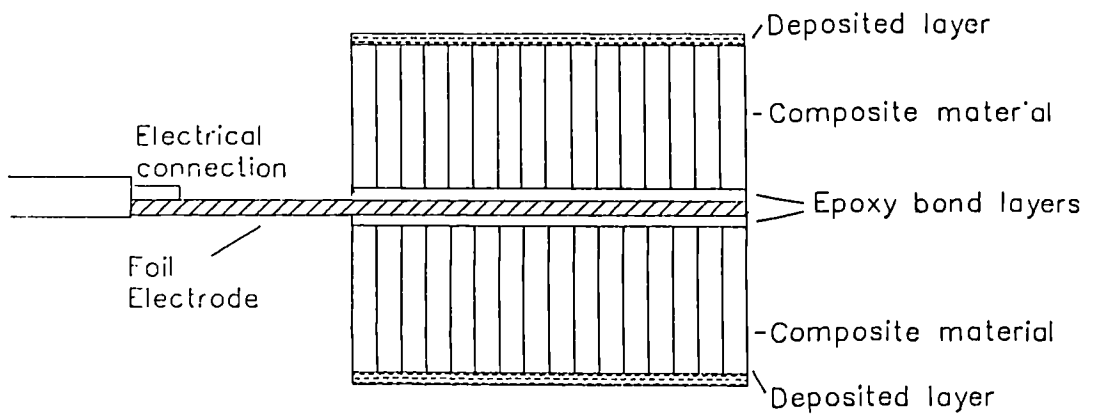


Figure 7.8 Stacked transducer with aluminium foil electrodes

layer devices respectively.

A comparison of the key electrical properties of four comparable composite transducers has been made. Double, and triple, layered composite transducers have been tested. These were fabricated using vacuum deposited electrodes. Additionally, a double layered composite transducer, utilising an aluminium foil electrode, has been tested. A description of the construction of these two types of stacked transducers is detailed below. In addition to the stacked transducers, a reference non-stacked transducer, of similar dimensions, was fabricated.

1) Vacuum deposited electrodes (Figure 7.7)

A 500nm thick coat of aluminium is deposited on the polished surfaces of the composite layers. Alternatively, chromium, followed by silver or gold, may be deposited. These layers are bonded together under a pressure of approximately 4MPa using CY1301/HY1300 low viscosity epoxy resin. A fine wire is trapped within the bond to provide electrical connection. A high quality electrical connection is obtained, but experience has indicated that this type of bond is susceptible to mechanical damage when the transducer is operated under practical excitation conditions.

2) Aluminium foil electrodes (Figure 7.8)

In this type of structure, the two polished surfaces of the composite material are bonded together with a $10\mu\text{m}$

TABLE 7.1

Electrical parameters of stacked transducers

	1 LAYER	2 LAYERS	3 LAYERS	2 LAYERS a
THICKNESS mm	5.11	5.07	5.20	5.15
f_m (Ω @ kHz)	69 Ω @ 289	36 Ω @ 283	22 Ω @ 262	48 Ω @ 271
f_n (Ω @ kHz)	12K @ 347	2.1K @ 333	481 Ω @ 290	1.8K @ 321
C_o nF	0.509	2.201	5.270	2.182
ϵ_R Exp.	327	1401	3472	1420
ϵ_R The.	345	1380	3104	1380
k_t Exp.	0.59	0.55	0.44	0.58
k_t The.	0.60	0.59	0.59	0.58
Q Exp.	34	19	24	15
Q The.	36	23	19	18
c ms ⁻¹ Exp.	3546	3377	3045	3317
c ms ⁻¹ The.	3610	3580	3480	3530

KEY

a) Two layer transducer incorporating a 10 μ m aluminium foil electrode (all others possess deposited electrodes).

All transducer are 40% PZT 5A ceramic and possess lateral dimensions 30 x 30mm.

aluminium foil electrode trapped between them. Again CY1301/HY1300 epoxy is used in combination with a static compressive pressure of approximately 4MPa. The epoxy bond layer is sufficiently fine ($<10\mu\text{m}$) that points of contact between the foil and the ceramic may be expected. This type of bond is considerably stronger than that described above, but it is thicker and the quality of the electrical connection is probably inferior.

The key electrical properties of the four transducers are presented in Table 7.1. All of these transducers were made from ceramic from the same batch and possessed very similar properties. Theoretical values, for permittivity, coupling coefficient, mechanical Q factor and wave velocity, are indicated. It is apparent that there are significant deviations between the theoretical and practical results. The layers of all the stacked transducers were bonded together in one clamping process. Therefore, the pressure exerted on all the bond layers was identical. This ought to have resulted in the bond layers possessing characteristics as near to identical as was practically possible. However, complete alignment between the pillars on adjacent surfaces was impossible to obtain.

The permittivity of each of the stacked transducers are at least as high as the theoretical value. This suggests that good electrical contact to each of the layers is being obtained. Any flaw in the electrical contact would tend to reduce the effective permittivity. The three layer transducer exhibits a significantly higher permittivity.

This is possibly a result of experimental error or as a consequence of the original ceramic possessing a permittivity 4% higher than nominal. The measurement of C_0 , even when measured at the second harmonic of the thickness mode resonance, where thickness activity is minimised, is still vulnerable to deviations caused by spurious resonant activity.

The coupling coefficients of the stacked transducers are generally lower than expected. This is despite the fact that the coupling coefficients of the individual layers of the double and triple layer stacked transducers were 0.60 and 0.59 respectively. This degradation may be a result of decreased efficiency caused by partial misalignment between the pillars. However, the volume fraction of the composites was 40% and therefore the ceramic pillars were wider than the gaps between them. Hence, total misalignment between adjacent pillars could not occur. It is probable that misalignment between adjacent pillars has a detrimental effect on device efficiency. Furthermore, the more layers that are employed, the more serious this problem will become.

The mechanical Q factor of the stacked transducers are lower than expected. This may be attributed to increased attenuation arising from the bond layers, since the attenuation in the composite layers themselves must be uniform. This attenuation may be a result of the bond layer material itself and/or attenuation resulting from misalignment between the pillars. One would naturally

expect this effect to increase with the number of layers. However, when examination of the Q factors for the two and three layer cases is made, it is evident that this has not occurred. It is believed that this reversal is due to variability in the characteristics of the bond layers. Hence, further investigation of these layers is necessary. Nevertheless, it is apparent that the design incorporating a foil electrode possesses a slightly higher attenuation than the design using deposited aluminium electrodes.

An estimate of the attenuation due to the bond layers has been made. The wave attenuation coefficient was increased during simulations of the stacked transducers until mechanical Q factors similar to those observed experimentally, were obtained. When an attenuation coefficient of 0.06dB, corresponding to a frequency of 300kHz, was employed, the simulation results for mechanical Q factors shown in Table 7.1, were obtained. This figure has provided an approximate estimate of the actual mechanical losses. The attenuation coefficient for each 10 μ m bond layer is approximately one quarter of the value of the attenuation coefficient in the rest of the composite material. However, since the composite material is five hundred times thicker than the bond layers, the apparent attenuation in the bond layers, relative to their thickness dimensions, are very high. Clearly, there is considerable scope for attempting to further minimise attenuation in the bond layers, and for obtaining a more accurate means of quantifying the mechanical loss

attributed to them. In all subsequent simulations, this attenuation coefficient, and the material parameters for CY1301/HY1300 epoxy are used in the evaluation of the simulated responses of stacked transducers. On occasion, theoretical results, obtained assuming loss free bond layers, are included for comparison.

The velocities of the stacked transducers are measurably lower than predicted. The velocities of the double layer and triple layer composite stacked transducers are 6% and 12% lower, respectively, than expected. No satisfactory explanation for this phenomena has been found. It has been hypothesised that the reduction in wave velocity may be related to misalignment between the pillars of adjacent layers. However, some limited finite element analysis of misaligned structures suggested that velocity is independent of pillar alignment. Clearly, further work on this aspect of the work is required.

7.3 ii) Transmission performance of stacked composite structures.

The reduced impedance of a stacked transducer should result in a greater transmission response for a given excitation voltage. However, the effects of source impedance will be more significant if the impedance of the transducer is almost as low as the source output impedance.

Zero source impedance

The case of zero source impedance is the simplest to analyse. Although a zero output impedance is physically unrealisable, it is possible to simulate one by compensating the supply voltage so that the transducer terminal voltage remains constant independent of the current drawn from the source. The following approximate expression may be derived from a complete piezoelectric transducer model [46]. This neglects the effects of reverberation, secondary piezoelectric activity and electrical loading effects. The expression permits first order approximations to be made regarding the expected performance of a stacked transducer. Clearly, if any of the approximations are not valid, the comprehensive stacked transducer model, as described in the literature [65], must be employed. The simulation results presented in this chapter were obtained using the full transducer model.

$$F \propto hC_0 \quad 7.6$$

As discussed previously, the value of C_0 in a stacked transducer is increased by a factor of N^2 , where N is the number of identical layers into which the original transducer has been sliced. The dependence of h , the piezoelectric constant, on the number of layers must now be established. This parameter depends on the permittivity, elastic stiffness and the electromechanical coupling coefficient. Clearly, the elastic stiffness is independent of the number of layers. The coupling coefficient defines the ratio of output converted energy

to available input energy, and hence it must also be independent of the ceramic geometry. Naturally, there may be some slight modification of both elastic stiffness and electromechanical coupling coefficient as a consequence of imperfect bonding. The dependence of h on the other parameters is defined in expression 7.8.

$$k_t = h \sqrt{(\epsilon / c_{33}^D)} \quad 7.7$$

Therefore:

$$h = k_t \sqrt{(c_{33}^D / \epsilon)} \quad 7.8$$

Therefore, since k_t and c_{33}^D are constant:

$$h \propto \frac{1}{\sqrt{\epsilon}} \quad 7.9$$

Alternatively:

$$h \propto \frac{1}{\sqrt{C_0}} \quad 7.10$$

Hence, since C_0 is a function of N^2 , then h is inversely proportional to N . Therefore, the following linear relationship may be derived from expression 7.6.

$$F \propto N \quad 7.11$$

This result, indicating that pressure output is a linear function of the number of layers, has been verified experimentally for both pure ceramic and composite stacked transducers. The composite transducers used were the same as those described in Table 7.1. The ceramic transducers were fabricated with virtually identical dimensions. The experimentally measured mechanical Q factors of the stacked transducers were not measurably lower than that of the non-stacked ceramic transducer. Therefore, the effects

TABLE 7.2

Peak CW transmission efficiency as a function of the number of layers in the stack (0Ω source impedance)

MATERIAL	NUMBER OF LAYERS				
	1	2	3	4	5
COMPOSITE Exp.	1.00	1.75	2.50		
COMPOSITE Sim1	1.00	1.74	2.39	2.97	3.50
COMPOSITE Sim2	1.00	1.98	2.88	3.80	4.73
CERAMIC Exp.	1.00	2.00	2.90		
CERAMIC Sim2	1.00	1.98	2.92	3.86	4.81

KEY

Sim1 : Simulated assuming attenuation of 0.06dB/ bond layer at 0.3MHz.

Sim2 : Simulated assuming no attenuation in bond layers

of bond layer attenuation are omitted from the simulations of stacked ceramic transducers. Table 7.2 illustrates the theoretical and simulated results for peak CW pressure output. Simulated results have been obtained for up to five layers. However, due to the manufacturing complexity and time requirement, experimental results have only been obtained for up to three layers. In this, and in all similar subsequent results, the responses have been normalised with respect to the result for a single active layer. The results for the ceramic transducers, and for the simulated stacked composite transducers, assuming loss free bond layers, indicate a linear increase in transmission efficiency as a function of the number of layers. However, it is apparent that when lossy bond layers are included in the simulations of stacked composite transducers, then measurable under performance is observed. The extent of this under performance correlates well with the experimentally measured values for transmission efficiency. This result indicates that, eventually, no further enhancement in transmission efficiency will be obtained by increasing indefinitely the number of active layers.

Finite source impedance

In this case, the net voltage across the transducer depends on the current drawn and the value of the source impedance. Since the operating impedance of a transducer is a complex function of frequency and loading, it is generally desirable to model the effects of source

TABLE 7.3

Impedance at electrical resonance in stacked structures

	NUMBER OF LAYERS				
	1	2	3	4	5
IMPEDANCE (Ω)	258	65	29	17	11

Simulated results for 40% PZT 5A transducers possessing dimensions 30 x 30 x 5mm with one face immersed in water.

TABLE 7.4

Peak CW transmission efficiency as a function of the number of layers in the stack (50 Ω source impedance)

	NUMBER OF LAYERS				
	1	2	3	4	5
COMPOSITE Exp.	1.00	1.38	1.25		
COMPOSITE Sim1	1.00	1.23	1.19	1.12	1.06
COMPOSITE Sim2	1.20	2.08	2.86	3.56	4.19

KEY

- Sim1 : Simulated assuming attenuation of 0.06dB/ bond layer at 0.3MHz and a source impedance of 50 Ω
- Sim2 : Simulated assuming attenuation of 0.06dB/ bond layer at 0.3MHz and a source impedance of 0 Ω . These results are normalised with respect to the case of a single layer operating with a 50 Ω source impedance.

impedance comprehensively using a complete transducer model in a manner similar to that discussed in Chapter V. However, the maximum power transfer theorem plays an important role in determining the performance of transducers operating with a finite source impedance. This theorem states that maximum power is delivered to a load, when the load impedance matches the internal source impedance. For the present analysis, only a 50Ω source is considered, as this corresponds to the output impedance of a general purpose signal generator which was available.

Table 7.3 indicates the theoretical magnitude of impedance at the electrical resonant frequency for a number of composite transducer configurations, similar to those described previously. This table indicates that the two layer composite may be expected to produce the optimum response because it possesses an impedance at resonance closest to the desired value (50Ω). Table 7.4 indicates the theoretical and measured CW peak pressure responses for these same transducers. This table indicates that a two layer structure does indeed produce an optimum response. The simulated response for a zero source impedance is included for interest. The attenuating effect caused by the 50Ω source impedance is readily apparent for those transducers possessing the lowest internal impedances.

7.3 iii) Reception performance of stacked composite transducers

The increased capacitance of stacked transducers implies that for a given charge generated in reception, a reduced voltage is generated. This is because the charge generated is a function of the geometry and type of ceramic, and is independent of the nature of the electrical connections made. However, if the receiver possesses a relatively low input impedance, then a stacked transducer may provide a sensitivity as high, or higher, than a similar non-stacked transducer operating into the same load. Nevertheless, peak reception voltage sensitivity will always be obtained when the receiver input impedance is virtually infinite.

Infinite receiver load impedance

Although an infinite load impedance is impossible to attain in practice, a receiver load impedance, providing a good approximation to this ideal condition, may be obtained. For the cases considered here, the transducer impedance is in the vicinity of 100Ω , and hence an oscilloscope input stage, presenting an impedance of $1M\Omega$, provides a satisfactory approximation to an infinite load. The following approximate expression for determining the voltage sensitivity, as a function of the transducer capacitance and piezoelectric constant, may be derived from the piezoelectric transducer model [46]. As before, this expression neglects the effects of reverberation, secondary piezoelectric activity and electrical loading. If any of these effects are significant, then the full

TABLE 7.5

Peak CW reception sensitivity as a function of the number of layers in the stack (1M Ω load impedance)

MATERIAL	NUMBER OF LAYERS				
	1	2	3	4	5
COMPOSITE Exp.	1.00	0.56	0.42		
COMPOSITE Sim1	1.00	0.33	0.18	0.12	0.08
COMPOSITE Sim2	1.00	0.45	0.28	0.20	0.16
CERAMIC Exp.	1.00	0.47	0.28		
CERAMIC Sim2	1.00	0.43	0.27	0.20	0.16

KEY

Sim1 : Simulated assuming attenuation of 0.06dB/ bond layer at 0.3MHz.

Sim2 : Simulated assuming no attenuation in bond layers

transducer model, as described in the literature [65], must be employed.

$$V \propto \frac{h}{C_0} \quad 7.12$$

The dependence of h and C_0 on the number of active layers has already been discussed in section 7.3 i). Hence, the following simplified expression is obtained when the modified values of h and C_0 have been substituted into expression 7.12.

$$V \propto \frac{1}{N} \quad 7.13$$

Thus, the voltage sensitivity is inversely proportional to the number of layers. The accuracy of this expression has been verified experimentally for the same one, two and three layer PZT 5A and composite stacked transducers as those described in the previous section. These results are presented in Table 7.5. Theoretical results were obtained for a $1M\Omega$ and a $1G\Omega$ load impedance and the maximum reduction in sensitivity caused by the $1M\Omega$ load, as opposed to the $1G\Omega$ load, was 0.3%. Therefore, the loading effect of the $1M\Omega$ impedance was insignificant. Excellent correlation has been achieved between the theoretical results and those for the PZT 5A transducers. However, the stacked composite transducers are providing measurably higher voltage sensitivities than those predicted theoretically. If significant wave attenuation was present, then reduced, and not higher, voltage levels would be expected. It is possible that the attenuating

effect within the bond layers is significant in the active, transmitting mode, but not in the passive reception mode. Furthermore, the attenuation coefficient may be a function of excitation level. The voltages, and displacements, in a transducer are generally lower when it is operating in reception mode than when it is operating in transmission mode. Since the model provides accurate replication of the results obtained experimentally for the stacked ceramic transducers, the possibility of a fundamental flaw within the model is discounted. It has already been shown in section 7.3 i) that the material parameters of composite transducers deviate, by a measurable extent, from those predicted theoretically. It is possible that the complex internal mechanisms responsible for these deviations are also responsible for slight deviations in overall transducer performance indicated here. These phenomena, which possibly include the effects of pillar misalignment between adjacent layers, merit further investigation.

Finite load impedance

The dependence of reception voltage sensitivity on the number of layers is now considered for the case that the magnitude of the reception load impedance is of the same order as the internal impedance of the transducer. Clearly, few practical designs use low impedance receivers. However, a low impedance is occasionally employed to broaden bandwidth, at the expense of peak sensitivity, where bandwidth is of prime importance.

TABLE 7.6

Peak CW reception sensitivity as a function of the number of layers in the stack (50Ω load impedance)

MATERIAL	NUMBER OF LAYERS				
	1	2	3	4	5
COMPOSITE Exp.	1.00	1.17	1.17		
COMPOSITE Sim1	1.00	0.97	0.88	0.81	0.75
COMPOSITE Sim2	1.00	1.09	0.99	0.94	0.92
COMPOSITE Sim3	18.7	6.11	3.36	2.21	1.59

KEY

Sim1 : Simulated assuming attenuation of 0.06dB/ bond layer at 0.3MHz.

Sim2 : Simulated assuming no attenuation in bond layers

Sim3 : Simulated assuming no attenuation in bond layers and a 1MΩ load impedance. These results have been normalised with respect to the case for a single layer operating into a 50Ω load.

In a manner analogous to that for transmission, a finite electrical loading results in potential division, between transducer and load. Again, it is generally necessary to model the entire system in a comprehensive model since the impedance of the transducer is a rather complex function of material characteristics, geometry, mechanical loading and frequency. As in the case of transmission, the maximum power transfer theorem is relevant to the determination of the optimal transducer configuration. Maximum power is delivered to the receiver load impedance when this impedance matches that of the transducer. However, it should be emphasised that peak sensitivity is always obtained when the load impedance tends towards an infinite value.

Table 7.6 provides a comparison of measured and theoretical peak CW reception sensitivity, operating into a 50Ω load, for the same configurations of transducers as discussed in section 7.3 ii). The simulated results for an infinite load impedance are included for comparison. These results indicate that, as would be expected, the most severe electrical loading effects occurs in the receivers possessing the highest internal impedance. The sensitivity level of the different transducers are relatively constant. The simulated results, assuming loss free bond layers, indicate that the two layer structure provides the highest sensitivity. However, the simulation which includes lossy bond layers suggests that sensitivity declines as soon as more than one layer is employed. The

TABLE 7.7

Peak pulse-echo sensitivity as a function of the number of layers in the stack (0Ω source / $1M\Omega$ load impedance)

MATERIAL	NUMBER OF LAYERS				
	1	2	3	4	5
COMPOSITE Exp.	1.00	0.91	0.87		
COMPOSITE Sim1	1.00	0.69	0.59	0.53	0.49
COMPOSITE Sim2	1.00	0.79	0.70	0.67	0.66
CERAMIC Exp.	1.00	0.91	0.85		
CERAMIC Sim2	1.00	0.85	0.79	0.77	0.76

KEY

Sim1 : Simulated assuming attenuation of 0.06dB/ bond layer at 0.3MHz.

Sim2 : Simulated assuming no attenuation in bond layers

TABLE 7.8

Peak pulse-echo sensitivity as a function of the number of layers in the stack (50Ω source / 50Ω load impedance)

MATERIAL	NUMBER OF LAYERS				
	1	2	3	4	5
COMPOSITE Exp.	1.00	1.33	1.41		
COMPOSITE Sim1	1.00	1.20	1.05	0.90	0.80
COMPOSITE Sim2	1.00	1.45	1.33	1.22	1.20

KEY

Sim1 : Simulated assuming attenuation of 0.06dB/ bond layer at 0.3MHz.

Sim2 : Simulated assuming no attenuation in bond layers

experimental results indicate that a higher sensitivity is obtained using the stacked transducers. Again, as in the previous section, it would appear that effective attenuation is less when the transducer is operating as a receiver.

7.3 iv) Pulse-echo performance of stacked composite structures

It is evident from the previous two sections, discussing the transmission and reception characteristics separately, that the overall pulse-echo sensitivity of a layered structure may be expected to be independent of the number of layers employed. This is because transmission, theoretically, increases linearly with the number of layers used, while the reception sensitivity decreases inversely with the number of layers used. Naturally, in making this statement, it is assumed that the source impedance is zero, the receiver load impedance is infinite and that no losses are occurring in the bond layers. Furthermore, in practice, the frequencies of peak transmission and peak reception sensitivity rarely coincide. The dependence of peak pulse-echo sensitivity on electrical loading, in both transmission and reception, is complex and requires careful analysis.

Zero source/ Infinite receiver load impedance

Although this configuration is physically unrealisable, a close approximation may be obtained by compensating for the potential drop across the source impedance, and by employing a high input impedance receiver. Table 7.7

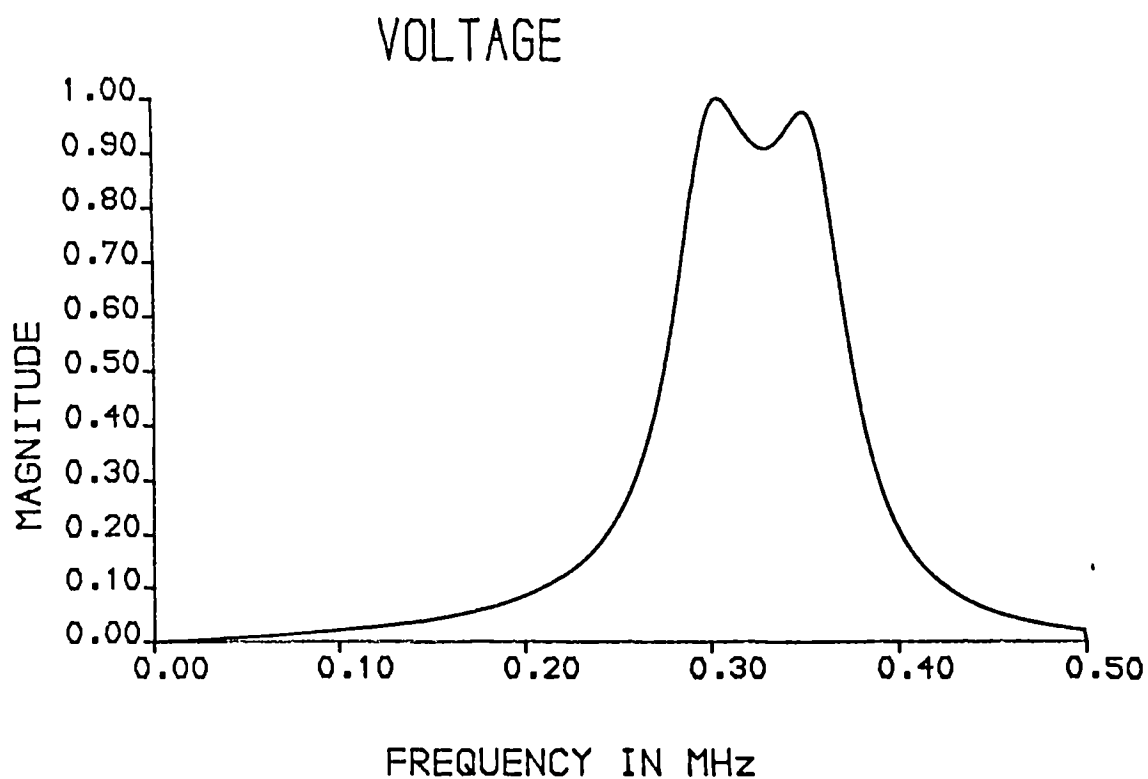


Figure 7.9 Simulated pulse-echo response, as a function of frequency, of a 40%, 300kHz composite transducer. Air backed and without a matching layer

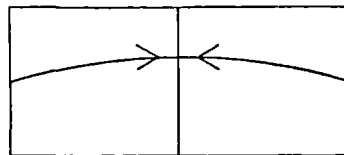
presents measured and simulated results for the same transducer configurations as considered in the previous sections. The prototype stacked composite transducers have performed better than expected from a theoretical viewpoint. Again, this may be due to them possessing a lower attenuation coefficient in reception than in transmission. The determination of peak CW pulse-echo sensitivity is susceptible to error because the frequencies of peak transmission efficiency and peak reception sensitivity are not coincident. This concept is illustrated in Figure 7.9. The lower peak corresponds to peak transmission efficiency. Furthermore, the extent of the deviation between the two frequencies depends on the electromechanical coupling coefficient. Since the coupling coefficients of the stacked transducers are lower than expected, this may account for the two frequencies being closer together, and hence a higher peak sensitivity being observed in the experimental results. The correlation between theoretical and simulated results for the PZT transducers is somewhat better. However, there is still a slight underestimate of device sensitivity in the simulations of the stacked transducers.

Finite source/ Finite receiver load impedance

Table 7.8 presents a comparison of the measured and simulated peak CW pulse-echo sensitivity for a similar configuration to that discussed previously, except that a 50Ω load is present in both the transmission and reception circuitry. The theoretical results, including and

excluding the effects of attenuation in the bond layers, indicate that a two layer structure provides the highest sensitivity. This is presumably because this structure possesses an internal impedance closest to the optimum for this case. Again, the experimental results indicate that the stacked structures are performing better than expected. In fact, their sensitivities are comparable to those obtained assuming loss free bond layers.

In conclusion, the model predicts most of the key features associated with stacked composite transducers. However, there is a requirement for a more thorough and complete investigation of the various complex phenomena which clearly exist. These results suggest that the effects of bond layer attenuation are relatively slight, except when the transducer is being operated purely as a transmitter of ultrasonic waves.



Symmetric transducer
operating at fundamental

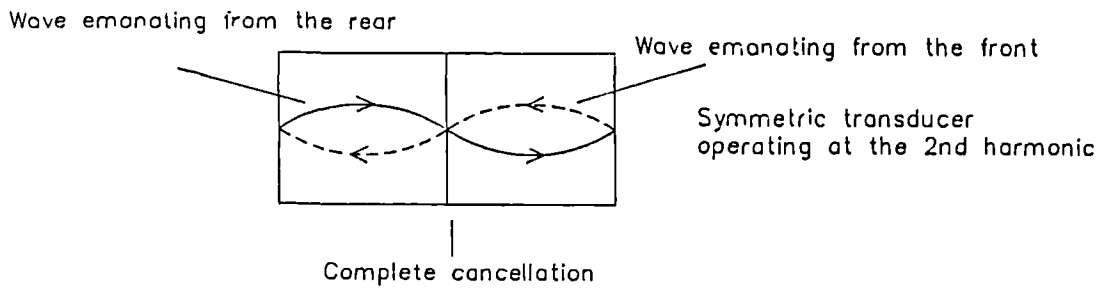


Figure 7.10 Operation of a symmetric, two layer stacked transducer at the fundamental and second harmonic resonant frequencies

7.4 ASYMMETRIC STACKED COMPOSITE STRUCTURES

Asymmetry in a stacked composite structure may be achieved by incorporating diverse layer thickness, electrical loading or material characteristics. Each of these techniques is briefly investigated. The motivation for producing asymmetric structures is that they possess a finite response over very wide bandwidths. Unlike symmetric transducers, they do not possess a null at the second harmonic of the fundamental mode. Some processing techniques involve pre-filtering the excitation function to obtain a desired output profile by taking account of the transfer function of the transducer. Clearly, this technique can only be implemented perfectly if the transducer produces a finite output for all the spectral components of the desired waveform. Therefore, the potential value of an asymmetric transducer is apparent.

A complete understanding of the physical phenomena occurring within an asymmetric transducer is difficult to achieve. However, the explanation for a null occurring in a symmetric transducer is that there is complete cancellation between extending and contracting waves of force. This is illustrated in Figure 7.10. Furthermore, voltages generated by secondary piezoelectric activity also cancel. Any process which destroys symmetry will result in incomplete cancellation occurring, and hence a finite output will occur.

Figure 7.11 Operation of a stacked transducer, with different layer thicknesses, at the second harmonic resonant frequency

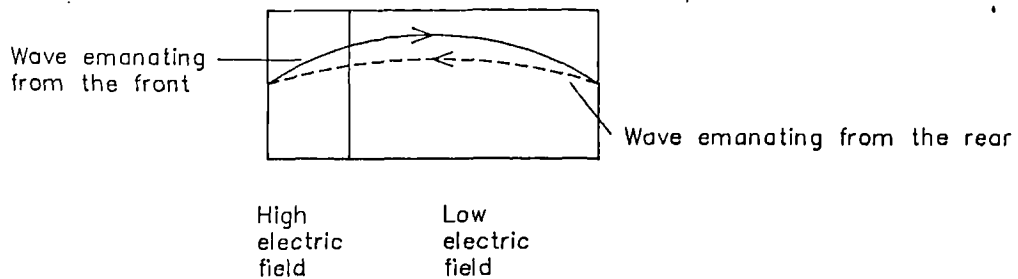
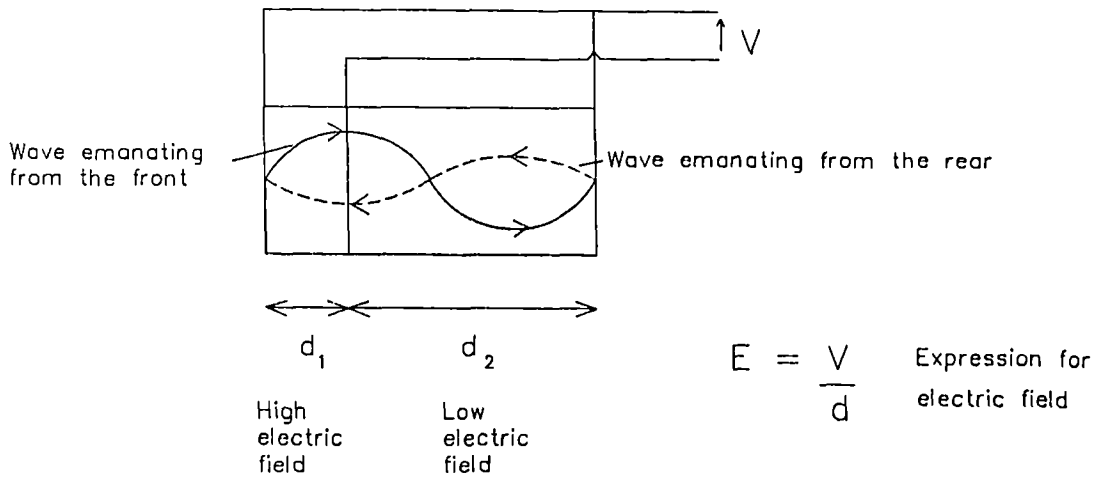


Figure 7.12 Operation of a stacked transducer, with different layer thicknesses, at the fundamental resonant frequency

7.4 i) Diverse layer thickness

Consider the structure in Figure 7.11 operating at the second harmonic of the fundamental thickness mode. Assuming that both layers are operating under identical voltage excitation, it is evident that the thinner layer experiences a higher electric field. Therefore, a larger pressure component emanates from the thinner layer, than from the thicker layer. Hence, complete cancellation cannot occur. Notice that the voltage generated by secondary piezoelectric activity will also be different and thus, these will not cancel. Consider the structure operating at the fundamental thickness resonant mode, as illustrated in Figure 7.12. It is evident that since both layers are not under equal excitation, perfect uniform vibration has been impeded to a certain extent. Therefore, it would appear that a finite output has been obtained at the second harmonic at the expense of reducing the fundamental thickness resonant mode. This concept, which will be verified, applies to all type of asymmetric structures.

Figure 7.13 illustrates both the theoretical and measured impedance response for a prototype 200kHz, 40% PZT 5A, asymmetric double layer composite stacked transducer. The layers are 6.68mm and 1.35mm thick. A resonance at the second harmonic is readily apparent in both curves. The theoretical curve for a reference symmetric transducer, possessing the same overall thickness, exhibits no evidence of resonant activity at this frequency. The

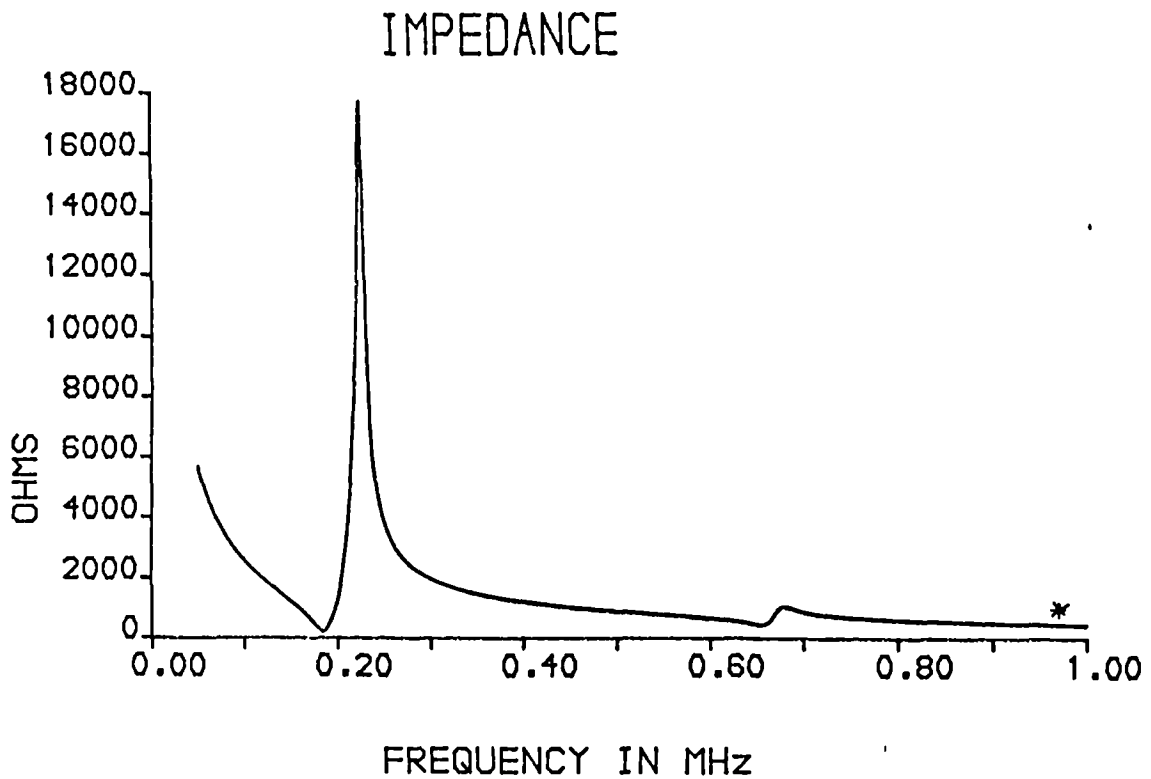
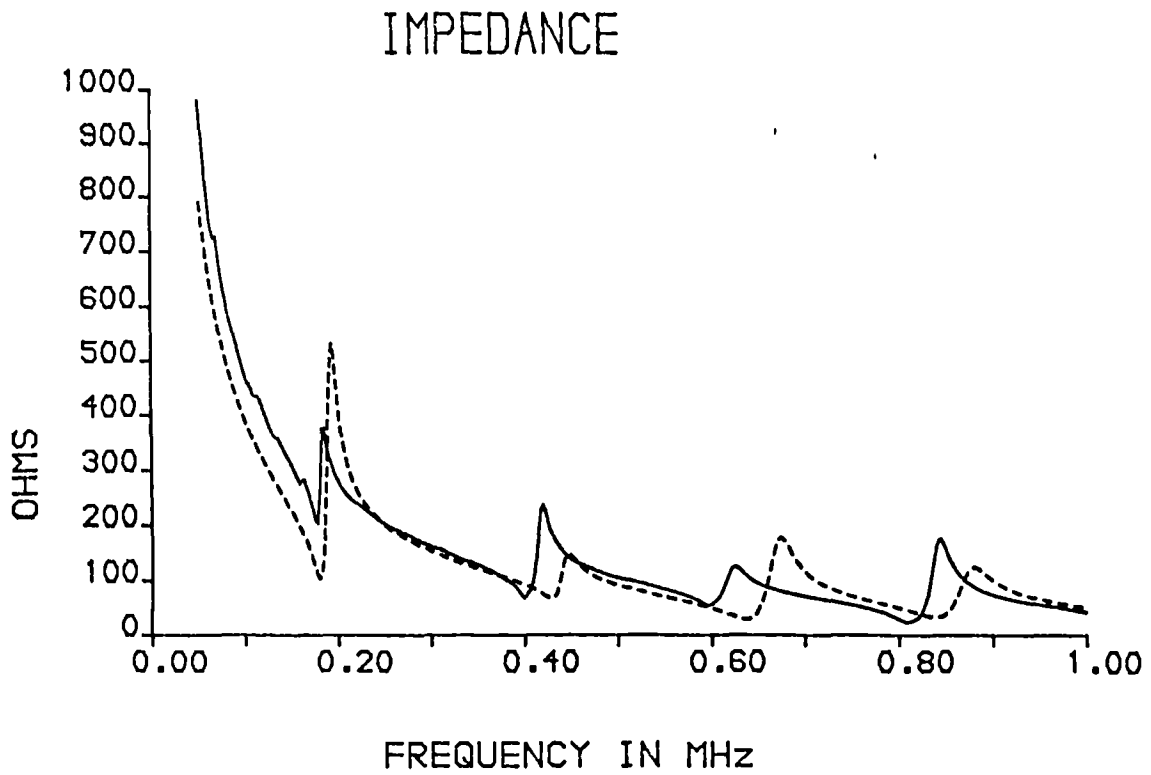


Figure 7.13 Measured and theoretical impedance characteristics of a 200kHz 40% composite comprising layers 6.68mm and 1.35 thick

- Measured
- Theoretical
- * Reference curve for a stack with two 4mm layers

slight deviation between the theoretical and experimental data is probably due to imperfect bonding. An unexpected reduction in longitudinal wave velocity in the stacked structure, similar to that discussed in section 7.3 i), is also apparent. In this case, the theoretical coupling coefficient, associated with the fundamental resonant mode is 0.60 in the symmetric structure and 0.38 in the asymmetric structure. The coupling coefficient associated with the second harmonic in the asymmetric structure is 0.32. Thus, it is evident that the response at the second harmonic in the asymmetric structure has indeed been obtained at the expense of reducing the strength of the fundamental thickness mode.

The transmission and pulse-echo performance of this design has also been briefly investigated. The prototype stacked composite structure was assembled into an air backed probe with no matching layer. The thinner layer was adjacent to the load medium. Figure 7.14 illustrates the measured and simulated CW pressure output response for a source possessing an internal impedance of 50Ω . The simulation has identified the key resonant features, but the overall accuracy is not very good. This may be a result of experimental error and the fact that the measured thickness mode coupling coefficient was 0.38 instead of the theoretical value of 0.34. Also, the measured coupling coefficient of the second harmonic mode was 0.32 instead of 0.30. Therefore, in relative terms, the prototype device possesses a weaker fundamental mode and a stronger

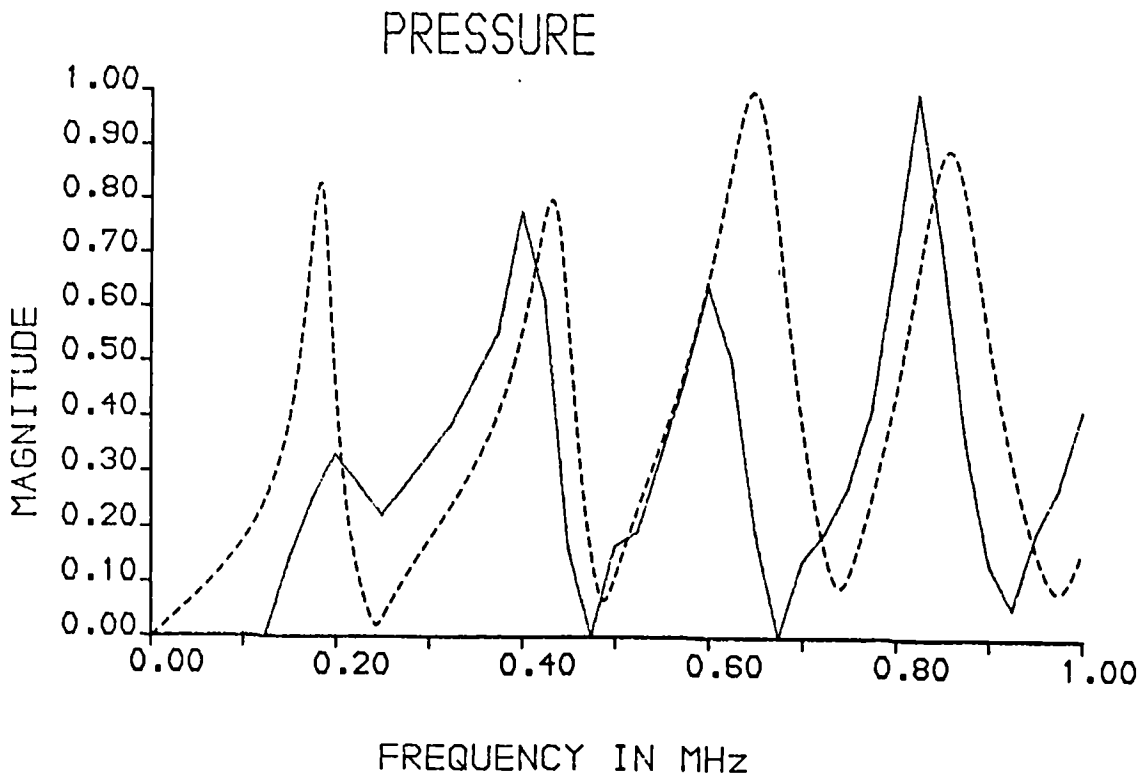


Figure 7.14 Measured and theoretical CW pressure output of an asymmetric stacked transducer, as a function of frequency
 Theoretical -----
 Measured _____

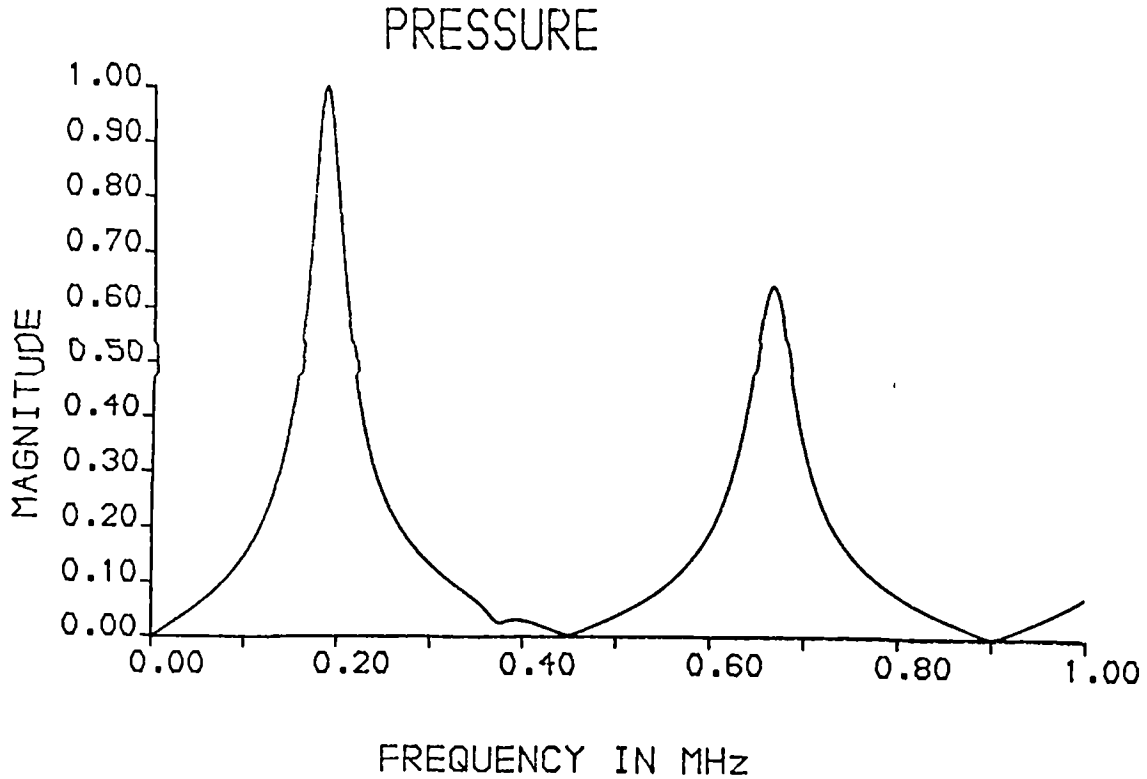


Figure 7.15 Theoretical CW pressure output of a symmetric stacked transducer, as a function of frequency.

second harmonic mode than predicted theoretically. The consequence of this is borne out in the figure. The precise cause of these effects requires further investigation. Notice that the asymmetric structure possesses additional nulls at several frequencies. Therefore, in this case, the problem presented by a null at the second harmonic has not been solved satisfactorily.

Figure 7.15 illustrates the simulated response for a symmetrical structure possessing the same overall dimensions. The peak transmission level, at the fundamental thickness mode frequency, in the symmetric structure is 22% higher than in the prototype asymmetric structure. However, The symmetric structure possesses a significant wide null at the second harmonic.

Figure 7.16 illustrates the measured and simulated CW pulse-echo voltage sensitivity of the same asymmetric stacked transducer. Again, the theoretical result has identified the important resonant features, but the experimental response at the fundamental mode is considerably weaker than predicted using the theoretical model. Figure 7.17 illustrates the simulated pulse-echo response of a similar symmetric transducer possessing the same overall thickness. In this case, the peak sensitivity level of the symmetric structure is 85% higher than that for the asymmetric structure. This is largely a result of the net capacitance of the asymmetric transducer being considerably higher since one of the layers is relatively thin and consequently possesses a high capacitance. This

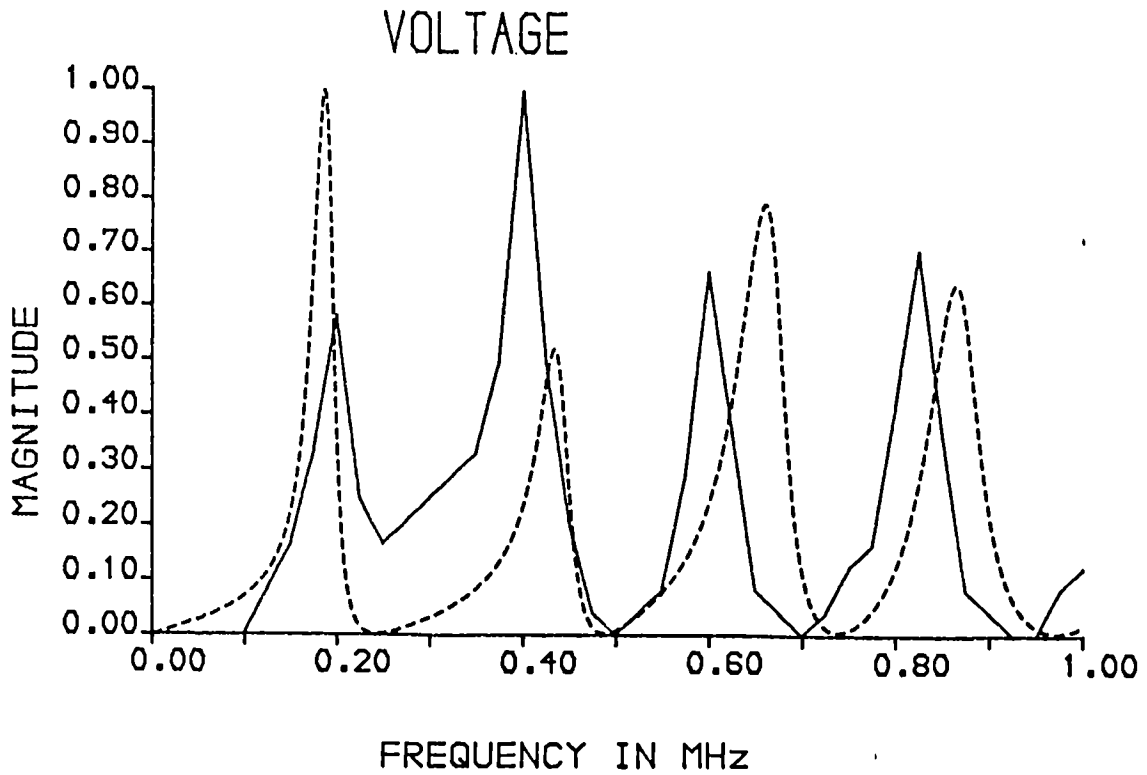


Figure 7.16 Measured and theoretical CW pulse-echo response of the asymmetric stacked transducer as a function of frequency

Theoretical -----
 Measured —————

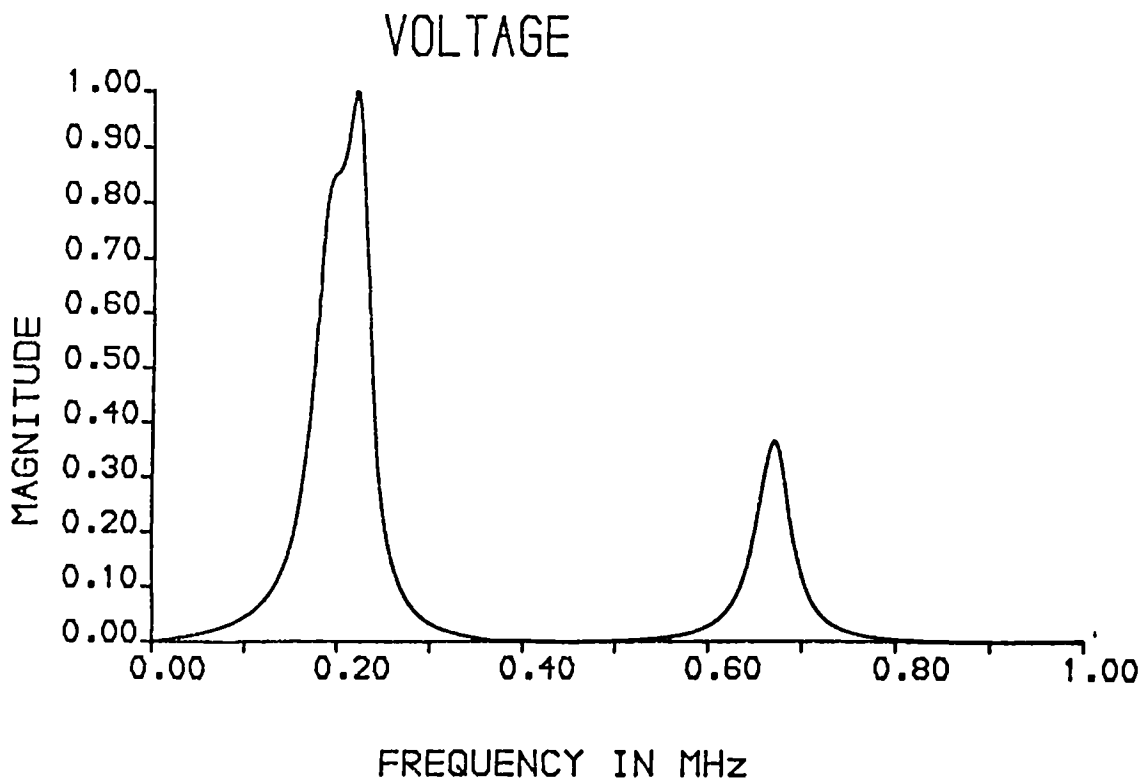


Figure 7.17 Theoretical pulse-echo response of a symmetric stacked transducer, as a function of frequency.

results in a smaller voltage being generated by a specific amount of charge. However, the symmetric device possesses a wide null in the vicinity of the second harmonic.

7.4 ii) Diverse layer electrical load

Steel et al [67] have investigated the effect of varying the electrical loading on one layer of a physically symmetric double layer ceramic stack. It was shown that significant resonant activity could be obtained at a variety of frequencies by varying the nature of the electrical load.

Although Steel used the Mason model [5] to predict his results, the multilayered version of the systems transducer model, already described in this chapter [65] is perfectly suited to making similar simulations. Figure 7.18 illustrates the simulated pressure output of a double layer 40% PZT 5A composite stacked transducer. The layers are 4mm thick and it is assumed that the transducer is operating directly into water, and possesses no backing. The figure illustrates the pressure output for a symmetric case in which both layers are excited, and for an asymmetric case, in which the front layer has been short circuited. It is readily apparent that by short circuiting one layer, peak transmission at the fundamental frequency has been significantly reduced but a higher level of activity at the second harmonic has been obtained. Furthermore, there is no null between the frequencies of the first and second harmonics. Clearly, a very wide variety of responses are obtainable simply by

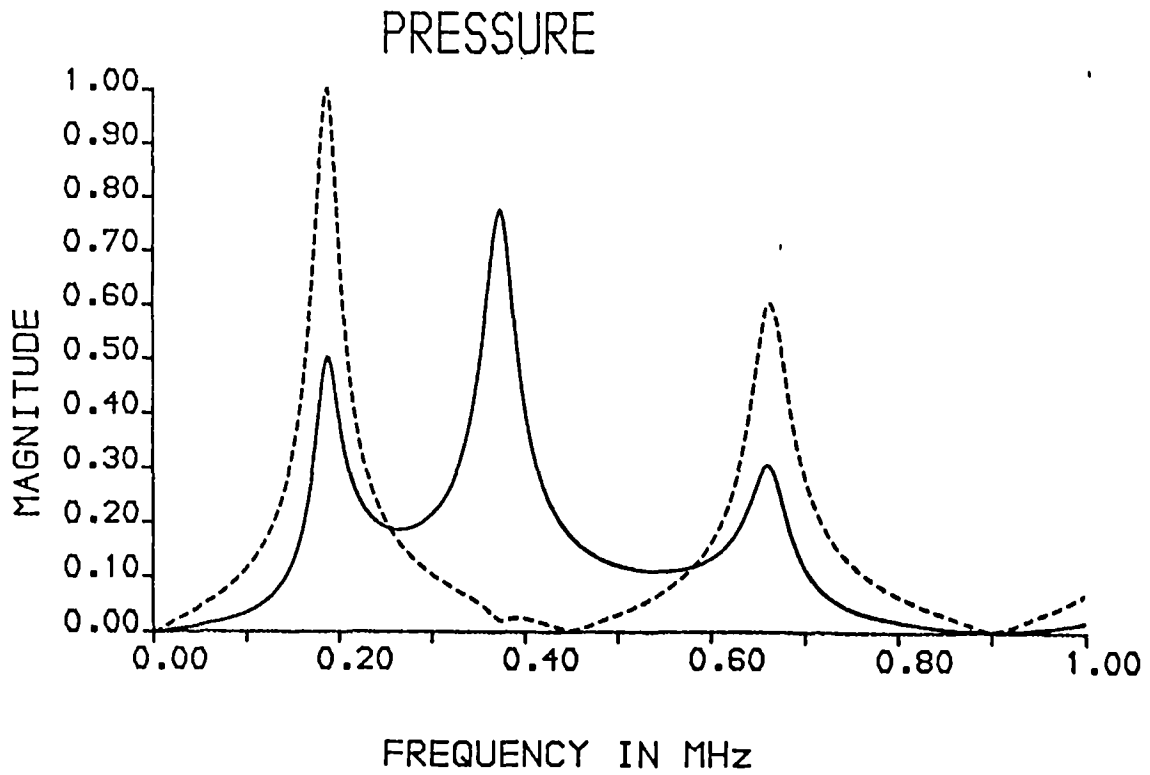


Figure 7.18 Simulated CW pressure output of a stacked transducer for two different electrical excitation conditions

- Identical excitation
- Front layer short circuited

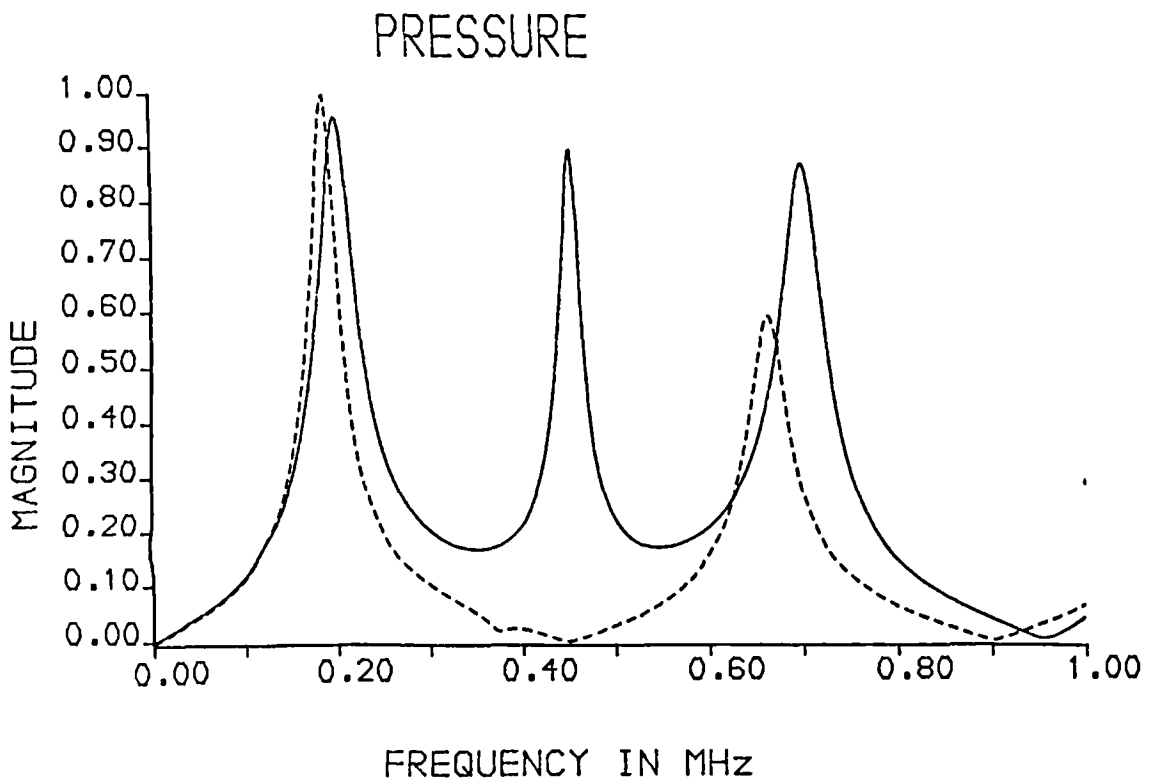


Figure 7.19 Simulated CW pressure output of two stacked transducers

- Double layer 40% composite
- Front layer 40% composite, rear layer PZT 5A

altering the electrical loading of one of the layers, or by varying the amplitude and phase of the excitation of each of the layers. This form of asymmetric design possesses the advantage of being versatile, since a different characteristic may be obtained by varying the excitation, without the need to alter the physical structure. There is a requirement for a complete and thorough investigation of the phenomena associated with this type of structure.

7.4 iii) Diverse layer material characteristics

Stacked transducers generally possess several layers of the same material. However, when composite materials are employed, there is considerable scope for manufacturing stacked transducers composed of layers possessing a range of material characteristics. Clearly, this will lead to a certain amount of asymmetry in the resulting structure. Figure 7.19 illustrates the simulated pressure response of a symmetric double layer 40% composite stacked transducer. The device is airbacked, operating directly into water and each layer is 4mm thick. The response of an identical device, except that the rearmost layer was replaced by pure PZT 5A is also illustrated. This second, asymmetric device possesses a significant level of activity at the second harmonic. Again, there is no null between the frequencies of the first and second harmonics. This type of design also merits further investigation.

7.5 CONCLUDING REMARKS

The validity of a new, versatile model for stacked, composite transducers has been verified using a range of experimental results. Generally, the model provides results which permit optimal design without the need for a wasteful 'trial and error' approach. In the absence of electrical source/ receiver loading effects, stacking results in higher transmission levels and lower reception levels. The pulse-echo sensitivity of stacked transducers are generally lower than that of similar non-stacked devices. If electrical loading effects are significant, the calculation of the net response is more complex. The maximum power transfer theorem will often determine which design provides highest transmission, reception or pulse-echo levels.

A number of complex phenomena have been revealed during the present work. In particular, the values of wave velocity, and wave attenuation in stacked composite structures appears to deviate from those values predicted theoretically. The accuracy of the modelling techniques, when used for stacked ceramic structures, suggests that the deviations are arising from internal characteristics, and not from an inaccuracy within the model itself. The factors responsible for these observations, which may include the effects of pillar misalignment between adjacent layers, deserve further investigation.

A selection of simulated results for asymmetric stacked composite transducers, verified by a limited number of experimental results, has been presented. These indicate that a diverse range of novel characteristics may be obtained by varying layer thickness, electrical loading or material characteristics. Fortunately, the model used here is sufficiently versatile to permit a thorough investigation with relative ease.

CHAPTER VIII

CONCLUSIONS, APPLICATIONS AND RECOMMENDATIONS FOR
FURTHER WORK

8.1 CONCLUDING SUMMARY

A comprehensive strategy for the analysis and design of composite transducer systems has been developed. A variety of aspects of composite transducer technology have been investigated. The major contributions of the thesis are outlined below.

- 1.) An investigation of the influence of constituent material parameters on composite transducer characteristics has been performed. This has involved a combination of finite element analysis of various configurations and the use of a simple one dimensional model.
- 2.) The vibrational and electromechanical characteristics of a diverse range of composite designs has been investigated using finite element analysis. This has permitted optimal geometrical configurations, which result in the greatest vibrational uniformity and electromechanical efficiency, to be established. A number of novel geometries have been considered, and some of these provide characteristics of practical importance.
- 3.) The electromechanical performance of practical composite transducer designs, under practical excitation and loading conditions, have been analysed using linear systems modelling techniques. This takes account of mechanical backing and matching, and electrical loading effects. The response for any arbitrary excitation function may be obtained. Distance and frequency related

attenuation are included in this model using parameters related to physically measurable quantities.

A high degree of correlation between modelled and experimental results has been obtained for a wide range of configurations. In particular, the model has proved particularly valuable for establishing optimal transducer designs for obtaining the highest peak sensitivity, bandwidth, or peak sensitivity - bandwidth product. High ceramic volume fraction transducers are favoured for situations where severe electrical loading is present. Conversely, low ceramic volume fractions generally provide wide bandwidth and perform reasonably well under lightly loaded conditions.

4.) A comprehensive investigation of the spatial field and electromechanical characteristics of composite transducer arrays has been undertaken. A novel, efficient and versatile algorithm for determining the pressure response, due to rectangular vibrating apertures, at arbitrary points in the acoustic field, and for arbitrary electrical excitation, has been developed. The accuracy of this model has been verified using a selection of experimental results.

The spatial characteristics of practical composite arrays have been considered in depth. This work has illustrated that, under some circumstances, significant laterally propagating modes of vibration exist within composite arrays. These can give rise to degraded directivity

characteristics.

The performance of steered ultrasonic arrays has been investigated theoretically and experimentally. A versatile model for predicting the spatial characteristics of steered arrays has been developed. Using a high specification array controller, it has been established that a composite array design has produced a directivity characteristic superior to that obtainable from similar sliced ceramic or monolithic ceramic arrays. The performance of the composite arrays, when used in a practical imaging configuration, was also superior to that of the other arrays.

A brief investigation of the characteristics of novel 2-D composite arrays indicate considerable potential. A satisfactory imaging performance was obtained although there is considerable scope for further development.

5.) Linear systems modelling techniques have been applied to stacked, multiple active layer composite structures. A reasonable degree of correlation between experimental and theoretical results has been obtained. The modelling technique is sufficiently accurate that it provides a useful design tool for novel 'asymmetric' stacked designs. Initial results, for stacked transducers comprising variable layer thickness, layer material characteristics and layer electrical loading are encouraging.

8.2 APPLICATIONS OF COMPOSITE TRANSDUCERS

A number of novel applications of the composite transducers have been identified during the course of the present work.

8.2 i) Advanced arrays

Composite materials offer great versatility to the designer of ultrasonic arrays. Provided that an appropriate design is used, a high quality electromechanical and spatial performance may be obtained from the individual array elements. However, the possibility of making flexible composite arrays, or to use lightly loaded composite elements within a flexible mounting, provides the potential for manufacturing surface conforming arrays. One application, of considerable importance to offshore NDE, is the detection of flooded cylindrical shell members in oil exploration/ recovery platforms. The viability of composite transducers for this task has been verified recently [68]. Additionally, there is scope for further development of composite arrays comprising complex shaped elements. In this case, 'complex shape' includes any irregular element geometry which cannot be fabricated easily using sawing techniques. These shapes include the curved elements used in axisymmetric arrays.

8.2 ii) Low frequency/ high bandwidth transducers

It is proposed that composite materials possess characteristics which make them suitable for use in low frequency/ high bandwidth applications. Although, composite materials have been used widely for low frequency passive (reception) applications, they have not been used for active (pulse-echo) applications. Although cost may appear to be a major disadvantage of low frequency composite transducers, measures can be taken to reduce the cost. Furthermore, the quality of the results obtainable may justify the slightly higher cost. The increasing sophistication of sonar signal processing has led to a requirement for high bandwidth transducers operating in the frequency range 20kHz to 200kHz. In the NDE field, there is growing interest in low acoustic impedance, high bandwidth transducers, for the inspection of porous and lossy media. These materials include concrete and wood, which are important structural materials. There is also the possibility of performing NDE through intermediate air gaps by taking advantage of the relatively low acoustic impedance of composite transducers [64]. These applications require considerable further work, but the potential rewards are significant.

8.3 RECOMMENDATIONS FOR FURTHER WORK

8.3 i) Manufacture

At this stage, the theory of operation of composite piezoelectric transducers is sufficiently well understood for the majority of practical applications. The greatest limitation on the technology is that imposed by manufacturing constraints and costs. Therefore, there is considerable scope for developing low cost, effective methods for manufacturing composites for both high and low frequency applications. Furthermore, the quality and robustness of the transducer electrodes requires further investigation.

8.3 ii) Wave attenuation

Although a simplified model for predicting wave attenuation in composite transducers has been proposed in Chapter V, there is considerable scope for improvement. It is recognised that the actual wave attenuation is a complex function of material properties, geometry and frequency, and consequently, a comprehensive model for predicting loss would probably be rather complex. The development of a suitable model would require a fundamental investigation of the loss mechanisms in both polymers and ceramics. Thereafter, the interaction between the loss mechanisms of the two materials, in a composite, could be investigated. If an accurate theoretical model is unobtainable, then a comprehensive analysis using experimentally observed results from a range of prototype

devices, may also result in an improved understanding of the physical processes involved.

8.3 iii) Uniformity of vibration within composite structures

Chapter IV included an investigation of the dependence of the vibrational uniformity within a composite, as a function of ceramic pillar shape and volume fraction. However, further work is required to verify experimentally the results obtained using finite element analysis. In particular, there is a requirement to investigate the vibrational behaviour of composites, on a microscopic scale, as functions of acoustic loading and matching.

8.3 iv) Performance of composite materials in arrays

There is clearly scope for extending the understanding of the vibrational characteristics of composite materials in arrays. The precise nature of the laterally propagating waves discussed in Chapter VI, and their influence on practical directivity characteristics merit further investigation. Further work on the effects of matching layers, backings and electrical and mechanical cross coupling, on the spatial characteristics of composite arrays is required. The use of lossy inter-element fillers is also worth consideration. These aspects could probably be analysed most readily using finite element techniques. Further investigation of the potential of composite materials for use in 2-D arrays is also desirable.

8.3 v) Stacked composite structures

The results presented in Chapter VII indicate that stacked composite structures possess considerable potential. In particular, the use of 'asymmetric' stacks, with irregular layer thickness, material characteristics, or electrical loading, offer most promise. Furthermore, a 'versatile model is available for predicting the probable characteristics of these complex structures. However, the results indicate significant, unexpected deviations in the material characteristics of stacked structures. Irregularities in the wave velocity and measured wave attenuation were observed. The phenomena which are causing these effects require further investigation. It is proposed that pillar alignment between adjacent layers may be critical to the successful operation of stacked structures. Some of these effects could be analysed using finite element techniques.

The use of prefiltering to obtain a desired output from a single layer transducer is well established [69]. However, multilayered structures offer the possibility of applying different voltage excitation waveforms to each of the layers, in order to achieve a particular net output pressure response. For example, the amplitude and phase of the excitation of the various layers may be varied in a controlled manner. It would be useful to develop a means of determining suitable excitation functions in order to achieve a particular response from a stacked transducer. This analysis could be performed in conjunction with an

investigation of the effects of diverse layer thickness and material characteristics.

Hence, the potential for future development of composite transducers, and accompanying modelling techniques, are considerable.

ACKNOWLEDGEMENTS

Foremost, I would like to thank Dr G Hayward of the Department of Electronic and Electrical Engineering at the University of Strathclyde, who supervised the development of the present work, and who provided many hours of helpful, active and enthusiastic advice and discussion.

I would also like to thank Professor T S Durrani for providing the necessary facilities required for this work.

Thanks are also due to all past and current members of the Ultrasonics Group at the University of Strathclyde, who contributed to this work by their own endeavours and enthusiasm. In particular, I would like to thank Dr Y Gorfu for his co-operation and assistance with the work on two dimensional arrays. I am also grateful to Dr D F Clark for assistance with the thesis production.

I gratefully acknowledge the financial support given by the SERC Marine Technology Directorate. I am also deeply indebted to Marconi-UDI Ltd for their financial, and considerable material, assistance.

Finally, I thank my family and friends for their continued support and encouragement.

REFERENCES AND BIBLIOGRAPHY

1. IEEE Standard in piezoelectricity STD 197611978
2. H P Savakus, K A Klicker and R E Newnham 'PZT Epoxy piezoelectric transducers: A simplified fabrication process' Mater. Res. Bull. 16 677-680 (1980)
3. W A Smith, A Shaulov and B A Auld 'Tailoring the properties of composite piezoelectric materials for medical ultrasonic transducers' 1985 IEEE Ultrasonics Symposium 642-647
4. A Shaulov and W A Smith 'Ultrasonic transducer arrays made from composite piezoelectric materials' 1985 IEEE Ultrasonics Symposium 648-651
5. W P Mason ' Electromechanical transducers and wave filters' Van Nostrand and Co. Inc. New York (1948)
6. D A Leedom, R Krimholtz and G L Matthei 'Equivalent circuits for transducers having arbitrary even-or-odd symmetry piezoelectric excitation' IEEE Tran. Sonics and Ultrason. SU-18 128-141 (1971)
7. G Hayward, C J MacLeod and T S Durrani 'A systems model of the thickness mode piezoelectric transducer' J. Ac. Soc. Am. 76(2) 369-382 (1984)
8. R E Newnham, A Safari, J Giniewicz and B H Fox 'Composite Piezoelectric sensors' Ferroelectrics (60) 15-21 (1984)
9. D P Skinner, R E Newnham and L E Cross 'Flexible composite transducers' Mater. Res. Bull. 13 (6) 599-607 (1978)
10. R E Newnham, D P Skinner and L E Cross 'Connectivity and piezoelectric - pyroelectric composites' Mater. Res. Bull. 13 (5) 525-536 (1978)
11. K A Klicker, W A Schulze and J V Bigger 'Piezoelectric composites with 3-1 connectivity and a foamed polyurethane matrix' Communications of the American Ceramic Society 208-210 (1982)
12. M J Haun, P Moses, T R Gururaja, W A Schulze and R E Newnham 'Transversely reinforced 1-3 and 1-3-0 piezoelectric composites' Ferroelectrics (49) 259-264 (1983)
13. J Runt, A Safari, E C Galgoci and R E Newnham ' The influence of interfacial adhesion on the piezoelectric response of electroceramic/polymer composites' Ferroelectrics Letters (5) 15-20 (1985)

14. F R Montero de Espinosa, V Pavia, J A Gallego-Juarez and M Pappalardo 'Fractured piezoelectric ceramics for broadband ultrasonic composite transducers' 1986 IEEE Ultrasonics Symposium 691-696
15. G Sa-Gong, A Safari, S J Jang and R E Newnham 'Poling flexible piezoelectric composites' Ferroelectrics Letters (5) 131-142 (1986)
16. T R Gururaja, W A Schulze, T R ShROUT, A Safari, L Webster and L E Cross 'High frequency applications of PZT/Polymer composite materials' Ferroelectrics (39) 1245-1248 (1981)
17. K R Erikson 'Tone burst testing of pulse-echo transducers' IEEE Trans. Sonics and Ultrason SU-26 1 7-14 (1979)
18. T R Gururaja, W A Schulze, L E Cross, R E Newnham, B A Auld and Y J Wang 'Piezoelectric composite materials for ultrasonic transducer applications, Part I: Resonant modes of vibration of PZT rod-polymer composites' IEEE Trans. Sonics and Ultrasonics SU-32 (4) 481-498 (1985)
19. T R Gururaja, W A Schulze, L E Cross, R E Newnham, 'Piezoelectric composite materials for ultrasonic transducer applications, Part II: Evaluation of ultrasonic medical applications' IEEE Trans. Sonics and Ultrasonics SU-32(4) 499-513 (1985)
20. G Kossoff 'The effects of backings and matchings on the performance of piezoelectric ceramic transducers' IEEE Trans. Sonics Ultrason. SU 13 20-30 (1966)
21. A Shaulov, W A Smith, J Zola D Dorman 'Curved annular array transducers made from composite piezoelectric materials' 1988 IEEE Ultrasonics Symposium
22. A Shaulov, B M Singer, W A Smith and D Dorman 'Biplane phased array for ultrasonic medical imaging' 1988 IEEE Ultrasonics Symposium 635-638
23. H L W Chan and J Unsworth 'Simple model for piezoelectric ceramic/polymer 1-3 composites used in ultrasonic transducer applications' IEEE Trans. Ultra. Ferro. Freq. Control. UFFC-36 (4) 434-441 (1989)
24. 'Physical Acoustics' Vol 1, Part A W P Mason (Editor) Academic Press, New York (1964)
25. K Y Hashimoto and M Yamaguchi 'Elastic, piezoelectric and dielectric properties of composite materials' 1986 IEEE Ultrasonics Symposium 697-702

26. W A Smith, A A Shaulov and B M Singer 'Properties of composite piezoelectric materials for ultrasonic transducers' 1984 IEEE Ultrasonics Symposium 539-544
27. J H Ih and B H Lee 'Performance analysis of piezoelectric composite plates with consideration of internal losses' IEEE Tran. Sonics and Ultrason. SU-35(1) 73-77 (1988)
28. J H Ih and B H Lee 'Attenuation coefficient of a piezoelectric resonator operating in the thickness mode' Electronics Letters (22) No 7 27th March 1986
29. B A Auld, H A Kunkel, Y A Shui and Y Wang 'Dynamic behaviour of periodic piezoelectric composites' 1983 IEEE Ultrasonics Symposium 554-558
30. B A Auld and Y Wang 'Acoustic wave vibrations in periodic composite plates' 1984 IEEE Ultrasonics Symposium 528-532
31. Y Wang, E Schmidt and B A Auld 'Acoustic wave transmission through one-dimensional PZT-Epoxy composites' 1986 IEEE Ultrasonics Symposium 685-689
32. M Yamaguchi, K Y Hashimoto and H Makita 'Finite element method analysis of dispersion characteristics for 1-3 type piezoelectric composites' 1987 IEEE Ultrasonics Symposium 657-661
33. J H Jeng, X Q Bao, V V Varadan and V K Varadan 'A complete finite element-eigenmode analysis for a 1-3 type of piezoelectric composite transducer including the effect of fluid loading and internal losses' 1988 IEEE Ultrasonics Symposium
34. R Holland and E P EerNisse 'Variational evaluation of the admittances of multielectroded three dimensional piezoelectric structures' IEEE Tran. Sonics and Ultrason. SU-15 119-132 1968
35. H Allik and T J R Hughes 'Finite element method for piezoelectric vibration' Int. Journal of numerical methods for engineering' 2, 151-157 (1970)
36. O C Zienkiewicz 'The Finite Element Method' McGraw-Hill, London, 1977
37. R Lerch 'Finite element analysis of piezoelectric transducers' 1988 IEEE Ultrasonics Symposium
38. R J Guyan 'Reduction of stiffness and mass matrices' AIAA Journal, Vol. 3 No.2 380 (1965)

39. 'ANSYS' available from Swanson Analysis Systems Inc., Houston, Pennsylvania USA
40. D F Ostergaard and P A Pawlak 'Three dimensional finite elements for analysing piezoelectric structures' 1987 IEEE Ultrasonics Symposium
41. IRE Standards on piezoelectric crystals: Measurements of piezoelectric ceramics. (1961)
42. J Hossack, G Hayward and D Gillies 'A new method for element analysis in piezoceramic arrays' Proc. Ultrasonics International 1987 477-482
43. M G Silk 'Predictions of the effect of some constructional variables on the performance of ultrasonic transducers' Ultrasonics (20) 27-33 (1985)
44. G Hayward and M N Jackson 'A lattice model of the thickness mode piezoelectric transducer' IEEE Tran. Ultrason. Ferro. and Freq. Cntrl. UFFC-33 (1) 41-50 (1986)
45. M Redwood 'Transient behaviour of a piezoelectric transducer' J. Ac. Soc. Am. 33(4) 527-536 (1961)
46. G Hayward 'Time and frequency modelling of the piezoelectric transducer' PhD Thesis, University of Strathclyde (1981)
47. A R Selfridge 'Approximate material properties in isotropic materials' IEEE Tran. Sonics and Ultrason. SU-32(3) 381-394 (1985)
48. M N Jackson 'Simulation and control of thickness mode transducers' PhD Thesis, University of Strathclyde (1984)
49. G K Lewis 'A matrix technique for analyzing the performance of multilayered front matched and backed piezoelectric ceramic transducers' Acoustical Imaging (8) 395-416 (1978)
49. G Hayward 'The influence of pulser parameters on the transmission response of piezoelectric transducers' Ultrasonics (23) 103-111 (1985)
50. G S Kino, 'Acoustic Waves: Devices, imaging, and analogue signal processing' Prentice Hall (1987)
51. A R Selfridge, G S Kino and B T Khuri Yakub 'A theory for the radiation of a narrow strip transducer' App. Phys. Lett. (37, 1) 35-36 (1980)
52. P R Stepanishen 'Transient radiation from pistons in an infinite planar baffle' J. Ac. Soc. Am. (49) 1629-1638 (1971)

53. J C Lockwood and JG Willette 'High-speed method for computing the exact solution for the pressure variations in the near field of a baffled piston' J. Ac. Soc. Am. (53) 735-741 (1973)
54. D H Turnbull and F S Foster 'Theoretical steered beam profile from a two-dimensional transducer array' 1989 IEEE Ultrasonics Symposium
55. L Gomez-Ullate and J L San Emeterio-Prieto 'On the impulse response of rectangular baffled pistons' Proc. Ultrasonics International 1989 566-571
56. G S Kino and C S DeSilets 'Design of slotted transducer arrays with matched backings' Ultrasonic Imaging (1) 189-209 (1979)
57. S W Smith, O T von Ramm, M E Haran and F L Thurston 'Angular response of piezoelectric elements in phased array ultrasound scanners' IEEE Tran. Sonics and Ultrason. SU-26(3) 185-191 (1979)
58. C M Sayers and C E Tait 'Ultrasonic properties of transducer backings' Ultrasonics 22(2) 57-60 (1979)
59. C S DeSilets 'Transducer arrays suitable for acoustic imaging' Ginzton Lab. Report 2833 Stanford (1978)
60. G Hayward, D Gillies and T S Durrani 'A multidimensional linear systems model of the piezoelectric transducer' 1984 IEEE Ultrasonics Symp.
61. T Kojima 'Matrix array transducer and flexible matrix array transducer' 1986 IEEE Ultrasonic Symp. 649-654
62. J Hossack, Y Gorfu and G Hayward 'The modelling and design of composite piezoelectric arrays' 1989 IEEE Ultrasonic Symp.
63. Y Gorfu 'Two dimensional composite arrays for three dimensional acoustic imaging' University of Strathclyde. Internal report for SERC (1990)
64. G Hayward and Y Gorfu 'An assessment of through air transmission for remote ultrasonic non-destructive testing' University of Strathclyde. Internal report for SERC/MOD (1988)
65. G Hayward, S Trench and J Hossack 'An approach for modelling the behaviour of multilayered, active piezoelectric structures' Submitted to J. Ac. Soc. Am.
66. G E Martin 'On the theory of segmented electromechanical systems' J. Ac. Soc. Am. 36 (7) 1366-1370 (1964)

67. G A Steel, B V Smith and BK Gazey 'Tunable sonar transducers' Electronics letters (22) 758-759 (1986)
68. G Stirling, J Pearson, G Hayward and C Kuo 'Improved ultrasonic flooded member detection for inspection of offshore structures' University of Strathclyde. Internal report for SERC (1990)
69. C Chassaigon and J F de Bellard 'Input signal optimisation of ultrasonic transducers for non destructive testing' Proc. Ultrasonics International 1985 557-561
70. Vernitron Ltd. Southampton UK. Applicatiосn Bulletin 66011/F
71. L I Maissel and R Glang 'Handbook of thin film technology' McGraw-Hill, New York (1970)
72. L Durney (Ed) 'Electroplating engineering handbook' (4th. Ed) Van-Nostrand, New York (1984)
73. G Hayward 'The influence of pulser parameters on the transmission response of piezoelectric transducers' Ultrasonics (23) 103-112 (1985)

APPENDIX A

MATERIAL PARAMETERS

A detailed description of the physical properties of the materials used for this thesis is presented. All figures quoted are derived from manufacturer's specifications, except where stated otherwise.

CERAMIC

The parameters of the commonly encountered piezoelectric ceramics are defined in Table A1. The material properties of the modified Lead Titanate (EC-97) and the Lead Metaniobate (EC-82) were measured from typical samples. Various manufacturers produce materials, with specifications equivalent to Vernitron's PZT 5A and PZT 5H [70]. After a thorough examination of quality and consistency, it was observed that EDO EC-65 (PZT 5A) and EC-76 (PZT 5H) were superior to the other products examined. EDO materials have been used throughout, except in a very few samples, where Vernitron ceramic was used. Rather than quote the individual properties of the actual piece of ceramic used in a particular device, all ceramic used has been tested according to the IEEE standard [1], and if any of the properties deviated by more than 10%, the ceramic was rejected. Actual parameters have been recorded, and in most cases the ceramic is closer to a 5% tolerance. These tolerances are a result of the complexity, and batch process nature of the manufacturing process.

TABLE A1

Properties of selected piezoelectric ceramics

	PZT 4	PZT 5A	PZT 5H	EC 97	EC 82
DENSITY ₁	7500	7750	7500	6900	5900
$c_{33}^D \times 10^{10}$ ₂	15.9	14.7	15.7	17.1	7.4
$c_{13}^D \times 10^{10}$ ₂	6.09	6.52	7.22	2.05	1.41
$h_{33} \times 10^8$ ₃	26.8	21.5	18.0	50.3	16.1
$h_{13} \times 10^8$ ₃	19.7	7.03	11.3	3.02	1.13
k_{33}	0.70	0.70	0.75	0.50	0.39
k_t	0.51	0.48	0.50	0.49	0.37
$\epsilon_{33} S / \epsilon_o$	635	830	1470	175	320
Q_m	500	75	65	1000	11

KEY

1. Units kgm^{-3}
2. units Nm^{-2}
3. Units Vm^{-1}

POLYMERS AND LOADED POLYMER MATERIALS

The parameters of these materials have been measured experimentally, or derived from experimental figures. These parameters depend on the accurate measurement and mixing of the constituent resin and hardener and on the cure cycle. A 10% tolerance in these materials parameters is the best that can be obtained. During manufacture, care was taken to follow the supplier's instructions precisely and curing occurred at between 40°C and 50°C. The parameters for stiffness and attenuation are frequency dependent and have been measured ultrasonically at 1MHz

[47]. The parameters for PVDF (Polyvinylidene fluoride) are taken from a standard reference text [50]. A table of the material properties of the polymers used in the thesis is presented in Table A2.

TABLE A2
 PROPERTIES OF SELECTED POLYMERS

POLYMER	A	B	C	D	E
DENSITY ₁	1140	1145	1150	8000	1780
$c_{33} \times 10^9$ ₂	8.0	6.2	3.0	1.25	8.7
$h_{33} \times 10^8$ ₃	0	0	0	0	1.60
σ	0.35	0.37	0.40	(a)	(a)
Atten. ₄	5	8	(b)	(b)	6.5
Z_{AC} MRayl	3.0	2.7	1.9	10	3.9
ϵ_{33}/ϵ_0	4	4	4	0	10
T_g	100	80	40	(a)	(a)

KEY

1. Units kgm^{-3}
 2. Units Nm^{-1}
 3. Units Vm^{-1}
 4. Units dB/cm @ 1MHz
- σ Poisson ratio
 T_g Glass transition temperature
 (a) Not measured
 (b) Attenuation too high to be measurable

A. CIBA-GEIGY CY1301/HY1300. A low viscosity, hard setting epoxy polymer. This polymer has been used in all the composite transducers manufactured, except where specified otherwise. It possesses excellent electrical stability and low water permeability.

B. CIBA-GEIGY 50:50 MY753:CY208/HY956. A soft setting CY208 resin is combined with MY753 hard setting resin. A moderately soft polymer, with characteristics between that of polymers A. and C. results.

C. CIBA-GEIGY CY208/HY956. A very lossy soft setting epoxy polymer. It has a low dielectric strength, relatively high water permeability and a low glass transition temperature.

D. POLYMER C. is mixed with 10 μ m tungsten powder to obtain a dense extremely lossy backing material. The mixture comprises of 90% tungsten powder by weight. Using a harder epoxy does not increase acoustic impedance significantly but does reduce attenuation.

E. PVDF (Polyvinylidene fluoride) is a piezoelectric polymer, frequently used in wideband hydrophones. The parameters quoted in Table A2 are typical values [50].

PROPERTIES OF WATER AND AIR

For the purposes of this thesis the following properties are assumed. Standard conditions of temperature (20°C) and pressure (1.013x10⁵Pa) are assumed.

	PURE WATER	AIR
DENSITY kgm ⁻³	1000	1.24
VELOCITY ms ⁻¹	1483	344
Z _{AC} MRayl	1.483	4.3 x 10 ⁻⁴

APPENDIX B

COMPOSITE TRANSDUCER MANUFACTURE

The following description details the manufacturing technique utilised for the manufacture of the prototype composite transducers described in the thesis.

Equipment: Diamond wire saw (WELL 3241), or diamond wheel saw
Ultrasonic cleaner (Nusonics)
Vacuum chamber/oven (Gallenkamp)
Lapping facility (Logitech PM2A)
Vacuum deposition unit (Edwards E306A)

- 1.) A sample of pre-polarised ceramic, slightly thicker than the required final dimension, is used. If necessary, the mechanical, electrical and piezoelectric parameters are verified. One side of the ceramic block is roughened and bonded via a strong epoxy resin to the saw mounting plate.
- 2.) Mount the ceramic in the saw and ensure accurate alignment in all three orthogonal directions.
- 3.) Check coolant level and then start the sawing process. Ideally, the saw should operate under computer control. The configuration of the saw used during the present programme of work is described at the end of this appendix.
- 4.) Remove finished workpiece and rinse under a tap.

- 5.) Place workpiece in ultrasonic cleaner for 2-3 minutes until all residue is observed to have been removed.
- 6.) Rinse under a tap and allow to dry thoroughly.
- 7.) Form a retaining mould around the circumference of the transducer. This is achieved using insulating tape and/or modelling clay.
- 8.) Mix the selected epoxy, paying particular attention to accurate measurement of the resin/ hardener ratio, and to the complete mixing. The viscosity of the epoxy may be reduced by gentle heating.
- 9.) Pour the resin on to the composite structure very slowly, starting from one side to avoid the entrapment of air. Leave an excess layer of epoxy on the top surface so that any surface bubbles are outwith the active structure.
- 10.) Place workpiece in a vacuum chamber and reduce the pressure to approximately 5mBar. Wait for the epoxy to completely degas before returning to ambient pressure. The transducer should be baked for 12 hours at 40°C.
- 11.) Remove the mould and carefully strip excess epoxy. Finish off to a fine surface, before remounting in the saw.
- 12.) Repeat steps 2.) to 11.) to obtain perpendicular slots so that square section elements remain.

13.) Mount in the saw and carefully slice off the required transducer thickness, allowing 0.5mm for final lapping.

14.) Lap the completed composite material to the required dimensions. A fine grade emery paper or polishing jig should be used.

15.) Clean device carefully and finish off by wiping briefly with an acetone soaked lint.

16.) Place the device in a vacuum deposition unit and obtain a vacuum of less than 0.2 μ Bar. For general purpose use, a 500nm layer of aluminium is perfectly adequate. A higher quality electrode may be achieved by applying a 20nm chromium layer, for good adhesion, followed by a 200nm layer of gold or silver. The relative merits of various thin film processes and materials are discussed very thoroughly in the standard texts on the subject [71].

It is also possible to apply a relatively thick coat of copper, or a similar metal, by means of electroplating. It is necessary to deposit firstly, under vacuum, a chromium base followed by a thin copper layer. Thereafter, the transducer is placed in a Copper Sulphate/ Sulphuric Acid solution. Copper may then be deposited electrolytically to any required thickness by making the transducer the cathode in an electric cell. A copper plate is also immersed in the solution and this forms a sacrificial anode. These techniques are described thoroughly in the literature [72]. The primary advantage of a moderately thick copper plated electrode is that it

is possible to solder to it. However, the adhesion of such a layer is limited by the strength of adhesion of the base layer to the composite material. Alternatively, a high quality silver paint is applied to the transducer.

17.) The composite transducer material is now complete. Any required measurements of material parameters should be performed at this stage, prior to encapsulation.

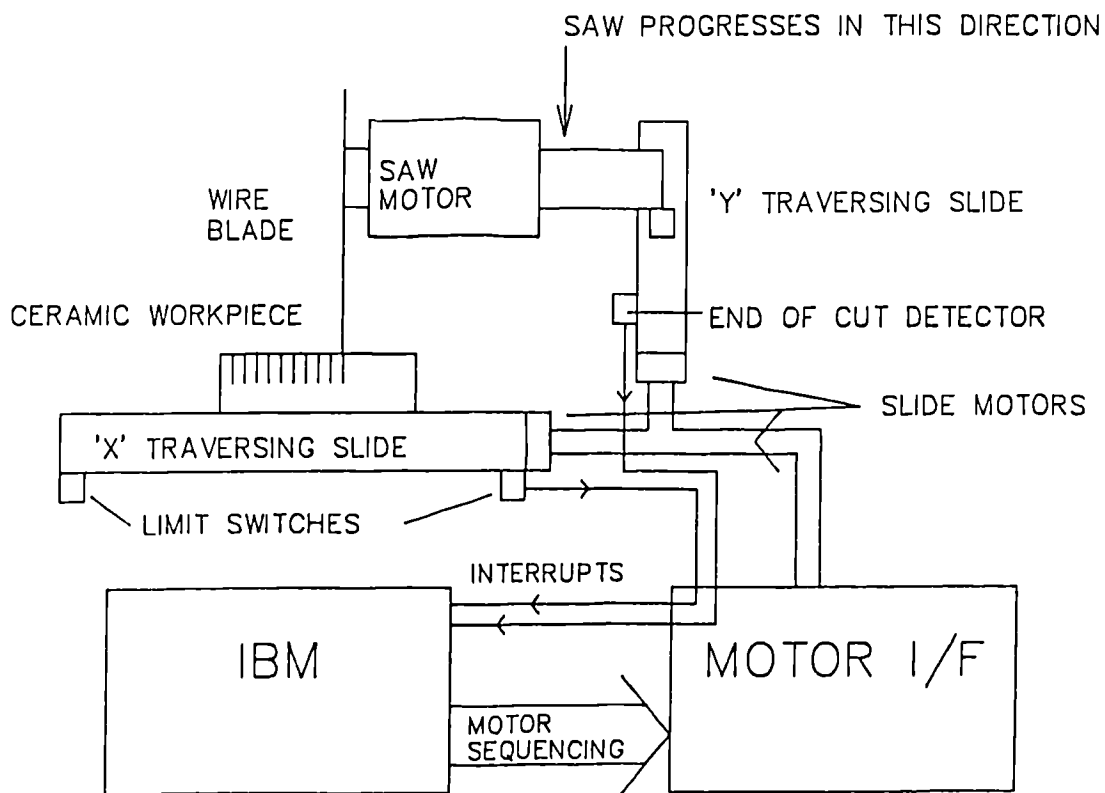


Figure B.1 Configuration of computer controlled saw

User decides : Number of cuts
 Increment between cuts
 Depth of cuts

User aligns saw and makes first cut

At this stage the IBM takes control

1. Supplies Y direction motor sequencing signals so that blade is clear of the workpiece.
2. Supplies X direction motor sequencing, so incrementing the blade location by the correct pitch.
3. Supplies Y direction motor sequencing signals so that blade engages the workpiece.
4. Allows sawing to proceed until 'end of cut' is detected.
5. Repeats 1 to 4 until task complete or a fault is detected.
6. Isolates electrical supply to saw.

APPENDIX C

i) TRANSDUCER PROBE MANUFACTURE

The following process is suitable for both composite and ceramic transducers. The only difference encountered during manufacture is that wires may be soldered to the fired-on silver coatings on ceramic, whereas silver loaded epoxy must be employed for composite transducer manufacture.

If required, a matching layer should be fitted prior to probe manufacture. A low loss, hard setting epoxy (CY1301/HY1300) is normally preferable. This is cast, taking care to eliminate bubbles. It is then lapped to the required thickness and bonded to the ceramic with CY1301/HY1300 epoxy, after a low profile electrical connection has been made to the front face metallisation.

1.) A cylindrical tube, slightly larger than the diameter, or diagonal dimension, of the transducer is machined to an appropriate length - typically 50mm. The choice of material for the tube is not critical except that it should possess a low water permeability.

2.) A small notch is cut in the tube to accommodate a fine 0.4mm insulated wire.

3.) A small quantity of silicone grease is smeared on to a clean, thin perspex sheet.

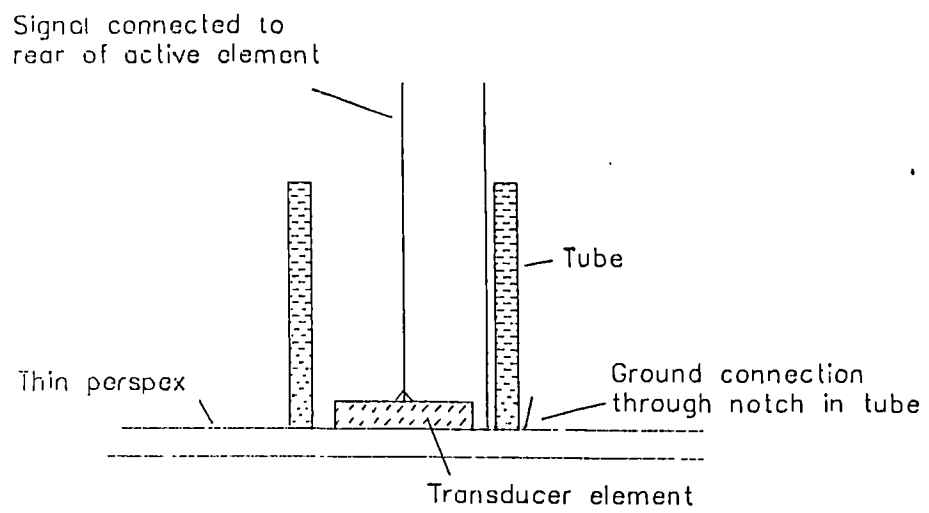


Figure C.1 Configuration of transducer within protective tube

10.) Sealed soldered connections are made from the thin transducer wires to a low loss, small diameter coaxial cable (typically RG179PE). The probe rear cover, which is a 'press fit' into the cylindrical tube, is fitted and sealed with a rapid setting epoxy. A BNC connector is fitted to the other end of the cable. The cable is kept as short as practically possible - normally 60cm.

ii) ARRAY MANUFACTURE

Materials: Transducer material
PCB
Copper clad board
Low loss, small diameter coaxial cable
(typically RG179PE)
Multipole connector

Equipment: Strong steel mould
Diamond wire saw

A PCB, similar to that illustrated in Figure C.2 is produced. The centre to centre spacing of the tracks matches precisely the required array element spacing. The gap between these tracks is similar to the cut width obtained using the saw (0.22mm). The plating is continued over the edge of the PCB as illustrated.

A strong steel mould, with internal dimensions large enough to provide a final encapsulant thickness of at least 3mm, is employed. The internal surfaces are ground

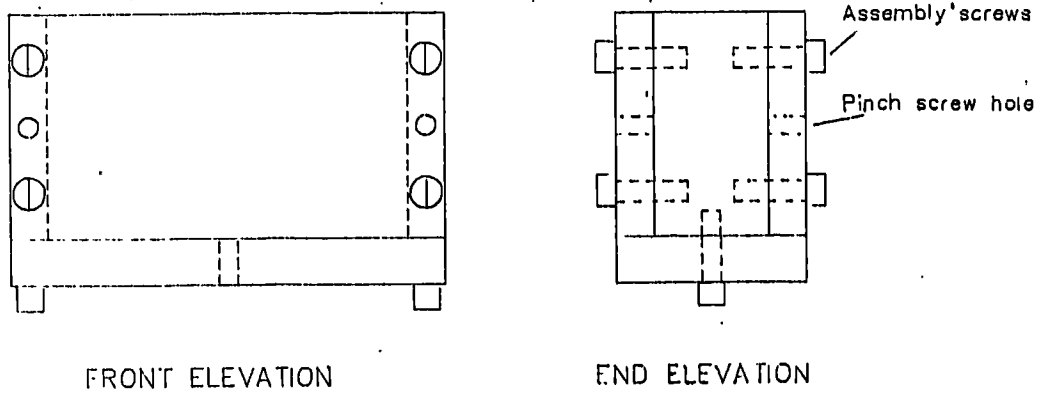


Figure C.3 Typical array encapsulant mould

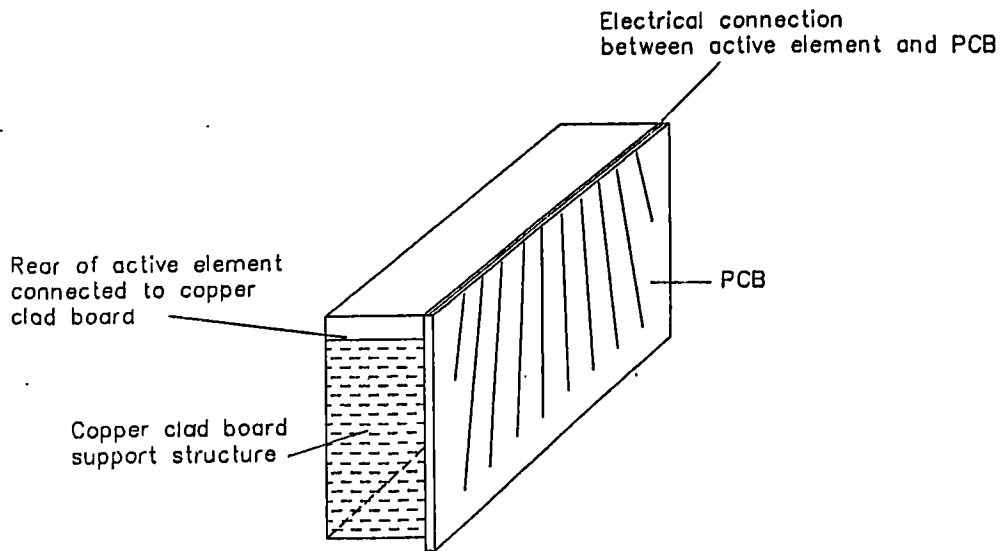


Figure C.4 Configuration of array prior to the sawing process

smooth, and pinch screws are provided to facilitate easy removal of the mould from the complete encapsulated array. Figure C.3 illustrates a typical design.

1.) A rectangular support structure is fabricated from copper clad board and the PCB. The transducer material is attached to the front surface. Any epoxy resin used during this procedure must have a high dielectric strength and a low water permeability. At this stage, both major surfaces of the array are fully electroded. In ceramic arrays, a soldered connection between the copper clad frame and the rear electrode surface is made. In a composite array, silver loaded epoxy is used. Also, in a composite array, care is taken to ensure alignment between the ceramic pillars and the PCB track geometry, so that after slicing the metallisation of the composite between groups of pillars, good alignment with the PCB tracks is obtained. Care is also taken to ensure that the metal tracks of the PCB are electrically isolated from the grounded copper planes. Figure C.4 illustrates the array at this stage.

2.) The front face electrical connections are made. In ceramic arrays, a continuous fine fillet of solder is employed between the PCB and the front surface of the array. This continuous strip is isolated into individual elements during the slicing process. Silver loaded epoxy is used for composite arrays.

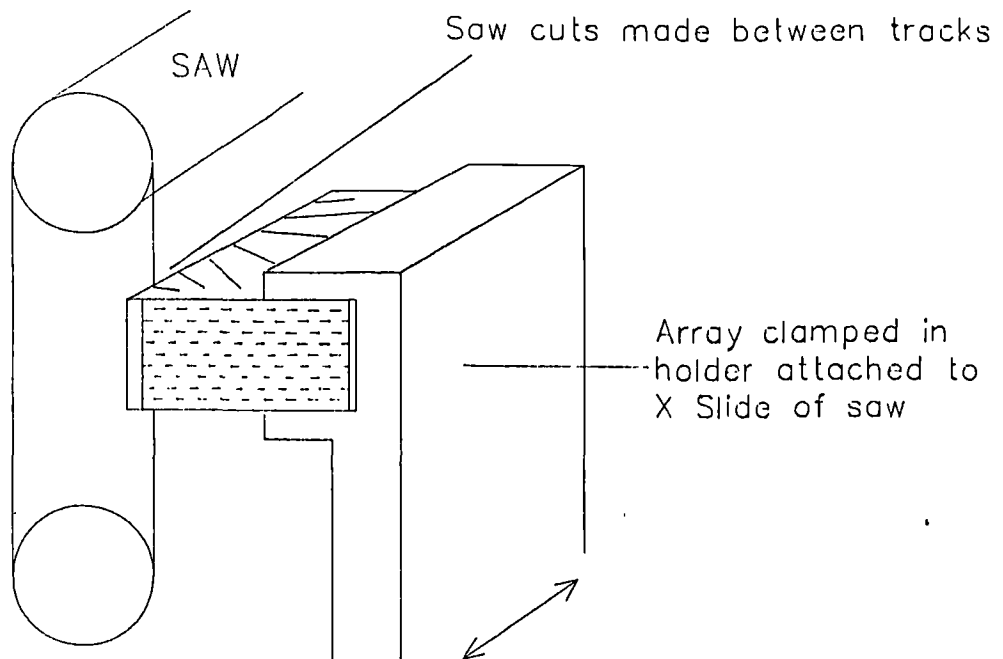


Figure C.5 Mounting of array with respect to the saw

- 3.) The backing material is mixed and poured carefully on to the rear array surface. Considerable attention is paid to achieving a complete and consistent coverage of the array surface in order that element uniformity across the array is maximised. The backing is allowed to set.
- 4.) The array is mounted in the saw, as illustrated in Figure C.5. Parallel cuts are made which align with the PCB tracks. In monolithic ceramic and composite arrays, the cut is only as deep as is required to electrically isolate the element electrodes. In a sliced ceramic array, the cuts are made through the ceramic and into the backing. These slots are slanting and of uneven depth, in order to minimise mechanical inter-element coupling. The slots are cleaned and dried thoroughly.
- 5.) An epoxy matching layer is cast and lapped to the required dimensions prior to bonding to the front face.
- 6.) Separate coaxial cables are terminated to each pad on the PCB. The cable screen braids are soldered to the copper clad boards, which form the array's electrical ground. A heavy electrical braid connects the copper clad boards in the array to the multipole connector, where a high quality ground connection is ensured by using typically nine ground pin connections. The signal cables are terminated to the appropriate pins in the connector, but the screen is trimmed back. Therefore, a star-connected ground is obtained, with no potential for circulating earth current loops.

7.) The PCB electrical connections are tested prior to being sealed with a layer of epoxy. Thereafter, a grounded copper foil screen is applied, which provides full electromagnetic screening, except at the front face.

8.) The encapsulant mould is assembled with its inner surfaces lightly coated with silicone grease. Spacers are bonded to the array so that the array is held rigidly in the correct position in the mould.

9.) Low viscosity epoxy, coloured if required, is poured slowly into the mould to form the encapsulant.

10.) Once the encapsulant has set, the mould pinch screws are used to gently ease the mould away from the array. The array is complete once the excess epoxy has been trimmed.

APPENDIX D

DEPOLARISATION IN A 1-3 COMPOSITE TRANSDUCER ATTRIBUTED TO THE SAWING PROCESS

Synthetic piezoelectric materials are polycrystalline, and therefore it is necessary to polarise them in order to align the dipoles in one direction. This process is normally achieved by subjecting the ceramic to a high DC electric field at an elevated temperature. However, these materials will depolarise if subjected to high thermal, mechanical or electrical stresses.

It has been observed that the electromechanical efficiency of composite transducers is frequently less than predicted by the theoretical approach described in Smith et al's paper [3]. This trend is borne out in the results in Figure 5.5. Furthermore, it is evident that the extent of the degradation is inversely proportional to volume fraction. It is proposed that the cause of the degraded performance is due to depolarisation occurring during the manufacturing process. This would explain why the depolarisation appears to be inversely proportional to volume fraction, as low volume fraction composites require more cutting during manufacture - if the same size of saw cut is used.

A simple model for predicting the dependence of depolarisation on volume fraction and saw cut width is presented. It is hypothesised that during the sawing, the ceramic adjacent to the cut surface is slightly

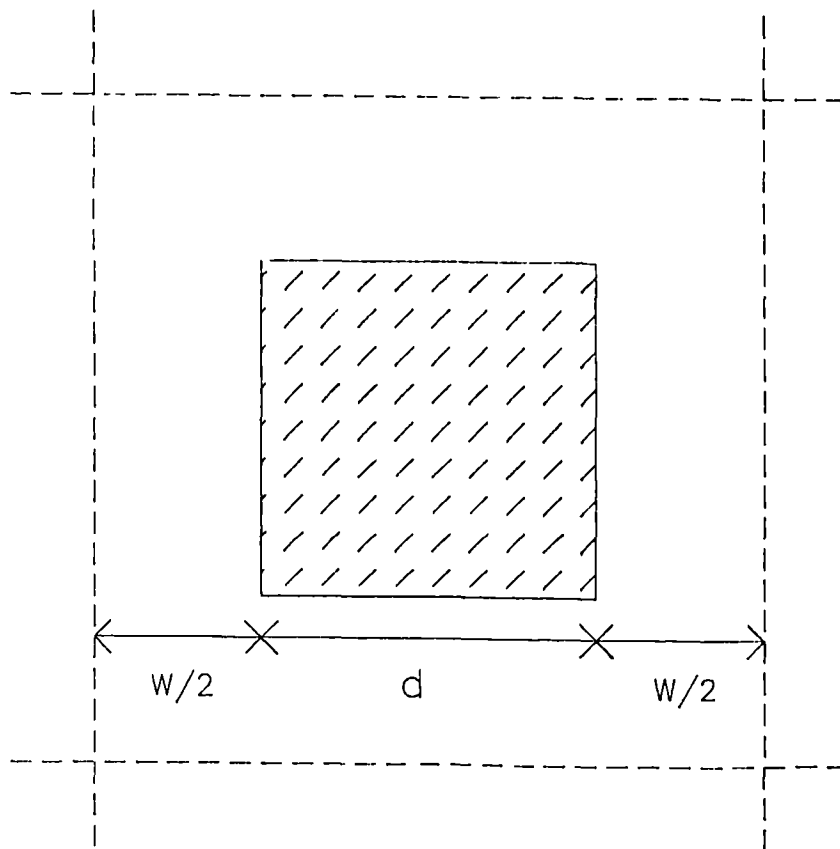


Figure D.1 Configuration of a composite unit cell

surface area to volume of ceramic. Consider the single unit cell in Figure D.1.

$$\text{By definition: } v = \frac{d^2}{(d+W)^2}, \quad \text{D1}$$

$$\text{Therefore: } d = \frac{\sqrt{vW}}{(1-\sqrt{v})} \quad \text{D2}$$

The depolarisation ratio may be defined as:

$$\frac{k \times \text{Area of Rod cut surface}}{\text{Volume of rod}}$$

Where k is a constant of proportionality, with units of length.

Since the thickness of the composite is uniform,

$$\begin{aligned} \text{Depolarisation ratio} &= \frac{k \times \text{Width of Rod}}{(\text{Width of Rod})^2} \\ &= \frac{k \times (1-\sqrt{v})}{(\sqrt{vW})} \end{aligned} \quad \text{D3}$$

The coupling coefficient, k_t , should therefore be modified by the following ratio:

$$k_t' = \delta k_t \quad \text{where } \delta = (1 - \text{depolarisation ratio})$$

Equation D3 indicates that the depolarisation is inversely proportional to volume fraction and saw cut width as expected from the discussion above. This result suggests that using fewer and wider saw cut widths can compensate for the depoling normally encountered in low volume fraction composites. However, wider spacings can lead to degraded vibrational characteristics, as discussed in Chapter IV.

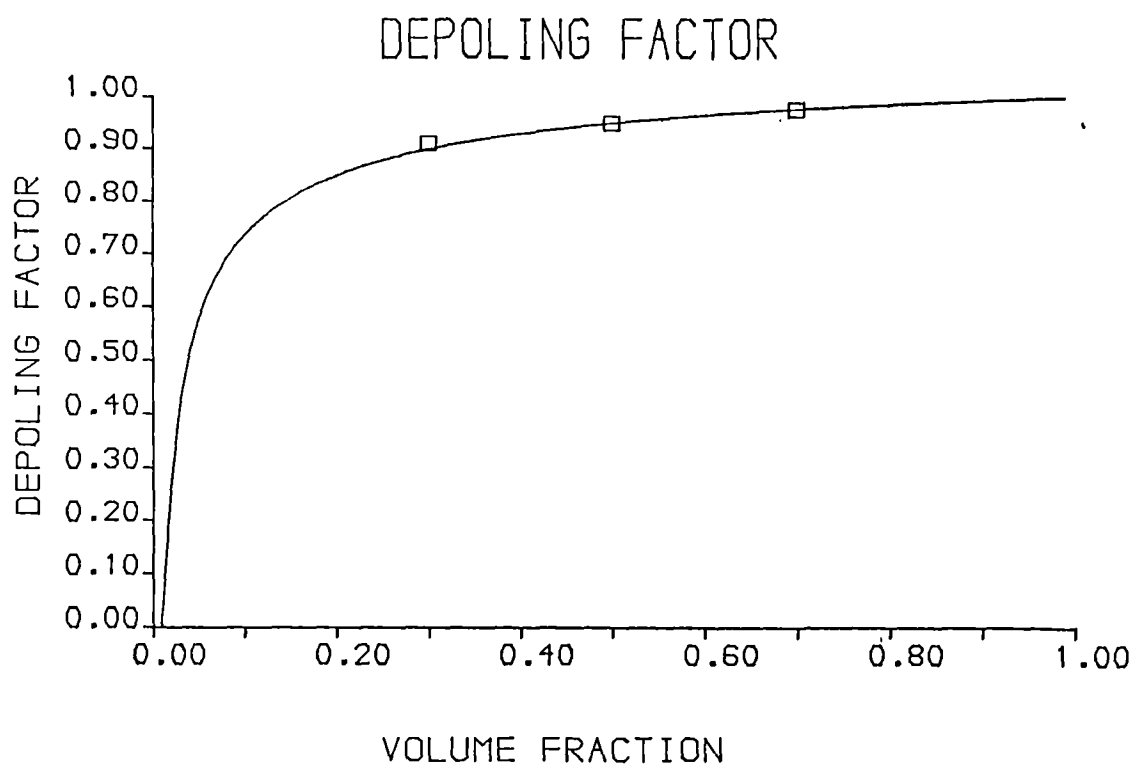


Figure D.2 Dependence of depolarisation factor on volume fraction. Saw cut width = 0.22mm
 Theoretical —————
 Measured □

degraded vibrational characteristics, as discussed in Chapter IV.

The depolarisation in 30%, 50% and 70% composites, similar to those described in the Chapter V, was measured. The k_t was monitored after manufacture and once again after repolarisation. Repolarisation was performed in accordance with the manufacturer's recommendations. A field on 2kVm^{-1} was applied at a temperature of 150°C for five minutes in an oil bath. The oil is necessary to maintain a constant temperature around the ceramic and to prevent dielectric breakdown through air. The measurement of k_t after repolarisation was delayed for one week to allow the value of k_t to stabilise. The resulting calculated depolarisation ratios ($k_{t \text{ OLD}}/k_{t \text{ REPOLED}}$) for the 30%, 50% and 70% devices were 0.909, 0.948 and 0.975 respectively. These results indicate that the proportionality constant in Equation D3 should be $2.7 \times 10^{-5} \text{m}$ for the saw cuts used here. This constant has been used to obtain the theoretical depolarisation ratio illustrated in Figure D.2. This curve correlates well with the experimental values which are also illustrated in Figure D.2. This constant has been used throughout to estimate the k_t value. A plot of the modified k_t is compared with a theoretical curve obtained by direct implementation of Smith's method, and with experimental results in Figure 5.5. The improved accuracy obtained by using this depolarisation factor is readily apparent.

It is clear that the actual depoling depends not only on the saw cut width and volume fraction, but also on the prevailing conditions encountered during the sawing process. Sawing at greater speed, using a higher cutting pressure, using a blunt blade/ wire, or cutting without adequate coolant will all contribute to a greater depolarisation effect than that predicted here. Care has been taken to minimise these effects for the results presented in the thesis.

An alternative method, which circumvents the depoling problem, is to repolarise all composite transducers after slicing. However, this is not recommended because of the severe thermally induced stresses encountered within the composite structure during the polarisation process. The linear coefficient of expansion of the polymer is approximately fifty times greater than that of the ceramic. The performance of a composite transducer depends critically on the quality of the bond between the ceramic pillar and the polymer, and therefore, this must not be damaged if at all possible.

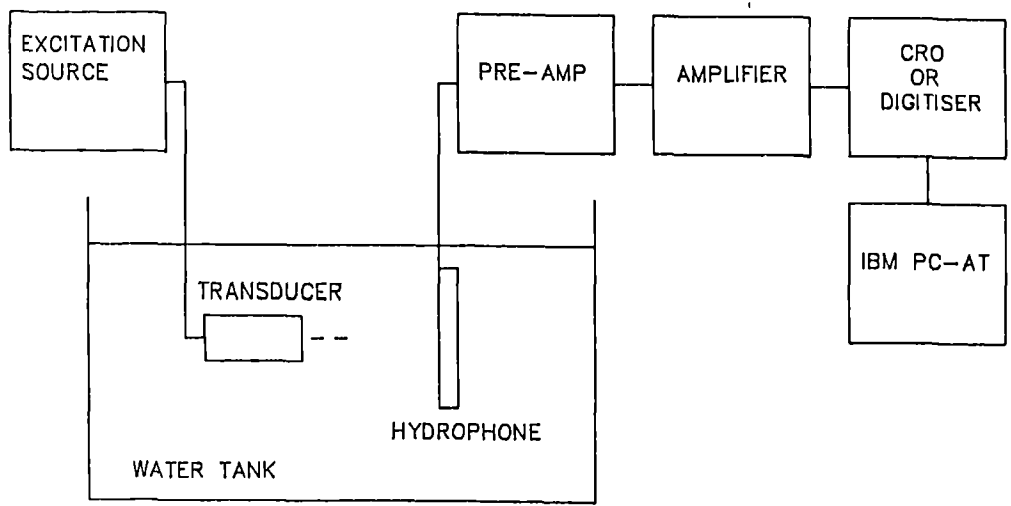


Figure E.1 Experimental apparatus for measuring pressure output

APPENDIX E

EXPERIMENTAL PROCEDURES

Details of the more important experimental configurations are outlined below. These are supplemented in the main text where necessary.

i) Impedance measurement

All impedance measurements were made using a HP 4194 impedance analyser. This instrument possesses a frequency stability of $\pm 0.1\text{ppm}$, an impedance magnitude accuracy of $\pm 0.2\%$ and a phase accuracy of $\pm 0.5^\circ$. The analyser possesses a GPIB. Hence, it was possible to transfer impedance data directly, via GPIB, from the HP 4194 to an IBM PC. The data was then transferred to a VAX mainframe for long term storage.

ii) Transducer pressure output measurement

The apparatus described in Figure E.1 has been used for monitoring transducer pressure output response. The hydrophone used was a PVDF membrane device supplied by GEC-Marconi. The active area is 0.8mm^2 and the mechanical resonant frequency is 44MHz. Unfortunately, the capacitance of the element is only 2.2pF and hence care is required in the design of a suitable pre-amplifier stage. Provided that the hydrophone is properly terminated, its response is flat to within +1dB over the range 50kHz to 20MHz. Although the hydrophone was expected to possess a very wide, undistorted directivity characteristic, very

recent work has indicated that the actual characteristic is somewhat degraded. However, the extent of any error in any of the results, caused by finite directivity is limited, since the hydrophone was generally sufficiently far from the source so as to minimise the effects of angular directivity.

The preamplifier was based on an OEI AH0013 precision, low noise operational amplifier. This amplifier possesses a gain of 12dB, ± 1 dB, over the range 20kHz to 5MHz. If necessary this preamplifier stage was supplemented by the voltage amplifier in a Panametrics 5052PR pulser. The gain of this amplifier is controllable.

The amplified waveform was monitored directly via an oscilloscope (Tektronix 466) or captured using a Tektronix 390AD programmable digitiser. This is a 10 bit digitiser possessing a maximum sampling rate of 60MHz. The digitised data was transferred to a host computer via a GPIB.

CW Excitation

A Tektronix FG 504 function generator was used to provide a gated sinusoidal burst of approximately twenty cycles. The length of the burst, and the repetition rate, were selected so that steady state CW conditions were obtained, without interference from multiple reflections within the tank. This generator possesses a measured output impedance of $50\Omega \pm 2\Omega$ over the range 100kHz to 1MHz. During the course of some experiments, the effect of this output impedance was effectively compensated out using the

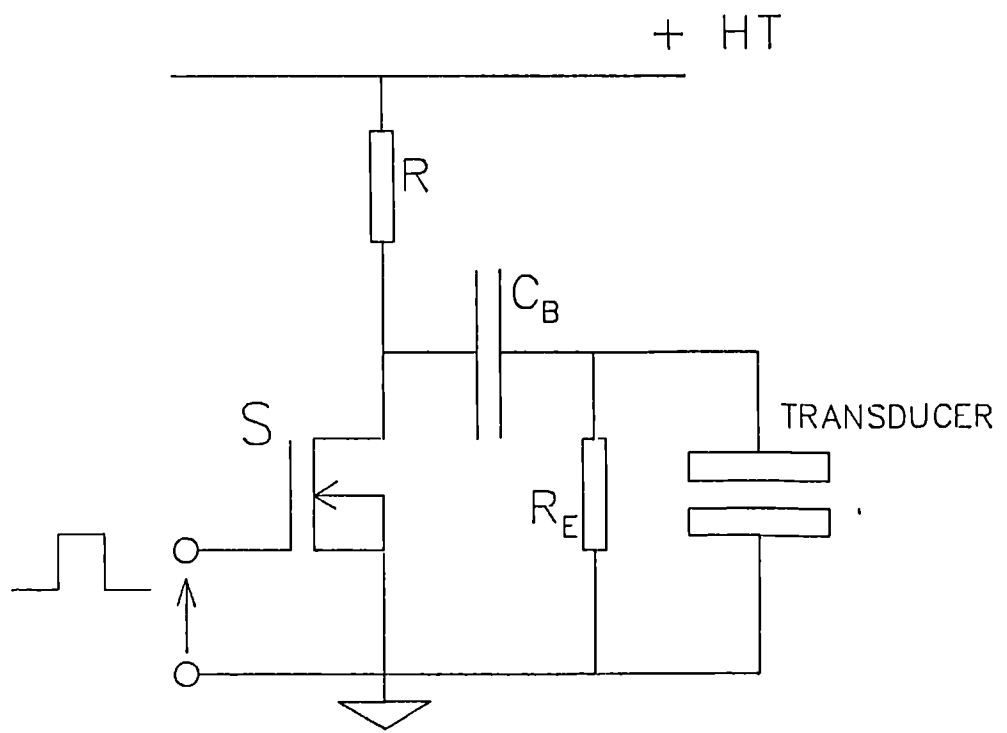


Figure E.2 Pulse Excitation circuit

following technique. The voltage applied at the transducer terminals was monitored and the generator output level adjusted so that the transducer terminal voltage remained constant, independent of the current drawn and the associated voltage drop across the internal 50Ω impedance.

Transient Excitation

A standard excitation circuit, similar to that described by Hayward [73], has been employed. This circuit is illustrated in Figure E.2. The circuit comprises of a transducer and matching load, R_E , in parallel. The blocking capacitance, C_B , is charged to a high voltage via R . When the fast electronic switch, S , is closed, the charge on C_B is transferred to the transducer and load. Unless specified otherwise, C_B is 10nF and R_E is 100Ω . The switch is an IRF830 fast MOSFET switch. This possesses a turn-on time of 30ns and an 'on' resistance of 1.3Ω . The influence of the characteristics of a similar pulser circuit on transducer performance has been described by Hayward [73].

The source was placed at range of either 60mm or 75mm , depending on the size of the source, from the hydrophone. Care was taken to ensure axial alignment of the source and hydrophone active area. These precautions minimised the influence of diffraction effects.

ii) Transducer reception sensitivity measurements

Measurement of the reception sensitivity of a transducer requires a calibrated acoustic source. Although no

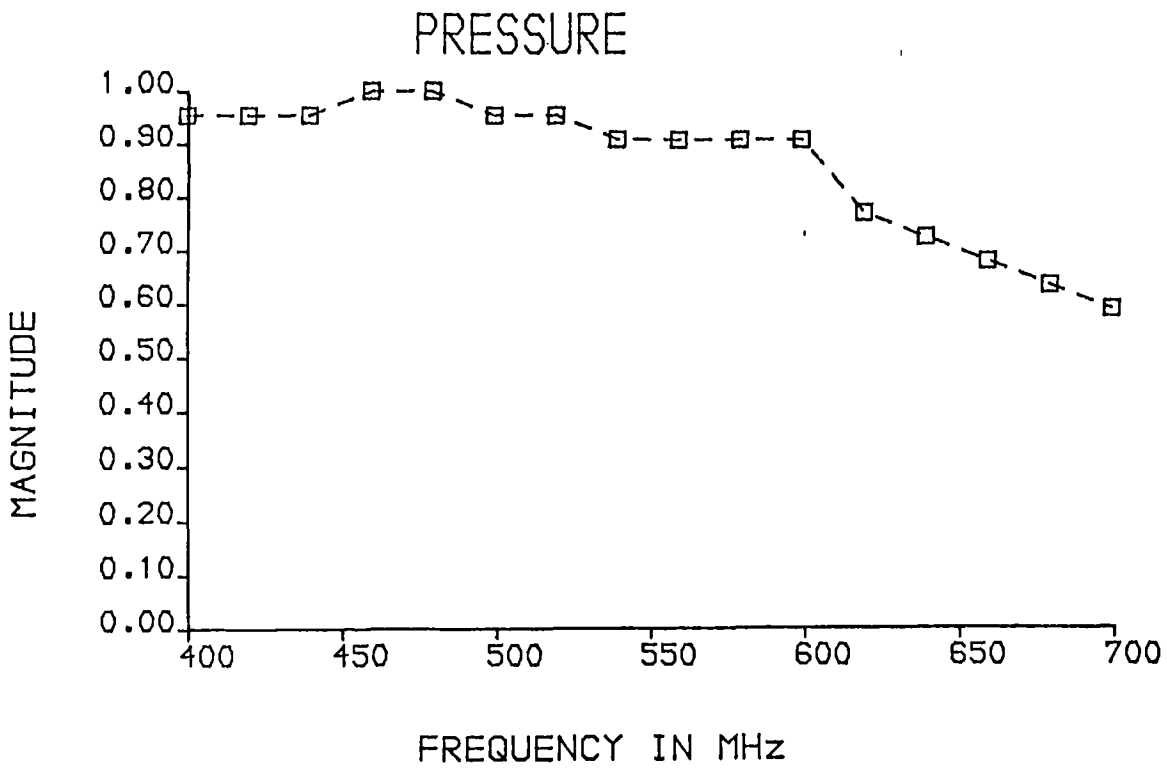


Figure E.3 Calibration curve for pressure output for the source used in the reception sensitivity tests. Range = 100mm.

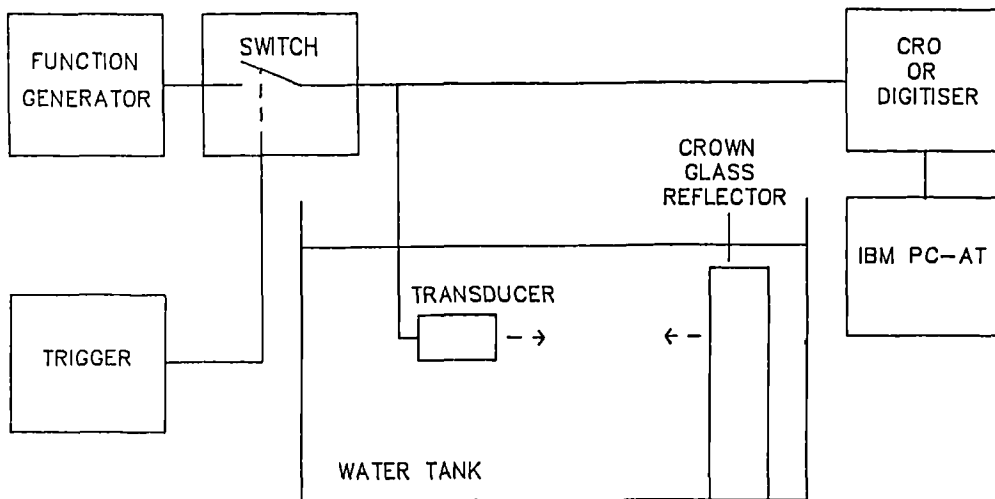


Figure E.4 Experimental apparatus for measuring pulse-echo response.

calibrated source existed, it was possible to calibrate a wideband, backed and matched 500kHz transducer by monitoring its output using a PVDF membrane hydrophone. The frequency of the CW excitation was varied from 400kHz to 700kHz and the output of the hydrophone monitored. It was known that the response of the hydrophone was flat to within ± 1 dB over this frequency range, and hence a relative measure of the output of the transducer could be obtained. A constant range of 100mm between source and receiver was used. This range is close to the nearfield/farfield transition zone at the upper end of this frequency range. Hence, variation in intensity due to diffraction effects were minimised. The measured transmission response of the calibrated source, illustrated in Figure E.3, is reasonably flat over the frequency range up to 600kHz. The calibrated source could then be used to produce a known pressure response, at a range of 100mm, as a function of frequency. Hence, the PVDF hydrophone was replaced by the transducer under test and a measure of voltage sensitivity, taking account of the calibrated pressure response of the source, could be obtained.

iv) Pulse-echo measurement

The pulse-echo measurement apparatus is illustrated in Figure E.4. A 50mm thick crown glass reflector was positioned at a range of 100mm from the transducer. This was carefully aligned to as to maximise the reflected response.

CW Excitation

A Tektronix FG 504 function generator was used to provide a gated sinusoidal burst of approximately twenty cycles. Since the generator possesses a 50Ω source impedance, it was necessary, for some of the experiments, to isolate this 50Ω impedance in reception. This was achieved using a DG 308 analogue switch, triggered by the same pulse as used to gate the sinusoidal packet. This device possesses an 'on' resistance of 50Ω .

Transient Excitation

The same circuit as that described in section ii) above was used. The matching resistance (100Ω) was not isolated in reception, and hence this impedance dominates the receiver load impedance.

The amplitude of the pulse-echo signals were generally large enough to be monitored directly, via an oscilloscope, or captured using a Tektronix 390AD digitiser.

v) Measurement of acoustic field characteristics

A versatile, automated acoustic test tank facility has been developed. The transducer is positioned near one end of the tank and a receiver probe manoeuvred within the field and the pressure response monitored at each position in the field. The transducer holder can be aligned by rotating it to the correct position. Additionally, it possesses a facility for tilting vertically so that accurate alignment in all directions is achievable.

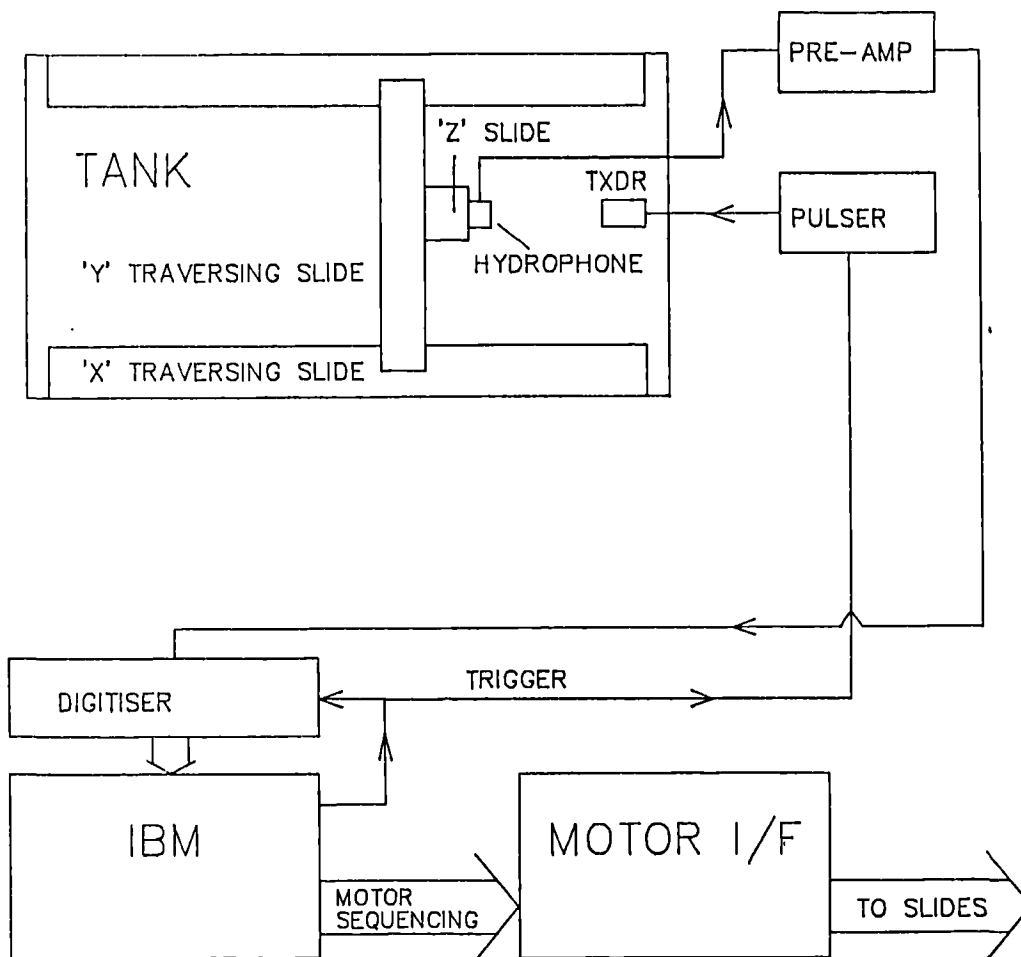


Figure E.5 Configuration of the automated acoustic calibration tank.

Figure E.5 illustrates the configuration of the test tank. The scanning range is 1.5m axially (Z direction), 75cm transversely (X direction) and 25cm vertically (Y direction). Aluminium dovetail slides, with lead screws driven by stepper motors are used for positioning the probe. Each of the motors operate in units of four steps which correspond to linear movements of 0.04mm axially and vertically, 0.02mm vertically and a rotational movement of the transducer holder of 0.144°. Microswitches are positioned at the limits of the slides. If the probe exceeds its permitted range, then a switch will close. This will be detected by the controlling computer which will immediately abandon the scan. The computer controls the slides by generating the motor control sequences on its output port. An interface generates the appropriate 24V motor coil pulses. Once the receiver is in the correct position, the computer simultaneously triggers the pulser and Tektronix 390AD digitiser. The computer controls the digitiser via GPIB and sets up the appropriate voltage range, sampling rate, trigger level, and the time cursor positions. Thus the digitiser only digitises in the vicinity of the expected pulse. The digitised pulse is transferred to the computer where the peak to peak value is detected and stored in a file. The process is repeated until the scan is complete. The system is equally capable of making angular directivity plots, linear (eg axial) directivity measurements or full 2-D or 3-D scans.

APPENDIX F

LIST OF PUBLICATIONS RESULTING FROM THE THESIS

1. G Hayward and J Hossack 'Computer models for the analysis and design of 1-3 composite transducers' Proc. Ultrasonics International 1989
2. J Hossack and G Hayward 'Design and evaluation of one and two dimensional composite transducer arrays using finite element analysis' Proc. Ultrasonics International 1989
3. J Hossack, Y Gorfu and G Hayward 'The modelling and design of composite piezoelectric arrays' Proc. IEEE Ultrasonics Symposium 1989
4. V Murray, G Hayward and J Hossack 'Spatial apodisation using modular composite structures' Proc. IEEE Ultrasonics Symposium 1989
5. G Hayward and J Hossack 'Unidimensional modelling of 1-3 composite transducers' J. Acoust. Soc. Am. (in print June 1990)
6. J A Hossack and G Hayward 'Finite element analysis of 1-3 composite transducers' submitted to J. Acoust. Soc. Am.
7. J A Hossack and G Hayward 'Efficient calculation of the transient radiation from a rectangular baffled piston' submitted to J. Acoust. Soc. Am.

8. J Hossack and G Hayward ' Assessment of different pillar geometries for 1-3 composite transducers using finite element analysis' IEEE Ultrasonics Symposium 1990 (provisional)

9. J Hossack and G Hayward 'Efficient calculation of the beam profiles of steered ultrasonic arrays' IEEE Ultrasonics Symposium 1990 (provisional)